



**HAL**  
open science

# Thermal control of all-optical switching in magnetic heterostructures and magnetoplasmonic metasurfaces

Maxime Vergès

► **To cite this version:**

Maxime Vergès. Thermal control of all-optical switching in magnetic heterostructures and magnetoplasmonic metasurfaces. Physics [physics]. Université de Lorraine, 2023. English. NNT: 2023LORR0042 . tel-04354050

**HAL Id: tel-04354050**

**<https://hal.univ-lorraine.fr/tel-04354050>**

Submitted on 19 Dec 2023

**HAL** is a multi-disciplinary open access archive for the deposit and dissemination of scientific research documents, whether they are published or not. The documents may come from teaching and research institutions in France or abroad, or from public or private research centers.

L'archive ouverte pluridisciplinaire **HAL**, est destinée au dépôt et à la diffusion de documents scientifiques de niveau recherche, publiés ou non, émanant des établissements d'enseignement et de recherche français ou étrangers, des laboratoires publics ou privés.



**UNIVERSITÉ  
DE LORRAINE**

**BIBLIOTHÈQUES  
UNIVERSITAIRES**

## AVERTISSEMENT

Ce document est le fruit d'un long travail approuvé par le jury de soutenance et mis à disposition de l'ensemble de la communauté universitaire élargie.

Il est soumis à la propriété intellectuelle de l'auteur. Ceci implique une obligation de citation et de référencement lors de l'utilisation de ce document.

D'autre part, toute contrefaçon, plagiat, reproduction illicite encourt une poursuite pénale.

Contact bibliothèque : [ddoc-theses-contact@univ-lorraine.fr](mailto:ddoc-theses-contact@univ-lorraine.fr)  
*(Cette adresse ne permet pas de contacter les auteurs)*

## LIENS

Code de la Propriété Intellectuelle. articles L 122. 4

Code de la Propriété Intellectuelle. articles L 335.2- L 335.10

[http://www.cfcopies.com/V2/leg/leg\\_droi.php](http://www.cfcopies.com/V2/leg/leg_droi.php)

<http://www.culture.gouv.fr/culture/infos-pratiques/droits/protection.htm>



# Thermal control of all-optical switching in magnetic heterostructures and magnetoplasmonic metasurfaces

## THÈSE

présentée et soutenue publiquement le 31 Mars 2023

pour l'obtention du

Doctorat de l'Université de Lorraine

(en Physique)

par

Maxime Vergès

### Composition du jury

<i>Rapporteurs :</i>	Oksana Chubykalo-Fesenko	Instituto de Ciencia de Materiales de Madrid
	Paolo Vavassori	CIC nanoGUNE - San Sebastian
<i>Examineurs :</i>	Emmanuelle Jal	LCPMR - Paris
	Bert Koopmans	TU Eindhoven ( <i>Président du jury</i> )
	Sebastiaan van Dijken	Aalto University - Espoo
<i>Invités :</i>	Jean-Loïs Bello	Vinci Technologies - Paris
	Julius Hohlfeld	Université de Lorraine
<i>Directeur de thèse :</i>	Stéphane Mangin	Université de Lorraine

---

Institut Jean-Lamour - UMR 7198 - Université de Lorraine

Département de Physique de la Matière et des Matériaux

Nanomagnétisme et Electronique de spin

Mis en page avec la classe thesul.

## Résumé

La possibilité de contrôler l'ordre magnétique sur des échelles de temps extrêmement courtes a concentré beaucoup d'attention autour du magnétisme ultra-rapide. Cette thématique de recherche est d'importance capitale pour le développement de futures mémoires de données exigeant moins d'énergie pour une vitesse d'écriture plus rapide. Ce n'est que lors de la dernière décennie qu'il a été montré qu'il est possible de renverser de manière déterministe l'aimantation avec des impulsions laser femtoseconde dans certains matériaux tels que GdFeCo ou MnRuGa. Le retournement tout optique de l'aimantation dans ces matériaux ne dépend pas de l'hélicité de la lumière incidente (on parle alors de *All Optical Helicity-Independent Switching* - AO-HIS) et peut être effectué après une impulsion laser femtoseconde unique. L'AO-HIS est cependant restreint à certains matériaux ferrimagnétiques, et loin d'être général. Le mécanisme clé est la quantité d'énergie transmise au système via la lumière.

Dans cette thèse nous proposons plusieurs stratégies pour contrôler cet effet thermique. Dans une première approche, nous considérons des arrangements périodiques de nano-disques de [Co/Gd/Pt] sur substrat de verre. Ces structures montrent des résonances de réseau de surface dans le domaine visible et se caractérisent par une forte absorption d'énergie lumineuse par le système considéré. Nous montrons que l'excitation de ce mode optique permet de réduire de 400 % la fluence seuil pour laquelle l'AO-HIS est observé. Par ailleurs, l'excitation de la résonance plasmonique augmente l'activité magnéto-optique par plus de 5000 %, ce qui est prometteur pour une sensibilité de lecture fiable. Une étude conjointe menée avec un angle d'incidence oblique a permis de mettre en lumière l'existence de résonances de réseau de surface dont l'origine est magnétique, résultat important d'un point de vue fondamental.

Dans une deuxième approche le système multicouche GdFeCo/Cu a été étudié. Nous montrons que pour une couche de Cu de plus en plus épaisse, le système électronique est mieux refroidi permettant ainsi d'observer l'AO-HIS pour une plage de fluences plus grande pour un temps d'impulsion donné. Ainsi la couche de Cu peut jouer le rôle de dissipateur de chaleur. La conséquence directe est la possibilité, pour les échantillons à grande épaisseur de Cu, d'étendre l'AO-HIS jusqu'à des temps d'impulsion de 25 picosecondes. Cette étude devrait faciliter l'intégration de l'AO-HIS dans les périphériques de stockage de données de demain.

**Mots-clés:** Magnétisme, Physique ultra rapide, Plasmonique.

## Abstract

The opportunity to control magnetic order at the short time scale focused a lot of attention around ultrafast magnetism. This research topic is of primary importance for the development of data storage devices that seek faster magnetization reversal combined with energy efficiency. It has been shown over the last decade that magnetization can be reversed deterministically by means of a single ultrafast arbitrary polarized laser pulse, so-called All Optical Helicity-Independent Switching (AO-HIS). So far, this kind of light-induced magnetization reversal is restricted to a few ferrimagnetic materials such as GdFeCo or MnRuGa. Since AO-HIS can be performed with linearly polarized ultrafast laser pulses, it is believed that the underlying physics stands for a pure thermal effect, meaning that only the amount of energy transferred from the incoming light to the electronic system matters.

In this work we propose various strategies to control this thermal effect. First we consider a periodic arrangement of [Co/Gd/Pt] nanodisks on glass substrate. These structures have been shown to exhibit surface lattice resonances in visible range, characterized by a strong absorption enhancement. In this way we demonstrate that the excitation of such optical mode leads to a reduction of the threshold fluence for observing AO-HIS by 400 %. Also, such collective resonances enhance the magneto-optical activity by 5000 %, promising for a reliable readout sensitivity. Probing the magneto-optical behaviour of the metasurfaces with an oblique angle of incidence reveals the existence of magnetism-induced surface lattice resonances. We believe that this latter result is important from fundamental point of view.

The second strategy involves the multilayer system GdFeCo/Cu. We show that thicker Cu layers allows the electronic system to cool down more efficiently so that AO-HIS can be observed for a larger range of fluences for a given pulse duration. Thus this adjacent Cu layer plays the role of a heat sink. A direct consequence is the possibility, for samples with thick Cu layers, to extend AO-HIS to larger pulse durations, until 25 picoseconds. This study must facilitate the integration of AO-HIS in future magnetism-based data storage devices.

**Keywords:** Magnetism, Ultrafast physics, Plasmonics.

## Acknowledgments

This manuscript concludes three years of intense work and I would like to thank all the people who supported me in reaching this point.

First of all, I would like to thank very much my Ph.D. supervisor Stéphane Mangin. First making me discover the field of magnetism in Taiwan in the research group of Chih-Huang Lai during my graduate studies. Second for hiring me as a Ph.D. student focusing on what I present in this thesis but also for all the subsequent opportunities. I am really grateful for your guidance and your kindness.

Secondly, I would like to thank my unofficial but very professional co-supervisor Julius Hohlfeld greatly. I substantially enjoyed working with you. We went through hard times and failures days and nights in the lab but we made it. It definitely would not have been the same journey without you. I appreciated your feedbacks, your suggestions and more than that, your endless kindness and support. You are one of the nicest person that I know.

Then I would like to thank Sebastiaan van Dijken for his significant involvement in my work. You are the collaborator everyone wants to work with. You always found some time for very interesting discussions and gave me nice advices so that I could improve myself. Concrete exchanges with Sreekanth Perumbilavil and Nikolai Kuznetsov brought a strong added value to my work. You also accepted to get involved in my monitoring committee and later on in my Ph.D. defense. I will be eternally thankful for your support.

I want to thank Vinci Technologies which funded this work. In particular I thank the trust given by Christine Walsh, Renaud Presberg and Jean-Marcel Vannieuwenhuyse for their flexible management and the freedom given in the management of my projects.

I am also grateful to the two reviewers of the jury, Oksana Chubykalo-Fesenko and Paolo Vavassori, for reading my manuscript very carefully and all the discussions we had during my Ph.D. defense. I also thank all the remaining members of the jury, Emmanuelle Jal, Bert Koopmans and Jean-Loïs Bello, for their interest in my work.

My work also could not have been possible without the professionalism of the other members of the Nanomagnetism and Spintronics team at Institut Jean Lamour. In particular, I thank Michel Hehn for sample growth (simply the best) and the relationship we have forged over the past few years, Daniel Lacour for the atomic and magnetic force microscopy sessions and intense discussions related to Jazz, Star Wars, offbeat shirts, François Montaigne for the good time spent together in the clean rooms.

Other people not from the Nanomagnetism and Spintronics team helped me as well to build myself. I would like to start with the dream team made of Laurent Badie and Demba Ba, you

made my life much easier in the clean rooms. I am also grateful to Silvère Barrat and Stéphane Andrieu for allowing me to be teaching assistants in their respective courses.

I could have overcome such journey without the support of my friends. Among them I would like to highlight Quentin R.<sup>1</sup>, Jean-Loïs B.<sup>2</sup>, Gregory M., Jon G.<sup>3</sup>, Alberto<sup>3</sup>, Héloïse<sup>3</sup>, Yi, Wei Z., Charles G., Yann L.-G.<sup>3</sup>, Sébastien P.-W., Valentin D., Sandrine L., Danny P., Victor P., Eva D. (the best of the best), Anna Maria F., Mariam M., Maryam M., Kosseila A.-O., Junta I., Junxiao L., Antoine M., Killian H., Thomas G., Nathan B., Corentin P., Lucie G., Sébastien G., Thiago, T. T. and Catalina R. M.. I could also rely on the support of friends outside of Institut Jean Lamour. I especially thank Thibaut D., Mickaël R.<sup>4</sup>, Louise R.<sup>4</sup>, Paul B.<sup>5</sup>, Sandra A.<sup>3</sup>, Pauline V., Ségolène F., Annabelle N., Eva C., Vincent C., Sophie G. Y., Julien Y., Robin D., Pierre-Alexis D., Sarah V., Ilsé R., François M., Laura K., Louise M., Pauline B., Ekaterina T., George Z. and Nikita K. I sincerely thank you for your support.

1) My co-worker Quentin who helped me to go through this unexcepted journey. Besides being an excellent scientist, your company gave me happiness even in the darket of times. We are now flying towards very different horizons (about 200 meters apart) but our friendship remains preserved.

2) My second brother in arms Jean-Loïs who gave me the honor to be in my Ph.D. defense jury. Your absolute mastery of sarcasm impressed me. This adventure has been dotted with very pleasant moments and for most of them you are the cause.

3) This three years experience was unique especially with the meeting of exceptional beings such as Jon, Alberto, Héloïse, Yann and Sandra. It was mostly based on extra professional moments with intense sessions of Dune Imperium, Nemesis, Clank and Lost Ruins of Arnak. Alberto you are as good a professional as a game master. I hope we will be able to keep in touch with Sandra.

4) Mes chers amis Louise et Mickaël qui m'ont transmis la valeur du travail et de la résilience à travers le sport. Vous m'avez appris des concepts forts qui m'ont guidé lors de mes études et qui m'ont permis de mener à bien cette thèse de doctorat. Merci pour tout.

5) Mon ami de toujours Paul B. avec qui j'ai traversé beaucoup d'épreuves depuis le début de mes études. C'est notamment grâce à toi que j'ai appris ce qu'est la rigueur et le professionnalisme. Je te dédié en partie ce travail de thèse en gage de toute l'affection que je te porte.

Rien de tout cela n'aurait été possible sans le soutien inconditionnel de ma famille, et ce depuis bien plus longtemps que depuis le début de cette thèse de doctorat. Ainsi je tiens à remercier mes cousins Amalia et Aurélien, ma tante Alexandra, mon oncle Arnault, mes grands parents Jeannine, Etienne, Michelle et Jean ainsi qu'Anne et Rodolphe, mes beaux-parents Flo-

rence et Henri et mon beau-frère Paul. Enfin je dédie ces travaux de thèse à mes parents, mon frère Louis et ma compagne Manon. Chaque enfant rêverait d'avoir des parents comme vous, je vous aime d'un amour inconditionnel. Louis, merci d'être le meilleur frère que l'on puisse espérer, je t'aime. Manon, cette thèse c'est aussi la tienne, je n'aurai jamais assez de mots pour te remercier à la hauteur de ton soutien. Je t'aime.





***"Fear is the worst enemy of progress" Noah (Dark)***

***"What we know is a drop, what we don't know is an ocean" Isaac Newton***

***A mes parents***

***A mon frère***

***A Manon***



# Contents

<b>1</b>	<b>General introduction</b>	<b>1</b>
1.1	Introduction . . . . .	2
1.2	Ultrafast magnetism . . . . .	3
1.3	Plasmonics . . . . .	4
1.4	Geopolitics of ressources . . . . .	5
1.5	Scope of this thesis . . . . .	6
<b>2</b>	<b>All-optical magnetization switching</b>	<b>9</b>
2.1	Introduction . . . . .	10
2.2	Conventional magnetization dynamics . . . . .	10
2.2.1	Landau-Lifschitz equation . . . . .	10
2.2.2	Landau-Lifschitz-Gilbert equation . . . . .	12
2.3	Rare-earth transition-metal alloys . . . . .	12
2.3.1	Magnetization . . . . .	13
2.3.2	Exchange . . . . .	13
2.3.3	Anisotropy . . . . .	14
2.3.4	Compensation temperatures . . . . .	17
2.4	From non-equilibrium electron heating to all-optical magnetization switching . . . . .	19
2.4.1	Emergence of ultrafast physics . . . . .	19
2.4.2	Ultrafast demagnetization . . . . .	20
2.4.3	All-optical magnetization switching . . . . .	23
2.5	Open questions . . . . .	30
2.6	Conclusion . . . . .	30

## CONTENTS

---

<b>3 Plasmonics</b>	<b>31</b>
3.1 Introduction . . . . .	32
3.2 Fundamentals of classical electrodynamics in solids . . . . .	32
3.2.1 Maxwell's equations . . . . .	32
3.2.2 Boundary conditions . . . . .	35
3.2.3 Importance of local response approximation . . . . .	35
3.2.4 Drude model, description and limits . . . . .	36
3.3 Plasmonics . . . . .	38
3.3.1 Surface plasmon polariton . . . . .	39
3.3.2 Localized surface plasmon resonance . . . . .	47
3.3.3 Surface lattice resonance . . . . .	54
3.4 Magneto-optical effects . . . . .	59
3.4.1 Light polarization . . . . .	59
3.4.2 Magneto-optical Kerr effect . . . . .	61
3.4.3 MOKE geometries . . . . .	62
3.4.4 Magnetic nanodisks . . . . .	62
3.5 Conclusion . . . . .	64
<b>4 Magnetoplasmonic, a constantly evolving topic</b>	<b>65</b>
4.1 Introduction . . . . .	66
4.2 Near-field transducer . . . . .	66
4.3 Energy efficient control of magnetization at nanoscale . . . . .	70
4.4 Magneto-optical activity enhancement . . . . .	75
4.5 Conclusion . . . . .	79
<b>5 Methodology</b>	<b>81</b>
5.1 Introduction . . . . .	82
5.2 Thin films deposition and characterizations . . . . .	82
5.2.1 DC sputtering technique . . . . .	82
5.2.2 E-beam evaporation . . . . .	82
5.2.3 MOKE magnetometer . . . . .	83

5.2.4	Measurement of optical spectra . . . . .	85
5.3	Fabrication techniques . . . . .	87
5.3.1	Electron-beam lithography . . . . .	87
5.3.2	Patterning transfer . . . . .	92
5.4	Ultrafast lasers . . . . .	94
5.4.1	Ultrafast laser pulses . . . . .	94
5.4.2	MOKE microscopy . . . . .	100
5.4.3	Time-resolved MOKE microscopy . . . . .	101
5.5	Simulations . . . . .	103
5.6	Conclusion . . . . .	104
<b>6</b>	<b>Energy efficient single pulse all optical switching</b>	<b>105</b>
6.1	Motivations . . . . .	106
6.2	Energy efficient all-optical magnetization switching with plasmonics . . . . .	106
6.3	Switching endurance of magnetic nanodisks . . . . .	114
6.4	Collective resonances enhance magneto-optical response . . . . .	119
6.5	Comment on periodic arrays of GdFeCo nanodisks . . . . .	121
6.6	Conclusion . . . . .	122
<b>7</b>	<b>Magnetism-induced surface lattice resonances</b>	<b>123</b>
7.1	Motivations . . . . .	124
7.2	Surface lattice resonances and Kerr effect . . . . .	124
7.3	Evidence of magnetism-induced surface lattice resonances . . . . .	128
7.4	Conclusion . . . . .	132
<b>8</b>	<b>Control of all-optical switching by means of Cu heat sinks</b>	<b>135</b>
8.1	Motivations . . . . .	136
8.2	Control of all-optical magnetization switching of GdFeCo with Cu heat sinks . . . . .	137
8.2.1	Determination of threshold fluences and beam spot size . . . . .	138
8.2.2	Impact of heat sink thickness on TIMS . . . . .	140
8.3	Theoretical approach . . . . .	143

## CONTENTS

---

8.3.1	First step : 2TM . . . . .	143
8.3.2	Second step : Spin dynamics . . . . .	144
8.3.3	Results . . . . .	147
8.4	Conclusion . . . . .	148
<b>9</b>	<b>Conclusion</b>	<b>151</b>
	<b>Bibliography</b>	<b>157</b>
	<b>Appendix</b>	<b>203</b>
<b>A</b>	<b>Matlab code for Mie theory</b>	<b>203</b>
<b>B</b>	<b>Jones formalism</b>	<b>207</b>
<b>C</b>	<b>Scanning electron microscopy of magnetic metasurfaces</b>	<b>209</b>
<b>D</b>	<b>Extinction spectra of magnetic metasurfaces</b>	<b>217</b>
<b>E</b>	<b>Magneto-optical spectra of magnetic metasurfaces</b>	<b>225</b>
<b>F</b>	<b>Demonstration of magnetism-induced surface lattice resonances in magnetic metasurfaces</b>	<b>233</b>

# List of Figures

2.1	Sketch of magnetization precession for (a) undamped motion (b) damped motion.	11
2.2	Coupling between a transition-metal element and a (a) heavy (b) light rare-earth element . . . . .	14
2.3	Macroscopic representation of (a) speromagnetism (b) asperomagnetism (c) sperimagnetism and (d) ferrimagnetism. . . . .	15
2.4	Saturation magnetization as function of temperature for (a) GdFe alloys, (b) GdCo alloys and (c) TbFe alloys. The solid and dashed lines are derived from the mean-field theory. Figure adapted from reference 58. . . . .	17
2.5	(a) Magnetization precession frequencies $\omega_{FMR}$ and $\omega_{ex}$ as function of temperature. $\omega_{FMR}$ and $\omega_{ex}$ denote the ferromagnetic and exchange resonances, respectively. The insets sketch these modes. The solid lines show what to expect theoretically. (b) Gilbert damping parameter $\alpha_{eff}$ as function of temperature. Lines are guides to the eye. Figure adapted from reference 64. . . . .	18
2.6	Transient reflectivity measured on gold films 50, 100, 200 and 300 nm thick. The sample is excited from thin film side while the system is probed from the substrate. Figure from reference 71. . . . .	19
2.7	Transient remanent longitudinal MOKE signal of a Ni(20 nm)/MgF2(100 nm) film for 7 mJ/cm <sup>2</sup> pump fluence. The signal is normalized to the signal measured in the absence of pump beam. The line is a guide to the eye. Figure and caption from reference 6. . . . .	21
2.8	(a) Direct comparison of experimental data for delay > 0.3 ps with the fit (solid line) describing equilibrium from reference 97. (b) Same kind of experimental for three fluences over all the time delay range. The deviations from the Weiss model indicate an out-of-equilibrium state of electron and spin systems in the first 0.3 ps. Figure from reference 85. . . . .	22

## LIST OF FIGURES

---

- 2.9 (a) MO image of the initial magnetic state of the sample before laser exposure. Bright and dark areas are attributed to magnetic domains whose magnetization points up and down, respectively. (b) Domain pattern resulting from sweeping the sample at low speed ( $30 \mu\text{m}/\text{s}$ ) with linearly (L), right-handed ( $\sigma_+$ ), and left-handed ( $\sigma_-$ ) circularly polarized beams with a laser fluence of about  $11.4 \text{ mJ}/\text{cm}^2$ . The central area of the remaining spots at the end of each scan line consists of small magnetic domains, where the ratio of up to down magnetic domains is close to 1. Figure from reference 7. . . . . 23
- 2.10 Transient dynamics of Fe (open circles) and Gd (filled circles) magnetic moments in the first (a) 3 ps and (b) 12 ps. The sample temperature has been fixed at 83 K and the fluence of the laser excitation was  $4.4 \text{ mJ}/\text{cm}^2$ . Experimental time resolution of 100 fs is depicted by the solid Gaussian profile. The fits (depicted in solid lines) stands for a double exponential fit function. The dashed line in both panels describes the magnetization of the Fe sublattice taken with the opposite sign. Figure from reference 8. . . . . 25
- 2.11 (a) and (b) Initial saturated magnetized state of the alloy thin film with magnetizations pointing up and down with light and dark grey colours, respectively. (c) and (d) Film after 5 consecutives pulses with a fluence of  $2.30 \text{ mJ}/\text{cm}^2$  for both initial saturated state. The scale bar on the right corresponds to  $25 \mu\text{m}$ . Figure from reference 123. . . . . 26
- 2.12 (a) MOKE images of  $\text{Gd}_{24}(\text{Fe}_{90}\text{Co}_{10})_{76}$  film after being subjected to a single linearly polarized laser pulse with 50 fs, 1 ps and 3 ps pulse lengths. The applied fluence has been varied between 9.5 to  $15 \text{ mJ}/\text{cm}^2$ . (b) MOKE images of  $\text{Gd}_{24}(\text{Fe}_{90}\text{Co}_{10})_{76}$  film after being subjected to a 4 ps single linearly polarized laser pulse with a fluence of  $17 \text{ mJ}/\text{cm}^2$ . (c) AO-HIS state diagram of the corresponding magnetic system delimited by the threshold fluence for switching (open black and full blue squares) and the observation of a stochastic multidomain state (full red circles). The values associated to the blue squares corresponds to a switched domain size of  $10 \mu\text{m}$  while the position of black squares have been from the method proposed by Liu *et al.*<sup>144</sup>. Figure from reference 141. 27



2.13	Thermally-induced magnetization reversal in GdFeCo by means of light and electric pulses. (a) MOKE images after four consecutive 6.4 ps laser pulses with an absorbed fluence of 1.8 mJ/cm <sup>2</sup> . (b) MOKE images after four consecutive 9 ps electrical pulses. The scale bars correspond to 5 μm. Figure from reference 142. . . . .	29
3.1	Dispersion relations of transverse and longitudinal EM modes in a bulk metallic system. . . . .	38
3.2	Dielectric function of Au. The circles are experimental measurements (from reference 171). The corresponding Drude function is represented in dashed lines with $\epsilon_\infty = 10.86$ , $\hbar\gamma = 9.08$ eV and $\hbar\omega_p = 78$ meV. Solid lines take into account the contribution of intraband transitions with a critical points model (from reference 186). Vertical dashed line shows gold ITT position. . . . .	39
3.3	Sketch of planar metal-dielectric interface at $z = 0$ . Metal and dielectric medium are characterized by frequency-dependent dielectric function $\epsilon_m(\omega)$ and $\epsilon_d(\omega)$ , respectively. . . . .	40
3.4	Dispersion curves of plasmon polaritons. We fix $\epsilon_d$ and $\epsilon_\infty$ at 1 and consider the metal as a Drude metal via equation (3.17). (a) Loseless Drude metal. (b) Lossy Drude metal with $\omega_p = 20\gamma$ . The line is mapped with $\Im(k)/\Re(k)$ whose value is represented by the color bar in order to quantify the compromise between propagation and attenuation. . . . .	42
3.5	Dispersion relation of plasmon polaritons for Au-glass (solid gold line), Ag-glass (solid silver line) and Cu-glass (solid red line) planar interfaces with $\epsilon_d = 2.25$ . Dielectric functions of the three metals have been interpolated from Johnson and Christy's datasets <sup>171</sup> . The three horizontal dashed lines show the ITT of Au, Ag and Cu. . . . .	43
3.6	Dispersion relations of light in air and prism (dashed lines) coming with an angle of incidence of 30° with in-plane projection. Both solid lines describe the behaviour of SPP at metal-air and metal-prism interfaces in black and red, respectively. . . . .	44
3.7	Dispersion curves of grating-induced SPP. . . . .	45
3.8	Sketch of a 1D grating with period $P$ . $\mathbf{k}_i$ is the in-plane projection of the incoming light wvector oriented along $-\mathbf{k}_x$ , $\mathbf{k}_g$ is the grating wvector, $\theta_i$ is the polar angle, $\phi$ is the azimuthal angle, $\beta_{\text{SPP}}$ is the SPP wvector. . . . .	45

## LIST OF FIGURES

---

3.9	Coupling conditions for (a) $ \beta_{\text{SPP}}  <  \mathbf{k}_g $ and (b) $ \beta_{\text{SPP}}  >  \mathbf{k}_g $ . The angles $\zeta_+$ and $\zeta_-$ are related to $\mathbf{k}_{i+}$ and $\mathbf{k}_{i-}$ , respectively. . . . .	46
3.10	Illustration of a spherical particle with dimension $a$ , described by the dielectric function $\epsilon_m$ and surrounded by a homogeneous medium with dielectric function $\epsilon_d$ . . . . .	49
3.11	Regimes of scattering for a sphere with 300 nm-radius and refractive index of 4, embedded in air. The extinction efficiency is defined as the ratio between the extinction cross section $\sigma_{ext}$ and the geometric cross section $\sigma_{geo} = \pi \times a^2$ . . . . .	50
3.12	Extinction efficiency maps for a (a) silver sphere, (b) silicon sphere, (c) gold sphere, (d) cobalt sphere. Any of them is embedded in air. . . . .	51
3.13	Sketch of localized surface plasmon resonance in a metallic nanoparticle induced by oscillating electric field. . . . .	52
3.14	Scanning electron (top) and dark-field images (middle) of metallic nanoparticles with different shapes (rod, disc, triangle, triangle). The dark-field spectra on bottom have been measured on the same particles. The thickness of the structures has been fixed to 30 nm and the substrates are made of silica glass coated with 20 nm of ITO. The scale bar on top images represents 300 nm. . . . .	53
3.15	(a) Depolarization factors $L_j$ for spheroids with $R_1 = R_2 \neq R_3$ depending on the aspect ratio $\frac{R_3}{R_1}$ . (b) Absorption cross-section spectra for a sphere ( $R_3 = R_1$ ), an arbitrary oblate spheroid ( $R_3 = 0.25R_1$ ) and a rod ( $R_3 = 4R_1$ ) whose shape factors are related to dotted lines in (a). All the particles are illuminated by light with electric field polarized along the longest axis of the particle. . . . .	54
3.16	Surface lattice resonances of gold dimer arrays. Experimental spectra describing ellipsometry, reflection and extinction for 2D periodic arrangements of nanostructures. (a) Ellipsometry parameter $\Psi$ . Inset shows the loss of reflection for $\theta = 64^\circ$ . (b) Ellipsometry parameter $\Delta$ . Right inset highlights humongous phase change in reflection for $\theta = 64^\circ$ . (c) Reflection spectra for incoming $p$ and $s$ light polarizations. (d) Extinction spectra for $p$ -polarization. Left inset provides scanning electron microscopy image of the 2D arrays of gold dimers. Right inset highlights the maximum in extinction for $\theta = 64^\circ$ . The array period is fixed at 320 nm, single particle diameter reaches 108 nm while the thickness is 90 nm. A dimer consists of two single particles separated by 140 nm. Figure from reference 279. . . . .	57

3.17	Experimental optical spectra of periodic arrays of magnetic nanodisks. Schemes at the left highlight the incident polarization direction and the induced pure optical electric dipole. The black, red, green and blue line graphs correspond to a $y$ -lattice period $p_y = 400, 460, 480$ and $500$ nm, respectively. The grey line corresponds to a random distribution of nanodisks. Optical reflectivity measured at normal incidence for incident light polarization (a) $E_x$ and (b) $E_y$ . Figure adapted from reference 248. . . . .	58
3.18	Electric field for a given spatial position decomposed along both direction $s$ and $p$ . The sketch gives a position azimuth $\theta_a$ and a negative ellipticity $\eta_a$ . . . . .	61
3.19	Three MOKE configurations with related reflection matrices for normal and oblique incidences. The terms $r_{pp,0}$ and $r_{pp,mag}$ are $r_{pp}$ that are experience non dependence and linear dependence to in plane magnetization $m_x$ , respectively. .	63
3.20	Sketch of two orthogonal electric dipoles induced by linearly polarized light in a magnetized disk. $p_x$ is aligned with the incident electric field polarization while $p_y$ , orthogonal to the latter, results from magnetic behaviour of the disk. Sum of both dipoles transforms the initial polarization into elliptical. . . . .	64
4.1	(a) Illustration of HAMR principle. (b) Coercivity of FePt media as a function of temperature. Figure from reference 317. . . . .	67
4.2	Principle of NFT. Figure from reference 317. . . . .	67
4.3	HAMR writing head. (a) Sketch of the recording head with 1.2-mm down-track (DT) and 700- $\mu$ m cross-track (CT). Air-bearing surface (ABS) lies on the underside. Recording media slides along the +DT direction. (b) Illustration of the Au NFT connected to the magnetic pole tip. (c) Temperature distribution within the NFT when it is subjected to a power of 15 mW in case of perfect efficiency for the laser and light delivery system. (d) Cross section of the temperature distribution within the NFT. (e) Cross section of the whole assembly. Figure from reference 324. . . . .	68
4.4	Normalized absorbed power by the NFT and the recording layer. (a) Cross-sectional view. (b) In-plane view of the media layer. Figure from reference 326.	69
4.5	Fluence thresholds for complete demagnetization, all-optical magnetization switching, and damage as a function of the structure size. Figure from reference 329. . . . .	71

**LIST OF FIGURES**

---

4.6 (a) Absorbed energy profiles in the structures. (b) Evolution of absorbed energy density as a function of pattern size. The trend expected without interference effects is depicted in blue circles. The vertical solid line indicates the pump wavelength. Figure from reference 329. . . . . 72

4.7 (a) Initial magnetic state. (b) Magnetic contrast after the system has been subjected to a laser pulse of 3.7 mJ/cm<sup>2</sup>. The switched domain has a typical size of 53.4 nm. (c) Magnetic state after being reset by external out-of-plane magnetic field. (d) Magnetic contrast after the system has been subjected to a laser pulse of 4.0 mJ/cm<sup>2</sup>. (e) Magnetic contrast after the system has been subjected to another laser pulse of 4.0 mJ/cm<sup>2</sup>. (f) Blue data presents the minimum fluence to reverse subwavelength-sized domains near the antennas while red data shows the same kind of data without near-field enhancement. AOS starts to be observed next to the two-wire plasmonic nanoantenna for a fluence of 3.7 mJ/cm<sup>2</sup>. The lower bound on continuous film reaches 5.8 mJ/cm<sup>2</sup> away from the antenna. (g) Calculated near-field distribution near the two-wire antenna for three different wavelengths. Figure from reference 168. . . . . 74

4.8 (a) Sketch of experimental configuration. Red and blue correspond to *p* and *s* polarization, respectively. (b, c) In depth distribution of EM energy  $|e|^2$  (dashed-dotted line), partial absorption  $\delta A$  and total absorption  $A$  (solid line) for incoming *p* and *s*-polarized light, respectively. The wavelength is fixed at 800 nm while the angle of incidence is 59°. (d, e) MOKE images of polarization-dependent AOS. The left (resp. right) arrow indicates the orientation of Gd sublattice magnetic moments within the top (resp. bottom) layer of the RE-TM alloy system. Images in (d) and (e) have been obtained for a measured fluence of 10 mJ/cm<sup>2</sup> and 12 mJ/cm<sup>2</sup>, respectively. Figure adapted from reference 213. . . . . 75

4.9 a) Sketch of the concept. b) Top view of the platform with photonic crystal (PhC) cavity parameters.  $d_{1-4} = 100, 110, 120$  and  $170$  nm,  $p = 370$  nm,  $w_1 = 570$  nm,  $h = 250$  nm and  $w_{Rt} = 120$  nm. c) Highlight on the double V-shaped gold plasmonic antenna (PNA) on the racetrack with  $l_{PNA} = 120$  nm,  $h_{PNA} = w_{PNA} = 30$  nm and  $h_{Rt} = 10$  nm. Subparts of the PNA are oriented at 45° from racetrack main axis. Figure from reference 346. . . . . 76

4.10 (a) Ferromagnetic nanodisks described by two orthogonal electric dipoles modeled as two damped harmonic oscillators. These latter are characterized by their spring constants $k$ and their mass $m$ . (b) Extinction spectra of elliptical magnetic nanostructures for the two main directions of polarization. (c) Calculated Kerr angle as function of the wavelength for the same system. (d) Corresponding Kerr angle spectra. (e) Calculated Kerr angle as function of the wavelength considering the effect of glass substrate. Figure adapted from reference 310. . . . .	77
4.11 (a) Sketch of the periodic array of magnetic nanodisks. The incident electric field comes with only $y$ component and induces two orthogonal electric dipoles within the magnetic nanostructures, a pure optical $d_x$ and a MO $d_y$ . (b) SEM image of the Ni metasurface. The scale bar corresponds to 200 nm. (c) Optical transmission spectra of an array with a unique lattice period of 400 nm and nanodisk diameter of 120 nm for several incidence angles. The DOs (+1, 0) and (-1,0) cross at normal incidence. (d) Reflection, (e) Kerr ellipticity and (f) Kerr rotation spectra probed at normal incidence with incoming polarization $E_x$ and varying periodic $p_y$ . (g) Reflection, (h) Kerr ellipticity and (i) Kerr rotation spectra probed at normal incidence with incoming polarization $E_y$ and varying periodic $p_y$ . Figure adapted from reference 248. . . . .	80
5.1 Sketch of DC magnetron sputtering. . . . .	83
5.2 Sketch of e-beam evaporation technique. . . . .	84
5.3 MOKE magnetometer at <i>Institut Jean Lamour</i> with following elements: analyzer (A); charge coupled device (CCD); polarizer (P); photoelastic modulator (PEM); mirror (M); sample (S). . . . .	85
5.4 MOKE and MOFE magnetometer at <i>Aalto University</i> with following elements: analyzer (A); charge coupled device (CCD); lens (L); polarizer (P); photoelastic modulator (PEM); mirror (M); sample (S). . . . .	86
5.5 Optical measurements at <i>Aalto University</i> with following elements: charge coupled device (CCD); lens (L); mirror (M); sample (S). . . . .	87
5.6 Fabrication work-flow. . . . .	88
5.7 Electron-beam lithography. . . . .	89
5.8 Effect of deflection. . . . .	90
5.9 Spot contamination for adjusting the focus and the stigmatism. . . . .	90
5.10 Scanning electron microscopy electron-beam profile after substrate interaction. Figure from reference 397. . . . .	91

## LIST OF FIGURES

---

5.11	(a) Periodic pattern unaffected by back-scattered electrons. (b) Periodic pattern affected by back-scattered electrons. . . . .	92
5.12	(a) Impact of two resist layers on pattern profile, (b) Undesirable side effects induced by the use of a single resist layer. . . . .	93
5.13	Example of SIMS profile for the system composed of glass//Ta(5 nm)/Pt(5 nm)/[Co(1 nm)/Gd(2 nm)/Pt(3 nm)] <sub>6</sub> /Pt(1 nm). . . . .	94
5.14	(a) Unchirped pulse. (b) Blue-chirped pulse. (c) Red-chirped pulse. . . . .	95
5.15	Principle of a grating compressor. . . . .	96
5.16	Double-chirped mirrors. Figure from reference 407. . . . .	97
5.17	Principle of mode-locking. . . . .	98
5.18	Autocorrelator with following elements: beam-splitter (BS); filter (F); mirror (M); target beam alignment (T). . . . .	99
5.19	Beam profiles. (a) Spatial distribution of the laser beam. Inset shows the corresponding image. Scale bar = 100 $\mu\text{m}$ . (b) 201 fs pulse length with gaussian fit. . . . .	100
5.20	MOKE microscopy involving Ti:sapphire laser at <i>Institut Jean Lamour</i> with following elements: analyzer (A); beam-splitter (BS); charge coupled device (CCD); filter (F); Fresnel lens (FL); lens (L); lens for focusing the lasser beam ( $L_F$ ); mirror (M); objective (O); polarizer (P); sample (S); half waveplate ( $\lambda/2$ WP). Raw MOKE images of a single GdFeCo layer (a) after saturation and (b) after getting subjected to an ultrafast laser pulse. . . . .	101
5.21	Time-resolved MOKE microscope Yt laser at <i>Institut Jean Lamour</i> with following elements: analyzer (A); charge coupled device (CCD); filter (F); lens (L); lens for focusing the laser beam ( $L_F$ ); mirror (M); polarizer (P); sample (S); half waveplate ( $\lambda/2$ WP). Processed MOKE images of a single GdFeCo layer subjected to an ultrafast laser pulse for a delay of (a) 0 ps, (b) 0.5 ps, (c) 5 ps, (d) 10 ps. The scale bars correspond to 20 $\mu\text{m}$ . . . . .	102
6.1	Hysteresis loops (Kerr rotation) of [Co/Gd/Pt] <sub>N</sub> continuous films for (a) $N = 1$ , (b) $N = 2$ , (c) $N = 3$ , (d) $N = 4$ , (e) $N = 5$ and (f) $N = 6$ . Hysteresis loops (Faraday rotation) of periodic arrays of [Co/Gd/Pt] <sub>N</sub> nanodisks with g) $D = 100$ nm,(h) $D = 150$ nm, (i) $D = 200$ nm, (j) $D = 250$ nm. Insets show MFM images of [Co/Gd/Pt] <sub>N</sub> thin films for (e) $N = 5$ and (f) $N = 6$ . The images were recorded under zero magnetic field. The scale bars correspond to 1000 nm. . . . .	107

6.2	SEM images of $[\text{Co}/\text{Gd}/\text{Pt}]_5$ nanodisk arrays with corresponding simulated normalized absorption of a single nanodisk embedded in an homogeneous medium of refractive index 1.5. The dashed lines represent the different array resonances. The scale bar corresponds to 200 nm. . . . .	108
6.3	Corrected extinction spectra of $[\text{Co}/\text{Gd}/\text{Pt}]_2$ nanodisk arrays with $D = 150, 200$ and $250$ nm and $P = 500$ nm. We define his quantity by the ratio between the raw extinction and the filling factor of the array. . . . .	109
6.4	Single-pulse AO-HIS for a continuous $[\text{Co}/\text{Gd}/\text{Pt}]_2$ film (top panels) and for a patterned $[\text{Co}/\text{Gd}/\text{Pt}]_2$ metasurface with $D = 150$ nm and $P = 500$ nm (bottom panels) at $\lambda = 650$ nm, and $\lambda = 825$ nm. Red and blue colors indicate magnetization pointing up and down, respectively. The laser fluence is indicated in the figure. The scale bar corresponds to $50 \mu\text{m}$ . Figure and caption from reference 421. . . . .	110
6.5	(a) Gain of energy as function of the wavelength for $[\text{Co}/\text{Gd}/\text{Pt}]_2$ metasurfaces. (b) Extinction spectra of the same structures scaled by their filling factor and normalized by the extinction spectrum of the corresponding continuous film. (c) Simulated normalized extinction spectra for the same metasurfaces. (d-f) Electric field intensity ( $ E / E_0 $ ) distribution near a nanostructure in a periodic arrangement of nanodisks with $P = 500$ nm at the SLR wavelength. The disk diameter takes the values (d) 150, (e) 200, and (f) 250 nm. The scale bar corresponds to 50 nm. . . . .	111
6.6	(a) Gain of energy as function of the wavelength for $[\text{Co}/\text{Gd}/\text{Pt}]_2$ metasurfaces. (b) Extinction spectra of the same structures scaled by their filling factor and normalized by the extinction spectrum of the corresponding continuous film. (c) Simulated normalized extinction spectra for the same metasurfaces. (d-f) Electric field intensity ( $ E / E_0 $ ) distribution near a nanostructure in a periodic arrangement of nanodisks with $P = 550$ nm at the SLR wavelength. The disk diameter takes the values (d) 150, (e) 200, and (f) 250 nm. The scale bar corresponds to 50 nm. . . . .	112
6.7	Measured refractive index of $[\text{Co}/\text{Gd}/\text{Pt}]_N$ metasurfaces for (a) $N = 1$ , (b) $N = 2$ , (c) $N = 3$ , (d) $N = 4$ , (e) $N = 5$ and (f) $N = 6$ . . . . .	113
6.8	Toggle switching on $[\text{Co}/\text{Gd}/\text{Pt}]_2$ continuous film with a fluence $F = 3.02 \text{ mJ}/\text{cm}^2$ at 650 nm. Red and blue colors indicate magnetization pointing up and down, respectively. The scale bar corresponds to $50 \mu\text{m}$ . . . . .	114



## LIST OF FIGURES

---

- 6.9 Repetitive switching of single-pulse AO-HIS in a [Co/Gd/Pt]<sub>2</sub> metasurface with  $D = 150$  nm and  $P = 500$  nm for a fluence of  $1.26$  mJ/cm<sup>2</sup> at  $650$  nm. Red and blue colors indicate magnetization pointing up and down, respectively. The scale bar corresponds to  $50$   $\mu$ m. . . . . 114
- 6.10 Repetitive switching of single-pulse AO-HIS in a [Co/Gd/Pt]<sub>2</sub> metasurface with  $D = 150$  nm and  $P = 500$  nm for a fluence of  $1.26$  mJ/cm<sup>2</sup> at  $650$  nm. (a) MOKE images for 1, 3, 5 and 7 consecutive pulses. (b) Corresponding switching rates line profiles across the reversed areas after each single ultrafast laser pulse was sent. (c) Switching rate at metasurface center a a function of pulse number.  $N_X$  denotes the event "The system has been subjected to  $X$  light pulses". The scale bar corresponds to  $50$   $\mu$ m. . . . . 115
- 6.11 Non-complete switching in a [Co/Gd/Pt]<sub>2</sub> metasurface with  $D = 150$  nm and  $P = 500$  nm for a fluence of  $1.26$  mJ/cm<sup>2</sup> at  $650$  nm. Reproduction of switching rates (a)  $m_3$ , (b)  $m_6$ , (c)  $m_7$  and (d)  $m_8$  with a combination of previous states. . . 116
- 6.12 Repetitive switching of single-pulse AO-HIS in a [Co/Gd/Pt]<sub>2</sub> metasurface with (a)  $D = 200$  nm and  $P = 500$  nm for a fluence of  $1.89$  mJ/cm<sup>2</sup> at  $650$  nm, (b)  $D = 250$  nm and  $P = 500$  nm for a fluence of  $2.77$  mJ/cm<sup>2</sup> at  $650$  nm. The scale bar corresponds to  $50$   $\mu$ m. . . . . 117
- 6.13 Repetitive switching of single-pulse AO-HIS in a [Co/Gd/Pt]<sub>2</sub> metasurface with (a)  $D = 200$  nm and  $P = 500$  nm for a fluence of  $1.89$  mJ/cm<sup>2</sup> at  $650$  nm, (b)  $D = 250$  nm and  $P = 500$  nm for a fluence of  $2.77$  mJ/cm<sup>2</sup> at  $650$  nm. (a,d) MOKE images for 1, 3, 5 and 7 consecutive pulses. (b,e) Corresponding switching rates line profiles across the reversed areas after each single ultrafast laser pulse was sent. (c,f) Switching rate at metasurface center a a function of pulse number. The scale bars correspond to  $50$   $\mu$ m. . . . . 118
- 6.14 Switching probability profile in a [Co/Gd/Pt]<sub>2</sub> metasurface with a)  $D = 150$  nm and  $P = 500$  nm for a fluence of  $1.26$  mJ/cm<sup>2</sup> at  $650$  nm, c)  $D = 200$  nm and  $P = 500$  nm for a fluence of  $1.89$  mJ/cm<sup>2</sup> at  $650$  nm, e)  $D = 250$  nm and  $P = 500$  nm for a fluence of  $2.77$  mJ/cm<sup>2</sup> at  $650$  nm. Comparison between measured and predicted switching rates  $m_X$  for b)  $D = 150$  nm, d)  $D = 200$  nm, f)  $D = 250$  nm. 119
- 6.15 Switching probability as function of nanodisk diameter . . . . . 120
- 6.16 (a) Optical and (b) MO spectra of [Co/Gd/Pt]<sub>5</sub> metasurface with  $D = 100$  nm and  $P = 400$  nm. . . . . 121



6.17 SLR enhanced Faraday readout sensitivity for [Co/Gd/Pt] <sub>N</sub> metasurfaces with (a) $N = 1$ , (b) $N = 2$ , (c) $N = 3$ , (d) $N = 4$ , (e) $N = 5$ and (f) $N = 6$ . . . . .	122
7.1 MOKE images of domain pattern measured for various $\alpha$ indicated on each images. The MOKE images have been recorded at 800 nm. $I(\alpha, +m)$ and $I(\alpha, -m)$ are derived from averaged intensities within the two indicated regions, yellow and red respectively. . . . .	125
7.2 Experimental intensity measurements of both $I(\alpha, +m)$ and $I(\alpha, -m)$ fitted by Equation (7.2). . . . .	126
7.3 Experimental measurements of (a) $\Delta(\alpha) / 2$ and $\Sigma(\alpha) / 2$ and (b) MO contrast as function of $\alpha$ compared to theory. . . . .	127
7.4 MO contrast of [Co/Gd/Pt] <sub>3</sub> metasurfaces. (a) MO contrast for $D = 150$ nm and $P = 400, 450, 500,$ and $550$ nm. (b–d) MO contrast for $P = 500$ nm with highlights at 700, 800, and 860 nm, respectively. . . . .	127
7.5 MO contrast of [Co/Gd/Pt] <sub>3</sub> metasurfaces for $P = 400, 450, 500,$ and $550$ nm and (a) $D = 200$ and (b) 250 nm. . . . .	128
7.6 (a) Kerr rotation and (b) ellipticity spectra of [Co/Gd/Pt] <sub>3</sub> metasurface with $D = 150$ nm and $P = 450$ nm for incoming s-polarized light. The vertical dotted lines in (a) highlight for which wavelength the rotation has been measured to be close to zero while the corresponding stars in (b) underline, for the same wavelengths, that ellipticity is maximum. . . . .	129
7.7 Reflection spectra of periodic arrays of Pt nanodisks with $D = 200$ nm and $P = 450$ nm. The incoming light was initially (a) $p$ , (b) $s$ and (c) $45^\circ$ -polarized. The solid lines are guides for the eye. The dashed lines points the DO positions. . . . .	129
7.8 (a) Kerr rotation and (b) ellipticity spectra of [Co/Gd/Pt] <sub>3</sub> metasurfaces with $D = 150$ nm and $P = 400, 450, 500$ and $550$ nm for incoming $s$ -polarized light. MO denotes the position of SLRs whose existence is possible due to the excitation of a MO electric dipole. For $P = 450$ nm, we illustrate the orientation of the corresponding electric dipole for a given electric field direction. We distinguish the pure optical dipole (purple) from MO dipole (cyan). . . . .	130
7.9 Kerr ellipticity spectra of [Co/Gd/Pt] <sub>3</sub> metasurfaces with $D = 100$ and 250 nm and $P = 450$ nm for incoming $s$ -polarized light. Solid lines are guides for the eye. . . . .	131

## LIST OF FIGURES

---

7.10	Spectra of intensity reflected by Pt metasurface with $D = 200$ nm and $P = 450$ nm for which polarizer and analyzer transmission axis are almost crossed as for the measurements of MO contrast (red circles). We compare this spectra with reflection spectra from Figure 7.7(c) (blue solid line). Solid lines are guides for the eyes. . . . .	132
8.1	Transients dynamics of $T_e$ within the GdFeCo layer in the studied samples calculated via the 2TM for $F_{las} = 8$ mJ/cm <sup>2</sup> and for combinations of $t_{Cu}$ and $\tau_{las}$ detailed in the legend. . . . .	137
8.2	Written domain size $r_{SW}$ as function of the pulse energy for various $t_{Cu}$ . We distinguish the distributions of (a) $r_{x,SW}$ and (b) $r_{y,SW}$ to take into account that the beam spot is elliptical. Thus we can extract the beam spot radius along both in-plane directions $x$ and $y$ to properly convert any threshold energy into threshold fluence. . . . .	139
8.3	Evolution of $F_{SW}$ and $F_{max}$ with $t_{Cu}$ for a single pulse length of 0.150 fs length with light coming with an incident angle of $\approx 5$ deg. Open triangles represent results of the fits used to determine the beam size. Other threshold fluences for the appearance of magnetization reversal and multidomain state are described by open and closed circles, respectively . . . . .	140
8.4	(a) $F_{SW}$ and (b) $F_{max}$ as function of $t_{Cu}$ for several $\tau_{las}$ . We detail the dependence of (c) $\Delta F_{SW} = F_{SW}(300 \text{ nm}) - F_{SW}(5 \text{ nm})$ and (d) $\Delta F_{SW} = F_{SW}(300 \text{ nm}) - F_{SW}(5 \text{ nm})$ on $\tau_{las}$ . Thin corresponds to $\Delta F = F(300 \text{ nm}) - F(5 \text{ nm})$ for $\tau_{las} \leq 4.5$ ps and $F(300 \text{ nm}) - F(50 \text{ nm})$ for $\tau_{las} \geq 5$ ps. Thick corresponds to $\Delta F = F(900 \text{ nm}) - F(300 \text{ nm})$ . . . . .	141
8.5	$F_{SW}$ (open symbols with solid lines) and $F_{max}$ (closed symbols) as function of $\tau_{las}$ for various $t_{Cu}$ . The dashed line gives the maximum pulse duration for the observation of TIMS with $t_{Cu} = 5$ nm. . . . .	142
8.6	Spin dynamics simulation of both Gd and FeCo sublattices with $t_{Cu} = 100$ nm and $\tau_{las} =$ (a,b) 0.25 and (c,d) 5 ps. The applied fluence has been fixed to (a) 1.1, (b) 1.2, (c) 4.8 and (d) 5.0 mJ/cm <sup>2</sup> . Corresponding electron and phonon temperature dynamics in the GdFeCo layer for $\tau_{las} =$ (e,f) 0.25 and (g,h) 5 ps. The applied fluence has been fixed to (e) 1.1, (f) 1.2, (g) 4.8 and (h) 5.0 mJ/cm <sup>2</sup> . . . . .	148

8.7	Spin dynamics simulation of both Gd and FeCo sublattices with $t_{Cu} = 100$ nm and $\tau_{las} =$ (a,b) 0.25 and (c,d) 5 ps. The applied fluence has been fixed to (a) 16.0, (b) 16.2, (c) 12.8 and (d) 13.0 mJ/cm <sup>2</sup> . Corresponding electron and phonon temperature dynamics in the GdFeCo layer for $\tau_{las} =$ (e,f) 0.25 and (g,h) 5 ps. The applied fluence has been fixed to (e) 16.0, (f) 16.2, (g) 12.8 and (h) 13.0 mJ/cm <sup>2</sup> . . . . .	149
8.8	Threshold fluences $F_{SW}$ and $F_{max}$ as a function of $t_{Cu}$ for light wavelength of 800 nm and pulse durations of 0.25 and 5 ps. The incidence angle has been fixed at 5°. . . . .	150
9.1	(a) Gain of energy as function of the wavelength for [Co/Gd/Pt] <sub>2</sub> metasurfaces with $P = 500$ nm. The nanodisk diameters are indicated in the legend. (b) Extinction spectra of the same structures scaled by their filling factor and normalized by the extinction spectrum of the corresponding continuous film. . . .	152
9.2	Kerr ellipticity spectra of [Co/Gd/Pt] <sub>3</sub> metasurface with $D = 150$ nm and $P = 450$ nm. . . . .	153
9.3	$F_{SW}$ (open symbols with solid lines) and $F_{max}$ (closed symbols) as function of $\tau_{las}$ for various $t_{Cu}$ . The dashed line gives the maximum pulse duration for the observation of TIMS with $t_{Cu} = 5$ nm. . . . .	154
C.1	SEM images of [Co/Gd/Pt] <sub>1</sub> nanodisk arrays. The scale bar corresponds to 200 nm. . . . .	210
C.2	SEM images of [Co/Gd/Pt] <sub>2</sub> nanodisk arrays. The scale bar corresponds to 200 nm. . . . .	211
C.3	SEM images of [Co/Gd/Pt] <sub>3</sub> nanodisk arrays. The scale bar corresponds to 200 nm. . . . .	212
C.4	SEM images of [Co/Gd/Pt] <sub>4</sub> nanodisk arrays. The scale bar corresponds to 200 nm. . . . .	213
C.5	SEM images of [Co/Gd/Pt] <sub>5</sub> nanodisk arrays. The scale bar corresponds to 200 nm. . . . .	214
C.6	SEM images of [Co/Gd/Pt] <sub>6</sub> nanodisk arrays. The scale bar corresponds to 200 nm. . . . .	215
D.1	Extinction spectra of [Co/Gd/Pt] <sub>1</sub> nanodisk arrays with (a) $D = 100$ nm, (b) $D = 150$ nm, (c) $D = 200$ nm and (d) $D = 250$ nm. . . . .	218

## LIST OF FIGURES

---

D.2	Extinction spectra of [Co/Gd/Pt] <sub>2</sub> nanodisk arrays with (a) $D = 100$ nm, (b) $D = 150$ nm, (c) $D = 200$ nm and (d) $D = 250$ nm. . . . .	219
D.3	Extinction spectra of [Co/Gd/Pt] <sub>3</sub> nanodisk arrays with (a) $D = 100$ nm, (b) $D = 150$ nm, (c) $D = 200$ nm and (d) $D = 250$ nm. . . . .	220
D.4	Extinction spectra of [Co/Gd/Pt] <sub>4</sub> nanodisk arrays with (a) $D = 100$ nm, (b) $D = 150$ nm, (c) $D = 200$ nm and (d) $D = 250$ nm. . . . .	221
D.5	Extinction spectra of [Co/Gd/Pt] <sub>5</sub> nanodisk arrays with (a) $D = 100$ nm, (b) $D = 150$ nm, (c) $D = 200$ nm and (d) $D = 250$ nm. . . . .	222
D.6	Extinction spectra of [Co/Gd/Pt] <sub>6</sub> nanodisk arrays with (a) $D = 100$ nm, (b) $D = 150$ nm, (c) $D = 200$ nm and (d) $D = 250$ nm. . . . .	223
D.7	Extinction spectra of [Co/Gd/Pt] <sub>N</sub> continuous films. . . . .	224
E.1	Faraday angle spectra of [Co/Gd/Pt] <sub>1</sub> nanodisk arrays with (a) $D = 100$ nm, (b) $D = 150$ nm, (c) $D = 200$ nm and (d) $D = 250$ nm. . . . .	226
E.2	Faraday angle spectra of [Co/Gd/Pt] <sub>2</sub> nanodisk arrays with (a) $D = 100$ nm, (b) $D = 150$ nm, (c) $D = 200$ nm and (d) $D = 250$ nm. . . . .	227
E.3	Faraday angle spectra of [Co/Gd/Pt] <sub>3</sub> nanodisk arrays with (a) $D = 100$ nm, (b) $D = 150$ nm, (c) $D = 200$ nm and (d) $D = 250$ nm. . . . .	228
E.4	Faraday angle spectra of [Co/Gd/Pt] <sub>4</sub> nanodisk arrays with (a) $D = 100$ nm, (b) $D = 150$ nm, (c) $D = 200$ nm and (d) $D = 250$ nm. . . . .	229
E.5	Faraday angle spectra of [Co/Gd/Pt] <sub>5</sub> nanodisk arrays with (a) $D = 100$ nm, (b) $D = 150$ nm, (c) $D = 200$ nm and (d) $D = 250$ nm. . . . .	230
E.6	Faraday angle spectra of [Co/Gd/Pt] <sub>6</sub> nanodisk arrays with (a) $D = 100$ nm, (b) $D = 150$ nm, (c) $D = 200$ nm and (d) $D = 250$ nm. . . . .	231
E.7	Faraday angle spectra of [Co/Gd/Pt] <sub>N</sub> continuous films. . . . .	232
F.1	(a) Kerr rotation and (b) ellipticity spectra of [Co/Gd/Pt] <sub>3</sub> metasurfaces with $D = 100$ nm and $P = 400, 450, 500$ and $550$ nm for incoming s-polarized light. . .	233
F.2	(a) Kerr rotation and (b) ellipticity spectra of [Co/Gd/Pt] <sub>3</sub> metasurfaces with $D = 150$ nm and $P = 400, 450, 500$ and $550$ nm for incoming s-polarized light. . .	234
F.3	(a) Kerr rotation and (b) ellipticity spectra of [Co/Gd/Pt] <sub>3</sub> metasurfaces with $D = 200$ nm and $P = 400, 450, 500$ and $550$ nm for incoming s-polarized light. . .	234
F.4	(a) Kerr rotation and (b) ellipticity spectra of [Co/Gd/Pt] <sub>3</sub> metasurfaces with $D = 250$ nm and $P = 400, 450, 500$ and $550$ nm for incoming s-polarized light. . .	235

# List of Tables

6.1	Filling factors of the metasurfaces studied in this thesis. . . . .	110
8.1	Material parameters used for the 2TM implementation. . . . .	144
8.2	Equilibrium parameters for the implementation of the spin dynamics model. . .	146
8.3	Other parameters for the implementation of the spin dynamics model. . . . .	147
B.1	Magneto-optical response of optics involved in MOKE magnetometer set-up expressed in the Jones formalism in the most general case. The angles $\alpha$ and $\beta$ denotes the angle between the plane of incidence and the main axis of the analyzer and polarizer, respectively. $\phi$ and $f$ correspond to the amplitude and modulation frequency of the photoelastic modulator, respectively. . . . .	207



# Chapter 1

## General introduction

*The purpose of this chapter is to highlight the motivation which drives this thesis. The chapter consists of a general introduction followed by a short presentation of the fields of plasmonics and ultrafast magnetism but also an awareness of the materials we need for our research works. Finally the scope of this thesis is described.*

### 1.1 Introduction

In 2022, a lot happened every minute online: 66 thousand videos and photos shared on Instagram, 510 thousand comments posted on Facebook, 452 thousand streaming hours on Netflix, 16.2 million texts are sent, 4 722 dollars spent on Amazon, 1.145 trillion MB per day. Society is changing, in which widely used items are connected leading to the emergence of the Internet of Things (IoT). If the number of such devices was around 7.74 billion in 2019, it is expected to overcome 25 billion in 2030 especially due to the development of autonomous vehicles and information technology (IT) infrastructures. This trend affects all facets of society: industrial control, logistics, retail, e-health, smart agriculture, smart cities, smart environment, smart energy. Everyday things get connected for a smarter future.

The "cloud" stores the information but it exists by means of data centers that are full of hard disk drives (HDDs) and cooling systems. HDDs rely on several magnetic effects. Writing process is usually performed with a magnetic field while recording is done with giant magnetoresistive sensors (GMR)<sup>1,2</sup>. The discovery of GMR, awarded by the Nobel Prize in Physics in 2007, led to a significant improvement of read-head sensitivity permitting a reduction of the bit size in HDDs for getting a greater areal density. This magnetism-based approach for storing data gave rise to non-volatile writing of information. However, the areal density of such devices was believed to never be able to overcome a limit of the order of 500 Gb/in<sup>2</sup>.

Since reduction of bit size makes the granular media magnetically harder, i.e. requires much higher magnetic field to reverse magnetization, the development of heat-assisted magnetic recording (HAMR) paved the path for larger areal density with the use of reasonable magnetic field amplitude<sup>3,4</sup>. Indeed a near-field transducer (NFT) confines the light at nanoscale and softens the magnetic system so that it can be switched with low magnetic field while a subsequent heat sink layer restores the granular media to its initial temperature for a stable magnetic recording. In this way the areal density could reach 4Tb/in<sup>25</sup>.

In this perspective future magnetism-based data storage devices require strategies that combine faster magnetization reversal, higher energy efficiency and larger areal density. The emergence of femtomagnetism gives opportunities to control magnetization over hundreds of femtoseconds combined while plasmonics enables a control of light at nanoscale below the diffraction limit. Thus magneto-plasmonic nanostructures made of materials that exhibit all-optical helicity-independent switching are of particular interest since they could enable energy efficient magnetization control of single nanometer sized magnetic elements (bits) at the femtosecond time scale and thus meet all requirements of future information technologies at once.



## 1.2 Ultrafast magnetism

Beaurepaire *et al.* opened the research topic of ultrafast magnetism by demonstrating experimentally ultrafast demagnetization of a 20 nm-thick Ni continuous film subjected to a single 60 fs laser pulse<sup>6</sup>. The system has been shown to lose half of its magnetization amplitude over the first picosecond then to recover its initial state at longer time scale. This pioneer work gained significant attention from both a fundamental and an application point of view.

The discovery of Stanciu *et al.* that the magnetization of a GdFeCo alloy film can be controlled by the helicity of circularly polarized femtosecond laser pulses put this field at another level of interest<sup>7</sup>. They first suggested that all-optical magnetization switching (AOS) depends on light helicity. In contrast to the initial interpretation Radu *et al.* pointed out that light-induced magnetization switching in this ferrimagnetic material can be performed for arbitrary polarized light<sup>8</sup>. This gave rise to a class of AOS so-called all-optical helicity-independent switching (AO-HIS). The underlying physics is an initial energy transfer between the light and the electron bath which then gives energy to the spin baths without dissipating this energy to the crystal lattice due to spin-orbit coupling. Then both spin subsystems can exchange angular momentum via exchange scattering. However AO-HIS is restricted to a few ferrimagnetic materials.

Less than ten years ago, Lambert *et al.* triggered a great interest from the community since they showed that AOS can be extended to a wide range of magnetic materials such as ferromagnetic thin films and granular media<sup>9</sup>. They gave birth to a new class of AOS, so-called all-optical helicity-dependent switching (AO-HDS), since unlike AO-HIS, the magnetization reversal requires circularly polarized light the helicity of which actually depends on the magnetic state. Also, a single laser pulse is rarely enough to switch deterministically the magnetization.

These recent progress sound of particular interest for the future photonic integrated circuits. Since fast current-induced domain wall motion and AO-HIS have been demonstrated simultaneously in the multilayer [Co/Gd]<sub>2</sub><sup>10-12</sup>, one could combine AOS for ultrafast energy efficient information writing on a racetrack memory<sup>13,14</sup>. These magnetic domains could then be moved by means of the spin Hall effect<sup>15-17</sup> and readout by means of magneto-optics (MO)<sup>18</sup>. In this manner it is possible to cut down intermediate electronic steps saving some time and energy.

Although light is used for magnetic recording in these hybrid platforms, it should be noted that the maximum achievable spatial resolution of optical read back, via magneto-optical Kerr effect (MOKE) microscopy, might hardly be able to go below 100 nm because the wavelengths in use are in the visible range or the loss of resolution in near-field magneto-optical imaging techniques<sup>19</sup>. Thus such photonic platforms must rely on GMR sensors for probing the magnetic orientation of the magnetic bits.

### 1.3 Plasmonics

The ability of metallic nanostructures to control the light at nanoscale gave rise to the field of plasmonics<sup>20,21</sup>. Excitation of plasmonic mode occurs when light drives coherent oscillations of free electrons of the nanoparticle. This electron density oscillation leads to EM fields enhancement in the vicinity of the nanostructures. Widespread applications of plasmonics in various fields were made possible thanks to the development of new strategies to synthesize nanoobjects such as top-down approach by means of nanoimprint, electron-beam lithography, chemistry and templated synthetic methods. The optical behaviour of metallic nanostructures can be controlled by nanoparticle size and shape but also by the way they are arranged. These parameters themselves can be controlled as well as the atomic composition to be in line with current and future needs of medical devices, electronics industry and energy science.

Plasmonics finds its applicability in the next generation of nanosensors. The resulting field enhancement allows to detect molecules with a high sensitivity and transduce biological events and enhance Raman signal<sup>22</sup>. Also thermoplasmonics provides new strategies for photothermal therapies and controlling light-induced drug release in living cells facilitating the healing of diseases<sup>23</sup>.

Plasmonics also explores new ways to fulfill the current needs for energy harvesting<sup>24,25</sup>. Absorption enhancement induced by the excitation of plasmonic modes lowers significantly the amount of material required for solar energy gathering in comparison to widely used photovoltaic devices. This leads to new designs of solar cells. Solar to chemical energy conversion by means of photocatalysts also matters in this kind of devices. In this context, the use of plasmonic metallic nanoparticles as photocatalysts has been shown to boost this energy conversion, promising for the current energetic transition.

For now, the integration of plasmonic nanostructures seems to be the only way to guide light below the diffraction limit with an efficient light-to-matter energy conversion in nanoscale regions. Thus plasmonics is of particular interest for the further developments of energy efficient densely packed signal-processing platforms. The ability of strongly localize and enhance the energy has been already integrated in HAMR technologies by means of plasmonic nanostructures, so called near-field transducer (NFT), that heat, and then soften, the granular media at nanoscale leading to much greater areal density. The underlying energy transfer is achieved by coupling the highly enhanced near-field around the NFT to the media. Thus, the impact of this coupling has to be taken into account when optimizing the plasmonic resonance NFTs. Moreover, NFTs need to be heat sinks to avoid their self-destruction by self-heating which accompanies the decay of coherent plasmon oscillations to electron-electron and electron-phonon scattering.

## 1.4 Geopolitics of resources

Geopolitics studies how geographical factors impact international policy and international relations. Then geopolitics of resources describes how natural resources are allocated all over the world. We use mainly rare earths as well as transition and heavy metals. We want to briefly address the geopolitical risks around these materials.

Most of the cobalt is extracted in the Democratic Republic of the Congo. The resulting massive mining requires the management of major problems such as environmental pollution leading to huge health issues due to food and water contamination, worker exploitation, unfair market practices, accident hazard but also corruption, widespread use of violence and local population forced to move. Everything that makes the democracy weaker. Amnesty International estimated that 40 000 children are involved in cobalt mining in this country synonym of Human Rights violation. Even more surprising, 80 % of the industrial exploitation is owned and funded by Chinese companies. This asymmetry gives rise to large hostility within the Democratic Republic of the Congo and creates unfair practices with local companies that extract cobalt.

In parallel, China predominates in the rare-earths market. These materials are necessary for the production of wind turbines, magnets, smartphones, rechargeable batteries, hybrid vehicles and many other equipments. Owning these resources means having decision-making power on energy transition. This monopoly of China is due to its ability to extract the interest elements from mining the initial rocks in which they are found. Geopolitical risks are important like when China stopped to supply Japan in rare-earths and metals in 2010 despite Japan needed it badly. Few alternatives have been proposed to reduce the geopolitical risks: stop dependence on China, recycling and change the way the technologies are produced but also relocate the mining and processing operations. Currently the best candidates are believed to be Australia and Greenland.

The last three materials that we use, copper, platinum and tantalum, have been identified as critical minerals. Institutions investigated the place of this ore in the energy and the transport and how global warming will impact demand. In any case they highlight that copper production will have to raise significantly. This request must have some implications. For instance Chile is one of the main suppliers but must extract this material in the most arid regions. The country then proposed to replace missing freshwater by seawater. However, transporting this water at high altitude areas combined with the aggravation of water desalination will need inexorably to further increasing energy consumption and brine discharge.

This way we want to make the reader aware about the impact of the extraction of the materials we used in this work on the environment, the energy consumption, the health of local populations of mining countries but also global economy and the stability of democracy.

### 1.5 Scope of this thesis

In this thesis, we aim to intervene on two aspects of the future HAMR technologies, the granular media and the heat sink layer. We design a magnetoplasmonic metasurface as future bit patterned media while we study how cooling of the magnetic media by an adjacent metallic heat sink layer can extend the scope of AO-HIS to much larger laser pulse durations. In Chapter 2 we introduce the conventional magnetization dynamics and we describe the magnetic properties of the materials that have been used in this work. We actually highlight that the magnetization of these materials can be reversed deterministically by an ultrafast arbitrary polarized laser pulse. The underlying mechanism of this light-induced magnetism switching is a pure thermal effect and we aim to support this absorption-based process with plasmonics.

Chapter 3 introduces some of the basic concepts in optics, plasmonics and magneto-optics that are crucial for the understanding of the systems we designed for energy efficient AO-HIS in plasmonic magnetic metasurfaces. In particular we highlight the different strategies to excite a plasmonic mode and stress the resulting effects such as absorption enhancement, requisite to enhance AO-HIS.

Chapter 4 reviews the continuing development of magnetoplasmonic platforms, in the context of the future HAMR technologies, with a more energy efficient control of magnetic order at nanoscale combined with enhanced magneto-optical (MO) effects by means of light. We stress how this thesis is part of this trend.

Chapter 5 details the experimental techniques that have been used in this thesis. After shortly describing how the samples have been grown and characterized by means of optical and MO experiments, we discuss how we obtain nanostructures through a top-down approach. We further explain the physics of ultrafast lasers and how we probe light-induced magnetization reversal with domain formation visible with a MOKE microscope. We also present the development of TR-MOKE microscopy that allows to probe magnetization dynamics with spatial resolution. We stress that this latter can be used as a simple MOKE microscope whose pump and probe wavelengths are tunable, very convenient to study the dependence of AO-HIS on the pump wavelength in magnetoplasmonic metasurfaces. Finally we detail how we performed numerical simulations with the software COMSOL Multiphysics®.

Chapter 6 gives a strategy of magnetoplasmonic metasurface design for energy efficient single pulse AO-HIS. By arranging magnetic  $[\text{Co}/\text{Gd}/\text{Pt}]_N$  nanodisks into periodic arrangements, we show that we can excite a surface lattice resonance mode that leads to a fivefold enhancement of optical absorption. More importantly, we demonstrate that this absorption enhancement leads to a reduction of the minimum fluence required for AO-HIS of the nanostructures by more

than 400 % compared to the unpatterned film. Also, the excitation of this collective resonance improves the MO activity by a factor up to 50 on resonance paving the path for future energy efficient highly sensitive all-optical data storage devices. The impact of the design of the periodic array on the position, width and amplitude of surface lattice resonances (SLRs) is discussed.

Along this line, Chapter 7 presents the dependence of the signal-to-noise ratio (SNR) on the wavelength of the probe pulses. We demonstrate that the MO contrast is strongly dependent on the wavelength and how it has been adjusted to optimize the analysis of AO-HIS MOKE images. The MO contrast is related to the complex Kerr angle of the metasurfaces and the intrinsic Kerr rotation and ellipticity have been extracted. In contrast to the expectation that the magnetic metasurfaces should exhibit either one or two SLRs for *s*- and *p*-polarized light at oblique incidence respectively, our data show three resonances for both polarizations. We explain this finding as the first demonstration of purely magnetism-induced SLRs.

Chapter 8 emphasizes that the maximum laser fluence and pulse duration resulting in AO-HIS in thin GdFeCo continuous films can be controlled by the thickness of adjacent Cu layer thickness since it plays the role of a heat sink. We demonstrate that increasing this latter from 5 nm to 900 nm considerably raise the maximum laser fluence while the switching threshold fluence remains almost unchanged. As a consequence making the heat sink layer thicker enables AO-HIS at laser pulse duration our results suggest to be much greater than 10 picoseconds. We stress that the measured increase of the maximum fluence limit of AO-HIS with the heat sink layer thickness unambiguously proves that this limit is not due to a breakdown of the underlying reversal mechanism but insufficient cooling of the electrons/spins.

Chapter 9 summarizes and concludes this thesis work and gives some perspectives.



## Chapter 2

# All-optical magnetization switching

*This chapter aims to first introduce the basics of conventional magnetization dynamics and the magnetic properties of the materials that we used in this thesis. Then, starting from pioneer works on non-equilibrium heating of electrons and ultrafast demagnetization, we highlight that the magnetization of these magnetic systems can be reversed deterministically by a single arbitrary polarized ultrafast laser pulse whose underlying mechanism relies on a pure thermal effect.*

## 2.1 Introduction

We start this chapter with conventional magnetization dynamics described by Landau-Lifschitz-Gilbert equation. Then we detail the magnetic properties of the magnetic materials that have been used in this work. We explain why rare-earth transition-metal amorphous alloys can exhibit perpendicular magnetic anisotropy and how temperature impact its magnetic properties for a fixed rare-earth concentration. After shortly mentioning pioneer works in ultrafast physics, we point out that the magnetization of such materials can be reversed deterministically by a single ultrafast laser pulse. Since the light helicity is not requisite to be circular, we stress that this kind of light-induced magnetization switching is driven by a pure thermal effect.

## 2.2 Conventional magnetization dynamics

We first describe the conventional magnetization dynamics in which magnetization amplitude is preserved.

### 2.2.1 Landau-Lifschitz equation

The dynamics of the space and time-dependent magnetization  $\mathbf{M}(r, t)$  of a ferromagnet driven by an effective magnetic field can be described by the following different equation

$$\frac{\partial \mathbf{M}}{\partial t} = -\gamma_{LL}(\mathbf{M} \times \mu_0 \mathbf{H}_{eff}) + \frac{\lambda}{M_S}(\mathbf{M} \times (\mathbf{M} \times \mu_0 \mathbf{H}_{eff})) \quad (2.1)$$

discovered by L. Landau and E. Lifschitz in 1935 with a phenomenological parameter  $\lambda$  to take into account the motion damping<sup>26</sup>.  $\gamma_{LL}$  is defined as the norm of the electronic gyromagnetic ratio  $\gamma$  as

$$\gamma_{LL} = |\gamma| = \left| \frac{g\mu_B}{\hbar} \right| \quad (2.2)$$

where  $g$  is the Landé factor,  $\hbar$  the reduced Planck constant,  $\mu_B$  the Bohr magneton and  $M_S$  the saturation magnetization. The magnetization is locally impacted by the effective field  $H_{eff}$  whose various origins are explained later. It should be mentioned that the norm of the magnetization  $\mathbf{M}(r, t)$  is conserved in Equation (2.1). The first term on the right side of Equation (2.1) is orthogonal to both the magnetization and the effective field as shown in Figure 2.1. It induces a torque that makes the magnetization precess around the effective field. The second term introduces a damping orthogonal to the magnetization but also the precessional term, tending



to return the magnetization to the equilibrium position whose orientation is collinear with the effective field.

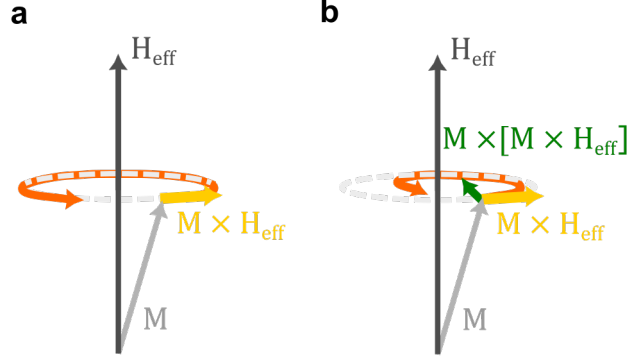


Figure 2.1: Sketch of magnetization precession for (a) undamped motion (b) damped motion.

The effective field finds its origin from the contributions of the interactions driving the atomic magnetic moments<sup>27,28</sup>:

- The Zeeman interaction takes into account the interaction between magnetic dipoles  $m_i$  and an external magnetic field  $H_{ext}$ :  $E_{zee} = -\mu_0 \sum_i \mathbf{m}_i \cdot \mathbf{H}_{ext}(r_i)$
- The magnetic dipolar interaction, standing for a long range interaction, shows the effects of different induced magnetic dipoles on macroscopic scale:  $E_d = -\frac{\mu_0}{2} \sum_{i \neq j} \frac{3(\mathbf{m}_i \cdot \mathbf{u}_{ij} \mathbf{m}_j \cdot \mathbf{u}_{ij}) - \mathbf{m}_i \cdot \mathbf{m}_j}{|\mathbf{r}_{ij}|^3}$  where  $\mathbf{r}_{ij} = \mathbf{r}_i - \mathbf{r}_j$  and  $\mathbf{u}_{ij}$  is the unit vector with the same direction as  $\mathbf{r}_{ij}$ . In a finite system, all the dipolar fields do not compensate each other resulting in demagnetizing field within, and a stray field outside the medium.
- The exchange interaction is characterized by the interaction at short range between two spins  $\mathbf{S}_i$  and  $\mathbf{S}_j$  as:  $E_{ex} = -J_{ex} \sum_{i \neq j} \mathbf{S}_i \cdot \mathbf{S}_j$  where  $J_{ex}$  is the exchange constant. A positive (negative) constant leads to a parallel (antiparallel) configuration of the spins that minimizes (maximizes) the energy. In metals, conduction electrons are responsible of exchange interactions. In transition metals (TM),  $3d$  electrons contribute to magnetism but also to exchange interactions. In rare-earths (RE), exchange interactions come from  $s$ ,  $p$ , and  $d$  while the magnetism is induced by  $4f$  electrons. That is why the exchange coupling is weaker in RE than in TM. This interaction is responsible of collective behaviour then long range magnetic order if the thermal activation is weak enough. The order is lost

above a critical temperature and leads to paramagnetism. This temperature corresponds to the so-called Curie temperature  $T_C$  and Neel temperature  $T_N$  for ferromagnetic and antiferromagnetic order, respectively.

- The spin orbit coupling  $E_{SO} = \lambda_{SO} \sum_i \mathbf{L}_i \cdot \mathbf{S}_i$  where  $\mathbf{L}_i$  and  $\mathbf{S}_i$  are the orbital and spin angular moments, respectively. This contributes to many effects, both volume like magnetocrystalline anisotropy and surface like Rashba and Edelstein effects. In particular, in case of crystalline anisotropy, the resulting energy orientation is determined by the magnetization direction and the anisotropy axes induced by the crystallographic structure.

### 2.2.2 Landau-Lifschitz-Gilbert equation

Another phenomenological formulation of the magnetization dynamics has been provided by T. Gilbert in 1955, taking into account a damping term proportional to the frequency of the precession and expressed as<sup>29</sup>

$$\frac{\partial \mathbf{M}}{\partial t} = -\gamma_{LLG}(\mathbf{M} \times \mu_0 \mathbf{H}_{eff}) + \frac{\alpha}{M_S}(\mathbf{M} \times \frac{\partial \mathbf{M}}{\partial t}) \quad (2.3)$$

with

$$\gamma_{LLG} = \gamma_{LL}(1 + \alpha^2) \quad (2.4)$$

where  $\alpha$  is the phenomenological Gilbert damping parameter. The damping finds its origin in different phenomena such as scattering of itinerant electrons, Foucault's currents from conductors, spin pumping into non-magnetic metallic materials or direct magnon-phonon coupling in conductors but also in insulators<sup>30,31</sup>. Thin films also contain defects (more than nanostructures) that can contribute to damping via for instance two magnon scattering<sup>32</sup>.

Also, considering a metallic magnetic layer/metallic non-magnetic layer interface where the non-magnetic layer plays the role of a capping layer for instance, the magnetization of the magnetic layer creates a spin current that is injected into the non-magnetic layer. Taking into account this contribution, two additional terms can be considered in equation (2.3) referring to field-like torque and damping-like torque. The losses associated to these terms lead to an additional effective damping term contributing to the total damping<sup>33-35</sup>.

## 2.3 Rare-earth transition-metal alloys

Now we detail the magnetic properties of the magnetic materials that we use in this work.

### 2.3.1 Magnetization

The net magnetization of rare-earth transition-metal alloys (RE-TM) is given by the sum of the magnetization of both sublattices. For a given temperature, one RE atomic composition  $x_{comp}$  leads to a zero net magnetization. Then, if  $x_{RE} \leq x_{comp}$  ( $x_{RE} \geq x_{comp}$ ), the resulting magnetization is determined by the magnetization orientation of the TM (RE) sublattice.

### 2.3.2 Exchange

In case of RE-TM amorphous alloys, three exchange interactions should be taken into account to describe its magnetic behaviour properly: the exchange interaction induced by two RE atoms  $J^{RE-RE}$ , another by two TM atoms  $J^{TM-TM}$  and the last one by a coupling between one RE atom and one TM atom  $J^{RE-TM}$ . In particular, the exchange interaction in TM originates from overlap of  $3d$  orbitals that are the source of magnetism. In metals such as Fe, Co and Ni, the constant  $J^{TM-TM}$  is positive that is why these elements are ferromagnetic. It is quite different in case of RE as this interaction is based on  $5d$  conduction electrons polarized by  $4f$  orbitals. They are localized close to the positively charged nucleus, do not contribute to interatomic bonds but are responsible of the total magnetic moment by summing all the single moments. Their interaction is a long range interaction that is positive in case of RE elements such as Tb and Gd<sup>36</sup>.

As a consequence, it is necessary to take into account the positive exchange between  $4f$  and  $5d$  orbitals in RE elements linked to a direct exchange coupling between  $3d$  and  $5d$  sites on TM and RE, respectively. Campbell described indeed this mechanism in 1972 through 3 different couplings<sup>37</sup>:

- Positive exchange interaction between spin moments of  $5d$  orbitals and  $4f$  orbitals in RE elements:  $J^{5d-4f} > 0$
- Negative exchange interaction between spin moments of  $3d$  electrons from TM atoms and spin moments  $5d$  electrons from neighbored RE atoms :  $J^{3d-5d} < 0$
- Spin-orbit coupling in RE elements between the orbital momentum  $\mathbf{L}_{4f}$  and the spin momentum  $\mathbf{S}_{4f}$  defined by  $-\lambda \mathbf{L}_{4f} \cdot \mathbf{S}_{4f}$  where a negative  $\lambda$  describes a light RE element (Ce, Pr, Nd, Pm, Sm and Eu) while a positive  $\lambda$  describes a heavy RE element (Gd, Tb, Dy, Er, Tm et Yb)

More precisely, the sign of  $\lambda$  will also dictate the alignment of the magnetizations of the two elements: ferromagnetic (negative constant) or antiferromagnetic (positive constant) as sketched

in Figure 2.2.

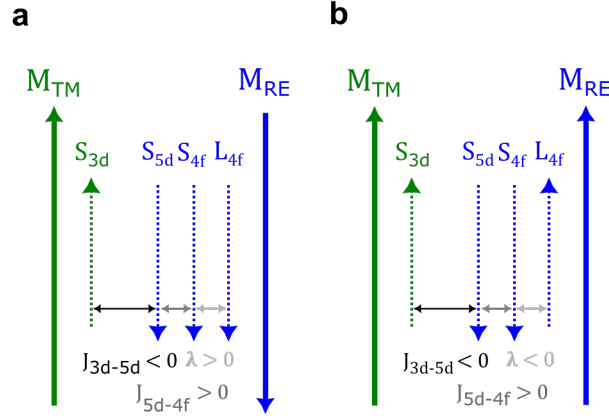


Figure 2.2: Coupling between a transition-metal element and a (a) heavy (b) light rare-earth element

In general,  $|J^{TM-TM}| > |J^{RE-TM}| > |J^{RE-RE}|$ . Thus the magnetized TM can induce a RE magnetization at temperature where the pure RE system would be paramagnetic<sup>38</sup>. The total magnetic moment can be obtained by adding the magnetic moments of each sublattice.

### 2.3.3 Anisotropy

#### Random anisotropy

In case of crystalline materials, the exchange and anisotropy properties are preserved in the volume. Thus studying the primitive cell of a crystal is sufficient to describe the properties of the bulk material. In case of amorphous materials, the disorder induces a non-equivalence of atomic sites, that leads to a distribution of exchange and anisotropy contributions. R. Harris, M. Plischke and M. J. Zuckermann introduced in 1973 the following Hamiltonian to explain the impact of a random anisotropy on the magnetic state of amorphous materials<sup>39</sup>

$$\hat{H} = \frac{1}{2} \sum_{i,j} J(r_{i,j}) \mathbf{S}_i \cdot \mathbf{S}_j - \frac{1}{2} \sum_i D_i (\mathbf{n}_i \cdot \mathbf{S}_i)^2 \quad (2.5)$$

The first term is the exchange contribution with  $J(r_{i,j})$  the nearest-neighbor exchange constant and the second term corresponds to the random anisotropy contribution where  $D_i$  is the single-ion anisotropy constant. They showed that the ratio  $D/J$  governs the magnetic state of the sample and distinguished three main cases.

The case  $|D/J| \gg 1$  corresponds to speromagnetism<sup>40</sup>. The random anisotropy is dominant and leads to a zero macroscopic moment at  $T = 0\text{K}$  as spins are randomly distributed over all directions as sketched in Figure 2.3(a). This occurs for alloys made of RE and TM with high concentration of RE such as  $\text{Tb}_{75}\text{Fe}_{25}$ <sup>41</sup> and  $\text{Tb}_{75}\text{Au}_{25}$ <sup>42</sup>. If speromagnetic materials can be considered as random antiferromagnets, a dominant random anisotropy can also lead to asperomagnetic structures with spontaneous magnetization, induced by spins randomly distributed over some directions with a given probability<sup>40,43</sup> as shown in Figure 2.3(b). Hence asperomagnetism can be described as random ferromagnetism.

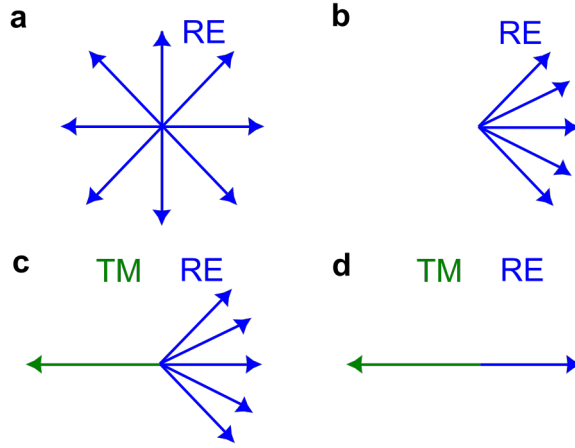


Figure 2.3: Macroscopic representation of (a) speromagnetism (b) asperomagnetism (c) sperimagnetism and (d) ferrimagnetism.

Another case corresponds to  $|D| \geq |J|$  that describes RE-TM alloys we study. Then, the energy of the system can be explained by the following Hamiltonian according to Harris' description

$$\hat{H} = -\frac{1}{2} \sum_{i,j} J(r_{i,j})^{RE-TM} \mathbf{S}_i^{RE} \cdot \mathbf{S}_j^{TM} - \frac{1}{2} \sum_{i,j} J(r_{i,j})^{TM-TM} \mathbf{S}_i^{TM} \cdot \mathbf{S}_j^{TM} - \frac{1}{2} \sum_i D_i^{RE} (\mathbf{n}_i \cdot \mathbf{S}_i^{RE})^2 \quad (2.6)$$

As  $|J^{TM-TM}| > |J^{RE-TM}| > |J^{RE-RE}|$ , the exchange contribution RE-RE is negligible and does not appear in Equation (2.6) while  $D_i^{TM}$  is neglected since the magnetocrystalline anisotropy is weak in  $3d$  metals comparing to RE elements. Two subcases can be distinguished. The first one consists of dominance of exchange contribution, that is to say  $|J^{TM-TM}| > |J^{RE-TM}| \gg |D^{RE}|$ , and leads to either ferromagnetic or ferrimagnetic order depending on the sign of  $J^{TM-TM}$  and  $J^{RE-TM}$ . Alloys such as GdCo, GdFe and GdFeCo are

## CHAPTER 2. ALL-OPTICAL MAGNETIZATION SWITCHING

---

concerned by this description. As  $J^{Gd-Co/Fe/FeCo}$  is negative and Gd atoms have no local orbital moment, a simple antiferromagnetic coupling is observed as shown in Figure 2.3(d).

The second subcase, illustrated in Figure 2.3(c), corresponds to  $|J^{TM-TM}| > |J^{RE-TM}| \approx |D^{RE}|$ , that is to say the moments orientation of the RE elements is determined by its anisotropy and the exchange interaction with the TM elements. It has been observed in systems such as DyCo<sub>3</sub>, DyNi<sub>3</sub><sup>40</sup>, TbFe<sub>2</sub>, YFe<sub>2</sub><sup>44,45</sup> or DyCu<sup>46</sup>. Its structure is sperimagnetic and consists of two spin sublattices (for instance one for Tb and the other for Fe). Basically, the exchange is dominant in Fe while each atom of Tb has a random uniaxial anisotropy, due to  $|J^{RE-TM}| \approx |D^{RE}|$ , resulting in a distribution of the Tb moment in a cone. As  $J^{RE-TM} < 0$ , the Tb moments are antiparallel to the Fe moments. The cone angle has been evaluated for DyCo<sub>3</sub> and TbFe<sub>2</sub> from XMCD or neutron reflexion measurements<sup>36,40</sup>.

### Pair-order anisotropy

R. J. Gambino, P. Chaudhari and J. J. Cuomo first discussed in 1974 the impact of the growth methods on the magnetic anisotropy with a selective resputtering mechanism resulting in a atomic short range ordering responsible of the perpendicular magnetic anisotropy<sup>47</sup> (PMA). This has been followed by the experimental demonstration of the PMA in a GdCo film<sup>48</sup>. In addition, in 1978, R. J. Gambino and J. J. Cuomo studied in details the mechanism responsible of PMA in amorphous alloys coming from pair-order anisotropy (POA) and described statistics on preferential orientation of the different types of bonds<sup>49</sup>. In particular, Co-Co and Gd-Gd pairs tend to be parallel to the film plane while Gd-Co tend to be parallel to the sputtering direction. Despite these convincing discussions, no clear experimental evidence could lead to the exact impact of POA on PMA. R. C. Taylor and A. Gangulee investigated the same system but prepared by thermal evaporation<sup>50</sup>. They highlighted that the preparation method is crucial for determining the preferential pair directions. In particular, opposite to the interpretations from sputtered magnetic films, they explained that Co-Co and Gd-Gd pairs contribute to the PMA while Gd-Co pairs appear to be in the film plane direction.

Advancements in extended x-ray absorption fine structures (EXAFS) standards<sup>51,52</sup> and EXAFS spectroscopy<sup>53</sup> allowed V.G. Harris *et al.* to demonstrate a short range structural anisotropy in sputtered TbFe films<sup>54,55</sup>. Indeed, using glancing and normal incidences, they showed that PMA is induced by like atom pairs preferentially oriented along the film plane and unlike atom pairs preferentially oriented out of the plane. This experimental evidence is in agreement with predictions from R. J. Gambino, P. Chaudhari, and J. J. Cuomo<sup>47</sup>. Another study from F. Hellman and E. M. Gyorgy underlines the importance of temperature during the growth process

and its impact on the texturation of the structure<sup>56</sup>. Finally, in 2001, V. G. Harris and T. Pokhil experimentally demonstrated enhancement of PMA in sputtered TbFe films due to selective re-sputtering of surface adatoms, leading to POA, that is to say atomic-scale structural anisotropy<sup>57</sup>.

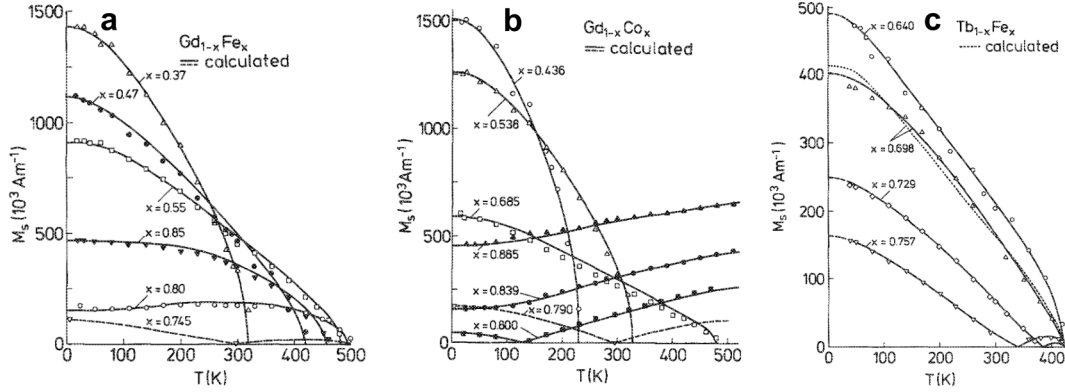


Figure 2.4: Saturation magnetization as function of temperature for (a) GdFe alloys, (b) GdCo alloys and (c) TbFe alloys. The solid and dashed lines are derived from the mean-field theory. Figure adapted from reference 58.

### 2.3.4 Compensation temperatures

The magnetic properties of RE-TM alloys depend strongly on the RE elements concentration<sup>59</sup>. In particular, in case of Gd<sub>x</sub>Fe<sub>1-x</sub>, the magnetization related to each sublattice evolves with the temperature, for a fixed Re concentration, according to Figure 2.4(a). For  $x < 0.15$ , the magnetization of the system is dominated by the Fe sublattice magnetization until the Curie temperature  $T_C$  while for  $x > 0.3$ , the magnetization of the system is dominated by the Gd sublattice magnetization until  $T_C$ . Hansen *et al.* demonstrated for the first time the existence of temperature compensation of magnetization  $T_M$  in GdFe ferromagnetic system<sup>58</sup>. For intermediate composition, both sublattices have similar magnetic behaviours and at the so-called temperature compensation, the sublattice magnetizations are equal but of opposite sign resulting in a net zero magnetization of the alloy. It should be noted that the Gd sublattice magnetization decays faster with increasing temperature than the Fe sublattice magnetization since the exchange in TM elements is stronger than in RE elements.

Increasing the Gd concentration tends to strengthen its magnetization at low temperatures and a higher temperature is needed to reach the compensation. This behaviour has been demon-

## CHAPTER 2. ALL-OPTICAL MAGNETIZATION SWITCHING

strated experimentally<sup>60</sup> but also predicted with atomic spin simulations<sup>61,62</sup>. For a given temperature, it also exists a composition, so-called compensation composition, at which magnetic moments of each sublattices have opposite contributions leading to a total zero magnetization or an infinite coercive field. Hansen *et al.* showed in the same period similar behaviour for RE-TM alloys based on the RE Dy and Ho with the same TM Fe and Co<sup>63</sup>.

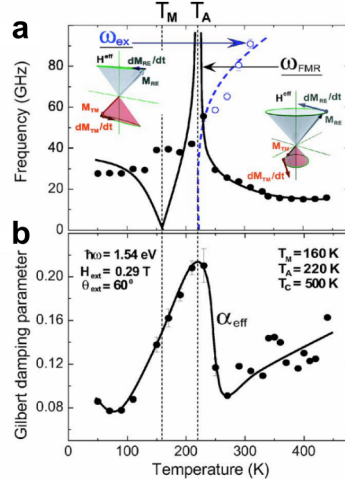


Figure 2.5: (a) Magnetization precession frequencies  $\omega_{FMR}$  and  $\omega_{ex}$  as function of temperature.  $\omega_{FMR}$  and  $\omega_{ex}$  denote the ferromagnetic and exchange resonances, respectively. The insets sketch these modes. The solid lines show what to expect theoretically. (b) Gilbert damping parameter  $\alpha_{eff}$  as function of temperature. Lines are guides to the eye. Figure adapted from reference 64.

These systems also exhibit compensation temperature of angular momentum resulting in zero net angular momentum at this specific condition<sup>65</sup>. This property has been observed in 2006 by Stanciu *et al.* during their investigation of the evolution of magnetization precession and Gilbert damping parameter with temperature<sup>64</sup>. As presented in Figure 2.5, they revealed the existence of such compensation temperature of angular momentum  $T_A$  in GdFeCo with a maximum of both parameters at the same temperature. The same year, Binder *et al.* demonstrated the same behaviour is GdCo alloys<sup>66</sup>. This property is believed to allow a faster manipulation of magnetization, speeding the motion of domain wall as suggested by Kim *et al.*<sup>67</sup> or accelerating spin dynamics in GdFeCo as demonstrated by Stanciu *et al.*<sup>64</sup>. Very recently, Hirata *et al.* stressed that both compensation temperatures  $T_M$  and  $T_A$  are not independent<sup>68</sup>. They even provided a theoretical framework to explain their experimental observations and proposed a method to determine  $T_A$  from  $T_M$  and  $T_C$ , paving the path for the development of spintronics devices based on ferrimagnetic materials.



## 2.4 From non-equilibrium electron heating to all-optical magnetization switching

This last section aims to review shortly the emergence of ultrafast physics, leading to the recent discovery of all-optical magnetization switching (AOS) that can be performed in the magnetic materials that we studied in this work.

### 2.4.1 Emergence of ultrafast physics

When a metal is illuminated by an ultrafast laser pulse whose pulse length is shorter or of the same order of magnitude as the hot carrier energy loss lifetime, then it was predicted that electron and phonon thermal baths are not thermalized<sup>69</sup>. Eesley observed first out-of-equilibrium electron heating in metals<sup>70</sup> followed by Brorson *et al.* who performed out-of-equilibrium electron heating in Au by measuring transient reflectivity in Au layer induced by an ultrafast laser pulse as shown in Figure 2.6<sup>71</sup>. They pumped from sample side while they probed reflected light from sapphire substrate side. The rise of reflectivity depends on Au thickness due to heat propagation time in the samples. However, all delays remain shorter than the electron-phonon relaxation time as both baths thermalize after 1-3 ps<sup>72</sup>. In this perspective their results suggested that heat transport is mediated by out-of-equilibrium electrons. This was confirmed by further studies<sup>72-74</sup> and similar measurements of transient reflectivities have been performed for Ag<sup>75</sup> and Cu<sup>76,77</sup>.

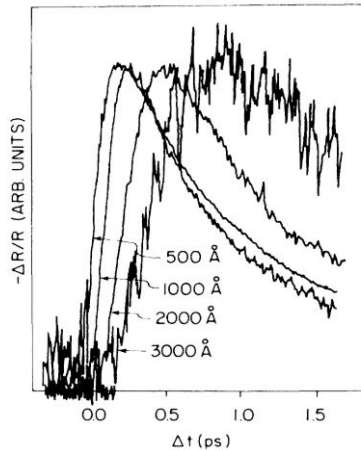


Figure 2.6: Transient reflectivity measured on gold films 50, 100, 200 and 300 nm thick. The sample is excited from thin film side while the system is probed from the substrate. Figure from reference 71.

The behaviour of hot carriers also depends on crystalline structure<sup>72,78</sup>. Electron-defect scat-

tering can impact electron-phonon and electron-electron coupling. As a consequence, the presence of grain boundaries in polycrystalline systems has been shown to make the transport slower than in single-crystalline structures<sup>72,78</sup>. Similar trend is observed in nanoparticles. Besides, the ballistic transports describes well the flow of hot electrons in thin films but diffusive motion is required to explain inhomogeneously heated thick films<sup>79</sup>. From these developments both ballistic and diffusive electronic transports have been combined to treat properly the flow of hot carriers in metallic systems<sup>79-81</sup>.

These pioneer works opened the way for intense studies in ultrafast physics. As we will discuss now, these studies have been followed by the demonstration of ultrafast demagnetization then by the opportunity to reverse deterministically magnetization by means of light only. The opening of such research topic fits with the ceaseless demand of data storage industry to switch magnetization faster with less requisite energy.

### 2.4.2 Ultrafast demagnetization

Vaterlaus *et al.* performed in 1991 time- and spin-resolved photoemission experiments to monitor the out-of-equilibrium magnetization dynamics of Gd. They concluded that spin and lattice thermalize after  $100 \pm 80$  ps<sup>82</sup>, further validated by theory<sup>83</sup>. Few years later, using time-resolved MOKE, Beaurepaire *et al.* induced ultrafast demagnetization of Ni under the excitation of 60 fs laser pulses<sup>6</sup>. They probed the magnetization dynamics for a unique laser fluence of 7 mJ/cm<sup>2</sup> as shown in Figure 2.7. Even if the relevance of linking the MOKE signal and the magnetization in ultrafast regime has been questioned<sup>84</sup>, ultrafast magnetization dynamics has been confirmed in further experiments with the use of different techniques such as Second-Harmonic Generation<sup>85,86</sup> (SHG), time-resolved spin polarized photoemission<sup>87</sup>, X-ray Magnetic Circular Dichroism<sup>88</sup> (XMCD).

Thrilled by this discovery, the scientific community started to build a framework which could explain these results. It was widely admitted at this time that the mechanism was based on hot electrons put in out-of-equilibrium state due to the absorption of ultrafast laser pulse<sup>88-96</sup>. Their energy is above the Fermi energy and they thermalize the spin bath characterised by a transfer of spin angular momentum. The flow of hot electrons can create a spin current which is in some metals highly spin-polarized.

After the pioneer work of Beaurepaire *et al.*<sup>6</sup>, Hohlfeld *et al.* were able, by means of SHG technique, to deduce electronic temperature  $T_e$  from  $\Delta I^+$  but also the normalized magnetization  $\mathbf{M}$  from  $\Delta I^-$  where  $\Delta I^\pm(t) = (I^\pm(t) - I_0^\pm(t))/I_0^\pm(t)$ . This method compares the sums and differences of the SHG signals of the two opposite magnetization directions  $I^\pm(t)$  with the

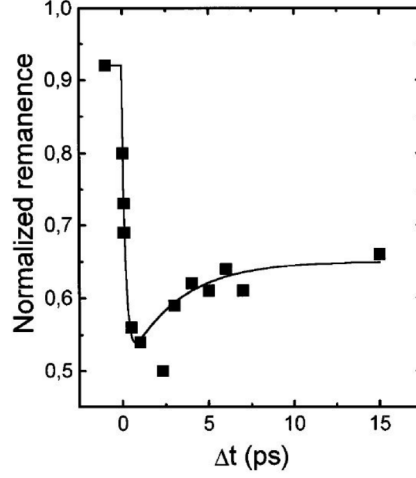


Figure 2.7: Transient remanent longitudinal MOKE signal of a Ni(20 nm)/MgF2(100 nm) film for 7 mJ/cm<sup>2</sup> pump fluence. The signal is normalized to the signal measured in the absence of pump beam. The line is a guide to the eye. Figure and caption from reference 6.

reference signal without the pump pulse  $I_0^\pm(t)$ . The following equations describe the evolution of  $T_e$  and  $M$  under the condition the electrons are thermalized

$$\Delta I^+ = \text{cons}(T_0 - T_e(t)) \quad (2.7a)$$

$$\Delta I^- = \frac{M(T_e(t))\cos(\phi)}{M(T_0)} - 1 \quad (2.7b)$$

where  $\phi$  is a phase term.

Figure 2.8 shows that electrons are already thermalized after 300 fs while some deviation for 3 fluences from Weiss model<sup>97</sup> is observed for delays smaller than 300 fs, suggesting that the system is out-of-equilibrium. Then a new context is required to describe properly ultrafast magnetization dynamics as the system is out of equilibrium<sup>98</sup>. Theoretical framework provided by Equation (2.3) is not suitable anymore to describe magnetization dynamics with the loss of magnetic moment because Equation (2.3) preserves magnetization amplitude.

However, this discovery raised many questions, mostly how is distributed angular momentum and the impact of light in ultrafast regime. In this perspective, Beaurepaire *et al.* developed a three temperature model (3TM) based on two temperature model (2TM) from Anisimov<sup>69</sup> with an additional spin thermal bath to describe the energy and angular momentum transfer between the electrons, the phonons and the spins, respectively<sup>6</sup>

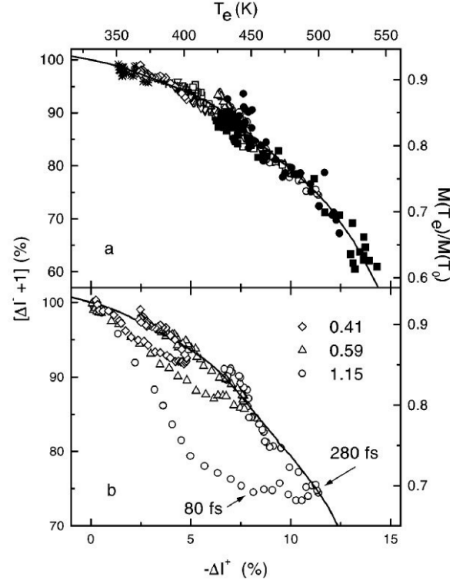


Figure 2.8: (a) Direct comparison of experimental data for delay  $> 0.3$  ps with the fit (solid line) describing equilibrium from reference 97. (b) Same kind of experimental for three fluences over all the time delay range. The deviations from the Weiss model indicate an out-of-equilibrium state of electron and spin systems in the first 0.3 ps. Figure from reference 85.

$$C_e(T_e) \frac{dT_e}{dt} = -g_{ep}(T_e - T_p) - g_{es}(T_e - T_s) + P(t) \quad (2.8a)$$

$$C_s(T_s) \frac{dT_s}{dt} = -g_{es}(T_s - T_e) - g_{sp}(T_s - T_p) \quad (2.8b)$$

$$C_p(T_p) \frac{dT_p}{dt} = -g_{ep}(T_p - T_e) - g_{sp}(T_p - T_s) \quad (2.8c)$$

where  $C_e$ ,  $C_p$  and  $C_s$  are the contributions to the specific heat of the system of the electrons, phonons and spins, respectively. In addition,  $g_{es}$ ,  $g_{ep}$  and  $g_{sp}$  stand for electron-spin, electron-phonon and spin-phonon interaction constants. The source term interacts only with the electron bath so then electrons transfer energy to the lattice and the spins. Even if it was admitted by the scientific community that electrons and phonons showing different temperature induce an out-of-equilibrium state within a period of the order of a picosecond<sup>69,99</sup> with the electronic bath not thermalized in subpicosecond time scale<sup>100</sup>, the spin system was not expected to react that fast to ultrafast external stimuli<sup>101</sup>. In this perspective, the results showing ultrafast demagnetization of Ni observed by Beaurepaire *et al.* and Hohlfeld *et al.* were really surprising, even more with the work of Vaterlaus *et al.* showing a spin relaxation time of hundreds of picoseconds, certainly

with strong uncertainty but actually supported by further experimental studies<sup>102,103</sup>.

### 2.4.3 All-optical magnetization switching

#### From multiple to single pulse all-optical switching in GdFeCo

Stanciu *et al.* first demonstrated in 2007 ultrafast magnetization reversal of a thin magnetic film of ferrimagnetic GdFeCo alloy with 40 fs circularly polarized laser pulse<sup>7</sup>. The switching depended on the helicity of light while linearly polarized light could only provide multidomain pattern so that no switching is observed as shown in Figure 2.9. Interestingly, right-handed (resp. left-handed) circularly polarized light pulses reversed the magnetization in black (resp. white) domains without affecting the domains with opposite orientation. The linearly polarized light did not induce magnetization switching but only a random distribution of small domains pointing up and down randomly leading to a multidomain state. Besides they demonstrated that the magnetization can be switched with a 40 fs single pulse whose polarization is circularly polarized leading to the so-called all-optical helicity-dependent switching (AO-HDS).

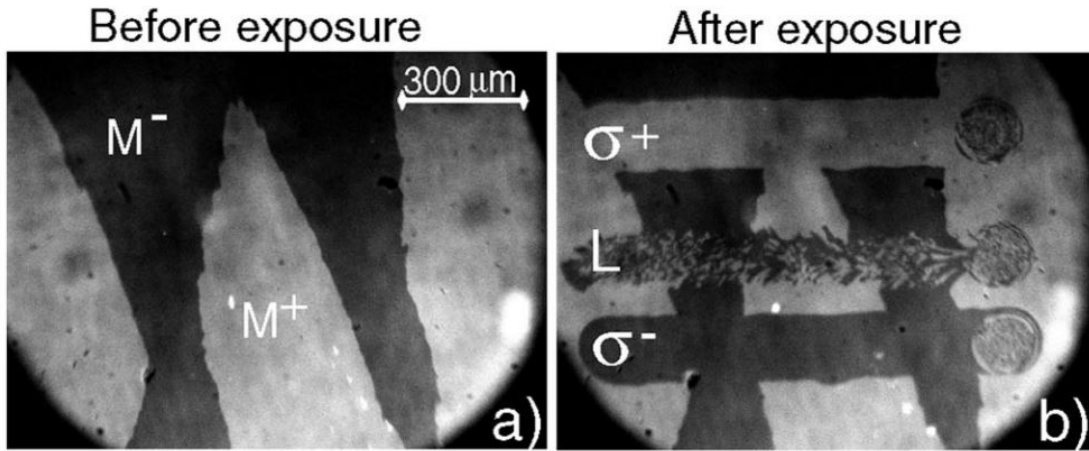


Figure 2.9: (a) MO image of the initial magnetic state of the sample before laser exposure. Bright and dark areas are attributed to magnetic domains whose magnetization points up and down, respectively. (b) Domain pattern resulting from sweeping the sample at low speed ( $30 \mu\text{m}/\text{s}$ ) with linearly (L), right-handed ( $\sigma_+$ ), and left-handed ( $\sigma_-$ ) circularly polarized beams with a laser fluence of about  $11.4 \text{ mJ}/\text{cm}^2$ . The central area of the remaining spots at the end of each scan line consists of small magnetic domains, where the ratio of up to down magnetic domains is close to 1. Figure from reference 7.

It should be noted this AO-HDS is a generic phenomenon observable, not restricted to Gd-based materials. Indeed, Alebrand *et al.* performed AO-HDS on  $\text{Tb}_x\text{Co}_{1-x}$  subjected to 400 fs

## CHAPTER 2. ALL-OPTICAL MAGNETIZATION SWITCHING

---

and 10 ps ultrafast laser pulses<sup>104</sup>. In particular, they swept the laser on the sample surface whose polarization was circular. The Tb concentration range to be able to observe AO-HDS suggested that a key ingredient for magnetization reversal was a compensation temperature between room temperature and Curie temperature. However, Hassdenteufel *et al.* managed to switch magnetization of  $\text{Tb}_x\text{Fe}_{1-x}$  with concentrations leading to compensation temperature below room temperature, meaning that it is not a necessary condition for AO-HDS<sup>105</sup>.

Then, AO-HDS has been shown to be possibly achieved in other ferrimagnetic materials<sup>106</sup>, granular media and ferromagnetic materials<sup>9</sup> but also artificial zero moment magnets<sup>107</sup>. The driving force of AO-HDS is still the subject of intense debates. Several origins have been proposed to explain how the symmetry breaking occurs to lead to magnetization switching.

One candidate stands for a pure thermal effect based on MCD, in other terms the magnetic media absorbs differently the light depending on its polarization. This mechanism is believed to be valuable for granular media<sup>108,109</sup> and thin films<sup>110</sup>. Another widely used explanation is the Inverse Faraday Effect (IFE), a concept introduced by Pitaevskii in 1961 for non absorbing medium<sup>111</sup>. In this context, Kimel *et al.* suggested in 2005 a way to non-thermally control the spin dynamics of  $\text{DyFeO}_3$  with this approach. From a theoretical point of view, the community tried to extend the IFE to metallic magnetic systems with the contribution of an extra optomagnetic field through micromagnetic simulations<sup>112,113</sup>. However this approach seemed to be nugatory since the effect should last longer than the effect origin, in other terms the laser pulse length.

In addition, Scheid *et al.* proposed an original mechanism based on Magnetization Induced during Light Absorption (MILA)<sup>114,115</sup>. *Ab initio* calculations performed with density functional theory suggested the presence of another helicity dependent contribution due to light absorption by the magnetic material which lasts longer than the light excitation. Despite many investigations, the real impact of helicity on AO-HDS is not fully understood<sup>116,117</sup>.

Direct transfer of angular momentum by the light to the magnetic system is another driving force that has been proposed<sup>106</sup>. One should keep in mind that light, even with specific helicity, does not inevitably carry angular momentum<sup>118–120</sup>. In the framework of ultrafast magnetism, mostly lasers with spatial gaussian profiles are used. In this perspective, because the amount of spin angular momentum is proportional to the derivative of the energy amplitude profile, then it could be possible that direct transfer of angular momentum from circularly incoming light to the magnetic material occurs<sup>118</sup>.

Since this thesis focuses only on AO-HIS for which light polarization can be chosen linear, we will not discuss the light helicity anymore.

All-optical helicity-independent switching

In 2011 Radu *et al.* took the opportunity to probe the magnetization dynamics of Gd and Fe sublattices after ultrafast laser excitation using time-resolved XMCD as presented in Figure 2.10<sup>8</sup>. They used only linearly polarized light. They observed that the Fe sublattice demagnetizes faster than the one of Gd leading to a transient ferromagnetic state. Indeed the Fe sublattice changes its magnetic orientation after 300 fs while Gd sublattice needs approximately 1.5 ps. This results in magnetization reversal due to transfer of spin angular momentum between the RE and TM sublattice by conservation of angular momentum. Indeed, since Gd can not dissipate energy to the lattice due to net zero orbital angular momentum, it transfers angular momentum to the Fe sublattice when this latter is demagnetized leading to a transient ferromagnetic state. Later, Fe sublattice gives back angular momentum to Gd sublattice when it experiences complete demagnetization, resulting in reversal of the magnetic orientation of both sublattices.

This gave rise to a new class of all-optical switching so-called all-optical helicity-independent switching (AO-HIS). This result seemed promising for the ceaseless demand in terms of information writing speed as the efficiency of an external magnetic field finds its limit for a time scale shorter than 2.3 ps<sup>121</sup>.

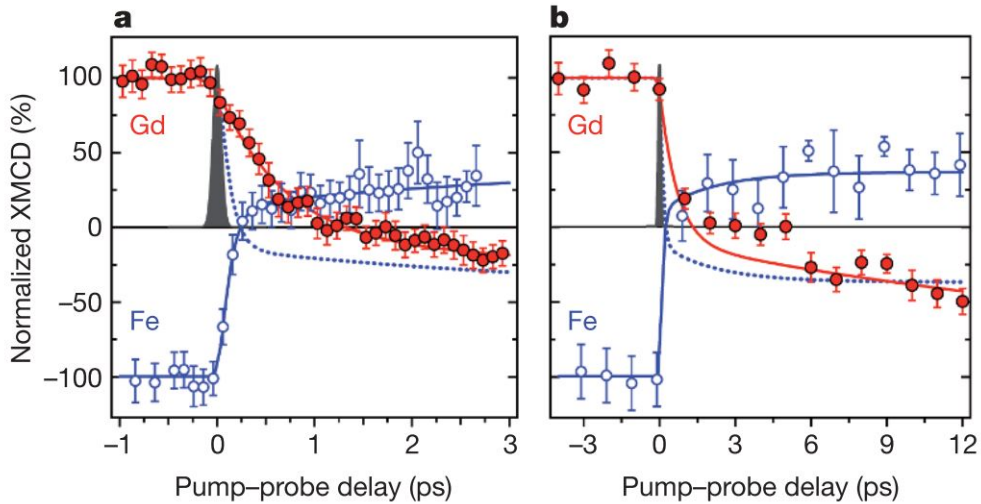


Figure 2.10: Transient dynamics of Fe (open circles) and Gd (filled circles) magnetic moments in the first (a) 3 ps and (b) 12 ps. The sample temperature has been fixed at 83 K and the fluence of the laser excitation was 4.4 mJ/cm<sup>2</sup>. Experimental time resolution of 100 fs is depicted by the solid Gaussian profile. The fits (depicted in solid lines) stands for a double exponential fit function. The dashed line in both panels describes the magnetization of the Fe sublattice taken with the opposite sign. Figure from reference 8.

Preliminary results of Stanciu *et al.* present characteristic demagnetization time of 100 and



## CHAPTER 2. ALL-OPTICAL MAGNETIZATION SWITCHING

400 fs for TM and RE sublattices, respectively, with corresponding switching time of 0.9 and 28 ps<sup>7</sup>. The data provided by Radu suggests that complete reversal occurs rather at 150 ps<sup>8</sup> that is more in line with the recent work of Wang *et al.*<sup>122</sup>.

A better understanding of the underlying physics has been provided by Ostler *et al.*<sup>123</sup>. They shined a GdFeCo alloy thin film with a single linearly polarized laser pulse whose pulse length and wavelength were 100 fs and 800 nm, respectively. As presented in Figure 2.11, they demonstrated that this material exhibits toggle switching, in other terms deterministic repetitive switching. As the light did not carry angular momentum due to its polarization, it was concluded that ultrafast heating provided by a single laser pulse was enough to perform magnetization switching. Angular momentum remained required to induce AO-HIS but occurred in the material itself with the transfer of spin angular momentum from one sublattice to another due to the transient ferromagnetic state. GdFeCo can actually show both mechanisms<sup>124</sup> and MCD explains the results of Stanciu *et al.*<sup>125</sup>. In other terms the magnetic material for a fixed magnetization orientation does not absorb equally light for different polarizations resulting in AO-HDS. In case of AO-HIS, the light polarization influences the minimum fluence required to perform magnetization switching due to MCD.

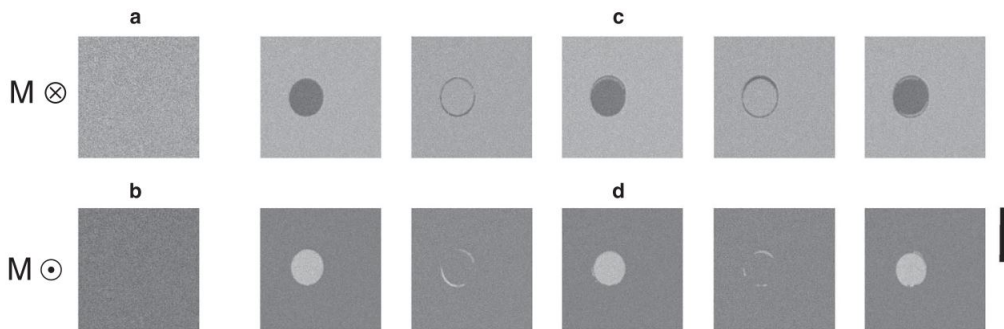


Figure 2.11: (a) and (b) Initial saturated magnetized state of the alloy thin film with magnetizations pointing up and down with light and dark grey colours, respectively. (c) and (d) Film after 5 consecutive pulses with a fluence of 2.30 mJ/cm<sup>2</sup> for both initial saturated state. The scale bar on the right corresponds to 25  $\mu\text{m}$ . Figure from reference 123.

AO-HIS has been reported in other ferrimagnetic alloy systems such as GdCo<sup>126</sup>, GdTbCo<sup>127,128</sup>, TbCo<sup>129–131</sup> and Mn<sub>2</sub>Ru<sub>x</sub>Ga<sup>132</sup> but also in synthetic ferrimagnetic systems based on multilayer arrangements like Tb/Co<sup>133–135</sup>, Tb/Fe<sup>135</sup> and Co/Gd<sup>10,11,136</sup>. The AO-HIS can be affected by many parameters such as the laser pulse length<sup>137–141</sup>, the pulse energy<sup>137,139,140,142</sup> as well as the composition in case of alloy systems<sup>62,138–141,143</sup>.

In particular, Wei *et al.* reported AO-HIS state diagrams in GdFeCo continuous layers<sup>141</sup>.



For that they investigated the effect of pulse duration and applied fluence on the single pulse AOS in GdFeCo. They also varied the thickness and the Gd composition in the full multilayer system. Figure 2.12 gives an example for  $\text{Gd}_{24}(\text{Fe}_{90}\text{Co}_{10})_{76}$ . They concluded that the fluence window for which AO-HIS is observable reduced for longer duration. The minimum fluence for achieving AO-HIS has been shown to increase with the pulse length while the minimum fluence requisite for observing a stochastic multidomain state remains almost unaffected. We discuss these points in Chapter 8.

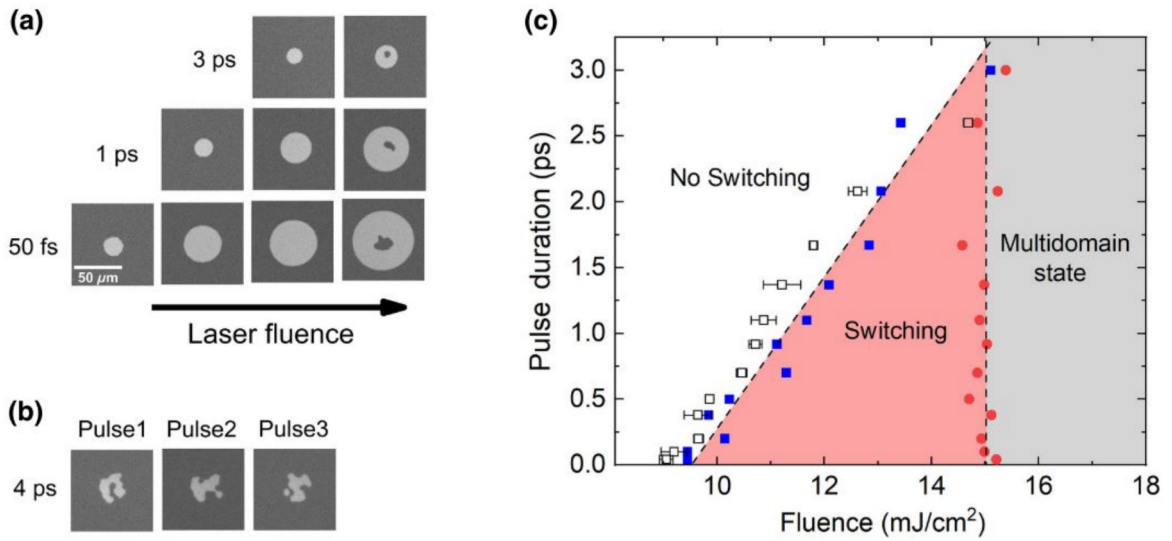


Figure 2.12: (a) MOKE images of  $\text{Gd}_{24}(\text{Fe}_{90}\text{Co}_{10})_{76}$  film after being subjected to a single linearly polarized laser pulse with 50 fs, 1 ps and 3 ps pulse lengths. The applied fluence has been varied between 9.5 to 15  $\text{mJ}/\text{cm}^2$ . (b) MOKE images of  $\text{Gd}_{24}(\text{Fe}_{90}\text{Co}_{10})_{76}$  film after being subjected to a 4 ps single linearly polarized laser pulse with a fluence of 17  $\text{mJ}/\text{cm}^2$ . (c) AO-HIS state diagram of the corresponding magnetic system delimited by the threshold fluence for switching (open black and full blue squares) and the observation of a stochastic multidomain state (full red circles). The values associated to the blue squares corresponds to a switched domain size of 10  $\mu\text{m}$  while the position of black squares have been from the method proposed by Liu *et al.*<sup>144</sup>. Figure from reference 141.

Steil *et al.* suggested, by performing AO-HIS with 13 ps single laser pulse, that putting the electrons and phonons strongly out-of-equilibrium is not crucial. Further studies done independently by the group of Rasing and group of Bokor confirmed this statement<sup>138,139</sup>. In particular, Gorchon *et al.* claimed an upper limit of 1 ps for  $\text{Gd}_{24}\text{FeCo}$  against 15 ps for  $\text{Gd}_{27}\text{FeCo}$ <sup>139</sup>. According to them, the slow energy transfer rates between the sublattices was responsible of the short pulse length limit for the lowest concentration of Gd.

Also AO-HIS has been observed for a large range of photon energy, first from 1.6 eV to 3.1

## CHAPTER 2. ALL-OPTICAL MAGNETIZATION SWITCHING

---

eV<sup>137</sup>, then from 70 meV to 1.55 eV<sup>140</sup>, meaning that AO-HIS does not depend on the incident light wavelength. Even if the applicability of this approach to high-speed magnetic recording seems clear, the issues about the maximum repetition rate of the switching have been addressed only very recently. Wang *et al.* showed in 2021 that a complete switching of GdFeCo occurs after 100 ps and that at least 300 ps are required to cool down the system in order to perform reswitching<sup>122</sup>. In this perspective, Steinbach *et al.* engineered the whole system to optimize the cooling resulting in faster writing frequency<sup>145</sup> with a delay of 7 ps, closer to the one observed by Banerjee *et al.* with Mn<sub>2</sub>Ru<sub>x</sub>Ga<sup>132</sup>.

At the moment, AO-HIS has been observed only in antiferromagnetically coupled systems in which each sublattice has its own dynamics as shown in GdFeCo<sup>8</sup> or Mn<sub>2</sub>Ru<sub>x</sub>Ga<sup>146</sup>. Demagnetizations of both sublattices are not independent and angular momentum during the process stays mostly in the electronic system. In this perspective, Bergeard *et al.* measured that the total angular momentum remains unchanged within a picosecond while TbCo experiences losses after 150 fs due most probably to non zero orbital momentum in Tb leading to significant spin-orbit coupling in its case<sup>147</sup>. This supports the statement that AO-HIS is possible once exchange scattering is greater than spin-orbit coupling. Hennecke *et al.* claimed that the complete transfer of angular momentum to the lattice is done in the first few femtoseconds based on the assumption that RE and TM sublattices do not exchange any<sup>148</sup> while Graves *et al.* confirmed earlier that the the angular momentum exchange occurs over the first picosecond<sup>149</sup>.

From these results, one can extract one key ingredient for being able to perform AO-HIS in a magnetic system. It should be driven into a regime where angular momentum transfer between the magnetic subsystems due to exchange scattering is greater than the transfer of angular momentum to the lattice via spin-orbit coupling. In other terms, the angular momentum should predominantly stay within the spin system and not be dissipated to the lattice. Gridnev discussed it theoretically, pointing out that once the conduction electrons are heated up by an ultrafast laser pulse, then they transfer energy and angular momentum to the phonons and the localized electrons. His spin dynamics model, accounting for angular momentum transfer between the subsystems and the lattice, reproduced successfully light-induced magnetization reversal<sup>150–152</sup>. In line with the statement of Hennecke *et al.*<sup>148</sup>, he stressed that angular momentum stays within the electronic system over the first picosecond.

Other theoretical studies performed over the last ten years supports the thermal nature of AO-HIS<sup>136, 139, 153–165</sup>. Certainly LLG is not adequate since magnetization magnitude changes during the switching process but Skubic *et al.* developed an atomistic approach, so-called atomistic LLG, that connects the electronic structure of a magnetic material and its spin dynamics<sup>166</sup>.

This method can make the electronic motion ultrafast and actually this theoretical framework successfully described the ultrafast spin dynamics of RE-TM amorphous alloys<sup>62</sup>. In parallel, Atxitia *et al.* derived the Landau-Lifschitz-Bloch (LLB) equation for ferrimagnetic system like GdFeCo subjected to ultrafast external stimuli which remains valid even for two-component ferromagnets or antiferromagnets<sup>154</sup>. They considered each sublattice as a macrospin with changes in amplitude and direction. Using a mean field approximation, they could describe the macroscopic motion of each sublattice in order to quantify magnetization relaxation times for both sublattices. They further confirmed the appearance of a transient ferromagnetic-like state<sup>156,167</sup> via large scale computer simulations solving the stochastic LLG equation for many individual atoms<sup>159</sup>. Another approach based on microscopic 3 temperatures model (M3TM) could also reproduce transient ferromagnetic-like state<sup>157</sup>.

Lately, the capability to perform ultrafast magnetization reversal in GdFeCo by means of picosecond electrical pulse is the most obvious demonstration that the reversal mechanism of AO-HIS in GdFeCo is solely temperature driven<sup>142</sup>. Once the electrons overcome a certain critical temperature after being subjected to ultrafast heat stimuli they are able to bring enough energy to the spins so that they can exchange angular momentum. This gives rise to a general class of magnetic order control namely temperature induced magnetization switching (TIMS). In this context, Figure 2.13 provides two strategies to achieve TIMS by means of light and electrical pulses.

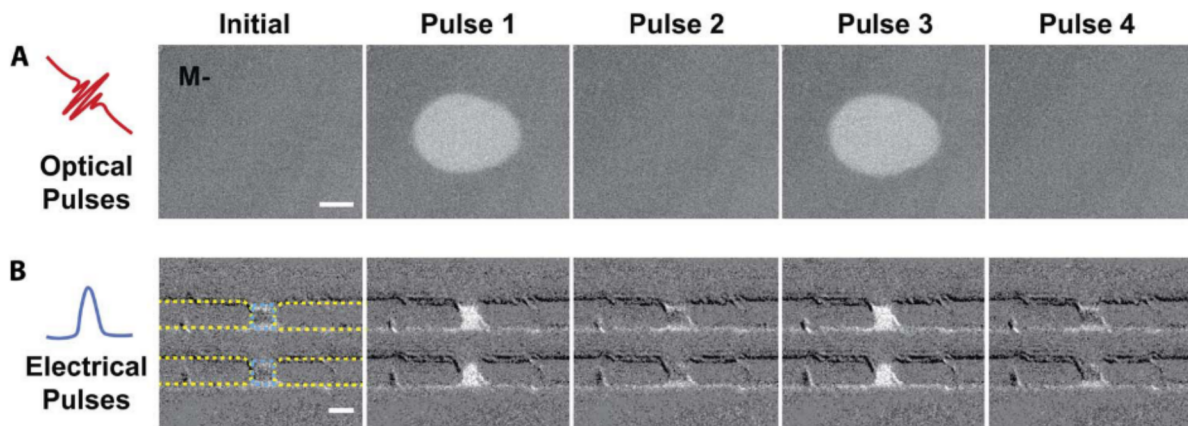


Figure 2.13: Thermally-induced magnetization reversal in GdFeCo by means of light and electric pulses. (a) MOKE images after four consecutive 6.4 ps laser pulses with an absorbed fluence of 1.8 mJ/cm<sup>2</sup>. (b) MOKE images after four consecutive 9 ps electrical pulses. The scale bars correspond to 5  $\mu$ m. Figure from reference 142.

### 2.5 Open questions

Since the underlying mechanism of AO-HIS is a pure thermal effect, one way to make it more energy efficient would be to improve light-matter interaction by means of plasmonics since the excitation of localized or collective modes enhance drastically the energy absorbed by the system from the light. Also, the size of written domains in continuous films resulting from AO-HIS remains limited at micrometer scale. This clearly does not compete with the areal density of current hard disks in the market, about 10 nm lateral width. Plasmonics is also a good candidate to confine light at nanoscale, below the diffraction limit<sup>20</sup>. Actually, some works already considered either GdCo nanodisks without plasmonic effects<sup>126</sup> or the use of external plasmonic non magnetic antennas on TbFeCo continuous films to achieve AO-HIS at nanoscale<sup>168</sup>. We propose in this work to reverse magnetization with light in periodic arrays of [Co/Gd/Pt] nanodisks by means of the excitation of a plasmonic resonance.

Another question that we want to address is the laser pulse duration limit for achieving AO-HIS to make it more easily applicable in a device. It is commonly believed that a longer pulse length makes the angular momentum transfer weaker since it does not lead to strong electron temperature transient state. We will show experimentally and theoretically that this limit is not determined by a breakdown of AO-HIS but by an unefficient cooling of the electron system. This issue can be overcome by adjacent heat sink layer that enables the electron system to be cooler than the Curie point before a certain characteristic time while a non-heat sink layer would just lead to a stochastic multidomain state.

### 2.6 Conclusion

We started this chapter by introducing the conventional magnetization dynamics and the magnetic properties of the materials we used in this thesis. After briefly highlighting some pioneer works on ultrafast physics and ultrafast demagnetization, we stress that the magnetization of the materials we considered in this thesis can be reversed deterministically with a single ultrafast arbitrary polarized laser pulse. In particular, this specific light-induced magnetization switching is driven by a pure thermal effect. We expect to support this mechanism with the excitation of plasmonic modes to increase the energy absorbed by the magnetic systems during AO-HIS. We introduce in the next chapter the relevant concepts in plasmonics for further developments of magnetoplasmonic platforms.

## Chapter 3

# Plasmonics

*We propose in this thesis to enhance AO-HIS with the excitation of a plasmonic mode that must increase absorption in the magnetic metallic system. After introducing the fundamental of classical electrodynamics in solids, we detail all the strategies given by plasmonics to increase absorption and justify the one we chose for this work. Since this thesis combines magnetism and optics, we also give the basics of magneto-optics that are useful for the understanding of this manuscript.*

### 3.1 Introduction

We dedicate this chapter to the different approaches given by plasmonics to improve light-matter interaction. We start with the fundamentals of classical electrodynamics in solids to provide a simple form of the dielectric function. This latter is crucial for describing the optical behaviour of nanostructures. Then we detail the underlying physics of the different approach and justify why we decide to consider surface lattice resonances. Finally we provide the basics of magneto-optics, needed for the understanding of this manuscript.

### 3.2 Fundamentals of classical electrodynamics in solids

Now we put into equations the fundamentals of classical electrodynamics in solids and detail the boundary conditions. We justify the importance of local response approximation. Then we present the Drude model, its relevance and its limits.

#### 3.2.1 Maxwell's equations

Macroscopic Maxwell's equations in the classical limit\* allow to understand the interactions between the electromagnetic (EM) fields and the metals through the relations<sup>169</sup>

$$\nabla \cdot \mathbf{D}(\mathbf{r}, t) = \rho_f(\mathbf{r}, t) \quad (3.1a)$$

$$\nabla \cdot \mathbf{B}(\mathbf{r}, t) = 0 \quad (3.1b)$$

$$\nabla \times \mathbf{E}(\mathbf{r}, t) = -\frac{\partial \mathbf{B}(\mathbf{r}, t)}{\partial t} \quad (3.1c)$$

$$\nabla \times \mathbf{H}(\mathbf{r}, t) = \mathbf{J}_f(\mathbf{r}, t) + \frac{\partial \mathbf{D}(\mathbf{r}, t)}{\partial t} \quad (3.1d)$$

$\mathbf{E}$  and  $\mathbf{H}$  denote the electric and magnetic fields, respectively<sup>†</sup>. In addition,  $\mathbf{D}$  and  $\mathbf{B}$  correspond to the electric displacement and magnetic induction.  $\mathbf{J}_f$  and  $\rho_f$  represent the current and charge densities produced by free charges. Then Equations (3.1) leads to the continuity equation

---

\*Atoms should be studied quantum mechanically. This failure is justified by similarities between quantum and classical mechanics discussions.

<sup>†</sup>In the macroscopic framework, both fields are supposed to be averaged over volumes that are in principle much larger than the characteristic length of the unit-cell of the crystal.

$$\nabla \cdot \mathbf{J}_f(\mathbf{r}, t) + \frac{\partial \rho_f(\mathbf{r}, t)}{\partial t} = 0 \quad (3.2)$$

Working with monochromatic fields harmonic of the form  $\mathbf{E}(\mathbf{r}, t) = \mathbf{E}_0(\mathbf{r})e^{-i\omega t}$ , one can rewrite Equations (3.1) and (3.2) in the frequency domain Maxwell's equations

$$\nabla \cdot \mathbf{D}(\mathbf{r}, \omega) = \rho_f(\mathbf{r}, \omega) \quad (3.3a)$$

$$\nabla \cdot \mathbf{B}(\mathbf{r}, \omega) = 0 \quad (3.3b)$$

$$\nabla \times \mathbf{E}(\mathbf{r}, \omega) = i\omega \mathbf{B}(\mathbf{r}, \omega) \quad (3.3c)$$

$$\nabla \times \mathbf{H}(\mathbf{r}, \omega) = \mathbf{J}_f(\mathbf{r}, \omega) - i\omega \mathbf{D}(\mathbf{r}, \omega) \quad (3.3d)$$

as well as the continuity equation

$$\nabla \cdot \mathbf{J}_f(\mathbf{r}, \omega) = i\omega \rho_f(\mathbf{r}, \omega) \quad (3.4)$$

$\mathbf{J}_f$  takes into account the induced current  $\mathbf{J}_{ind}$  and external current  $\mathbf{J}_{ext}$  densities. In particular the first contribution exists due to the electric field in the medium. Then, in order to describe properly the EM response of the medium, the constitutive equations link  $\mathbf{D}$  and  $\mathbf{E}$  as well as  $\mathbf{B}$  and  $\mathbf{H}$  according to<sup>169\*</sup>

$$\mathbf{D}(\mathbf{r}, t) = \epsilon_0 \mathbf{E}(\mathbf{r}, t) + \mathbf{P}(\mathbf{r}, t) = \epsilon_0 \int \int \epsilon(\mathbf{r}, \mathbf{r}', t - t') \mathbf{E}(\mathbf{r}', t') d\mathbf{r}' dt' \quad (3.5a)$$

$$\mathbf{B}(\mathbf{r}, t) = \mu_0 (\mathbf{H}(\mathbf{r}, t) + \mathbf{M}(\mathbf{r}, t)) \quad (3.5b)$$

$$\mathbf{J}_{ind}(\mathbf{r}, t) = \int \int \sigma(\mathbf{r}, \mathbf{r}', t - t') \mathbf{E}(\mathbf{r}', t') d\mathbf{r}' dt' \quad (3.5c)$$

with  $\mathbf{P}$  the polarization and  $\mathbf{M}$  the magnetization coming from electric and magnetic dipoles induced by bound charges. Throughout this thesis we work at optical wavelengths, even lower. This means, according to Landau and Lifschitz<sup>170</sup>, that magnetization is not well-defined because charges generating it cannot be considered as bound charges in these spectral ranges so that  $\mathbf{B}$

---

\*We assume isotropy and time homogeneity.

## CHAPTER 3. PLASMONICS

---

and  $\mu_0 \mathbf{H}$  are almost the same variables.  $\epsilon_0$  and  $\mu_0$  are the vacuum permittivity and permeability, respectively\*, while  $\epsilon$  and  $\sigma$  define the dielectric function and the conductivity, respectively. The constitutive equations can be rewritten in  $\mathbf{k}$ -space after Fourier transforms in time and space as<sup>†</sup>

$$\mathbf{D}(\mathbf{k}, \omega) = \epsilon_0 \epsilon(\mathbf{k}, \omega) \mathbf{E}(\mathbf{k}, \omega) \quad (3.8a)$$

$$\mathbf{J}(\mathbf{k}, \omega) = \sigma(\mathbf{k}, \omega) \mathbf{E}(\mathbf{k}, \omega) \quad (3.8b)$$

From Equations (3.8) we distinguish the contribution of free charges with the conductivity  $\sigma$  and the one of bound charges with the permittivity  $\epsilon$  noted as  $\epsilon_\infty^\ddagger$ . By replacing  $\mathbf{D}$  by  $\mathbf{D} + i\omega^{-1} \mathbf{J}_{ind}$  we can combine both contributions resulting in a new dielectric function

$$\epsilon(\mathbf{r}, \mathbf{r}', \omega) = \epsilon_\infty(\mathbf{r}, \mathbf{r}', \omega) + \frac{i\sigma(\mathbf{r}, \mathbf{r}', \omega)}{\omega\epsilon_0} \quad (3.9)$$

leading to new definition of Maxwell's equations

$$\nabla \cdot \mathbf{D}(\mathbf{r}, \omega) = \rho_{ext}(\mathbf{r}, \omega) \quad (3.10a)$$

$$\nabla \cdot \mathbf{B}(\mathbf{r}, \omega) = 0 \quad (3.10b)$$

$$\nabla \times \mathbf{E}(\mathbf{r}, \omega) = i\omega \mathbf{B}(\mathbf{r}, \omega) \quad (3.10c)$$

$$\nabla \times \mathbf{H}(\mathbf{r}, \omega) = \mathbf{J}_{ext}(\mathbf{r}, \omega) - i\omega \mathbf{D}(\mathbf{r}, \omega) \quad (3.10d)$$

so that only external charge and current densities are apparent because induced contributions are taken into account in  $\mathbf{D}$ . Equations (3.10) makes  $\mathbf{D}$  a useful tool to determine the impact of free carriers on induced current and polarization with the absence of external charges.

---

\* $\mu$  is set to be  $\mu_0$  at high EM energies

<sup>†</sup>In this work we use these specific conventions for Fourier and inverse Fourier transforms:

$$a(t) = \int a(\omega) e^{-i\omega t} \frac{d\omega}{2\pi}; \quad a(\omega) = \int a(t) e^{i\omega t} dt \quad (3.6)$$

$$b(\mathbf{k}) = \int b(\mathbf{r}) e^{-i\mathbf{k} \cdot \mathbf{r}} d\mathbf{r}; \quad b(\mathbf{r}) = \int b(\mathbf{k}) e^{i\mathbf{k} \cdot \mathbf{r}} \frac{d\mathbf{k}}{(2\pi)^3} \quad (3.7)$$

<sup>‡</sup>This term actually depends on  $\omega$  due to interband transitions and the  $d$ -band of noble metals



### 3.2.2 Boundary conditions

Most of systems throughout this work involve different media so that inclusion of interfaces when solving Maxwell's equation is primordial. Considering medium 1 and medium 2 separated by an arbitrary interface and defining  $\mathbf{n}$  a unit vector normal to the interface pointing from medium 1 to medium 2, the relation between the electric and magnetic fields gives<sup>171</sup>

$$\mathbf{n} \times (\mathbf{E}_2 - \mathbf{E}_1) = 0 \quad (3.11a)$$

$$\mathbf{n} \times (\mathbf{H}_2 - \mathbf{H}_1) = \mathbf{J}_s \quad (3.11b)$$

This holds also for electric displacement and magnetic induction

$$\mathbf{n} \times (\mathbf{D}_2 - \mathbf{D}_1) = \rho_s \quad (3.12a)$$

$$\mathbf{n} \times (\mathbf{B}_2 - \mathbf{B}_1) = 0 \quad (3.12b)$$

Surface current density and charge density are defined by  $\mathbf{J}_s$  and  $\rho_s$ , respectively. Actually, Equations (3.11) for tangential components are enough for the applicability of the boundary conditions as Equations (3.12) are satisfied once Equations (3.11) are properly met.

### 3.2.3 Importance of local response approximation

We can for instance rewrite the first constitutive Equation (3.5a) in frequency domain as

$$\mathbf{D}(\mathbf{r}, \omega) = \epsilon_0 \int \epsilon(\mathbf{r}, \mathbf{r}', \omega) \mathbf{E}(\mathbf{r}', \omega) d\mathbf{r}' \quad (3.13)$$

meaning that any value of  $\mathbf{D}(\mathbf{r}, \omega)$  is related to the electric field at any  $\mathbf{r}'$ . Taking into account all these non local terms and not knowing the spatial distribution of the permittivity make the problem hard to assess. That is why the local-response approximation (LRA) is crucial and neglects g these non local terms. This is clearly valid as optical excitation wavelengths are much larger than Fermi wavelength so that non local effects act on a short range only<sup>172</sup>. The LRA allows to give Equation (3.13) a simpler form

$$\mathbf{D}(\mathbf{r}, \omega) = \epsilon_0 \epsilon(\mathbf{r}, \omega) \mathbf{E}(\mathbf{r}, \omega) \quad (3.14a)$$

$$\mathbf{J}(\mathbf{r}, \omega) = \sigma(\mathbf{r}, \omega)\mathbf{E}(\mathbf{r}, \omega) \quad (3.14b)$$

Here  $\epsilon(\mathbf{r}, \omega)$  is the bulk dielectric function defined locally in a homogeneous medium.

### 3.2.4 Drude model, description and limits

Generally speaking, metals with crystallographic structure can be described as static ions forming the lattice and free electrons gas of effective mass  $m$  and volume density  $n$  propagating in the matter<sup>28</sup>. Using this description, P. Drude developed a model to describe the behaviour of conduction electrons under an external electric field  $\mathbf{E}$  in metals<sup>\*173</sup>. Starting from Newton's second law, momentum of electrons  $\mathbf{p}$  and electric field  $\mathbf{E}$  are linked according to<sup>174</sup>

$$\mathbf{p}(t) = \frac{e}{i\omega - \gamma}\mathbf{E}(t) \quad (3.15)$$

with  $e$  the elementary charge and  $\gamma$  the velocity relaxation rate<sup>†</sup>. Because the induced current and electron velocity are connected, Equation (3.14b) leads to<sup>174</sup>

$$\sigma(\omega) = \frac{e^2 n_e}{m} \frac{1}{\gamma - i\omega} \quad (3.16)$$

where  $n_e$  denotes the electron density. Equation (3.9) provides the general Drude dielectric function<sup>174</sup>

$$\epsilon(\omega) = \epsilon_\infty - \frac{\omega_p^2}{\omega^2 + i\gamma\omega} \quad (3.17)$$

We note the real and imaginary parts of the dielectric function  $\epsilon_1$  and  $\epsilon_2$ , respectively. The term  $\epsilon_\infty$  comes from the residual polarization induced by the positive background of the ions cores. The plasma frequency  $\omega_p = \sqrt{\frac{e^2 n_e}{m\epsilon_0}}$  defines the frequency at which collective oscillations of the free electron gas are observed so-called plasmons. In the low-frequency region ( $\omega_p \gg \gamma \gg \omega$ ), Equation (3.17) can be simplified to

$$\epsilon(\omega) \approx -\frac{\omega_p^2}{\gamma^2} + i\frac{\omega_p^2}{\gamma\omega} \quad (3.18)$$

We notice that  $\epsilon_1$  is constant and negative and  $|\epsilon_2| \gg |\epsilon_1|$ . Defining the refractive index as  $N = \sqrt{\epsilon}$  with real and imaginary parts  $n$  and  $k$ , we obtain that  $n(\omega) \approx k(\omega) \approx \sqrt{\frac{\omega_p^2}{2\omega\gamma}}$ . In particular,  $n(\omega) \gg 1$  implies that metals are strongly reflective. In the high frequency regime ( $\omega_p \gg \omega > \gamma$ ), Equation (3.17) becomes

---

\*Actually the Drude model is one example of the applicability of the LRA.

†This term corresponds exactly to one half of the energy loss rate<sup>175</sup>.

$$\epsilon(\omega) \approx -\frac{\omega_p^2}{\omega^2} + i\frac{\omega_p^2\gamma}{\omega^3} \quad (3.19)$$

Now  $\epsilon_1$  remains negative but frequency-dependent and  $|\epsilon_1| \gg |\epsilon_2|$  so that  $k(\omega) \gg n(\omega) \gg 1$  and metals stay highly reflective. The last case encompasses the ultraviolet frequency region with  $\omega \approx \omega_p$ . Then Equation (3.17) can be then rewritten

$$\epsilon(\omega) \approx \epsilon_\infty - \frac{\omega_p^2}{\omega^2} \quad (3.20)$$

One can notice that  $\epsilon_1$  changes its sign from negative to positive and  $\epsilon_2$  vanishes once  $\omega$  overcomes  $\omega_p$  making the metals transparent. Plasmons in bulk metals are longitudinal oscillations while photons are transverse so that they do not match. These longitudinal waves are then not observed. A representation of the modes is provided by the dispersion relation resulting from Equation (3.20) assuming  $\epsilon_\infty = 1$

$$\omega(k) = \sqrt{\omega_p^2 + c^2k^2} \quad (3.21)$$

The dispersion curve is almost flat for longitudinal EM modes\* and transverse ones are visible in bulk metallic systems for  $\omega > \omega_p$ . A representation of the dispersion curves of the different modes is reported in Figure 3.1. At large wavevectors the dispersion curve of transverse modes is close to the one of the light. In this framework the losses induced by the excitation of the mode can be quantified with the quality factor<sup>175</sup>.

$$Q(\omega) = \frac{\Re(\epsilon)}{\Im(\epsilon)} \approx \frac{\omega}{\gamma} \quad (3.22)$$

The higher this parameter is the more efficient the free electrons are driven. In general,  $Q$  does not overcome 40<sup>169,175-178</sup>. The Drude model is reasonable to use for metals in infrared and visible regions below the interband transition threshold (ITT) as shown in Figure 3.2 for Au. The general Drude dielectric function from Equation (3.9) has been fitted with experimental measurements done by Johnson's and Christy<sup>171</sup> (coloured circles). The Drude model remains relevant at low frequency but a drop in  $\Im(\epsilon(\omega))$  is observed for higher frequency as a signature of interband transitions. Lorentz-Drude model is more adequate to describe the optical behaviour of metals in the visible range with intraband effects related to free electrons but also interband effects induced by bound electrons<sup>179,180</sup>. The second contribution is often implemented through a Lorentz model involving critical points<sup>181-183</sup>. Despite Lorentzian-like approach combined by

---

\*For small  $k$ ,  $\omega(k)$  can be approached as  $\omega_p[1 + \frac{3}{10} \frac{v_F^2 k^2}{\omega_p^2} + \dots]$ .

## CHAPTER 3. PLASMONICS

---

free-electrons effects is quite accurate<sup>184–186</sup>, considering Gaussian curves seems to be much better, in particular for not overestimating absorption far from the major critical points<sup>77,79,187–190\*</sup>.

Overall the Drude model as a single band approach remains a key tool to describe the optical behaviour of metals. This can be improved by taking into account bound charges effects through a Drude-Model but its applicability might induce deviations with the inherent physical parameters of the systems considered. Thus a more rigorous solution could be needed with quantum approach<sup>191,192</sup> and *ab initio* calculations<sup>193,194</sup> for getting the electronic structures of the metals.

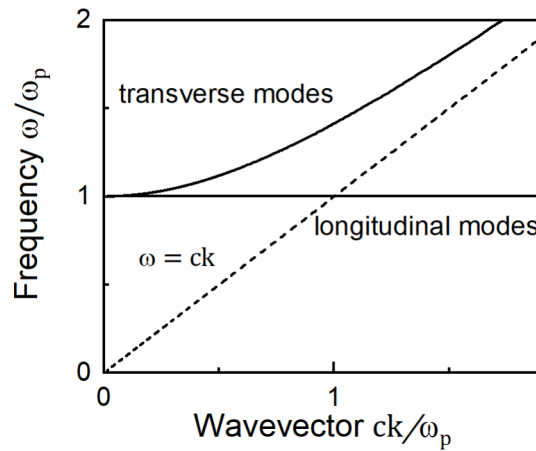


Figure 3.1: Dispersion relations of transverse and longitudinal EM modes in a bulk metallic system.

### 3.3 Plasmonics

Following previous section we aim to provide the fundamentals of plasmonics in the classical limit. The so-called "surface plasmons" give an alternative way to obtain resonantly collective oscillations of free electrons in a metal under an incident illumination<sup>195,196</sup>. We highlight in this section three types of optical modes with surface plasmon polaritons (SPPs) appearing at planar dielectric-metal interfaces, localized surface plasmon resonances (LSPRs) supported by single particles and delocalization of LSPRs in periodic arrays of particles well-known as surface lattice resonances (SLRs).

---

\*It should be noted that these optimization methods modulate parameters such as  $\epsilon_\infty$ ,  $\omega_p$ ,  $\sigma$ ,  $\gamma$ . Thus, a good agreement is sometimes obtained at the expense of a misrepresentation of the physics of the material studied like the real plasma frequency or the actual interband transitions.

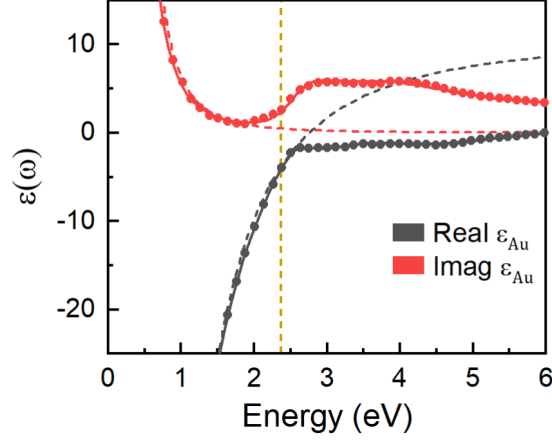


Figure 3.2: Dielectric function of Au. The circles are experimental measurements (from reference 171). The corresponding Drude function is represented in dashed lines with  $\epsilon_\infty = 10.86$ ,  $\hbar\gamma = 9.08$  eV and  $\hbar\omega_p = 78$  meV. Solid lines take into account the contribution of intraband transitions with a critical points model (from reference 186). Vertical dashed line shows gold ITT position.

### 3.3.1 Surface plasmon polariton

We examine a planar interface separating half-infinite metal ( $z < 0$ ) and half-infinite dielectric ( $z > 0$ ) as sketch in Figure 3.3. The metal is described by the frequency-dependent dielectric function  $\epsilon_m$  while the dielectric media is characterized by  $\epsilon_d$  whose value is assumed to be constant with frequency. Besides, we suppose both domains non-magnetic, linear, isotropic and not subjected to external stimuli. The system is uniform along  $y$ -axis as the surface plasmon propagates, in this configuration, along  $x$ -axis. We set the incident light polarization as  $p$  (looking at transverse magnetic (TM) modes) leading to a new formulation of Equations (3.10)\*

$$H_y(z) = A_d e^{i\beta x} e^{-k_d z} \quad (3.23a)$$

$$E_x(z) = iA_d \frac{1}{\omega\epsilon_0\epsilon_d} k_d e^{i\beta x} e^{-k_d z} \quad (3.23b)$$

$$E_z(z) = -A_d \frac{\beta}{\omega\epsilon_0\epsilon_d} e^{i\beta x} e^{-k_d z} \quad (3.23c)$$

in dielectric region and

\*Solving the Maxwell's equations for  $s$ -polarized illumination leads to the non-existence of the SPP<sup>195</sup>.

$$H_y(z) = A_m e^{i\beta x} e^{k_m z} \quad (3.24a)$$

$$E_x(z) = -iA_m \frac{1}{\omega \epsilon_0 \epsilon_m} k_m e^{i\beta x} e^{k_m z} \quad (3.24b)$$

$$E_z(z) = -A_m \frac{\beta}{\omega \epsilon_0 \epsilon_m} e^{i\beta x} e^{k_m z} \quad (3.24c)$$

in metallic region.

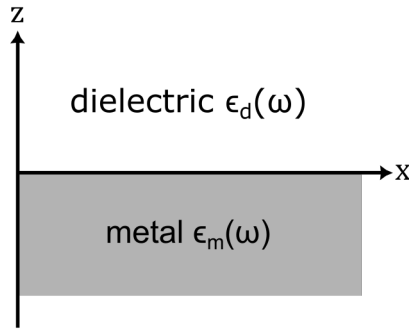


Figure 3.3: Sketch of planar metal-dielectric interface at  $z = 0$ . Metal and dielectric medium are characterized by frequency-dependent dielectric function  $\epsilon_m(\omega)$  and  $\epsilon_d(\omega)$ , respectively.

$A_m$  and  $A_d$  are the amplitudes related to the metal and dielectric, respectively. Besides,  $1/k_m$  and  $1/k_d$  quantify the evanescent decay length of both fields along the direction orthogonal to the planar interface according to

$$k_m^2 = \beta^2 - k_0^2 \epsilon_m \quad (3.25a)$$

$$k_d^2 = \beta^2 - k_0^2 \epsilon_d \quad (3.25b)$$

with the definition  $\frac{\partial}{\partial x} = i\beta$ . The boundary conditions in Equations (3.11) impose<sup>195</sup>

$$A_m = A_d \quad (3.26a)$$

$$\frac{\epsilon_m}{k_m} = \frac{\epsilon_d}{k_d} \quad (3.26b)$$

In particular, Equation (3.26b) require that real parts of both domains have opposite signs in order to preserve the evanescent behaviour of the SPP perpendicularly to the interface<sup>195</sup>. This is in agreement with the consideration of a metal and a dielectric at the beginning of this section. Equations (3.26) lead to the SPP wavevector formula<sup>195,197-200</sup>

$$\beta_{SPP} = \frac{\omega}{c} \sqrt{\frac{\epsilon_m \epsilon_d}{\epsilon_m + \epsilon_d}} \quad (3.27)$$

This expression remains valid for complex dielectric functions\*. Figure 3.4 plots the dispersion relation of the optical modes on planar dielectric/metal interface. The upper red branch in loseless case represents the bulk plasmon polariton (BPP) as in Figure 3.1. This mode corresponds to the light propagating within the Drude metal. The other contribution in blue is a surface mode so-called SPP which couples the surface EM waves to collective oscillations of free-electrons in the Drude metal. It should be noted that due to the position of this branch according to the light line, the fields associated to the SPP remain confined next to the interface. Furthermore, an inherent mismatch of wavevector between the incident light and the SPP does not allow an excitation of the polaritonic mode under direct illumination.

Thus several approaches have been developed over last decades to couple incident light with surfaces waves such as prism coupling, gratings, surface roughness or dielectric particles<sup>195,198,201-204</sup>. In contrast, Figure 3.4(a) highlights that the SPP branch approaches at large wavenumbers the frequency  $\omega_{SP} = \omega_p / \sqrt{\epsilon_\infty + \epsilon_d}$  resulting in a pure longitudinal mode not subjected to dispersion. In the opposite configuration, at small wavenumbers, the SPP dispersion is aligned with the line light limiting the field confinement.

Figure 3.4(b) takes into account the losses in Drude metal as in Equation (3.17). Figures 3.4(a,b) are similar but the right panel shows how the SPP line gets to a finite value of  $\Re(k)$  until it goes backwards which is the signature of the imaginary part of  $k$ <sup>198,205</sup>. Indeed in this more realistic case the SPP propagates along the planar interface with attenuation proportional to  $e^{-x\Im(k)}$ . To understand the impact of losses on the SPP propagation we mapped the dispersion curve with the ratio  $\Im(k)/\Re(k)$ . From this perspective we see that the SPP travels until attenuation dominates opening a frequency range that is forbidden for the SPP excitation.

---

\*It is possible to demonstrate equation (3.27) from the poles of Fresnel reflection coefficients coming from  $p$ -polarized waves defined as<sup>169</sup>

$$r_p = \frac{\epsilon_d k_m - \epsilon_m k_d}{\epsilon_d k_m + \epsilon_m k_d} \quad (3.28)$$

leading to the condition  $\epsilon_d k_m + \epsilon_m k_d = 0$  equivalent to equation (3.26b).

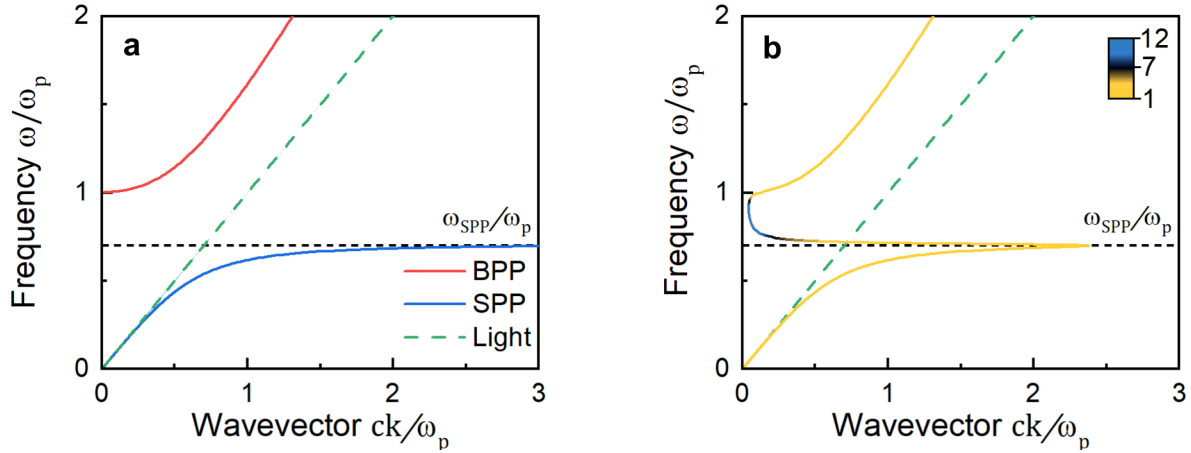


Figure 3.4: Dispersion curves of plasmon polaritons. We fix  $\epsilon_d$  and  $\epsilon_\infty$  at 1 and consider the metal as a Drude metal via equation (3.17). (a) Loseless Drude metal. (b) Lossy Drude metal with  $\omega_p = 20\gamma$ . The line is mapped with  $\Im(k)/\Re(k)$  whose value is represented by the color bar in order to quantify the compromise between propagation and attenuation.

Figure 3.5 plots the real dispersion curves of the three noble metals Au, Ag and Cu according to Johnson and Christy’s experimental measurements. It should be noted that Cu is the most impacted by the losses due to large attenuation even at low wavenumbers while Ag remains a choice of interest for plasmonics. However, both Ag and Cu are subjected to oxidation so that Au, stable as it is, is also a good candidate despite its significant attenuation near the surface plasmon frequency<sup>206</sup>.

### Prism coupling

An elegant and widespread way to excite these plasmonic modes to improve light-matter interaction has been provided by E. Kretschmann and H. Raether in 1968<sup>201</sup>. This technique consists of depositing a thin metallic film on top of a dielectric prism (in general made of glass) characterized by a refractive index  $n_{prism} > 1$  and illuminating the system by p-polarized light through the prism with an incidence angle  $\theta_i$ . For a specific combination  $(\lambda_{SPP}, \theta_i)$ , the SPP wave vector is equal to the in-plane component of the wave vector of the p-polarized incoming light  $k_{//} = k_0 n_{prism} \sin(\theta_i)$  that leads to the excitation of the SPP and a drastic loss of reflection. This phenomenon is well-known as attenuated total reflection (ATR)<sup>207</sup>.

It should be noted that the SPP does not propagate at the prism/metal interface but at the metal/air interface<sup>208</sup>. In principle, the SPP excitation should lead to a 300-times enhancement of the incident intensity<sup>209</sup>. This enhancement factor can be drastically reduced due to parameters



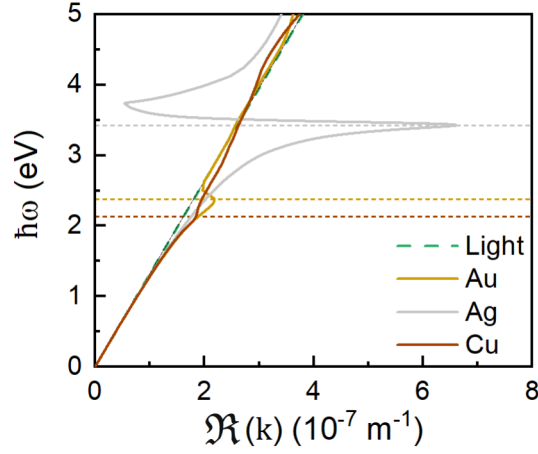


Figure 3.5: Dispersion relation of plasmon polaritons for Au-glass (solid gold line), Ag-glass (solid silver line) and Cu-glass (solid red line) planar interfaces with  $\epsilon_d = 2.25$ . Dielectric functions of the three metals have been interpolated from Johnson and Christy's datasets<sup>171</sup>. The three horizontal dashed lines show the ITT of Au, Ag and Cu.

such as surface roughness<sup>210,211</sup>, impacting the propagation length of the SPP along the interface. Exciting the SPP can also be achieved via an air gap between the prism surface and the metallic surface, geometry introduced by A. Otto in 1968<sup>212</sup>. While Kretschmann configuration provides a SPP at bottom surface, the latter geometry makes it at the top surface.

The phase-matching of the in-plane projection of the wavenumbers is necessary to induce SPP at metal-dielectric interface as

$$\beta_{SPP} = k_0 n_{prism} \sin(\theta_i) \quad (3.29)$$

and this is visible in Figure 3.6 which represents prism coupling and SPP dispersion. The crossing of light line within the prism with the black SPP branch leads to the excitation of a SPP at metal-air interface. It should be mentioned that launching a SPP in this configuration leads not only to losses in the metal but also in the prism. Then ATR, the signature of the SPP, is caused by destructive interferences between the reflected light and the leaky wave. However, the reflection minimum can be optimized in order to approach zero and minimize the contribution of the attenuated waves.

This approach allows absorption enhancement in the target metallic layer and has been shown to be a successful approach for promote energy efficient AO-HIS in GdFeCo layer<sup>213</sup>. We actually did not consider this approach since it is not the simplest experimental configuration to set. In particular the Otto geometry is challenging to control, especially the gap between the multi-

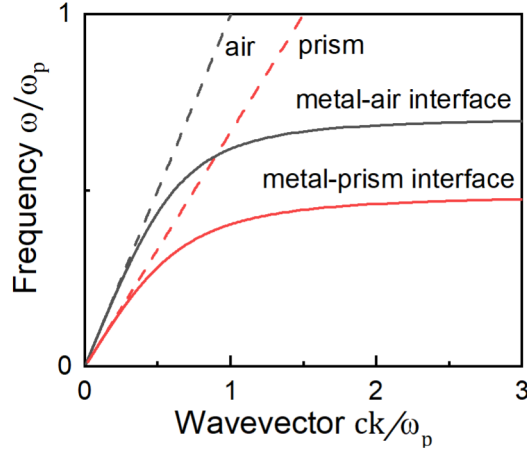


Figure 3.6: Dispersion relations of light in air and prism (dashed lines) coming with an angle of incidence of  $30^\circ$  with in-plane projection. Both solid lines describe the behaviour of SPP at metal-air and metal-prism interfaces in black and red, respectively.

layer stack and the prism. We preferred to consider gratings to improve light-matter interaction to enhance AO-HIS. In this context, we detail the challenges of coupling the light and the matter with a grating.

### Grating coupling

Another smart way to achieve momentum matching between the incoming wave and the SPP is provided by grating coupling<sup>195</sup>. The first experimental observation of a SPP excited by a periodic roughness occurred in 1902<sup>214</sup>. The projection in the film plane of the incoming light wave vector is simply  $k_x = k_0 n_d \sin(\theta_i)$  where  $n_d$  is the refractive index of the surrounding media and  $\theta_i$  is the incident angle. Then this wave scatters from the grating leading to different diffracted orders (DOs). In case the DO has a wave vector greater than  $k_x$ , the wave becomes evanescent and may be coupled to the SPP according to the relation

$$\beta_{\text{SPP}} = \mathbf{k}_x \pm m k_g \mathbf{u}_g \quad (3.30)$$

where  $m$  is an integer providing the DO,  $k_g = \frac{2\pi}{P}$  the grating wavevector vector,  $\mathbf{u}_g$  the grating unit vector and  $P$  the grating period. In principle, in case of evanescent waves, the propagation at an interface along one direction or the opposite one should lead to an in-plane torque on magnetization whose direction depends on the direction propagation of the evanescent wave<sup>215</sup>. This behaviour allowed A. L. Chekhov *et al.* to induce sub-THz spin precession of dielectric garnet

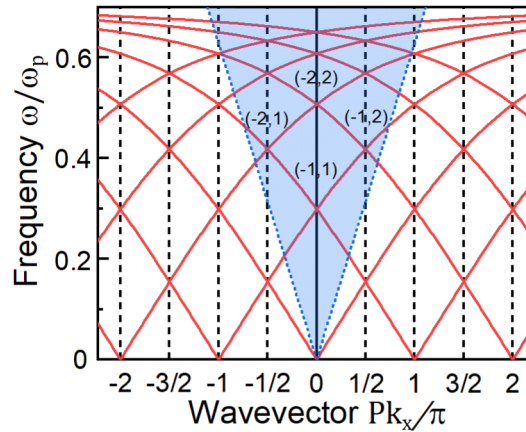


Figure 3.7: Dispersion curves of grating-induced SPP.

thanks to a SPP at the interface of an unidirectional gold grating and a thick dielectric magnetic layer<sup>216</sup>. Figure 3.7 depicts the dispersion curves of grating-induced SPP in case of 1D grating with periodicity  $P$ . Radiative coupling through SPP excitation by  $p$ -polarized illumination is possible in the cone delimited by the light lines. Some DOs in this region subtract or add momentum to the in-plane projection of incoming light that are integer multiples of the grating wvector  $k_g$ . In addition to the non-zero polar angle  $\theta_i$  we can also consider the azimuthal angle  $\phi$  between  $\mathbf{k}_g$  and the plane of incidence as shown in Figure 3.8.

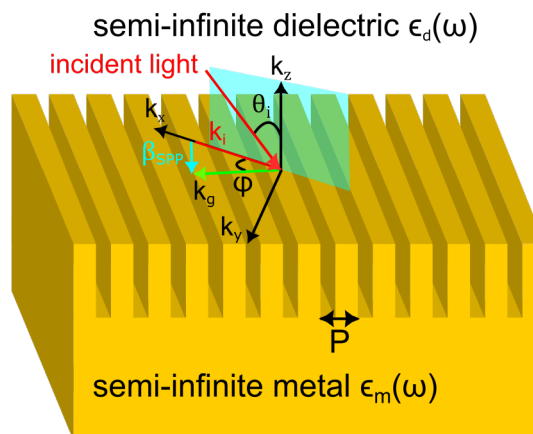


Figure 3.8: Sketch of a 1D grating with period  $P$ .  $\mathbf{k}_i$  is the in-plane projection of the incoming light wvector oriented along  $-\mathbf{k}_x$ ,  $\mathbf{k}_g$  is the grating wvector,  $\theta_i$  is the polar angle,  $\phi$  is the azimuthal angle,  $\beta_{\text{SPP}}$  is the SPP wvector.

This general configuration leads to even more solutions. Matching wvectors is possible

## CHAPTER 3. PLASMONICS

whenever  $|\beta_{SPP}| > |\mathbf{k}_g|$  or  $|\beta_{SPP}| < |\mathbf{k}_g|$ . To describe all the solutions we fix the polar angle and allow  $\phi$  to change\*. We define the angle between  $\beta_{SPP}$  and  $\mathbf{k}_g$  as  $\zeta$  leading to four resonances<sup>217,218</sup> as shown in Figure 3.9. In this case it is convenient to write coupling conditions as angle  $\zeta$  conditions. We consider a first case with the grating wavenumber greater than the SPP wavenumber leading to

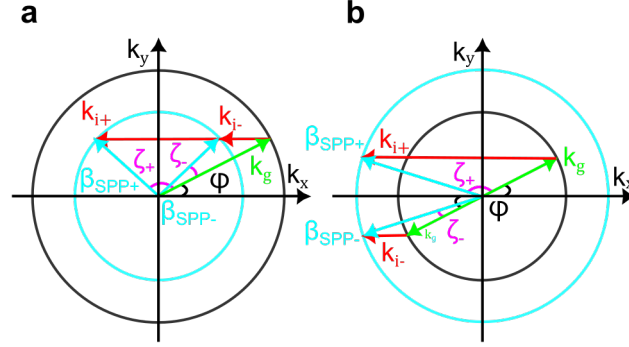


Figure 3.9: Coupling conditions for (a)  $|\beta_{SPP}| < |\mathbf{k}_g|$  and (b)  $|\beta_{SPP}| > |\mathbf{k}_g|$ . The angles  $\zeta_+$  and  $\zeta_-$  are related to  $\mathbf{k}_{i+}$  and  $\mathbf{k}_{i-}$ , respectively.

$$\beta_{SPP} \cos(\phi + \zeta) = k_g \cos(\phi) - k_i \quad (3.31a)$$

$$\beta_{SPP} \sin(\phi + \zeta) = k_g \sin(\phi) \quad (3.31b)$$

We can deduce the  $\zeta$  coupling conditions

$$\zeta = -\phi + \arctan\left(\frac{k_g \sin(\phi)}{\sqrt{\beta_{SPP}^2 - k_g^2 \sin(\phi)^2}}\right) \quad (3.32)$$

This works for both plus and minus configurations. In case  $|\beta_{SPP}| > |\mathbf{k}_g|$ , we also obtain

$$\zeta_+ = \pi - \phi + \arctan\left(\frac{k_g \sin(\phi)}{\sqrt{\beta_{SPP}^2 - k_g^2 \sin(\phi)^2}}\right) \quad (3.33a)$$

\*Usually  $\theta$  is fixed during the experiments and the sample is rotated in the  $(x0y)$  plane.

$$\zeta_- = \phi - \arctan\left(\frac{k_g \sin(\phi)}{\sqrt{\beta_{SPP}^2 - k_g^2 \sin(\phi)^2}}\right) \quad (3.33b)$$

One can notice that even for a non-azimuthal angle the number of resonances can not exceed two for a given ratio  $|\beta_{SPP}|/|\mathbf{k}_g|$ . This point is crucial for the evidence of magnetism-induced SLRs in Chapter 7. Equation (3.30) can be extended to describe 2D gratings. Then both periods should be included as for metasurfaces consisting of periodic arrays of nanodisks<sup>219–222</sup>. In this perspective we can write at normal incidence

$$\beta_{SPP} = \pm m_x \frac{2\pi}{P_x} \mathbf{u}_x \pm m_y \frac{2\pi}{P_y} \mathbf{u}_y \quad (3.34)$$

Considering  $P_x = P_y = P$ , one can deduce the wavelengths at which the SPP can be excited<sup>219</sup>

$$\lambda_{m_x, m_y} = \frac{P}{\sqrt{m_x^2 + m_y^2}} \sqrt{\frac{\epsilon_m(\omega)\epsilon_d(\omega)}{\epsilon_m(\omega) + \epsilon_d(\omega)}} \quad (3.35)$$

Then we clearly see here the dependence of the excitation wavelength on the dielectric functions of both materials but also on the array period and the DOs. We note that a 1D grating allows a SPP to propagate along one single direction. It is possible to overcome this intrinsic limitation by placing single dielectric nanospheres on metallic surface. This way a SPP can be launched along any direction by rotation invariance.

We want to be even more specific. We just explained how a grating can exhibit a resonance. However SLRs consist of coupling each plasmonic resonance of each nanoparticle to give a collective resonance. After explaining the underlying physics of single particle plasmonic resonance, we detail how a grating resonance can couple to each single particle resonance to give rise to a SLR. This kind of optical mode is of primary importance in this work to enhance AO-HIS.

### 3.3.2 Localized surface plasmon resonance

Even if the SPP propagating at planar dielectric-metal interface seems to be the simplest plasmonic mode to study, other configurations are of particular interest such as single particles. This mode, well-known as localized surface plasmon resonance\* (LSPR), occurs in finite-sized structures whose volume is below the diffraction limit<sup>195, 198, 223</sup>.

This optical mode does not allow propagation due to the finite size of the system. However, displacing free charge carriers with incoming EM waves induces a restoring force through the

---

\*In principle localized surface plasmon are polaritons as strong coupling between incoming illumination with electric dipole excitation but most of the literature does not refer to it so we adopt this convention throughout this work.

## CHAPTER 3. PLASMONICS

---

depolarization field  $\mathbf{E}_{pol}$  (analogous to demagnetization field) which maintains coherent oscillations of free electrons. Unlike the SPP, excitation of LSPRs does not require any coupling techniques<sup>195</sup>. Next we introduce the theoretical framework to describe the optical behaviour of spherical particles with specific emphasis on LSPRs. We also stress how plasmonic response can be tailored by particle shape. We were initially more interested in exciting a plasmon in nanoparticle than in continuous films since we wanted to perform energy efficient AO-HIS (due to absorption enhancement coming from plasmonic mode excitation) in nanoobjects.

### Mie Theory

A full electrodynamics approach is needed to describe consistently the absorption and scattering of EM waves by spherical particles. A widespread strategy is provided by the Mie theory<sup>224–229</sup>. This framework does not only consider electric dipole resonance involved in the excitation of LSPRs but all the multipole resonances for a complete description of the optical behaviour of spherical particles. For now we consider spherical particles embedded in homogeneous medium as shown in Figure 3.10. Usually, after expanding the incident fields into the series of vector spherical harmonics, one can further expand both scattered fields and fields inside the sphere into the series of vector spherical harmonics as well. Applying the boundary conditions at the interface of the sphere, one can solve the resulting linear system to deduce the expansion coefficients. Thus, the Mie theory allows to calculate scattering coefficients related to the EM waves scattered by a sphere<sup>\*169,225,227,228</sup>

$$a_l = \frac{\epsilon_m j_l(x_m) S'_l(x_d) - \epsilon_d j_l(x_d) S'_l(x_m)}{\epsilon_m j_l(x_m) \xi'_l(x_d) - \epsilon_d h_l^{(1)}(x_d) S'_l(x_m)} \quad (3.37a)$$

$$b_l = \frac{j_l(x_m) S'_l(x_d) - j_l(x_d) S'_l(x_m)}{j_l(x_m) \xi'_l(x_d) - h_l^{(1)}(x_d) S'_l(x_m)} \quad (3.37b)$$

---

\*In addition the Mie theory describes the fields inside the sphere with the following coefficients<sup>169,225,227,228</sup>

$$c_l = \frac{j_l(x_d) \xi'_l(x_d) - h_l^{(1)}(x_d) S'_l(x_d)}{j_l(x_m) \xi'_l(x_d) - h_l^{(1)}(x_d) S'_l(x_m)} \quad (3.36a)$$

$$d_l = \sqrt{\epsilon_m \epsilon_d} \frac{j_l(x_d) \xi'_l(x_d) - h_l^{(1)}(x_d) S'_l(x_d)}{\epsilon_m j_l(x_m) \xi'_l(x_d) - \epsilon_d h_l^{(1)}(x_d) S'_l(x_m)} \quad (3.36b)$$

where  $x_i = k_i a$ ,  $a$  the particle radius and  $k_i = \sqrt{\epsilon_i} \omega / c$  with  $i \in \{m, d\}$ . Equation (3.37) introduce the spherical Bessel and Hankel functions of the first kind  $j_l$  and  $h_l^{(1)}$  as well as the Riccati-Bessel functions  $S_l$  and  $\xi_l$  satisfying  $S_l(x) = x j_l(x)$  and  $\xi_l(x) = x h_l^{(1)}(x)$  respectively. From the scattering coefficients we can deduce the cross-sections attributed to extinction, scattering and absorption considering the incident light as a monochromatic plane wave<sup>225</sup>

$$\sigma_{ext} = \frac{2\pi}{k_d^2} \sum_{l=1}^{\infty} (2l+1) \text{Re} \{a_l + b_l\} \quad (3.38a)$$

$$\sigma_{sca} = \frac{2\pi}{k_d^2} \sum_{l=1}^{\infty} (2l+1) (|a_l|^2 + |b_l|^2) \quad (3.38b)$$

$$\sigma_{abs} = \sigma_{ext} - \sigma_{sca} \quad (3.38c)$$

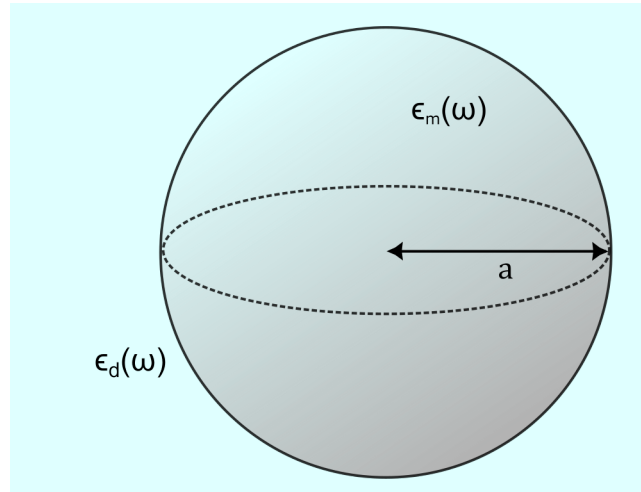


Figure 3.10: Illustration of a spherical particle with dimension  $a$ , described by the dielectric function  $\epsilon_m$  and surrounded by a homogeneous medium with dielectric function  $\epsilon_d$ .

Calling  $I_0$  the irradiance of the incident illumination, the quantity  $\sigma_{abs} I_0$  is defined as the rate at which the particle absorbs energy. We provide in Appendix A a code we developed in Matlab to calculate the scattering and absorption behaviours of small spherical nanoparticles in homogeneous media. In Equations (3.37) and (3.38),  $l$  corresponds to the angular momentum then refers to the resonance order<sup>225,230</sup>. For instance the coefficient  $a_1$  and  $b_2$  describe electric dipole and magnetic quadrupole resonances, respectively. The Mie theory is applicable in any scattering regimes as only one order is needed for small particles ( $a \ll \lambda$ ), sometimes two or

## CHAPTER 3. PLASMONICS

three for particles whose size is comparable to the wavelength. However, in case of optical geometry ( $a \gg \lambda$ ), even if the Mie theory can be used, it would require too many orders to describe properly the optical behaviour of such system synonym of a large calculation time. A regime of scattering spectra is sketched in Figure 3.11 for a sphere with 300 nm-radius and refractive index of 4, embedded in air.

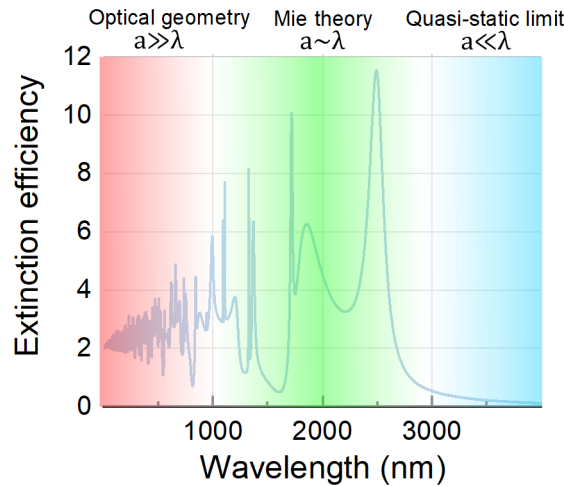


Figure 3.11: Regimes of scattering for a sphere with 300 nm-radius and refractive index of 4, embedded in air. The extinction efficiency is defined as the ratio between the extinction cross section  $\sigma_{ext}$  and the geometric cross section  $\sigma_{geo} = \pi \times a^2$ .

An intuitive representation of extinction efficiency, defined as the ratio between the extinction cross section  $\sigma_{ext}$  and the geometric cross section  $\sigma_{geo} = \pi \times a^2$ , as a function of the light wavelength and the particle radius is a two dimensional colormap that highlights optical resonances for specific combinations of wavelength and radius. Figure 3.12 plots some examples for noble metals and silicon spheres embedded in air. This view allows to optimize the extinction efficiency, to a lesser extent scattering and absorption efficiencies, for any system as long as the dielectric function is known.

### Rayleigh scattering

Rayleigh scattering regime, also well-known as the quasi-static limit, allows to describe the elastic scattering of light by sub-wavelength particles whose dimensions are much smaller than the light wavelength. In other terms, this framework is applicable once  $a \ll \lambda$ <sup>231–233</sup>. This regime neglects retardation effects\* so that describing the optical behaviour only requires the

\*For instance the finitude of light speed can induce such effects.



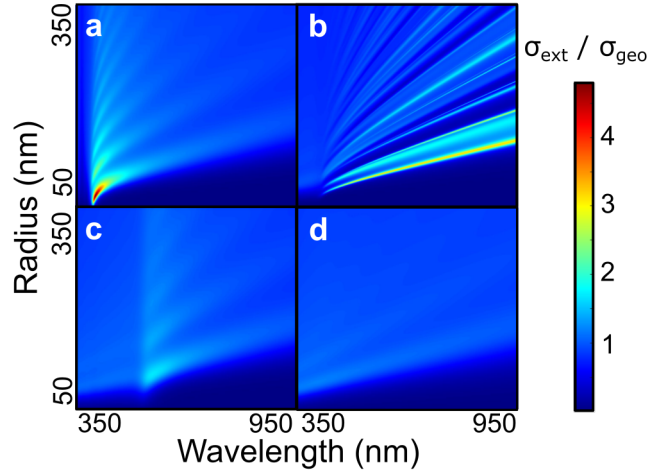


Figure 3.12: Extinction efficiency maps for a (a) silver sphere, (b) silicon sphere, (c) gold sphere, (d) cobalt sphere. Any of them is embedded in air.

resolve of Laplace's equation<sup>169</sup>. It consists of expressing the potential inside and outside the sphere taking into account that both formula are equal for  $r = a$ . The multipolar polarizability  $\alpha_l$  is the quantity of interest and can be written as<sup>225,230,234,235</sup>

$$\alpha_l = 4\pi a^{2l+1} \frac{\epsilon_m - \epsilon_d}{\epsilon_m + \frac{l+1}{l}\epsilon_d} \quad (3.39)$$

At the LSPR the polarizability is very large and the LSPR of  $l$ -th order occurs at\*

$$\epsilon_m + \frac{l+1}{l}\epsilon_d = 0 \quad (3.41)$$

This leads to the plasmon frequency for a loseless Drude sphere<sup>†</sup>

$$\omega_{SP} = \frac{\omega_p}{\sqrt{\epsilon_\infty + \frac{l+1}{l}\epsilon_d}} \quad (3.42)$$

Since we only consider electric dipole resonance for the excitation of LSPRs, we place ourselves in the dipole limit polarizability  $\alpha$  equals the dipolar polarizability  $\alpha_1$  according to<sup>169,225,227</sup>

\*We can reorganize the Frölich condition for dipole-type resonance<sup>195,229</sup>

$$\Re(\epsilon_m) = -2\epsilon_d \quad (3.40)$$

†We find back the formula of plasmon frequency for  $l = 1$  from previous subsection.

$$\alpha = 4\pi a^3 \frac{\epsilon_d(\epsilon_m - \epsilon_d)}{\epsilon_m + 2\epsilon_d} \quad (3.43)$$

In this approximation,  $\omega_{SP} = \frac{\omega_p}{\sqrt{3}}$  and cross sections can be calculated as

$$\sigma_{sca} = \frac{k_d^4}{6\pi} |\alpha|^2 \propto a^6 \quad (3.44a)$$

$$\sigma_{abs} = k_d \text{Im}(\alpha) \propto a^3 \quad (3.44b)$$

Figure 3.12 shows for 4 materials several branches. The lower branches depict dipolar modes while upper modes describe higher order modes. This is clear on this figure that optical behaviour of subwavelength particles is dominated by the dipolar-type LSPR that is in agreement with the applicability of the nonretarded limit. Throughout this work we study only electrically-induced electric dipolar-type plasmon resonances where incoming illumination drives coherent oscillations of electrons in metallic particles resulting in a dipole moment in the structure as illustrated in Figure 3.13.

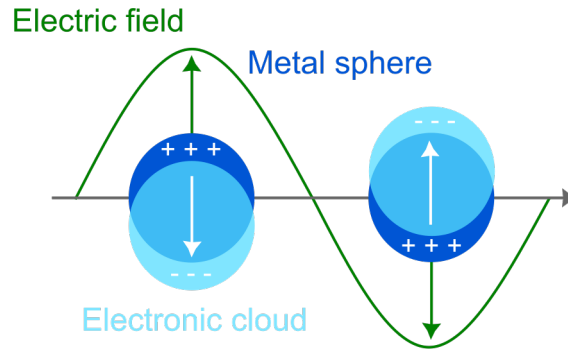


Figure 3.13: Sketch of localized surface plasmon resonance in a metallic nanoparticle induced by oscillating electric field.

### Why shape matters

The polarizability is a factor of interest for controlling the spectral position and strength of the plasmon resonance. Equation (3.39) is written in the simplest case with a spherical particle but a factor is necessary when considering an arbitrary shape. In this perspective, controlling particle

shape is a nice way to tailor the frequency and polarization dependence of the LSPRs<sup>235–247</sup>. Murray *et al.* showed in 2007 some examples as presented in Figure 3.14.

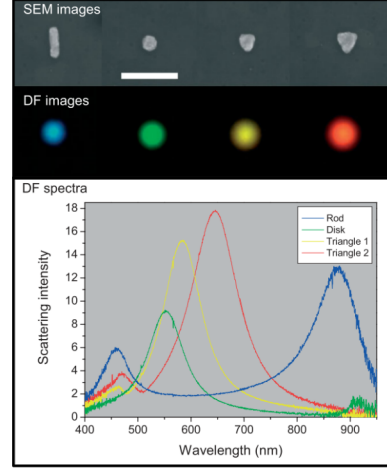


Figure 3.14: Scanning electron (top) and dark-field images (middle) of metallic nanoparticles with different shapes (rod, disc, triangle, triangle). The dark-field spectra on bottom have been measured on the same particles. The thickness of the structures has been fixed to 30 nm and the substrates are made of silica glass coated with 20 nm of ITO. The scale bar on top images represents 300 nm.

Figure 3.14 also involve volume variations while comparing different particle shapes. One can fix the volume  $V$  for an ellipsoidal particle in order to rewrite Equation (3.43) as<sup>235</sup>

$$\alpha = V \frac{\epsilon_d(\epsilon_m - \epsilon_d)}{\epsilon_d + L(\epsilon_m + \epsilon_d)} \quad (3.45)$$

$L$  stands for shape factor, equal to  $1/3$  for a sphere. In general case  $L$  depends on the symmetry axes of the ellipsoid. Ellipsoidal particles have three symmetry axis  $j$  related to corresponding radius  $r_j$  and  $L_j$  so that  $\sum_j L_j = 1$ . The shape factors can be written as<sup>223,234,235</sup>

$$L_j = \frac{r_1 r_2 r_3}{2} \int_0^\infty \frac{dx}{(x + r_j^2) \sqrt{(x + r_1^2)(x + r_2^2)(x + r_3^2)}} \quad (3.46)$$

Optical behaviour of rods, oblate spheroids and spheres can be described knowing the relevant symmetry axis as shown in Figure 3.15. For instance, disks exhibit electric dipole response in  $(x0y)$  plane while rod-shape particles are polarized along  $z$  axis. However the applicability of such resonance remains limited due to its spectral width, around 100 nm for LSPR for Au as the quality factor of the plasmonic resonance can be also defined as

$$Q = \frac{\lambda_r}{\Delta\lambda} \quad (3.47)$$

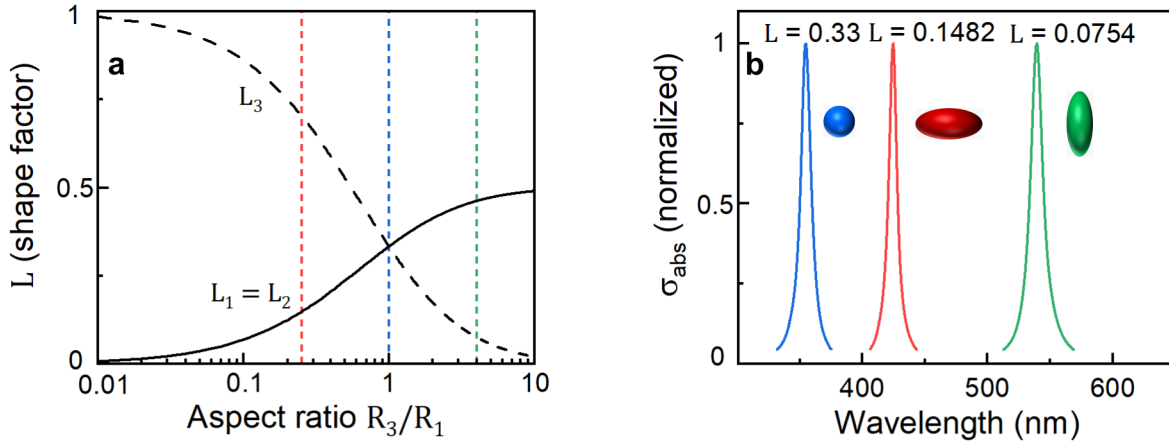


Figure 3.15: (a) Depolarization factors  $L_j$  for spheroids with  $R_1 = R_2 \neq R_3$  depending on the aspect ratio  $\frac{R_3}{R_1}$ . (b) Absorption cross-section spectra for a sphere ( $R_3 = R_1$ ), an arbitrary oblate spheroid ( $R_3 = 0.25R_1$ ) and a rod ( $R_3 = 4R_1$ ) whose shape factors are related to dotted lines in (a). All the particles are illuminated by light with electric field polarized along the longest axis of the particle.

where  $\Delta\lambda$  defines the full width at half maximum (FWHM) of the resonance and  $\lambda_r$  the resonance wavelength. One way to induce more intense resonances with higher quality factor is to arrange particles into periodic arrangements resulting in SLRs. We first considered single nanoparticles for performing energy efficient AO-HIS at nanoscale by means of the excitation of LSPRs. However, it is much more easier to probe a collective behaviour on metasurface than what happens within a single nanoparticle. This practical reason was another reason why we decided to consider SLRs for enhancing AO-HIS at nanoscale. We now explain the underlying physics of such plasmonic mode.

### 3.3.3 Surface lattice resonance

The optical behaviour of single particles can be improved by coupling each of them in a periodic arrangement of antennas resulting in SLR. Coupled surface modes have been studied for many different shapes such as metasurfaces based on disks<sup>220–222,248–250</sup>, bow ties<sup>251–253</sup>, holes<sup>254–256</sup>, slits<sup>257–259</sup> and split rings<sup>260–262</sup>. We consider periodic arrays of metallic nanodisks for enhancing optical and MO responses. The mechanism is based on hybridization of localized modes with DOs through radiative coupling.

### Theoretical framework

The theory describing the underlying physics has been introduced by DeVoe in 1990s with the study of aggregates of molecules<sup>263,264</sup>, followed by Purcell and Pennypacker with the consideration of phase retardation effects induced by the propagation of EM waves<sup>265</sup>. Few years later, Laor and Schatz developed another approach involving the coupled dipole approximation (CDA) to describe the optical behaviour of molecules aggregates<sup>266</sup> whose model has been improved with inclusion of phase retardation effects<sup>267,268</sup>. This research field had a modest interest for decades until Zou *et al.* predicted in 2004 extremely narrow resonances, around 1 meV, giving a new approach for the usefulness and applicability of such radiative coupling<sup>269,270</sup>. Markel as well as Zou *et al.* provide a rigorous method through CDA to consider  $N$  particles of a periodic array as electric dipoles characterized by a polarizability  $\alpha_i$ , a position  $\mathbf{r}_i$ , a local electric field  $\mathbf{E}_{loc,i}$ , a dipole moment  $\mathbf{P}_i$ , an incident field  $\mathbf{E}_i$  and a retarded field induced by the  $N - 1$  electric dipoles  $\mathbf{E}_{dip,i}$ <sup>269-272</sup>. Then a dipole feels the local field for a fixed wavelength<sup>269,270</sup>

$$\mathbf{E}_{loc,i} = \mathbf{E}_{inc,i} + \mathbf{E}_{dip,i} = \mathbf{E}_0 e^{i\mathbf{k}\cdot\mathbf{r}_i} - \sum_{j=1, j \neq i}^N A_{ij} \cdot \mathbf{P}_j \quad (3.48)$$

$(i = 1, 2, \dots, N)$

where  $\mathbf{E}_0$  and  $k$  are the amplitude and the wave number of the incident light, respectively. Besides, the dipole interaction matrix  $A_{ij}$  is written as<sup>269,270</sup>

$$A_{ij} \cdot \mathbf{P}_j = k^2 e^{i\mathbf{k}\cdot\mathbf{r}_{ij}} \frac{\mathbf{r}_{ij} \times (\mathbf{r}_{ij} \times \mathbf{P}_j)}{\mathbf{r}_{ij}^3} + e^{i\mathbf{k}\cdot\mathbf{r}_{ij}} (1 - i\mathbf{k}\cdot\mathbf{r}_{ij}) \frac{\mathbf{r}_{ij}^2 \mathbf{P}_j - 3\mathbf{r}_{ij}(\mathbf{r}_{ij} \cdot \mathbf{P}_j)}{\mathbf{r}_{ij}^5} \quad (3.49)$$

$(i = 1, 2, \dots, N, j = 1, 2, \dots, N, i \neq j)$

with  $\mathbf{r}_{ij}$  representing the vector from dipole  $i$  to dipole  $j$ . Then  $3N$  equations linking the dipole interactions matrices, the electric dipoles and the electric fields have to be solved, leading to the polarization  $P$  assuming an infinite array of identical particles with a characteristic polarizability  $\alpha$ <sup>269,270</sup>

$$\mathbf{P} = \frac{\mathbf{E}_0}{1/\alpha - S} \quad (3.50)$$

Here  $S$  is the so-called structure factor and is given, in case of normal incidence, by<sup>269,270</sup>

$$S = \sum_{j \neq i} \left[ \frac{(1 - i\mathbf{k}\cdot\mathbf{r}_{ij})(3\cos(\theta_{ij})^2 - 1)e^{i\mathbf{k}\cdot\mathbf{r}_{ij}}}{\mathbf{r}_{ij}^3} + \frac{k^2 \sin(\theta_{ij})^2 e^{i\mathbf{k}\cdot\mathbf{r}_{ij}}}{\mathbf{r}_{ij}} \right] \quad (3.51)$$

## CHAPTER 3. PLASMONICS

---

where  $\theta_{ij}$  is the angle between  $\mathbf{r}_{ij}$  and the polarization induced by the incident field. The resulting effective polarizability of the array from Equation (3.50) depends on both the polarizability of a single particle and the structure parameter. The extinction cross-section of a particle from the array takes the form<sup>273</sup>

$$\sigma_{ext} = 4\pi k \text{Im}(P/E_0) \quad (3.52)$$

Analog to the Frölich condition in case of single particles described by Rayleigh scattering, the polarization so the polarizability becomes very large when  $\Re(1/\alpha) = \Re(S)$ , the condition for SLR<sup>272</sup>. The structure parameter from Equation (3.51) highlights that the lattice period as well as intrinsic properties of the particles determine the quality of the collective resonance. Indeed  $\Im(1/\alpha - S)$  determines the width of the SLR that is to say how the structure factor can counter the radiative damping term. Finally, the central wavelength of the LSPR and the spectral positions of the DOs impact the SLR and a widespread criteria consisting of  $\lambda_{DO} > \lambda_{LSPR}$  ensures a narrow SLR<sup>268–272,274</sup>.

### Experimental observations

Excitation of SLRs requires enough particles to establish well defined DOs that couple the LSPR of each nanoparticle over the whole system. Thus the incoming light has to be coherent over the area defined by the periodic arrangement of the nanostructures. However the first attempts to observe SLRs involved a high numerical aperture (higher than 0.5) so that only few electric dipoles could oscillate in phase<sup>275–278</sup>. One of the first demonstration of sharp collective resonances came out in 2008 with a numerical aperture of 0.1<sup>279</sup>.

Figure 3.16(a) gives examples of observed narrow SLRs in visible range for few angles of incidence on 2D periodic arrays of gold dimers. This study is of great interest since measurements of ellipsometry spectra both demonstrate the existence of collective resonances but also provide a better understanding of the signature of such optical modes. Ellipsometry can be decomposed as the amplitude  $\Psi$  and the phase  $\Delta$  of the light reflected by an illuminated sample. Once the  $p$  and  $s$  components of the reflected electric field  $E_p$  and  $E_s$  are well-known, the ratio  $E_p/E_s$  can be expressed as  $\tan(\Psi)e^{i\Delta}$ <sup>280</sup>. Besides, the gold dimers are not embedded in surrounding homogeneous medium so that radiative coupling can occur in the substrate or in the superstrate.

In the same study they could predict, for a zero azimuthal angle, the spectral positions of SLRs whose waves diffract in either in glass substrate or in air superstrate<sup>279</sup>

$$\lambda_{R_m}^{air} = \frac{a}{m}(1 \pm \sin(\theta)) \quad (3.53a)$$

$$\lambda_{R_m}^{sub} = \frac{a}{m}(n_s \pm \sin(\theta)) \quad (3.53b)$$

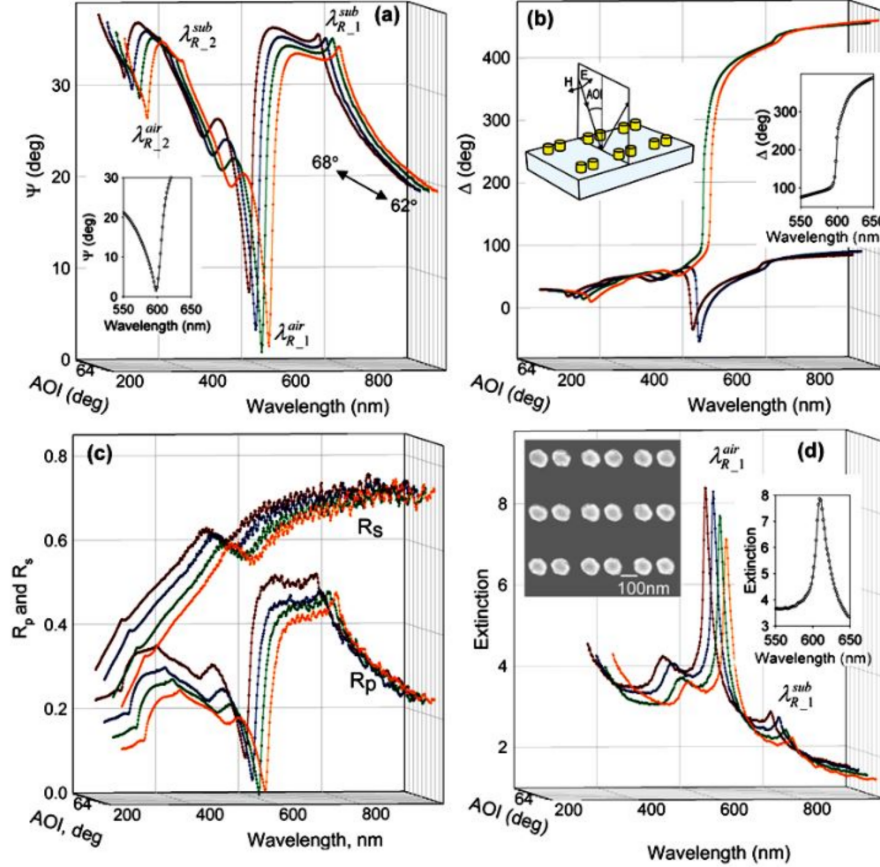


Figure 3.16: Surface lattice resonances of gold dimer arrays. Experimental spectra describing ellipsometry, reflection and extinction for 2D periodic arrangements of nanostructures. (a) Ellipsometry parameter  $\Psi$ . Inset shows the loss of reflection for  $\theta = 64^\circ$ . (b) Ellipsometry parameter  $\Delta$ . Right inset highlights humongous phase change in reflection for  $\theta = 64^\circ$ . (c) Reflection spectra for incoming  $p$  and  $s$  light polarizations. (d) Extinction spectra for  $p$ -polarization. Left inset provides scanning electron microscopy image of the 2D arrays of gold dimers. Right inset highlights the maximum in extinction for  $\theta = 64^\circ$ . The array period is fixed at 320 nm, single particle diameter reaches 108 nm while the thickness is 90 nm. A dimer consists of two single particles separated by 140 nm. Figure from reference 279.

with  $a$  the array period,  $m$  an integer,  $\theta$  the angle of incidence and  $n_s$  the glass refractive index. At the same period some studies demonstrated similar effects for different particles geometries<sup>281–283</sup> leading to further development of this research field<sup>248,273,284–287</sup>. In particular, these

## CHAPTER 3. PLASMONICS

collective resonances consist of low-loss tunable plasmonic resonances characterized by high quality factors  $Q$  reaching in general 50<sup>279,281,282,284</sup>, recently closer to several hundred<sup>288–292</sup> and even more than 2000<sup>293</sup>.

The spectral position and the shape of the SLR depend strongly on the particle design and the lattice parameters which control the energy detuning between the LSPR and the diffracted waves<sup>284</sup>. Such systems supporting collective resonances find their interest in enhancing spontaneous<sup>294–296</sup> but also stimulated<sup>249,297–299</sup> emission. In addition, a homogeneous surrounding media is required to support the radiative coupling else an asymmetric refractive-index environment between the substrate and the superstrate weakens the lattice resonance<sup>300</sup>. Thus index matching liquid with the same refractive index as the substrate is conventionally used in studies of SLRs.

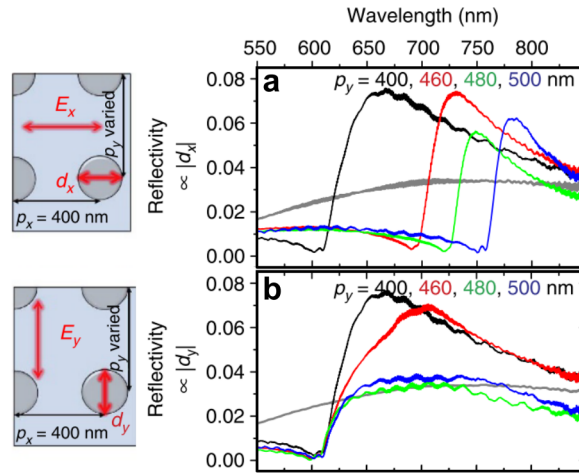


Figure 3.17: Experimental optical spectra of periodic arrays of magnetic nanodisks. Schemes at the left highlight the incident polarization direction and the induced pure optical electric dipole. The black, red, green and blue line graphs correspond to a  $y$ -lattice period  $p_y = 400, 460, 480$  and  $500$  nm, respectively. The grey line corresponds to a random distribution of nanodisks. Optical reflectivity measured at normal incidence for incident light polarization (a)  $E_x$  and (b)  $E_y$ . Figure adapted from reference 248.

While LSPRs of single nanoparticles can be controlled by particles shape, SLRs can be modulated with array parameters. To prove this, Kataja *et al.* probed in 2015 reflection spectra of metasurfaces based on rectangular periodic arrays of nickel nanodisks with diameter of 120 nm along  $x$  and  $y$  axes<sup>248</sup>. The period along  $x$  axis  $p_x$  was fixed at 400 nm while the other along  $y$  axis  $p_y$  varies from 400 nm to 500 nm. The incoming light was linearly polarized with electric field aligned with  $x$  or  $y$  axis as shown in Figure 3.17. The first and second cases make the electronic cloud oscillating along  $x$  and  $y$  axis, respectively. However, SLRs are sensitive to  $p_y$



in the first case while only  $p_x$  affects them when the electric field is oriented along  $y$  axis. Indeed, SLRs result from radiative coupling between LSPRs driven by oscillating electric field and DOs orthogonal to the orientation of induced electric dipoles. This means that only a variation of  $p_y$  in the array can affect SLRs involving coherent oscillations of electrons along  $x$  axis. Figure 3.17 supports this statement and provides a deeper understanding about the mechanism driving the SLRs.

### 3.4 Magneto-optical effects

In this work, we aim to write and read the information with light by means of magneto-optics (MO). In this context we introduce the magneto-optical Kerr effect (MOKE) as well as magneto-optical Faraday effect (MOFE) to bring the key ingredients for our studies.

The emergence of MO started with M. Faraday in 1846 who evidenced that the linear light polarization could be rotated after propagating through a glass rod subjected to a magnetic field aligned with the propagation direction of the EM waves<sup>301</sup>. This rotation, namely the Faraday rotation, was directly proportional to the applied magnetic field. Similarly, J. Kerr demonstrated in 1877 that the light properties could be changed by being reflected by a magnetic material<sup>302</sup>. He showed that the resulting MO effect was proportional the magnetization of the iron mirror. Currently, MOKE is a very strong tool to study the magnetization of ferromagnetic as well as ferrimagnetic materials since it competes, in terms of sensitivity, with the magnetometry techniques<sup>303</sup>. MOKE-based techniques also allow to measure very fast the magnetic state, even with time resolution down to 100 fs with ultrafast lasers<sup>84</sup>.

The spatial resolution of such approach reaches  $0.2 \mu\text{m}$  permitting the observation of magnetic domains<sup>304</sup> as well as the studies involving for instance nanostructures<sup>305</sup>. Last but not at least, MOKE is sensitive to depth so that it is possible to extract the signal of a single magnetic layer that is inserted in a magnetic heterostructure<sup>306,307</sup>. Using our convention of EM waves, we now present the description of light polarization.

#### 3.4.1 Light polarization

Any EM wave in three directions  $x$ ,  $y$  and  $z$  is defined by its maximum value  $E_{max}$  and its absolute phase  $\delta$  according to

$$E_x(\mathbf{r}, t) = \Re(E_{x,max}(\mathbf{r}, \omega)e^{i\delta_x(\mathbf{r}, \omega) + i\mathbf{k}\cdot\mathbf{r} - i\omega t}) \quad (3.54a)$$

$$E_y(\mathbf{r}, t) = \Re(E_{y,max}(\mathbf{r}, \omega)e^{i\delta_y(\mathbf{r}, \omega) + i\mathbf{k}\cdot\mathbf{r} - i\omega t}) \quad (3.54b)$$

$$E_z(\mathbf{r}, t) = \Re(E_{z,max}(\mathbf{r}, \omega)e^{i\delta_z(\mathbf{r}, \omega) + i\mathbf{k}\cdot\mathbf{r} - i\omega t}) \quad (3.54c)$$

Considering an isotropic medium, the solutions of Equations (3.10) give transverse waves so that  $\mathbf{E}$  and  $\mathbf{H}$  are perpendicular to each other but also to light propagation direction. Then the electric field can be decomposed in the 2D basis

$$\mathbf{E}(\mathbf{r}, \omega) = A_s(\mathbf{r}, \omega)\mathbf{u}_s + A_p(\mathbf{r}, \omega)\mathbf{u}_p \quad (3.55)$$

where the unit modal vector polarizations  $\mathbf{u}_s$  and  $\mathbf{u}_p$  are perpendicular to the light propagation direction.  $A_s$  and  $A_p$  correspond to the modal amplitudes and aim to weight the contribution of their polarization. In this work we only consider linearly polarized light in isotropic media so that  $s$  and  $p$  directions describe directions perpendicular and parallel to the plane of incidence of light, respectively<sup>280</sup>.

For a complete description of a general elliptical polarization, we need to determine four quantities that are represented in Figure 3.18. The first parameter is the azimuth  $\theta_a$  which gives the rotation angle between the main polarization axis and the  $s$  direction. Because we consider an ellipse, the ellipticity  $\eta_a$  is a relevant parameter. It stands for the ratio between the minor and major axis  $b$  and  $a$  of the elliptic polarization. A negative ratio gives an anti-clockwise rotation leading to a left-handed polarized wave. We can also define the ratio between the modal amplitudes  $\tan \Omega_a = |A_p(\mathbf{r}, \omega)|/|A_s(\mathbf{r}, \omega)|$  as well as the phase shift between the two configurations  $\xi_a = \arg(A_p(\mathbf{r}, \omega)) - \arg(A_s(\mathbf{r}, \omega))$ . These four variables are connected through the equations<sup>280</sup>

$$\tan(2\theta_a) = \tan(2\Omega_a) \cos(\xi_a) \quad (3.56a)$$

$$\sin(2\eta_a) = \sin(2\Omega_a) \sin(\xi_a) \quad (3.56b)$$

$$\tan(\Omega_a)e^{i\xi_a} = \frac{\tan(\theta_a) - i \tan(\eta_a)}{1 + i \tan(\theta_a) \tan(\eta_a)} \quad (3.56c)$$

We use the Jones formalism to determine the polarization state after the light propagates through optics (the sample is included). We report the representation of any optical element of interest in Jones formalism framework in Appendix B. In particular, the interaction of light, either  $s$  or  $p$  polarized, with the magnetic system results in

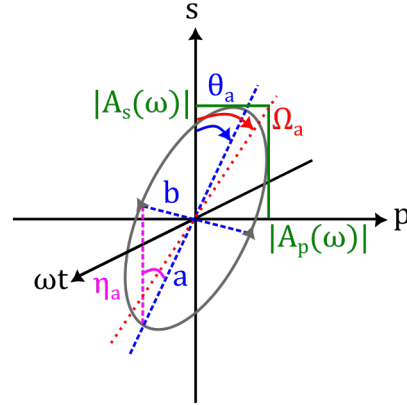


Figure 3.18: Electric field for a given spatial position decomposed along both direction  $s$  and  $p$ . The sketch gives a position azimuth  $\theta_a$  and a negative ellipticity  $\eta_a$ .

$$\begin{pmatrix} E_p^r \\ E_s^r \end{pmatrix} = \begin{pmatrix} r_{pp} & r_{ps} \\ r_{sp} & r_{ss} \end{pmatrix} \times \begin{pmatrix} E_p^i \\ E_s^i \end{pmatrix} \quad (3.57)$$

$$\begin{pmatrix} E_p^t \\ E_s^t \end{pmatrix} = \begin{pmatrix} t_{pp} & t_{ps} \\ t_{ss} & t_{ss} \end{pmatrix} \times \begin{pmatrix} E_p^i \\ E_s^i \end{pmatrix} \quad (3.58)$$

where the coefficients in the square matrices in Equations (3.57) and (3.58) correspond to ratios of reflected and transmitted electric field amplitudes to incident electric field amplitudes with corresponding initial polarizations, respectively.

### 3.4.2 Magneto-optical Kerr effect

Let us consider a magnetic system subjected to a purely  $s$ -linearly polarized plane wave. As sketched in Figure 3.18, the reflected light holds  $s$  and  $p$  components in its polarization. We fix as a convention a positive Kerr rotation when  $\theta_a$  turns clockwise. Similarly we consider a positive ellipticity when the electric field turns clockwise. Since MOKE is widely defined as the ratio between reflection coefficients, one can obtain the complex Kerr effect in the small angle limit

$$\Phi_s = -\frac{r_{ps}}{r_{ss}} = \theta_s + i\eta_s \quad (3.59a)$$

$$\Phi_p = \frac{r_{sp}}{r_{pp}} = \theta_p + i\eta_p \quad (3.59b)$$

Then  $\Phi_s$  and  $\Phi_p$  lead to  $s$ -MOKE and  $p$ -MOKE, respectively. The real part of this complex quantity is the Kerr rotation  $\theta$  while the imaginary part is the Kerr ellipticity  $\eta$ . The polar form depends on the Kerr amplitude  $\Omega$  and Kerr phase  $\xi$  leading to  $\Phi = \Omega e^{i\xi}$ . This form is more convenient for describing heterostructures containing more than one magnetic subsystem.

### 3.4.3 MOKE geometries

We define the  $z$  direction as perpendicular to the sample plane while the plane of incidence is delimited by  $x$  and  $y$  axis. The configurations ( $\mathbf{M} \parallel \mathbf{z}$ ), ( $\mathbf{M} \parallel \mathbf{x}$ ) and ( $\mathbf{M} \parallel \mathbf{y}$ ) define the polar (P-MOKE), transverse (T-MOKE) and longitudinal (L-MOKE) MOKE configurations, respectively. We detail these geometries in Figure 3.19 with the related reflection matrices. Historically the positive orientation of the first two configurations is given along the opposite direction of the  $z$  and  $x$  axis, respectively. Thus the resulting definitions involve the normalized magnetization  $\mathbf{m} = (0, 0, -1)$  and  $\mathbf{m} = (-1, 0, 0)$ , respectively. Only polar and longitudinal geometries conduct to non-diagonal reflection coefficients. Then the complex Kerr angle is only related to the components induced by the latter configurations. The transverse case only varies the term  $r_{pp}$  for a non-zero angle of incidence giving the complex transverse Kerr effect

$$\Phi_{tra} = \frac{r_{pp,mag}}{r_{pp,0}} \quad (3.60)$$

In this work we only probe P-MOKE. Concerning T-MOKE, one should know that a simple measure of reflected light intensity is a direct estimation of the MO effect through

$$I \approx |r_{pp,0}|^2 (1 + 2\Re(\Phi_{tra})m_x) \quad (3.61)$$

Equation (3.61) remains valid as long as  $|r_{pp,0}| \gg |r_{pp,mag}|$ . We know discuss the peculiar case of magnetic nanodisks.

### 3.4.4 Magnetic nanodisks

Magnetic nanodisks sound of particular interest as they can, when patterned into periodic arrays, enhance drastically the MO response very locally comparing to the corresponding continuous thin film. The permittivity tensor exhibits non-diagonal terms accounting the presence of magnetization with the MO Voigt constant. Then the polarizability tensor takes the form

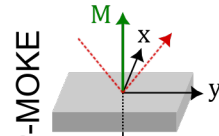
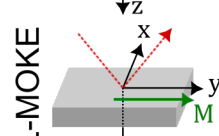
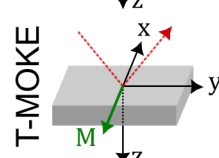
	normal incidence	oblique incidence
P-MOKE 	$\begin{pmatrix} r_{ss} & r_{ps} \\ r_{ps} & -r_{ss} \end{pmatrix}$	$\begin{pmatrix} r_{ss} & r_{ps} \\ r_{ps} & r_{pp} \end{pmatrix}$
L-MOKE 	$\begin{pmatrix} r_{ss} & 0 \\ 0 & -r_{ss} \end{pmatrix}$	$\begin{pmatrix} r_{ss} & -r_{ps} \\ r_{ps} & r_{pp} \end{pmatrix}$
T-MOKE 	$\begin{pmatrix} r_{ss} & 0 \\ 0 & -r_{ss} \end{pmatrix}$	$\begin{pmatrix} r_{ss} & 0 \\ 0 & r_{pp,0} + r_{pp,mag} \end{pmatrix}$

Figure 3.19: Three MOKE configurations with related reflection matrices for normal and oblique incidences. The terms  $r_{pp,0}$  and  $r_{pp,mag}$  are  $r_{pp}$  that are experience non dependence and linear dependence to in plane magnetization  $m_x$ , respectively.

$$\alpha = \begin{pmatrix} \alpha_{xx} & \alpha_{xy} & 0 \\ \alpha_{yx} & \alpha_{yy} & 0 \\ 0 & 0 & \alpha_{zz} \end{pmatrix} \quad (3.62)$$

Due to rotation invariance in case of a nanodisk,  $\alpha_{xx} = \alpha_{yy}$  and  $\alpha_{xy} = -\alpha_{yx}$ . Considering an electric field polarized along x, two electric dipoles are obtained. The first one,  $\mathbf{p}_x = \alpha_{xx}\mathbf{E}_x$ , is pure optical dipole while the second one,  $\mathbf{p}_y = -\alpha_{xy}\mathbf{E}_x$ , is non zero due to off-diagonal components in the polarizability tensor as shown on Figure 3.20.

The ratio of both scattered electric dipoles gives the complex Kerr angle<sup>308–311</sup>

$$\Phi_K = \arctan\left(\frac{p_y}{p_x}\right) \quad (3.63)$$

Actually the measured angles are small enough to assume that ratio of both dipoles is a good approximation to quantify the Kerr angle. Equation (3.63) can be rewritten for a square array of magnetic nanodisks as

$$\Phi_K = \frac{-\alpha_{xy,array}}{\alpha_{xx,array}} \quad (3.64)$$

Assuming  $\alpha_{xx} \gg \alpha_{xy}$ , then  $\alpha_{xx,array} \gg \alpha_{xy,array}$  meaning that the pure optical dipole is far larger than the MO dipole. This statement is supported by experimental measurements of Kerr angle that are usually below 1<sup>o220,309–312</sup>. Equation (3.64) highlights how magnetization

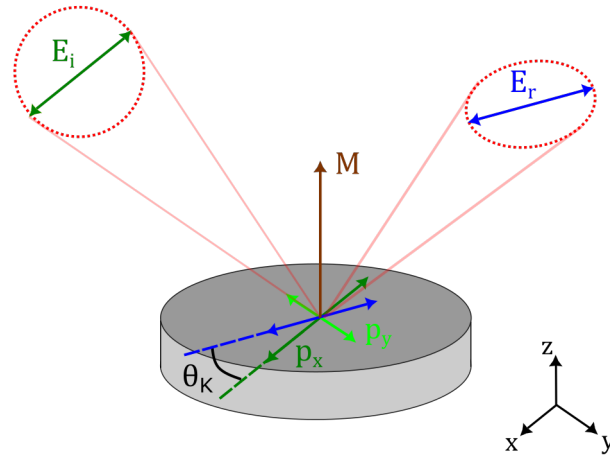


Figure 3.20: Sketch of two orthogonal electric dipoles induced by linearly polarized light in a magnetized disk.  $p_x$  is aligned with the incident electric field polarization while  $p_y$ , orthogonal to the latter, results from magnetic behaviour of the disk. Sum of both dipoles transforms the initial polarization into elliptical.

impacts the reflected or transmitted light from a periodic array of magnetic nanodisks. The phase difference between the two orthogonal dipoles depends on the wavelength of the incoming light. At LSPR, both of them oscillate in phase leading to Kerr rotation enhancement and a zero Kerr ellipticity. Similarly, exciting a SLR in periodic arrangements of magnetic nanodisks makes the local electric field within the particle much higher than the incident electric field so that collective resonances lead to intense MO activity.

### 3.5 Conclusion

In this chapter, we introduced the fundamental concepts of optics and plasmonics to understand this thesis. In particular, we highlighted different ways to excite plasmon polariton modes, detailed the origin of LSPRs and reviewed the emergence and early development of SLRs. In particular we stressed that the excitation of plasmonic mode must enhance absorption. This behaviour sounds of particular interest for enhancing AO-HIS since it is driven by a pure thermal effect. We also explained how plasmonic magnetic particles could change incident light polarization so that they can monitor the magneto-optical response with the wavelength. Indeed, we expected that the excitation SLRs must also enhance MO response leading to drastically enhanced readout sensitivity.

## Chapter 4

# Magnetoplasmonic, a constantly evolving topic

*The work presented in this thesis aims to combine two subfields of physics, all-optical magnetization switching and plasmonics. This chapter tends to put the future presented work into context by reviewing existing studies that designed magnetoplasmonic systems for either enhancing AO-HIS due to absorption enhancement or strong MO response coming from local electric field enhancement within the magnetic nanoparticles.*

### 4.1 Introduction

The opportunity to control magnetization with low energy ultrafast laser pulse sounds of particular interest for the development of future magnetic data storage. In particular, switching speed can be faster than half a picosecond while reswitching can also occur at subpicosecond time scale<sup>306</sup>. These performances clearly compete with current HDDs in the market. In this perspective, AO-HIS needs to ensure all-optical areal recording densities that compete with the resolution of current data storage devices. All-optical magnetic recording then requires nanostructures to overcome the diffraction limit. Plasmonics provides an approach to manipulate beyond the diffraction limit<sup>20</sup>. We detail in this section how plasmonics is already integrated in data storage technologies. Also, we review how plasmonics has been combined either to AO-HIS for a more energy efficient manipulation of magnetic order at nanoscale or to enhance the MO activity that must result in a more sensitive readout.

### 4.2 Near-field transducer

According to the International Data Corporation, the global data creating and replication should show a compound annual growth of 23 % from 2020 to 2025. This statement supports the ceaseless demand for increasing areal density, making magnetic recording faster and more energy efficient. The emergence of perpendicular data recording (PMR) in 2004 conceived by the hard disk industry fits with these needs<sup>313</sup> despite superparamagnetic limit must lower the signal to noise ratio (SNR) when the bits are narrowly packed<sup>314,315</sup>.

Conventional PMR based-devices only use a magnetic field to write the information. This latter has to be confined over an area of tens of nanometers and the magnetic field gradient determines the recording quality. The data storage industry is facing a "trilemma" since it aims to combine smaller grain size, recording media with higher anisotropy (to avoid thermal fluctuations leading to unexpected magnetization reversal) and stronger magnetic field induced by the writing head. In this context heat assisted magnetic recording (HAMR) provides a new approach to allow magnetic recording with PMR whose areal density reached 1 Tb/in<sup>23,4,316,317</sup>.

The resolution of HAMR technologies is bounded by the optical spot size whose dimension lies above the diffraction limit<sup>5</sup>. The local heating of the magnetic granular media makes its coercivity lower significantly lower as sketched in Figure 4.1 so that materials exhibiting high anisotropy with grain size smaller than 7 nm such as FePt can be involved in the design of hard disk drives<sup>318-321</sup>. This allows to rapidly decrease the coercive field when the bits are irradiated but also to restore magnetic properties fast when the laser is switched off.



## CHAPTER 4. MAGNETOPLASMONIC, A CONSTANTLY EVOLVING TOPIC

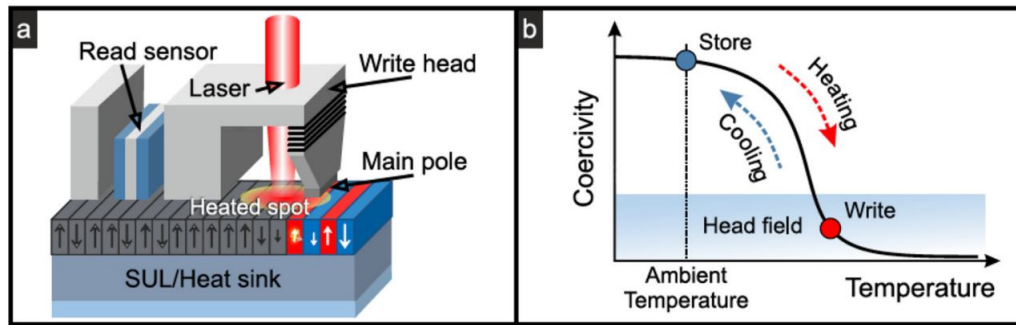


Figure 4.1: (a) Illustration of HAMR principle. (b) Coercivity of FePt media as a function of temperature. Figure from reference 317.

Now one of the main criteria that determines the recording quality is the thermal gradient. The highest is the better since the peak temperature at the center should be above  $T_C$  while the edges of the spot should not affect the recording media. To be in with the chance in the race for high areal density, one should be able to heat locally one single bit to perform magnetic recording selectively in a single magnetic grain. In this perspective some works proposed the insertion of a plasmonic near field transducer (NFT) in HAMR technologies to create localized heat source with the excitation of LSPRs<sup>5,322,323</sup>. This strategy combines HAMR head and engineered media multilayer as sketched in Figure 4.2.

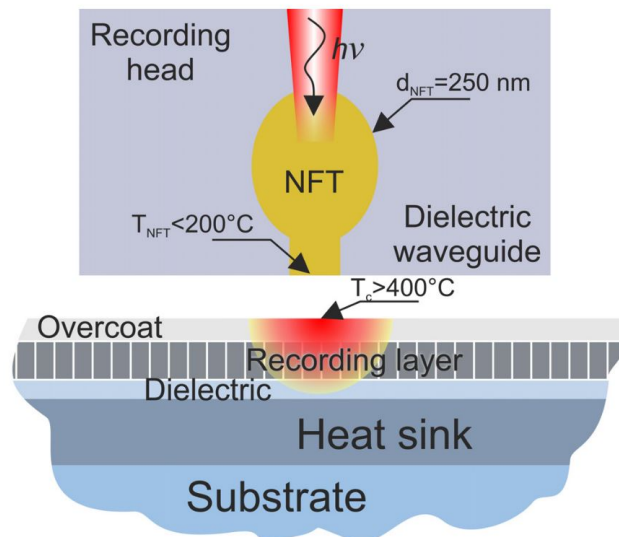


Figure 4.2: Principle of NFT. Figure from reference 317.

The media cooling time should be fast enough to allow fast magnetic recording but slow enough for the media to reach the lowest energy state, here the crystal<sup>324,325</sup>. Many NFT ge-

## CHAPTER 4. MAGNETOPLASMONIC, A CONSTANTLY EVOLVING TOPIC

ometries have been developed but the most widespread one consists of a lollipop in which a disk launches the plasmon while a rectangular peg focuses the energy. Figure 4.3 gives an 3D overview of the HAMR writer combined with a plasmonic NFT. The issues related to the external environment near the writing position has been addressed for years to maintain performance due to high temperature and pressure. In particular, the choice of material for the NFT seems complicated since it should fulfill many criteria such as cheap price, robust to the aggressive environment, good adhesion to the dielectric waveguide and low-lossy for plasmonic applications<sup>324,325</sup>. Au appears as the best candidate but remains problematic for interface adhesion with oxides. Alternatives are still investigated for the optimal NFT material.

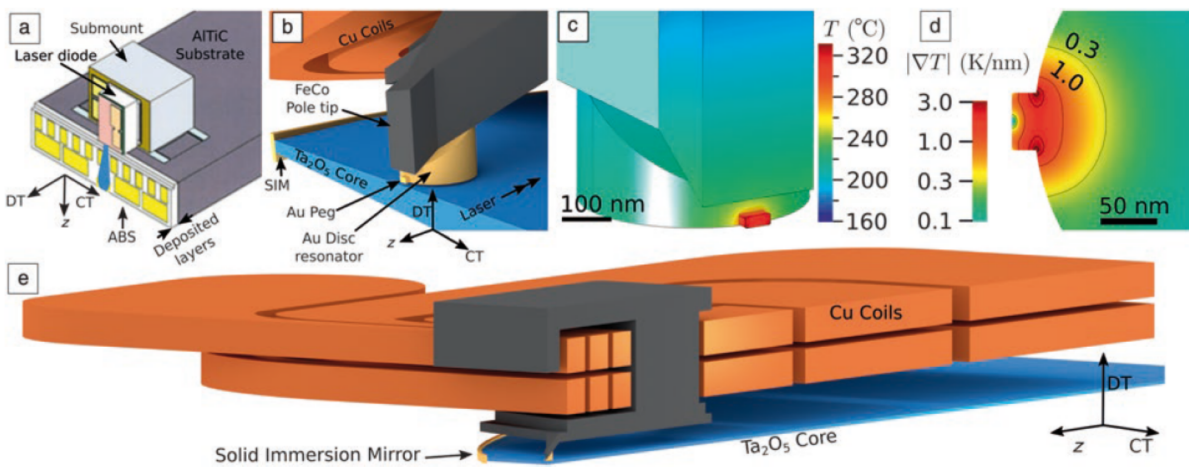


Figure 4.3: HAMR writing head. (a) Sketch of the recording head with 1.2-mm down-track (DT) and 700- $\mu\text{m}$  cross-track (CT). Air-bearing surface (ABS) lies on the underside. Recording media slides along the +DT direction. (b) Illustration of the Au NFT connected to the magnetic pole tip. (c) Temperature distribution within the NFT when it is subjected to a power of 15 mW in case of perfect efficiency for the laser and light delivery system. (d) Cross section of the temperature distribution within the NFT. (e) Cross section of the whole assembly. Figure from reference 324.

Another key ingredient for plasmonic HAMR technologies is an efficient heat sink to cool fast the recording media. Indeed, as illustrated in Figure 4.2, the stack below the NFT consists of substrate, plasmonic heat sink, seed dielectric layer, FePt recording media and C-based coating layer. Hu *et al.* performed Finite-Difference Time-Domain simulations to obtain the normalized power absorption distribution in the NFT and the recording media<sup>326</sup> as shown in Figure 4.4. The area of highest absorption in the recording layer has a characteristic lateral dimension of 50 nm. This approach provides a means to develop energy efficient HAMR technologies with opportunities to increase areal density.

We would like to make these advancements in perspective with the work presented in this

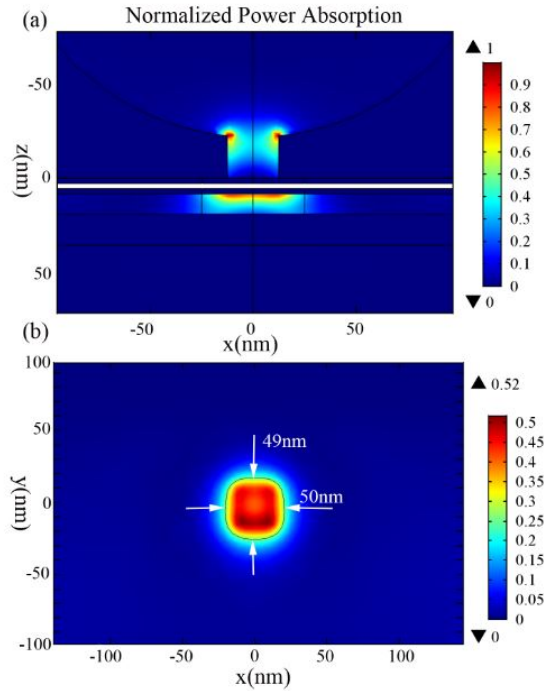


Figure 4.4: Normalized absorbed power by the NFT and the recording layer. (a) Cross-sectional view. (b) In-plane view of the media layer. Figure from reference 326.

thesis. The use of significantly smaller magnetic field holds true as long as HAMR technologies use continuous, even long pulsed lasers (at least half a nanosecond). The situation is completely different if we would consider the integration of ultrafast lasers in such devices. Indeed the involved time scales would make the Zeeman energy lower than the thermal energies so that the recording media would freeze in the wrong direction. Then, considering ultrafast laser in HAMR technologies would lead inexorably to the use of much higher magnetic fields and we would lose the benefits for which these technologies have been developed. One way to avoid this issue would be to find an alternative to reverse magnetization without magnetic field, only by means of light.

As mentioned before, it is possible to switch deterministically the magnetization of a short range of magnetic materials with an arbitrary polarized single ultrafast laser pulse. We consider periodic arrangements of magnetic nanodisks, mimicing a granular media, that can be switched by a single laser pulse. An external NFT could provide an optical spot that involves enough nanoparticles to excite a SLR with a central peak energy that would lead to AO-HIS only in the nanodisk at the center of the periodic array. We focus on two aspects of future plasmonic HAMR technologies: the design of artificial granular media with periodic arrangements of magnetic nanodisks whose magnetization can be reversed with a single laser pulse of low energy due to

the excitation of a plasmonic mode and the extension of AO-HIS to larger pulse duration by means of Cu heat sinks. This latter is also an essential building block to manage the temperature of the recording media and to avoid the deterioration of the external NFT.

### 4.3 Energy efficient control of magnetization at nanoscale

The first demonstration of optical control of magnetization with light in GdFeCo showed reversed area with a characteristic size of 10 of micrometers<sup>7</sup>. Graves *et al.* pointed out nanoscale chemical and magnetic inhomogeneities in RE-TM amorphous alloy GdFeCo that impact spin dynamics leading to a lower bound for domain stability at 1 micrometer<sup>149</sup>. Then Le Guyader *et al.* provided the opportunity through their work to reverse the magnetization of 200 nm GdFeCo nanostructures in sub-100 ps time scale<sup>327,328</sup>. In this context, Savoini *et al.* investigated a large range of GdFeCo structure sizes but also the corresponding continuous film and compared the minimum energy to observe 100 % light-induced demagnetization, AOS and damage as shown in Figure 4.5<sup>329</sup>. They could reduce the threshold fluence by 60 % on a single 1x1  $\mu\text{m}^2$  magnetic structure compared to the continuous thin film. They excluded the impact of heat diffusion and transport of hot carriers to explain the trend observed in Figure 4.5 because magnetization reversal and the loss of magnetization amplitude were seen to occur at picosecond time scale. Xun *et al.* suggested in this context that the effects related to electron diffusion and heat capacity last over nanosecond time scale<sup>330</sup>. We show in this thesis that this description is not complete since we can control, by means of Cu heat sinks, the cooling speed of GdFeCo, extending the scope of AO-HIS to much larger pulse durations and larger pulse energy. Indeed, when the electronic bath temperature cools down early enough from below  $T_C$  we can observe AO-HIS while we would observe only demagnetization of GdFeCo for very thin Cu layer at the interface of GdFeCo layer.

They attributed the drop of threshold fluence to an increase of absorption caused by the creation of standing waves within the particle due to interferences as the wavelength of the incoming illumination and the structure were of the same order. To support their statement they performed FDTD simulations of absorbed energy line profiles in the structures with lateral size of 1, 2, 5 and 5 micrometers as shown in Figure 4.6. They evidenced that interferences played a key role in absorption enhancement because the structures with greatest energy efficiency were subwavelength-sized. However they concluded that reducing the particle size does not significantly improve the light-matter interaction. The alloy TbFeCo was also believed to be a promising candidate for all-optical magnetic recording at nanoscale since Finazzi *et al.* could generate

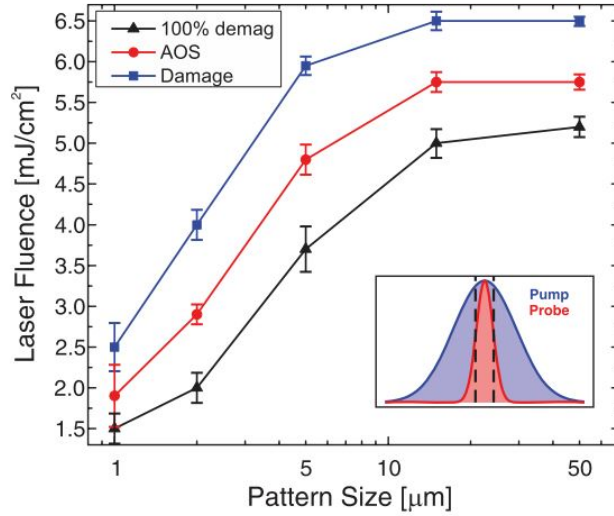


Figure 4.5: Fluence thresholds for complete demagnetization, all-optical magnetization switching, and damage as a function of the structure size. Figure from reference 329.

skyrmions and stabilize them without magnetic field, with characteristic lateral size of 150 nm. In fact magnetic skyrmions, standing for nanoscale spin textures, are believed to be promising for ultradense data storage and logic devices<sup>331</sup>. All the strategies in these studies did not allow to perform all-optical magnetic recording with an areal density that competes with HDDs in the market. A new approach has been proposed by Liu *et al.* in 2015 by considering two-wire plasmonic gold nanoantennas on TbFeCo continuous film<sup>168</sup>. Both antennas are aligned and their close proximity is believed to induce near field intensity enhancement<sup>332</sup>. The geometry has been optimized to switch magnetic domain subjected to low energy laser pulse whose lateral size depended strongly on the two-wire antenna geometry<sup>333</sup>. In order to observe magnetic structures at nanoscale, they used X-ray based imaging approach.

Figure 4.7 evidences deterministic repetitive switching of TbFeCo domains near the plasmonic antenna. They compared the minimum fluence to perform AOHIS near and away from the two-wire gold structures and concluded that the absorption enhancement induced by LSPR decreases the minimum energy to reverse magnetization with light by 37 % near the antenna in comparison to the single continuous film. This trend was supported by subsequent simulations showing the near-field distribution when the Au nanostructures were on the TbFeCo film. Typical lateral dimension of switched area reached 53 nm, significantly smaller than any domain wrote by AO-HIS before this time. However they pointed out strong chemical inhomogeneities that may conflict with magnetic properties such as compensation temperature leading to local changes of minimum energy density to observe magnetization switching. This concern seemed

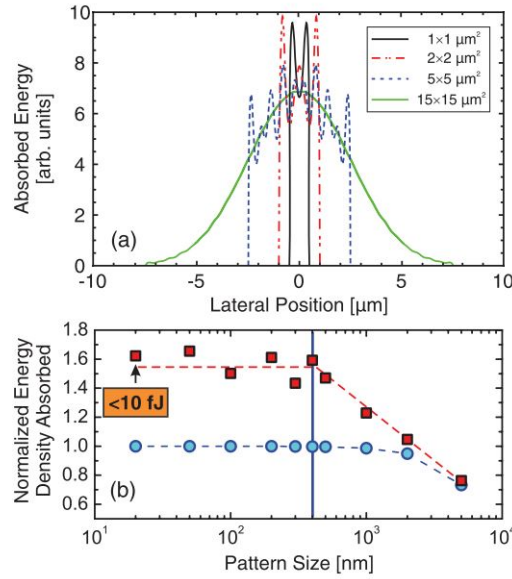


Figure 4.6: (a) Absorbed energy profiles in the structures. (b) Evolution of absorbed energy density as a function of pattern size. The trend expected without interference effects is depicted in blue circles. The vertical solid line indicates the pump wavelength. Figure from reference 329.

crucial since AO-HIS in GdFeCo is strongly dependent on Gd concentration<sup>167</sup> so that the same trend was expected for TbFeCo. The age of the samples can make the situation even harder with the segregation of certain elements from the alloy systems changing significantly the magnetic properties, questioning the long-term usefulness of such system<sup>334</sup>.

In this perspective, a reliable control of spatial distribution of magnetization switching could be more adequate in multilayer and/or crystalline systems such as Co/Gd bilayer<sup>11,335</sup> or  $\text{L}_{10}\text{FePt}$ <sup>336</sup>. That is why Granitzka *et al.* aimed to reverse magnetization of FePt granular media throughout near-field enhancement<sup>336</sup>. They obtained a more complex response as they would have expected since they noticed that 10-20 % of the FePt nanoparticles did not react to ultrafast laser pulses. They attributed this behaviour to a non-uniform absorption of the granular media. They considered the impact of surrounding nanoparticles in the light absorption distribution but also the role of the bottom heat sink layer commonly integrated in HAMR technologies. This latter aimed to manage temperature in the recording media to cool it quick enough to not freeze the system along the wrong magnetic orientation. However it made also the heat flow propagating out of the nanoparticles so that increased the number of FePt grains not reacting to external illumination.

In this quest to increase areal density, Mishra *et al.* considered a random arrangement of silver nanorings on TbCo alloy film<sup>337</sup>. They showed that the incoming energy was funneled



## CHAPTER 4. MAGNETOPLASMONIC, A CONSTANTLY EVOLVING TOPIC

---

through the noble metal particles resulting in a reduction of demagnetization amplitude compared to the free single continuous film. This provided a nice opportunity to concentrate all the incoming illumination into tiny areas giving a new strategy to perform ultrafast magnetic recording at nanoscale. The same research group patterned periodic arrays of truncated-nanocone-shaped Au-TbCo antennas and, by means of plasmonic resonance, could increase the demagnetization amplitude of the TbCo by a factor of three in comparison to off-resonance conditions<sup>338</sup>. Similarly Kataja *et al.* patterned periodic arrays of Ni disks and observed that the excitation of SLRs could enhance the demagnetization process by means of greater absorption of the metallic particles induced by the collective resonances<sup>339</sup>. These studies are part of the development of hybrid magnetoplasmonic systems for energy efficient all optical data storage at nanoscale.

Another approach has been proposed by Cheng *et al.* by fabricating many gold nanoislands on ferromagnetic Co/Pt multilayer system<sup>340</sup>. They excited LSPR of the noble metal nanoparticles, whose average size was 10 nm, leading to local absorption enhancement in Co/Pt films. Along this line they could control magnetization on plasmonic resonance with a threshold energy reduced by 18.5 %. Since the nanoislands fabrication technique was simple as it only required annealing, this study provided a strategy to develop low cost and low energy all-optical magnetic recording at nanoscale. The use of plasmonic nanostructures seemed promising for the development of energy-efficient nanoscale ultrafast magneto-optics<sup>341,342</sup>.

The use of surface plasmon polaritons (SPPs) also found its interest in recent progress for all-optical data storage technologies. Their properties have been used for increasing areal density via multi-level AOS. For instance Ignatyeva *et al.* sputtered  $\text{Si}_3\text{N}_4/\text{Gd}_{26}\text{Fe}_{64.8}\text{Co}_{9.2}/\text{Si}_3\text{N}_4/\text{Gd}_{27}\text{Fe}_{63.9}\text{Co}_{9.1}/\text{Si}_3\text{N}_4$  on a prism to selectively reverse the magnetization of top or bottom magnetic layer depending on the polarization of the incoming ultrafast laser pulse<sup>213</sup>.

As explained in the Chapter 3, *p*-polarized light is required to launch a SPP at metal/dielectric interface<sup>195</sup>. Thus Ignatyeva *et al.* could induce strong absorption in the first GdFeCo with incoming *s*-polarized light while *p*-polarization allowed them to selectively enhance absorption in the second layer as shown in Figure 4.8. This way they favored light absorption at GdFeCo/air interface rather than the GdFeCo/glass interface. MOKE images showed switched areas where the sample was subjected to optical excitations. In particular, Figures 4.8(d,e) present different contrast with white and black colours related to top and bottom GdFeCo layers, respectively. They evidenced the opportunity to perform all-optical magnetic recording at different levels validating another approach to increase areal density with plasmonics.

They improved this capability few years later by increasing the number of GdFeCo layers

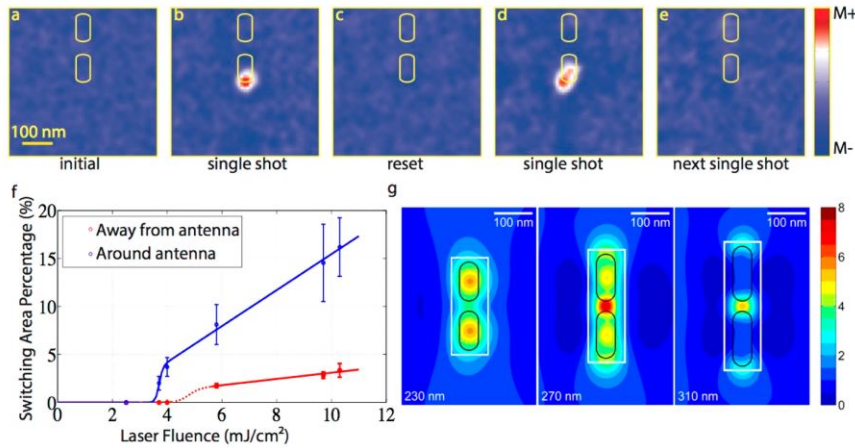


Figure 4.7: (a) Initial magnetic state. (b) Magnetic contrast after the system has been subjected to a laser pulse of  $3.7 \text{ mJ/cm}^2$ . The switched domain has a typical size of  $53.4 \text{ nm}$ . (c) Magnetic state after being reset by external out-of-plane magnetic field. (d) Magnetic contrast after the system has been subjected to a laser pulse of  $4.0 \text{ mJ/cm}^2$ . (e) Magnetic contrast after the system has been subjected to another laser pulse of  $4.0 \text{ mJ/cm}^2$ . (f) Blue data presents the minimum fluence to reverse subwavelength-sized domains near the antennas while red data shows the same kind of data without near-field enhancement. AOS starts to be observed next to the two-wire plasmonic nanoantenna for a fluence of  $3.7 \text{ mJ/cm}^2$ . The lower bound on continuous film reaches  $5.8 \text{ mJ/cm}^2$  away from the antenna. (g) Calculated near-field distribution near the two-wire antenna for three different wavelengths. Figure from reference 168.

in the heterostructure<sup>343</sup>. One remaining scientific challenge is the integration of AOS on-chip compatible with complementary metal–oxide–semiconductor (CMOS) technologies. That is why Dutta *et al.* studied nanodisks consisting of a multilayer arrangement with plasmonic material (noble metal), ferrimagnetic perpendicularly magnetized system (GdFeCo and BIG) and capping layer (titanium nitride)<sup>344</sup>. They predicted through numerical simulations that this kind of CMOS-compatible structures could induce an opto-magnetic field when subjected to external light, being an important step for the development of hybrid devices for all-optical magnetic recording technologies.

Now the question is how to integrate such designs in photonic platforms<sup>345</sup>. Recent works of Pezeshki *et al.* proposed a design involving a photonic crystal cavity coupled to a double V-shaped gold plasmonic antenna for being able to write nanoscale magnetic bits with low energy on racetrack memories as illustrated in Figure 4.9<sup>346</sup>. They predicted that AOS must be more energy efficient through absorption hot spot induced by the cavity but could also detect the magnetic state of a  $200 \times 100 \text{ nm}^2$  bit with a relative contrast greater than  $0.6 \%$ .

In this perspective they proposed a method to integrate photonics in CMOS technologies



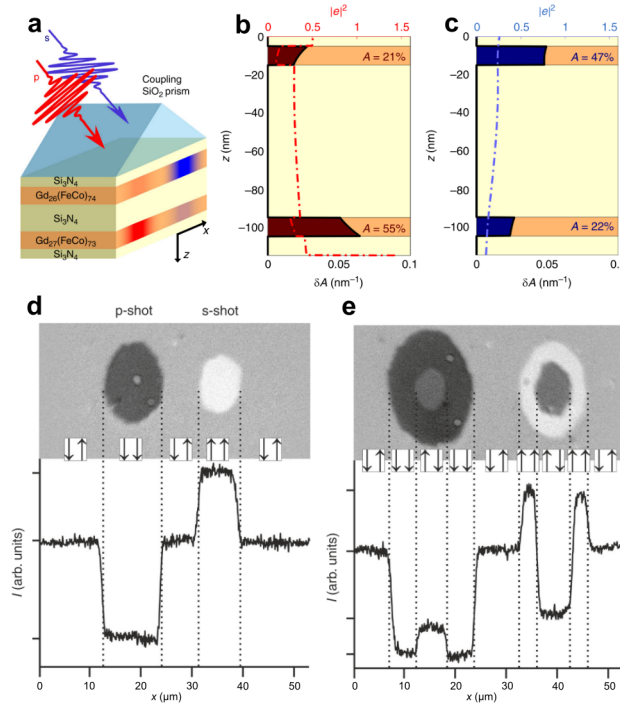


Figure 4.8: (a) Sketch of experimental configuration. Red and blue correspond to  $p$  and  $s$  polarization, respectively. (b, c) In depth distribution of EM energy  $|e|^2$  (dashed-dotted line), partial absorption  $\delta A$  and total absorption  $A$  (solid line) for incoming  $p$  and  $s$ -polarized light, respectively. The wavelength is fixed at 800 nm while the angle of incidence is  $59^\circ$ . (d, e) MOKE images of polarization-dependent AOS. The left (resp. right) arrow indicates the orientation of Gd sublattice magnetic moments within the top (resp. bottom) layer of the RE-TM alloy system. Images in (d) and (e) have been obtained for a measured fluence of 10 mJ/cm<sup>2</sup> and 12 mJ/cm<sup>2</sup>, respectively. Figure adapted from reference 213.

for energy efficient and reliable all-optical magnetic recording. In parallel they numerically investigated the possibility to integrate plasmonic-photonic component in Indium-Phosphide Membrane on Silicon (IMOS) to offer a light polarization control in active photonic integrated circuits<sup>347</sup>. This work seems to be a key progress for the integration of AOS in magnetic storage technologies<sup>345</sup>. This could be combined with recent work of Abendroth *et al.* in which they observed sixfold enhancement of electric field rotation in [Co/Pt] continuous films with periodic arrangement of Si nanodisks fabricated on top of the multilayer stack once the whole system is subjected to a circularly polarized light excitation<sup>348</sup>.

## 4.4 Magneto-optical activity enhancement

Plasmonics can provide new functionalities to write the information with light. Through

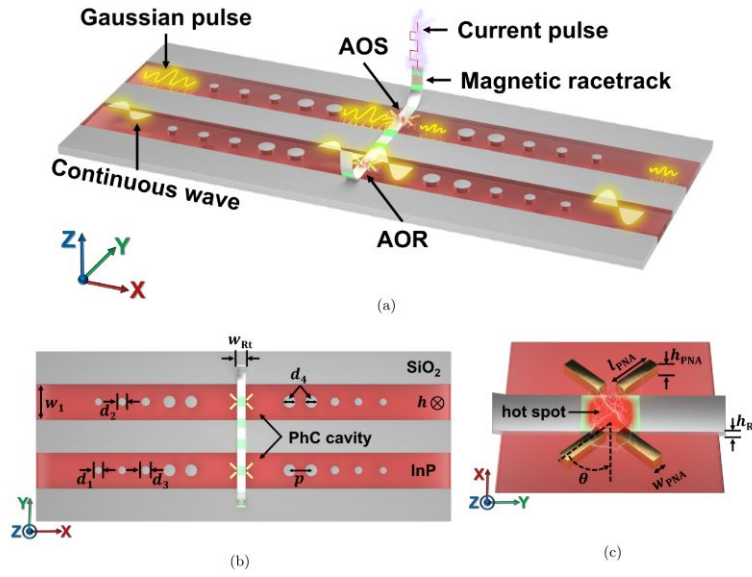


Figure 4.9: a) Sketch of the concept. b) Top view of the platform with photonic crystal (PhC) cavity parameters.  $d_{1-4} = 100, 110, 120$  and  $170$  nm,  $p = 370$  nm,  $w_1 = 570$  nm,  $h = 250$  nm and  $w_{Rt} = 120$  nm. c) Highlight on the double V-shaped gold plasmonic antenna (PNA) on the racetrack with  $l_{PNA} = 120$  nm,  $h_{PNA} = w_{PNA} = 30$  nm and  $h_{Rt} = 10$  nm. Subparts of the PNA are oriented at  $45^\circ$  from racetrack main axis. Figure from reference 346.

the development of all-optical magnetic recording devices, information should be also read by means of light. In this section, we stress how the combination of magnetism, plasmonics and photonics is the corner stone of the future approaches for magnetic recording through the enhancement of MO activity<sup>312,349,350</sup>. The pioneer work of Sepulveda *et al.* explains how noble metals nanodisks can exhibit strong MO activity when they are subjected to low external magnetic fields. Since they applied a magnetic field they created an artificial magnetic moment, this latter led to a Lorentz force. As the magnetic Lorentz force depends on the polarizability of the system, they attributed the increase of MO activity to a rise of this force coming from large coherent oscillations of the electronic cloud within the Au nanodisk. They could induce such behaviour through the excitation of LSPR.

Some studies already suggested that the excitation of LSPR in magnetic nanostructures could enhance the MO resulting signal while changing its phase<sup>309,312,351</sup>. Maccaferri *et al.* developed a theoretical model to describe the behaviour of such enhancement of MO signal coming from Ni nanodisks and explained that the excitation of LSPR induces two electric dipoles with the structure. The first one, purely optical, is aligned with the direction of the incoming electric field while the second one, orthogonal to the latter, exists because of the off-diagonal terms in

the permittivity tensor, terms that contains the MO Voigt constant<sup>310</sup>. He could reproduce his experimental results by modeling a ferromagnetic nanodisk by two coupled orthogonal damped harmonic oscillators as presented in Figure 4.10. The same approach has been used by Kataja *et al.* in 2015 to reproduce the MO spectra of periodic arrays of magnetic nanodisks<sup>248</sup>.

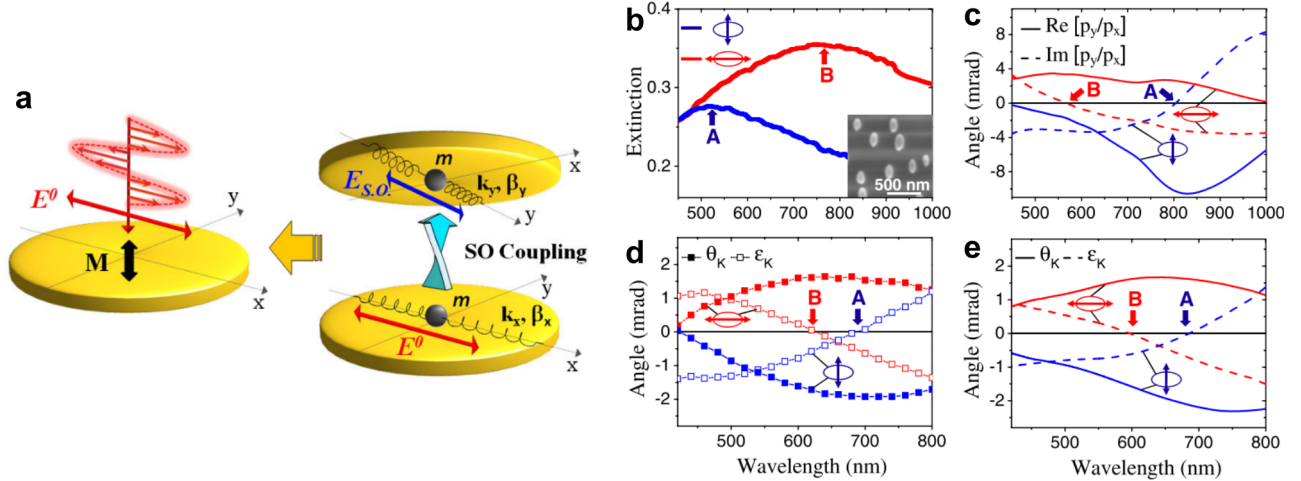


Figure 4.10: (a) Ferromagnetic nanodisks described by two orthogonal electric dipoles modeled as two damped harmonic oscillators. These latter are characterized by their spring constants  $k$  and their mass  $m$ . (b) Extinction spectra of elliptical magnetic nanostructures for the two main directions of polarization. (c) Calculated Kerr angle as function of the wavelength for the same system. (d) Corresponding Kerr angle spectra. (e) Calculated Kerr angle as function of the wavelength considering the effect of glass substrate. Figure adapted from reference 310.

Then Floess *et al.* developed a full analytical model involving a coupled oscillator to describe the MO activity of hybrid magnetoplasmonic system consisting of a 1D wire-based Au grating on top of a dielectric continuous film<sup>352</sup>. In comparison to noble metals based nanostructures, widely used magnetic materials exhibit large dissipative losses resulting in huge interest in using hybrid magnetoplasmonic structures. This finding led some research groups to the investigation of MO activity of Au/Co/Au trilayers<sup>353–355</sup>, nanosandwiches<sup>356</sup> and nanorods<sup>357</sup>. Other approaches considered Co-noble metal core-shell particles<sup>358,359</sup>, hybrid metasurfaces<sup>360</sup> or covering a magnetic dielectric continuous film by a periodic arrangement of noble metals nanostructures<sup>361–364</sup>. Another way to improve the  $Q$ -factor of the resonance combined with a stronger coupling between the two orthogonal electric dipoles is to arrange the magnetic nanoparticles into periodic arrangements<sup>220–222,248,250,365</sup> or the use of 3D ferromagnets<sup>366</sup>. In like manner as Liu *et al.*<sup>168</sup>, proximity of nanoparticles can also give rise to a strong near-field interaction leading here to substantial MO effect<sup>367–370</sup>.

## CHAPTER 4. MAGNETOPLASMONIC, A CONSTANTLY EVOLVING TOPIC

---

In particular, systems consisting of periodic structures of metal and/or dielectric materials that can launch SPPs belong to the family of magnetoplasmonic crystals (MPC). It has been shown that T-MOKE signal can be significantly enhanced by all metallic ferromagnetic 1D grating<sup>371,372</sup>, hybrid magnetic grating 1D grating<sup>373</sup>, Au/Co/Au multilayer<sup>354,374–376</sup>, nanocorrugated thin films<sup>377,378</sup>. These geometries also allow L-MOKE signal enhanced at plasmon resonance<sup>379</sup>. The family of MPC also contains the metasurfaces<sup>348,360</sup>. Inherent losses coming from the metallic ferromagnetic materials favor the use of low-loss dielectric magnetic materials<sup>361,364</sup>. A more exotic investigation has been proposed by Kalish *et al.* in 2018 with a magnetoplasmonic quasicrystal<sup>380</sup>. Indeed, after depositing an Au layer on a magnetic dielectric continuous film, they etched selectively the capping layer to create a sequence of slits reproducing a Fibonacci chain. Structures corresponded either to 0 or to 1. Then the whole system could exhibit several plasmon resonances giving more freedom to enhance T-MOKE signal.

We want to stress the importance of periodic arrangements of metallic nanostructures, made of antidots or nanoparticles, since they exhibit SLRs and SPPs, promising for enhancing MO effects. These kind of geometries strike to the very heart of this thesis. The first configuration consists of perforating periodically the magnetic film giving rise of for the instance widely used hexagonal antidot arrays<sup>255,381–383</sup>. The field enhancement within the magnetic system impacts directly the MO reflection coefficients  $r_{sp}$  and  $r_{ps}$  that we detail in Chapter 3 so that Kerr rotation is significantly increased. The opposite approach which also induces SLRs is to arrange a periodic arrangement of magnetic metallic nanoparticles<sup>248,273,279,365</sup>. Kataja *et al.* stressed in 2015 that the excitation of SLRs in such systems also enhanced MO activity. More than that, by breaking the array geometry, they pointed out that the position of the SLR is determined, for a given nanodisk size, by the lattice period orthogonal to the incoming electric field polarization. That is why Figure 4.11 presents redshifted SLRs for greater orthogonal period while varying longitudinal period does not affect the position of the resonance. This important result is in line with the work of Kravets *et al.* that suggests that probing the same kind of metasurface with  $p$ -polarized light at oblique incidence should not affect the position of SLRs while  $s$ -polarized light splits. The underlying physics is an additional phase term along the radiation direction for  $s$ -polarized source while this latter occurs along the non-radiative direction for  $p$ -polarized source. This means that only  $s$ -polarized light whose polarization axis is orthogonal to the plane of incidence breaks the symmetry and impact the spectral position of SLRs. These concepts are key ingredients to evidence magnetism-induced SLRs, detailed in Chapter 7.

We would like to make these recent developments in perspective with societal needs. First of all, since future magnetism-based information need faster manipulation of magnetization with

higher energy efficiency, it seems that the integration of magnetoplasmonics in all-optical magnetic recording platforms should fulfill these needs. From one side, plasmonics gives opportunity to write information by means of light at nanoscale with significantly lower threshold fluence. From another side, the MO activity enhancement at resonance could provide a reliable way to get strong readout sensitivity. These points will be developed in Chapters 6 and 7. The applicability of such systems is even more general. Indeed magnetoplasmonics can be also dedicated to chemical and biological sensing in which enhancing the reflecting MO signal paving the path for the new generation of highly sensitive biotechnologies<sup>355,384–392</sup>.

### 4.5 Conclusion

We revealed how plasmonics and ultrafast magnetism can be combined as part of the development of photonic platforms for the next generation of heat-assisted magnetic recording technologies. In particular we showed that magnetoplasmonics can associate energy efficient all-optical magnetic reversal with strong reliable readout sensitivity since plasmonics enhance MO effects. We aim in this thesis to intervene in two aspects of HAMR technologies: the granular media via the excitation of SLRs in periodic arrays of magnetic nanodisks and the heat sink layer via a study of the impact of heat sink layers on the maximum laser pulse duration for which AO-HIS is achievable. We explain in the next chapter the experimental and numerical methods we used to lead these works.

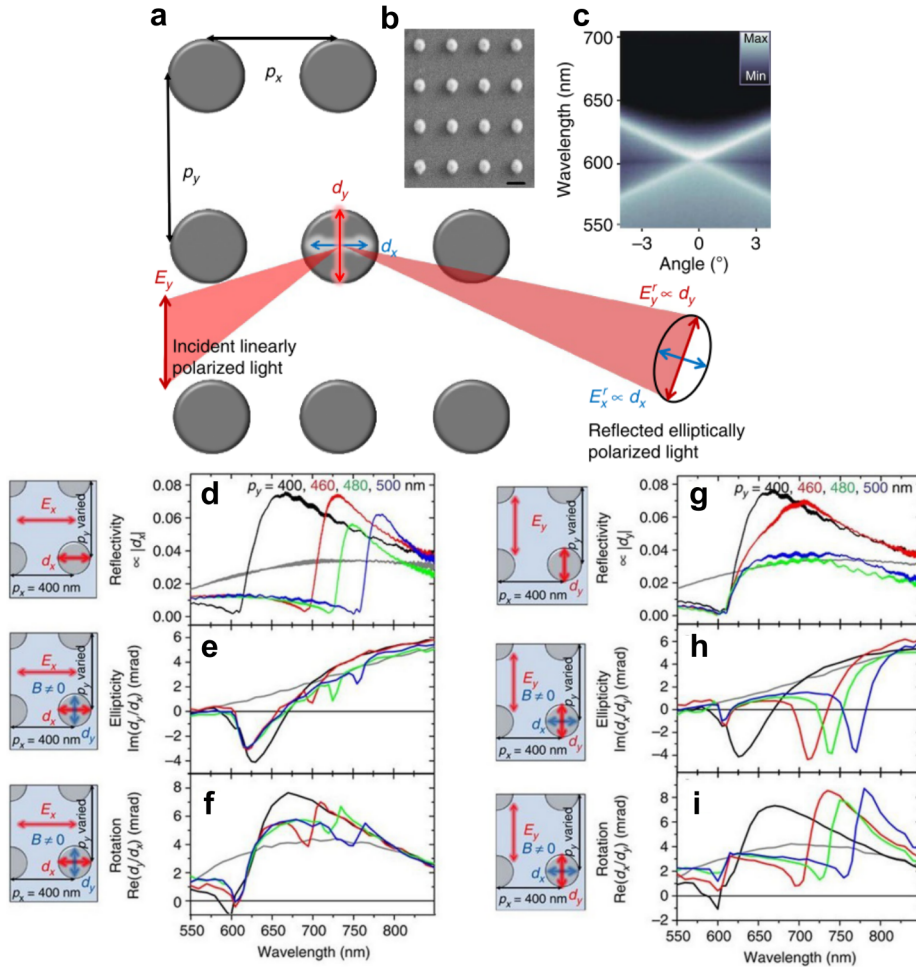


Figure 4.11: (a) Sketch of the periodic array of magnetic nanodisks. The incident electric field comes with only  $y$  component and induces two orthogonal electric dipoles within the magnetic nanostructures, a pure optical  $d_x$  and a MO  $d_y$ . (b) SEM image of the Ni metasurface. The scale bar corresponds to 200 nm. (c) Optical transmission spectra of an array with a unique lattice period of 400 nm and nanodisk diameter of 120 nm for several incidence angles. The DOs  $(+1, 0)$  and  $(-1, 0)$  cross at normal incidence. (d) Reflection, (e) Kerr ellipticity and (f) Kerr rotation spectra probed at normal incidence with incoming polarization  $E_x$  and varying periodic  $p_y$ . (g) Reflection, (h) Kerr ellipticity and (i) Kerr rotation spectra probed at normal incidence with incoming polarization  $E_y$  and varying periodic  $p_y$ . Figure adapted from reference 248.

# Chapter 5

## Methodology

*This chapter dedicated to methodology aims to present the different techniques that have been used for this work. After introducing the thin films deposition methods and the following characterizations, the fabrication techniques to get the nanostructures are detailed. In a third part, the physics of ultrafast lasers is explained as a part of this thesis has been devoted to the development of experimental set-ups involving femtosecond lasers. Finally, we emphasize the finite-element method that we used to simulate the optical behaviours of the systems of interest.*



### 5.1 Introduction

All the samples of this work have been grown by DC magnetron sputtering. We explain how they have been characterized with a MOKE magnetometer to ensure they exhibit PMA. Also, since we considered metasurfaces, we present the experimental set ups that allowed us to extract their optical and MO spectra. Also, we explain how we optimized the fabrication technique to get properly defined periodic arrays of nanodisks. Lately we describe the ultrafast lasers that we considered to perform AO-HIS, including the development of an ultrafast laser experiment in which the wavelength of both pump and probe sources is tunable.

### 5.2 Thin films deposition and characterizations

We start this chapter with the thin films deposition techniques and subsequent optical and MO characterizations.

#### 5.2.1 DC sputtering technique

A wide range of thin film deposition techniques exists, including atomic layer deposition, pulsed laser deposition, molecular beam epitaxial, chemical vapour deposition, physical vapour deposition (PVD), etc. In this thesis, we mainly focused on PVD techniques, in particular DC sputtering and e-beam evaporation. The first one consists of ejecting atoms from a pure element "target" by the bombardment of high-energetic ions from Ar inert gas, resulting in coatings onto the substrate. The plasma is induced by an applied DC voltage between the target and the anode. A high vacuum is required, around  $5e^{-8}$  Torr, to ensure high quality plasma but also a large mean free path for getting straight line trajectories for the ejected neutral particles. Besides, cooling systems are required to avoid large heat radiation. A way to improve the process is to consider a magnetron as sketched in Figure 5.1. The idea is to insert permanent magnets below the target in order to confine the plasma near the target. Then ionizing collisions with the Ar gas occur more often resulting in a more stable plasma and higher quality coatings. This method has been used for depositing the initial thin films before going to the clean rooms for nanofabrication.

#### 5.2.2 E-beam evaporation

The second main deposition technique involved in this thesis is electron beam evaporation, consisting of evaporating the target material resulting in depositon onto the substrate as sketched



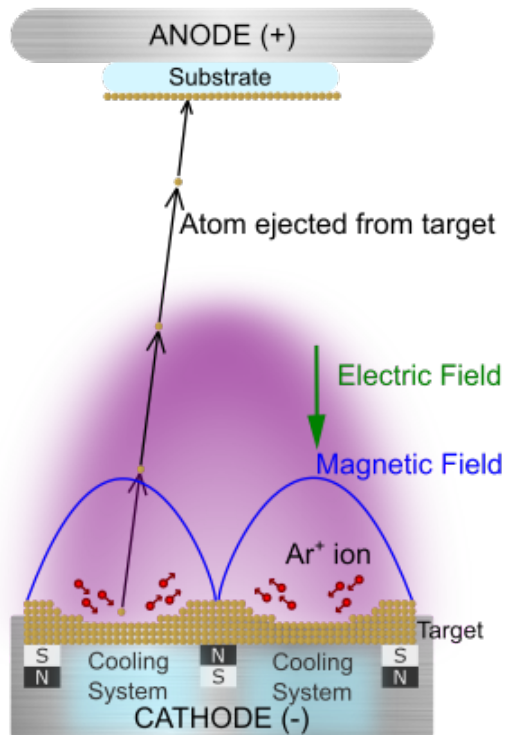


Figure 5.1: Sketch of DC magnetron sputtering.

in Figure 5.2. More precisely an electron beam coming from a charge tungsten filament bombards the crucible that contains the target material in order to obtain a vapour gas. A high vacuum pressure is also needed, around  $1e^{-7}$  Torr, to ensure high quality deposition and to reduce significantly the melting points. High deposition rates are reachable, ranging from 0.1 nm/min to 100 nm/min. Contamination as well as substrate damages related to heat are limited as heating focuses only on the desired crucible. The deposition rate, that is to say the electron beam power, can be controlled with the help of a quartz crystal. Basically, the crystal oscillation frequency rises as the crystal weight increases due to coating from the crucible on it. This allows a fine control of the deposition rate. This PVD method has been used only for depositing Au and Al, the sputtering technique has been preferred for growing thin films before additional preparation in the clean rooms.

### 5.2.3 MOKE magnetometer

A way to characterize the magnetic properties of thin films is to probe the MOKE as sketched in Figure 5.3.

The charge coupled device (CCD) probes the first and second harmonic MOKE intensities

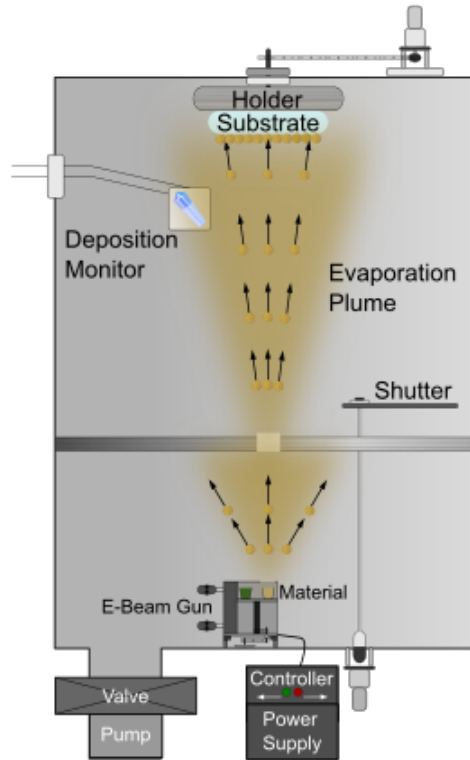


Figure 5.2: Sketch of e-beam evaporation technique.

$I(f)$  and  $I(2f)$  whose origin is details in Appendix B, where  $f$  is the modulation frequency of the photoelastic modulator (PEM). van Genuchten pointed out that the  $2f$ -component of the signal gives the Kerr rotation while the  $f$ -component provides the Kerr ellipticity<sup>393</sup>. This approach is a fast reliable technique to know the magnetic properties of magnetic systems and helped us to know if the as-grown samples exhibit PMA. The light source at *Institut Jean Lamour* consists of He-Ne laser at wavelength of 632.8 nm so that the MOKE measurements are sensitive to the MO response of Co. As stressed by Polisetty *et al.* we work in the configuration for the greatest signal-to-noise ratio (SNR) for P-MOKE and L-MOKE geometries<sup>394</sup>. The transmission axis of the polarizer is at oriented  $90^\circ$  regarding the plane of incidence while the analyzer transmission axis has been fixed either at  $45^\circ$  or at  $135^\circ$ . The lock-in which aims to increase the SNR is set on  $f$  and  $2f$  to measure both Kerr ellipticity and rotation.

Similar measurements have been performed at *Aalto University* with the same kind of experimental techniques as sketched in Figure 5.4. This allows probing the Kerr effect as well as the Faraday effect (in transmission). It should be mentioned that in order to distinguish the rotation and the ellipticity in this latter, two PEM at two different frequencies are involved (50 kHz for the ellipticity, 100 kHz for the rotation), linked to two lock-in amplifiers.

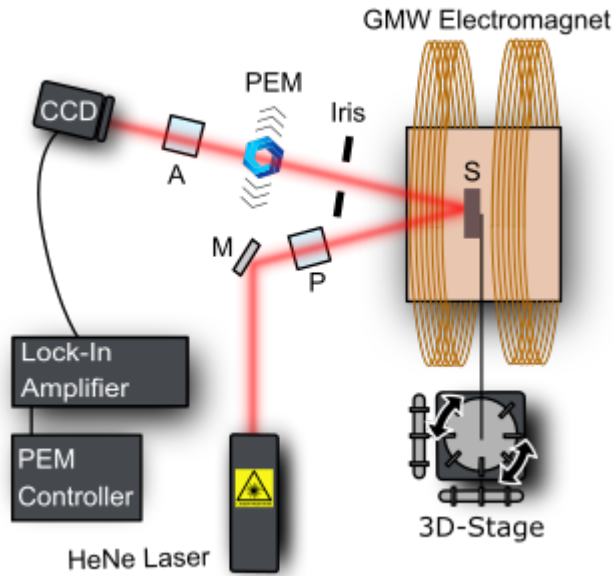


Figure 5.3: MOKE magnetometer at *Institut Jean Lamour* with following elements: analyzer (A); charge coupled device (CCD); polarizer (P); photoelastic modulator (PEM); mirror (M); sample (S).

### Photoelastic modulator

The PEM introduces a time-dependent phase shift oscillating at the frequency  $f$  between the two components of the incoming light polarization<sup>395,396</sup>. We aligned the main axis of the PEM with the directions  $s$  or  $p$ . This means that if the incoming light is  $45^\circ$  polarized, the PEM makes its polarization oscillating between linear and circular states. This tool is crucial to induce first and second harmonic MOKE signals.

### Lock-in amplification

Lock-in amplification aims to improve the SNR. This technique is phase-sensitive and allows extracting a signal for a given frequency and phase. The principle consists of multiplying the signal with a reference sine wave at the PEM modulation frequency. After averaging during enough time by propagating through a low-pass filter, only components of the output signal with the same frequency as the reference signal remain and most of components related to noise are suppressed.

## 5.2.4 Measurement of optical spectra

The optical response of the metasurfaces has been carried at *Aalto University* by measuring

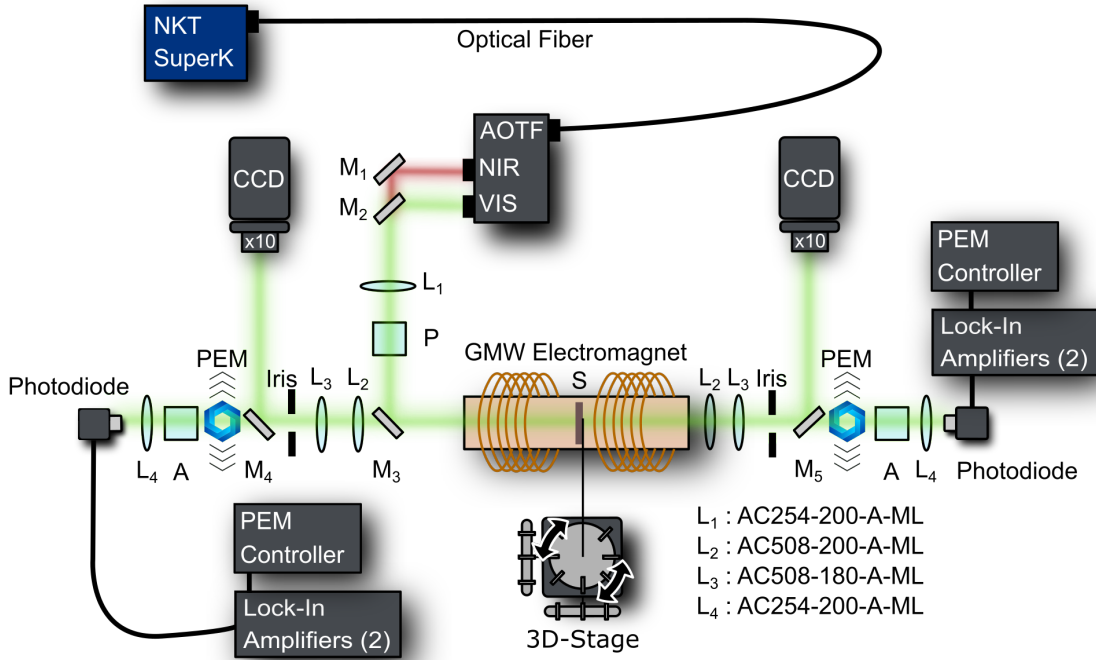


Figure 5.4: MOKE and MOFE magnetometer at *Aalto University* with following elements: analyzer (A); charge coupled device (CCD); lens (L); polarizer (P); photoelastic modulator (PEM); mirror (M); sample (S).

the reflection and transmission spectra. We used index matching liquid to avoid strong refractive index mismatch between the substrate and the surrounding media so that the system of interest is embedded in homogeneous media. The experimental set-up, that involves an NKT SuperK EXW-12 supercontinuum laser as a light source linked to an acousto-optical tunable filter (AOTF), is sketched in Figure 5.5. Even if the wavelength can be tuned from 450 nm to 2000 nm, the sensitivity of the photo-diode allows relevant measurements between 500 nm and 1100 nm.

For instance, for an intensity reflected by the periodic array  $I_r$ , the resulting reflectivity  $R$  is given by

$$R = \frac{I_r - I_d}{I_{ref} - I_d} \quad (5.1)$$

where the reference signal  $I_{ref}$  is the substrate reflected signal and  $I_d$  the dark current signal of the detector. The silver D-shaped mirror  $M_3$  permits to probe either the reflectivity or the transmittivity. CCD cameras associated to a x10 objective help to visualize the systems while

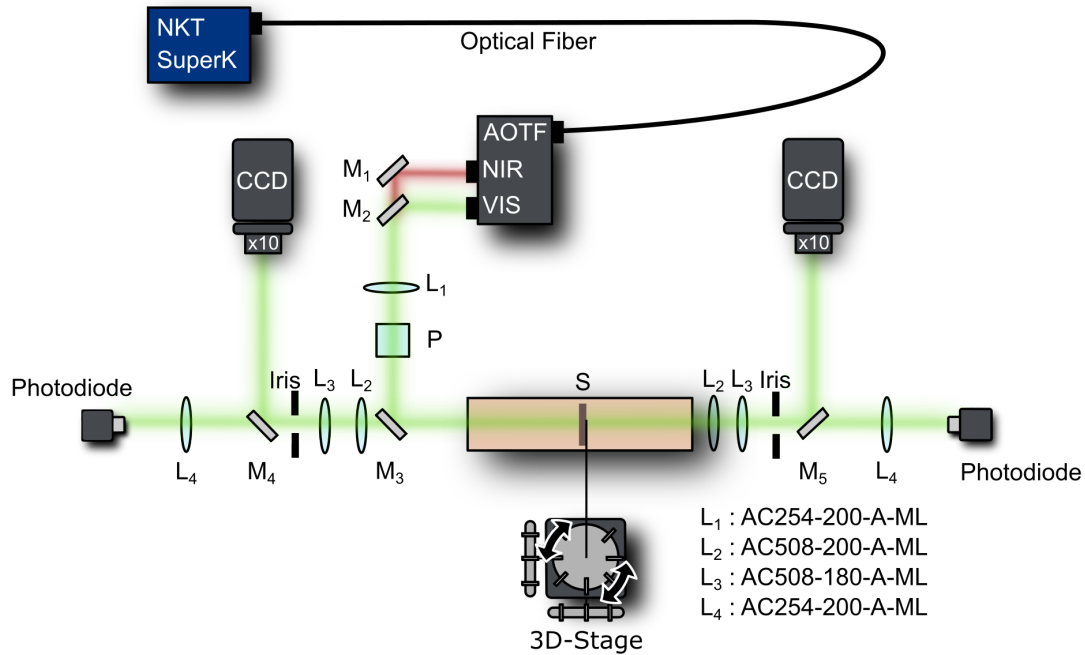


Figure 5.5: Optical measurements at *Aalto University* with following elements: charge coupled device (CCD); lens (L); mirror (M); sample (S).

the photodiodes measure the signals.

## 5.3 Fabrication techniques

Fabricating periodic arrays of nanoparticles requires rigor and combines plenty of steps. We favored a top-down approach involving e-beam lithography (EBL), PVD, lift-off and IBE whose parameters have been optimized to obtain structures as alike as we want and as reproducible as possible. An usual fabrication process is illustrated in Figure 5.6.

### 5.3.1 Electron-beam lithography

EBL consists of insulating locally an electro-sensitive material with a focused electron beam. During this thesis, we used a resist made of poly(methylmethacrylate)(PMMA) which is a positive resist meaning that exposing it leads to its removal during the development step. Spin-coating is required for providing uniform resist distribution over the film. Baking is needed to evaporate the remaining solvent but also to relax the accumulated constraints and to improve its

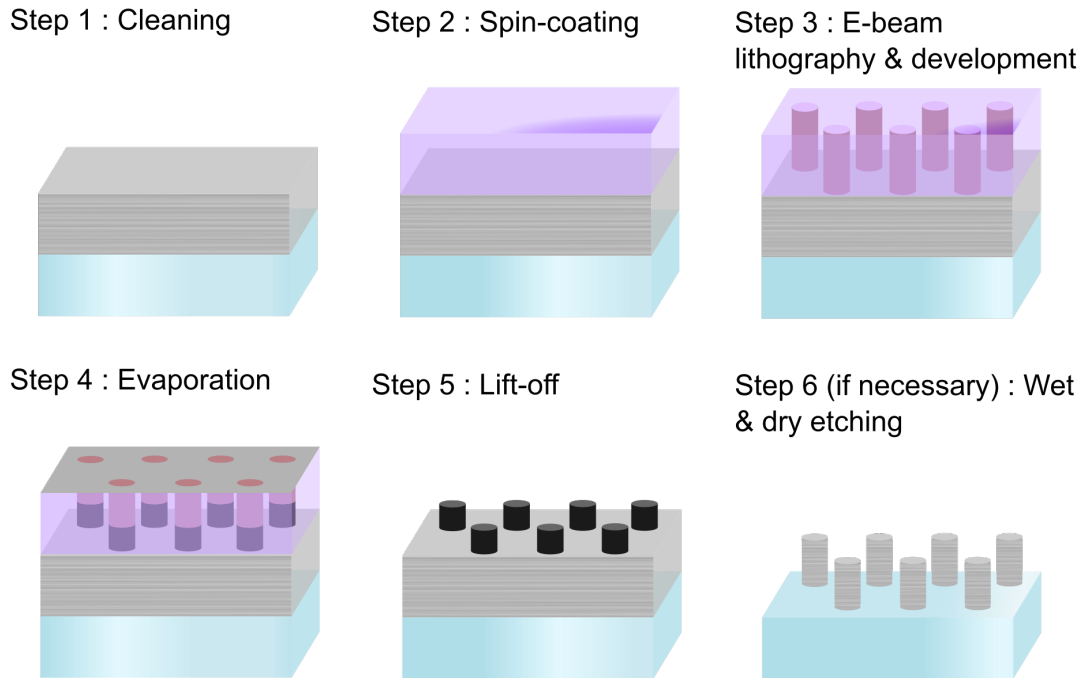


Figure 5.6: Fabrication work-flow.

adhesion to the substrate. The optimal conditions are discussed later. It should be mentioned that the resist should be coated on a conductive layer to avoid charging effects. Indeed when an electron-beam scans an insulator surface, surface charges accumulate resulting in unwanted pattern distortions as the electron-beam is deviated randomly. In this thesis we used a hybrid system that includes a lithography system and a scanning electron microscope (SEM) RAITH 150-2. The system is sketched in Figure 5.7.

### Principle

First electrons are accelerated in the electron gun, usually with a tension of 20 kV in our system. The resulting beam is related to a current that depends on the aperture size. We always used the smallest aperture dimension to reach the best resolution of the set-up, around 40 nm. However, the writing time is increased significantly comparing to a larger aperture. A compromise is necessary between high resolution and fast writing time. Also the electronic lenses focus the electron-beam. They are comparable to optical lenses and are mostly convergent. They have corrections to avoid spherical and chromatic aberrations. In addition, as the electron-beam is constantly emitted, the beam blanker plays the role of a shutter to not make it interact with the resist continuously.

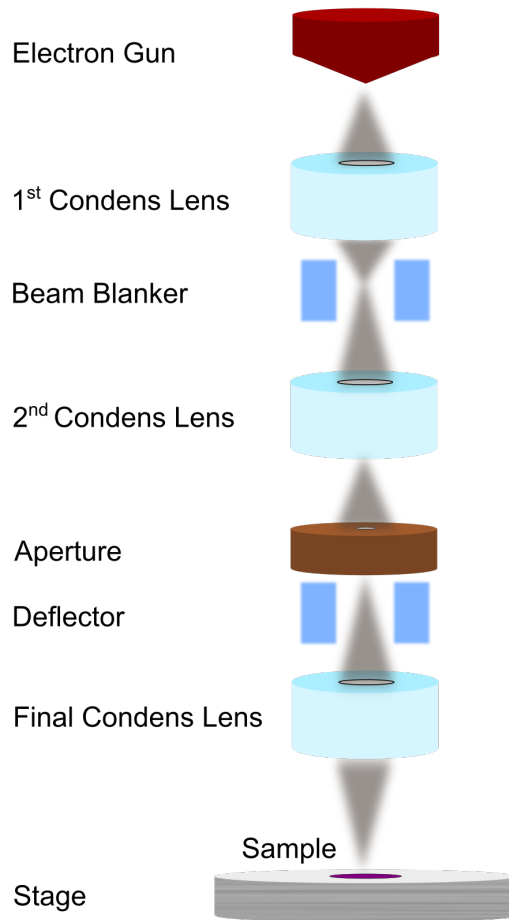


Figure 5.7: Electron-beam lithography.

EBL is a maskless technique (in opposite to optical lithography) and fits with resolution and design flexibility requirements. The main drawback of this technique is the writing time that can last days in some cases. For ensuring high quality patterns, the size of the exposed area, so-called writefield, has to be limited else deflections might occur when patterning away from the centered area as illustrated in Figure 5.8. Thus a large writefield divided in smaller writefields has been preferred when the periodic arrays of nanodisks have been patterned. Besides, we usually worked with a working distance of 9.0 mm. This parameter should be as short as possible in order to improve the resolution at high magnification.

### Adjustments and critical parameters

The most important step during the process is the adjustment of the focus. This is achieved by creating a "point of contamination" (the electron-beam interacts with the resists over a very tiny

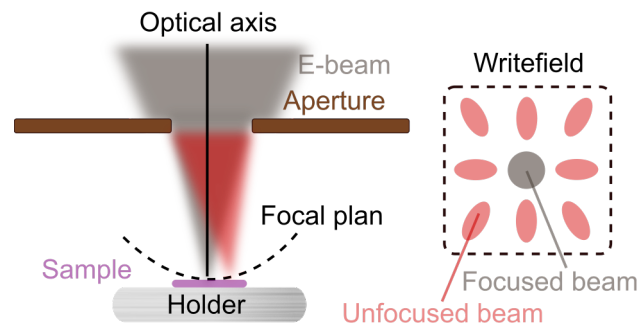


Figure 5.8: Effect of deflection.

area) to control the working distance and to correct the stigmatism. Most of time the focal length is not the same along  $x$  and  $y$  axes of the lenses and it is crucial to solve this issue, in particular when the target pattern consists of periodic arrays of disks else it must impact significantly the shapes and the positions of the plasmonic resonances. A typical adjustment is shown in Figure 5.9.

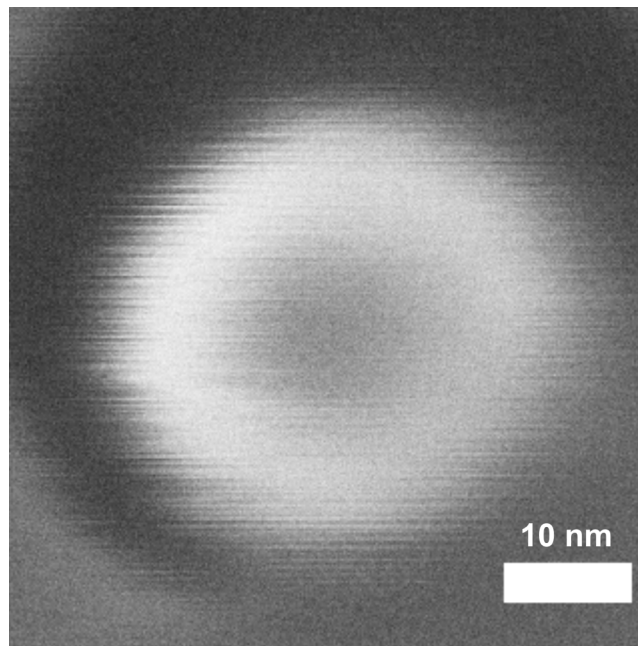


Figure 5.9: Spot contamination for adjusting the focus and the stigmatism.

In this work, we considered only surface dose with a standard nominal dose of  $120 \mu\text{C}/\text{cm}^2$ . Then the strategy consists of moving the electron-beam on the areas that should be exposed on the writfield that is divided into pixels. The beam blarker is closed between two exposed areas and the beam speed is controlled by the step size (distance between each exposed area) and the dwell time (insulation time of a pixel). The dose  $D$ , the beam current  $I$ , the dwell time  $\tau$  and



the step size  $s$  are interconnected following

$$D = \frac{I \times \tau}{s^2} \quad (5.2)$$

The step size has to be small enough to avoid pixelation problems. Typically we used a 5 nm-size for 100 nm-sized structures.

### Back-scattered electrons

The electron-beam interacts with the sample through an interaction volume as sketched in Figure 5.10. Depending on the penetration depth of the primary electrons from the electron-beam, one can extract different signals that are useful for microscopy. For instance back-scattered imaging mode is achieved with the help of reflected high-energy back-scattered electrons (elastic scattering) while secondary electrons are reflected through inelastic scattering.

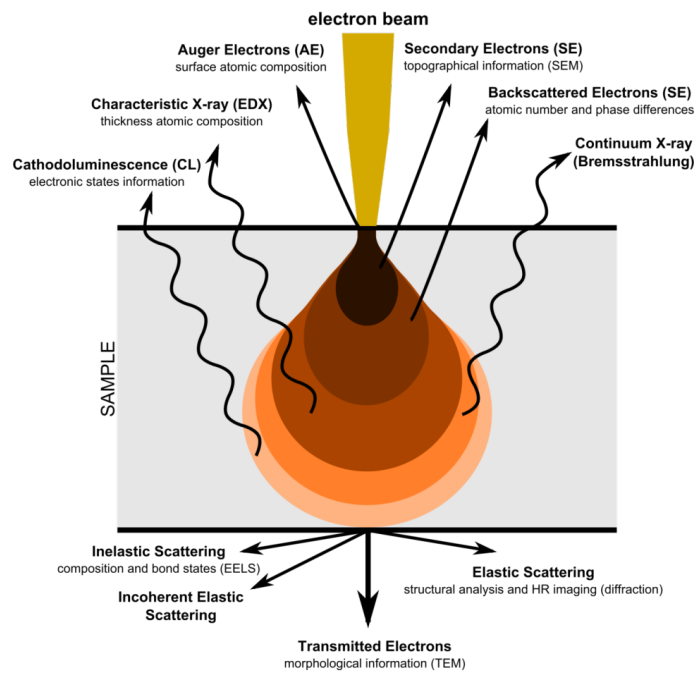


Figure 5.10: Scanning electron microscopy electron-beam profile after substrate interaction. Figure from reference 397.

In particular, during the writing step, back-scattered electrons can induce unwanted effects. Indeed, due to their reflection, they can affect periodic patterns of nanostructures, implying their enlargement or even worse as shown in Figure 5.11. This can be solved in two ways: reducing

## CHAPTER 5. METHODOLOGY

---

the atomic mass of the substrate to induce less reflection and/or decreasing the surface dose to send fewer electrons.

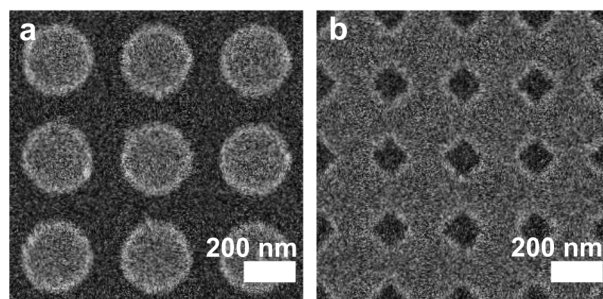


Figure 5.11: (a) Periodic pattern unaffected by back-scattered electrons. (b) Periodic pattern affected by back-scattered electrons.

### 5.3.2 Patterning transfer

Several techniques can be used to transfer the patterns after the lithography step. We considered a subtractive method that we believed more adequate for getting periodic arrays of magnetic disks on glass. We evaporated Al on the sample right after the development step followed by a lift-off step for getting an etching mask. After that we used an ion-beam to etch both the mask and the unprotected full film at the same time as illustrated in Figure 5.6. Most of time wet etching is needed after dry etching to remove the remaining Al.

#### Lift-off

The expected tomography is better obtained with a bilayer resist system. It consists of two layers of resist with different sensitivity resulting in specific shape after development as sketched in Figure 5.12. In this work we used acetone to remove the resist with the help of ultrasounds.

This approach unfavors side effects such as "rabbit ears". Indeed if the sides of the apertures are not hidden by an upper resist layer then additional deposition can occur on the edges of the patterns as in Figure 5.12. However, in this work, most of the samples were significantly sensitive to the temperature. As each layer of resist requires in principle 5 min of baking at 180°C, we decided to develop a method involving a single layer of resist baked at 115°C during 1 min and we managed to limit the side effects on the structures as we deposited the Al etching mask with evaporation. It should be mentioned that the roughness of the sample before spin-coating impacts the lift-off. Indeed a more pronounced roughness increases the contact surface between

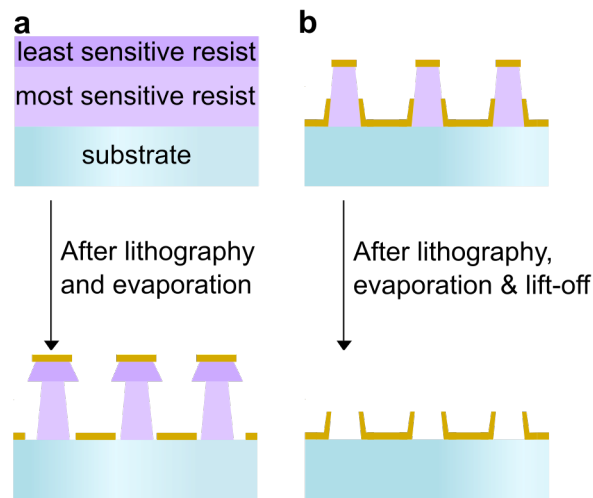


Figure 5.12: (a) Impact of two resist layers on pattern profile, (b) Undesirable side effects induced by the use of a single resist layer.

the capping layer of the multilayer system and the bottom layer of the resist. This makes the lift-off step more difficult. In addition to the quality of the film, the deposition thickness should not exceed 30 % of the global resist system thickness to favor the lift-off.

### Ion beam etching

IBE aims to etch any system, metallic or dielectric, by means of ion beam. We considered this technique in the nanofabrication workflow because it is easier to keep out-of-plane magnetization by patterning thin films than to get perpendicular magnetic anisotropy (PMA) when filling periodic arrays of 100 nm sized-holes of GdFeCo or [Co/Gd/Pt] during the sputtering step. Besides, sputtering step must heat the resists, hardening it and making the lift-off step more complicated to do. IBE involves high energy Ar ions bombarding the films in order to etch both the protected mask and the unprotected continuous films. It provides profiles with great anisotropy with sub-micron resolution. In addition our equipment includes a selected ion monitoring (SIMS) that plays the role of a mass spectrometer. Thus etching can be followed in-situ and allows a better control over the time as shown in Figure 5.13. However materials with very close atomic mass can not be distinguished completely such as Si that is the substrate and Al that is the material that composes the etching mask. Most of time dry etching is followed by wet etching to remove the remaining material from the etching mask. We used MF-319 developer that is compatible with plenty of materials while it etches Al with an etching rate around 35 nm/min.

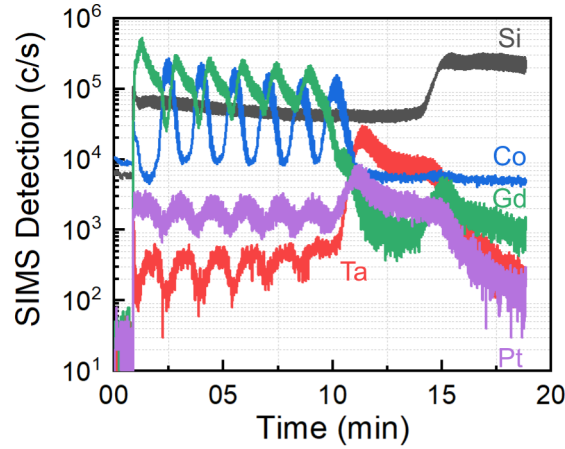


Figure 5.13: Example of SIMS profile for the system composed of glass//Ta(5 nm)/Pt(5 nm)/[Co(1 nm)/Gd(2 nm)/Pt(3 nm)]<sub>6</sub>/Pt(1 nm).

## 5.4 Ultrafast lasers

AO-HIS experiments have been performed with ultrafast lasers. The opportunity to produce sub-picosecond light pulses opens new paths of ultrafast magnetism, in a time range significantly faster than usual time scales of magnetization dynamics in HDDs. This section aims to present ultrafast laser pulses, the related issues and how to overcome them. Then we will describe the physical principle of ultrafast laser pulse generation. In this work we considered a Ti:sapphire femtosecond laser source with regenerative amplifier and a Yt femtosecond fiber laser with regenerative amplifier and two optical parametric amplifiers (OPA) to tune the light wavelength.

### 5.4.1 Ultrafast laser pulses

Ultrafast laser pulses correspond to light pulses with duration below few picoseconds. They can be described in time domain but also in frequency domain by

$$\tilde{E}(\omega) = \int_{-\infty}^{+\infty} E(t)e^{i\omega t} dt \quad (5.3a)$$

$$E(t) = \frac{1}{2\pi} \int_{-\infty}^{+\infty} \tilde{E}(\omega)e^{-i\omega t} d\omega \quad (5.3b)$$

It comes that for a given duration the pulse is characterized by a spectral bandwidth following<sup>398</sup>

$$\langle \Delta t \rangle = \frac{\int_{-\infty}^{+\infty} t |E(t)|^2 dt}{\int_{-\infty}^{+\infty} |E(t)|^2 dt} \quad (5.4a)$$

$$\langle \Delta \omega^2 \rangle = \frac{\int_{-\infty}^{+\infty} \omega^2 |\tilde{E}(\omega)|^2 d\omega}{\int_{-\infty}^{+\infty} |\tilde{E}(\omega)|^2 d\omega} \quad (5.4b)$$

These standard statistical definitions are interconnected through the quantum mechanical time-energy uncertainty principle

$$\langle \Delta t \rangle \langle \Delta \omega \rangle \geq \frac{1}{2} \quad (5.5)$$

As a consequence the shorter the pulse is, the broader the spectrum is. In principle it is convenient to measure  $\Delta t$  and  $\Delta \nu$  at half-maximum values and to compare their product to a characteristic constant  $K$  that describe the shape of the pulse as

$$\Delta t \Delta \nu \geq K \quad (5.6)$$

$K$  typically reaches 0.142 for Lorentzian shapes and 0.441 for Gaussian shapes<sup>398</sup>. It should be mentioned that expressing the complex electric field in time domain, one can notice a phase term depending on time. That is why the electric field possesses a varying frequency that makes the pulse chirped as shown in Figure 5.14.

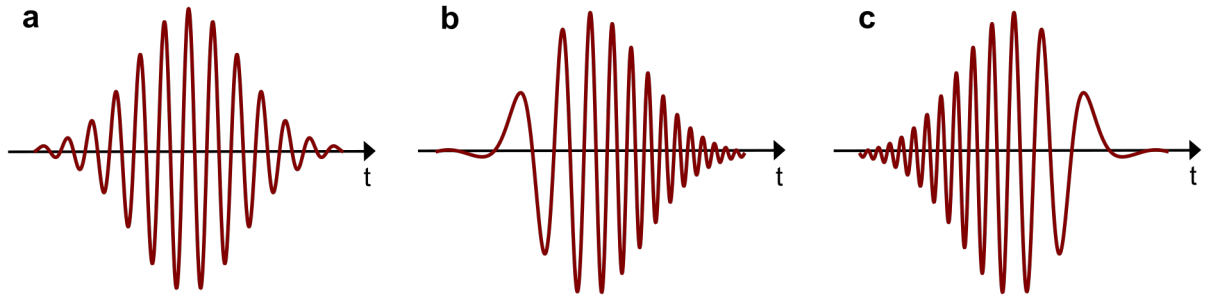


Figure 5.14: (a) Unchirped pulse. (b) Blue-chirped pulse. (c) Red-chirped pulse.

## Dispersion

A broad bandwidth is required to get ultrafast laser pulses. One way is to include a dispersive medium in the laser system. Dispersion compensation is also required. One way is to use grating

## CHAPTER 5. METHODOLOGY

---

compressors as illustrated in Figure 5.15 that consists of a pair of reflective gratings where the first one splits the light into different spectral components while the second one corrects the spatial dispersion and recombines the pulses<sup>399</sup>. This method allows reaching time scales below 30 fs<sup>400</sup>. The two main drawbacks are the high losses induced by the compressor and that only the first order of diffraction is used in this configuration. Replacing grating compressors by prism compressors reduces drastically the losses<sup>401</sup>. However dispersion and recombination efficiency are quite limited comparing to the diffraction gratings. Combining gratings and prisms seems then to be a good compromise<sup>402,403</sup>.

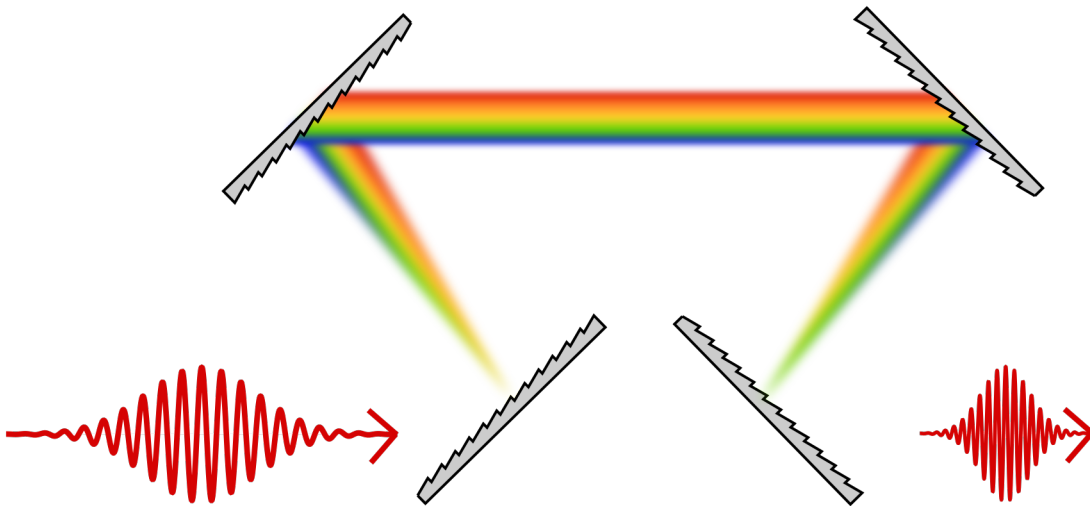


Figure 5.15: Principle of a grating compressor.

Another common way to compensate dispersion is the integration of chirped mirror compressors made of dielectric mirrors<sup>404</sup>. This method consists of stacking different quarter-wave layers so that waves with larger wavelengths can propagate through a longer distance in the system than the ones with shorter wavelengths. As a consequence all the wavelengths are reflected. This technique is efficient but shows several issues such as the strong refractive index mismatch between the mirror system and the top of the stack that may induce unwanted interferences resulting in dispersion oscillations<sup>405,406</sup>. This impedance-matching problem can be solved by considering double-chirped mirrors<sup>407</sup> as depicted in Figure 5.16.

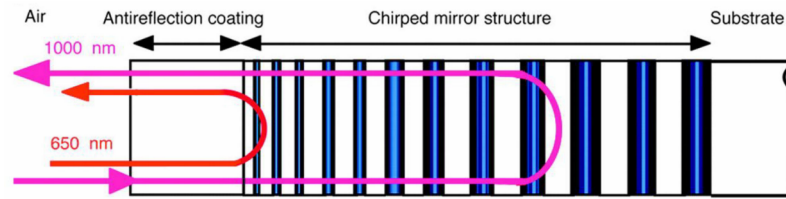


Figure 5.16: Double-chirped mirrors. Figure from reference 407.

### Mode-locking

A widespread method to generate ultrafast laser pulses is to use mode-locking. A gain medium is needed to create ultrashort laser pulses. First Moulton studied Ti:sapphire oscillators in 1986 for generating sub-5 fs laser pulses<sup>408</sup>. The use of gain medium is justified by the Kerr-lens mode-locking that is based on intensity-dependent refractive index. Since the center of the gaussian beam is more intense than its edge, it will propagate differently resulting in the excitation of multiple modes. These latter oscillate independently in a simple Fabry-Perot laser cavity. If the corresponding phases of the modes are random, only noise emitted but locking the phases resulting in constructive interferences creating a train of intense pulses with a characteristic repetition rate linked to the cavity round-trip as shown in Figure 5.17. The higher the number of modes is, the faster the resulting pulse is.

In case of passive mode-locking, a saturable absorber is required in order to selectively transmit high intensity light. As a consequence, continuous wave (CW) experiences constant absorption losses while the pulse will briefly saturate the absorber resulting in low losses for the most intense part of the pulse. Thus the saturable absorber plays the role of a shutter whose activation is induced by the pulse itself. Active mode-locking involves electronically based shutters with a slower modulation rate than in passive mode-locking. Indeed it consists of modulating the signal at the repetition rate with the use of a shutter that is synchronized with the round trip time of the pulse in the system.

### Chirped-pulse amplification

One efficient way to generate ultrafast high energy light pulse is the so-called chirped-pulse amplification (CPA) awarded by a Nobel prize in Physics in 2018<sup>409</sup>. This technique consists of stretching the pulse in time before amplification in the gain medium then to compress the resulting amplified stretched pulse through the help of gratings and/or prisms- based compressors or double-chirped mirrors. In addition, it should be mentioned that the resulting pulse is not as short as the seed pulse, before the stretching. This is due to a narrower spectral bandwidth

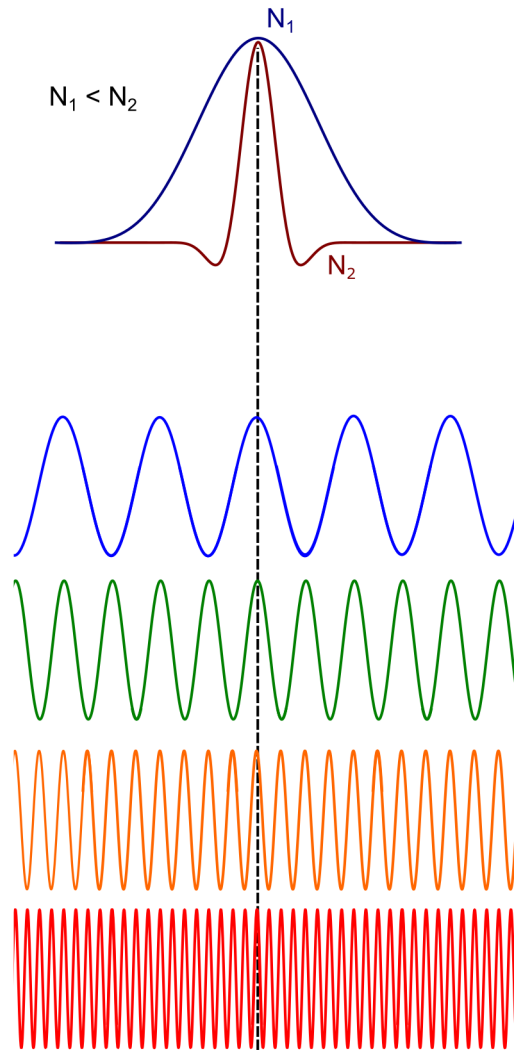


Figure 5.17: Principle of mode-locking.

induced by the bandwidth of the gain<sup>410</sup>.

### Pulse characterization with an auto-correlator

In this work we used various auto-correlators to characterize the ultrafast pulse spatial distribution. Measuring an event requires an event even shorter. The only opportunity that seems reasonable is to use the laser pulse itself to know its pulse duration that is why this method is called auto-correlation. In practice, the pulse is split into two components which experience a delay  $\tau$ . They propagate through a non-linear optical crystal then are recombined on a detector as sketched in Figure 5.18.

The crystal introduces an electric field with a frequency twice larger than the incoming light



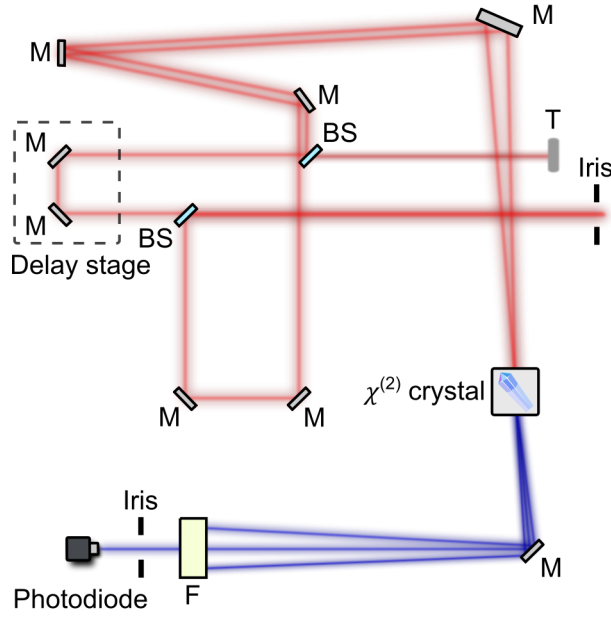


Figure 5.18: Autocorrelator with following elements: beam-splitter (BS); filter (F); mirror (M); target beam alignment (T).

(Second Harmonic Generation) that correlates the electric fields of the components, resulting in an auto-correlated intensity proportional of the intensities of the two components. The system links then the full-width half-maximum (FWHM) of the output signal  $\tau_0$  to the time pulse  $\tau_P$ . The auto-correlated signal takes the form

$$S(\tau) = \int_{-\infty}^{+\infty} I(t)I(t - \tau)dt \quad (5.7)$$

where  $I$  is the intensity of the laser pulse. Knowing the signal  $S$  and assuming a certain pulse shape, it is possible to link  $\tau_0$  and  $\tau_P$ . For instance, in case of gaussian shape,  $\tau_0 = 1.41 \times \tau_P$  and other constants exist for many other different pulse types. Besides the laser beam has to be spatially characterized so we analyzed images of the beam spot as shown in Figure 5.19(a). The time averaged intensity of the EM field, from a superposition of different waves, can be deduced from Poynting's vector in the beam propagation direction  $z$  as

$$I(r, z) = I_0 \left( \frac{w_0}{w(z)} \right)^2 e^{-\frac{2r^2}{w(z)^2}} \quad (5.8)$$

where  $I_0 = \epsilon_0 E_0^2 / 2\mu_0$  is the time averaged intensity at the center of the beam spot when perfectly focused and  $w_0$  the waist radius. At a given distance  $z$  from the focal point and at a distance  $w_z$  from the propagation direction of the light,  $I(w(z), z) = I(0, z)e^{-2}$ . Then we deter-

## CHAPTER 5. METHODOLOGY

mined the diameter of the beam spot with the  $1/e^2$  convention. We combined this measurement with another approach to determine the beam spot size that we detail in Chapter 8.

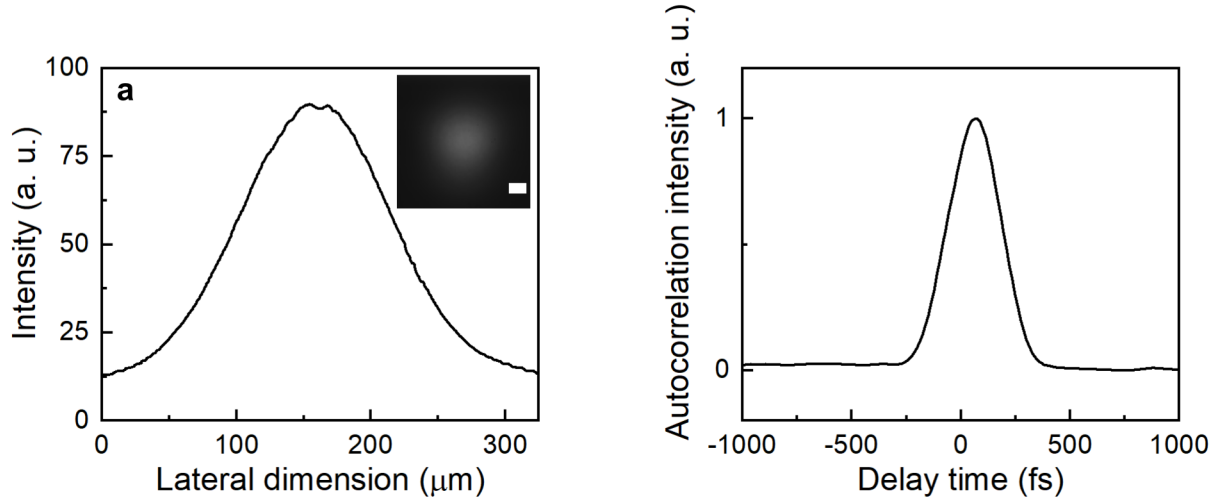


Figure 5.19: Beam profiles. (a) Spatial distribution of the laser beam. Inset shows the corresponding image. Scale bar = 100  $\mu\text{m}$ . (b) 201 fs pulse length with gaussian fit.

### 5.4.2 MOKE microscopy

We used a MOKE microscope to determine if magnetization was switched or not after the action of a single femtosecond laser pulse. Figure 5.20 presents typical AOS MOKE images obtained in the corresponding experimental set-up. The schematic representation does not show laser pumping and amplification and the pulse picker required to provide single pulse. The half wave-plate ( $\lambda/2$  WP) and the polarizer (P) provide a linearly polarized pulse whose fluence is controlled carefully. The light is focused on the sample with the lens ( $L_F$ ) placed on a delay stage so that the size of the beam spot can be tuned. In addition microscopy imaging is made possible with a light emitting diode (LED) whose emitted light is centered at 630 nm. First the incoming light propagates through a Fresnel lens (FL) and then is collimated by a lens (L). The probe source becomes then linearly polarized ( $P_1$ ) and reaches the sample after reflecting partially on the beam-splitter (BS) and going through the objective (O). The filter (F) is a bandpass filter so that only the light from the LED can propagate and CCD alteration related to laser light is avoided.

It should be mentioned that the light coming from LED source propagates through a first polarizer (P) before interacting with the sample then goes through an analyzer as in the MOKE magnetometer (A). If their transmission axis are aligned the CCD probes pure optical signal

while orthogonal geometry, despite it is predicted to give the strongest MO signal, do not let light propagating to the CCD. These optics should be then almost crossed to probe the strongest MO signal. At any pixel of an image, the difference of light intensities for magnetizations pointing upwards and downwards is directly related to the magnetization of the system. We properly determined the scale bars by means of patterned samples with well-known typical dimensions.

Before sending any ultrafast laser pulse to the sample we always take a background image with an homogeneously saturated magnetization. After that we subtract the image after laser excitation by the reference. Knowing the intensity levels for both perpendicular orientations we can deduce if light reversed or not the magnetization of the sample. We processed the raw images with the open source software ImageJ and colored them with the lookup table phase. We consistently attributed the red (blue) color to a magnetization pointing up (down).

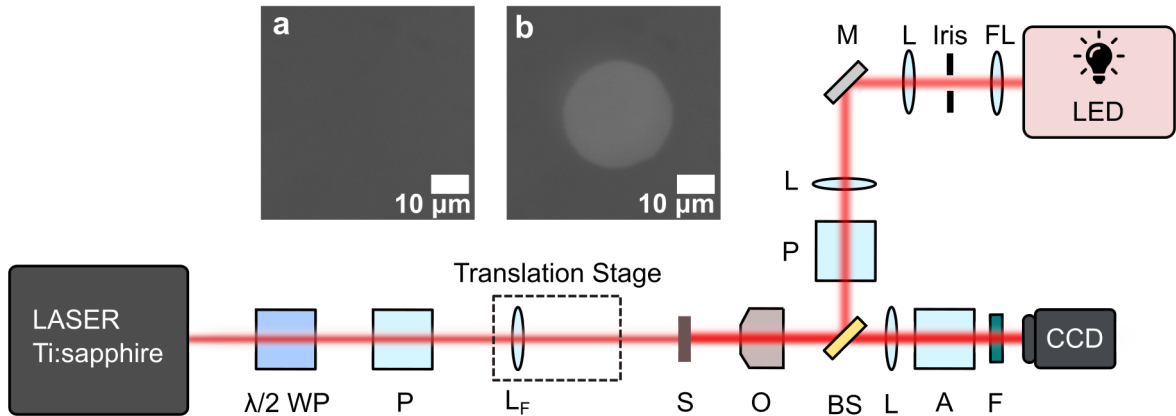


Figure 5.20: MOKE microscopy involving Ti:sapphire laser at *Institut Jean Lamour* with following elements: analyzer (A); beam-splitter (BS); charge coupled device (CCD); filter (F); Fresnel lens (FL); lens (L); lens for focusing the lasser beam ( $L_F$ ); mirror (M); objective (O); polarizer (P); sample (S); half waveplate ( $\lambda/2$  WP). Raw MOKE images of a single GdFeCo layer (a) after saturation and (b) after getting subjected to an ultrafast laser pulse.

### 5.4.3 Time-resolved MOKE microscopy

This subsection retains a line of continuity from the previous one as it highlights the design and development of time, spatial and depth resolved MOKE technique whose pump and probe wavelengths are tunable in visible and infrared ranges.

One way to measure magnetization dynamics is to employ time-resolved magneto-optical Kerr effect (TR-MOKE) whose principle consist of probing MOKE in time while the system is

## CHAPTER 5. METHODOLOGY

excited by external light. This is a so-called pump-probe technique. In practice the laser provides continuously a train of pulses at a given rate and splits the initial beam into two. One of them propagate on a longer optical path so that its arrival is delayed in comparison to the other. In particular, one pulse is the source of the out-of-equilibrium magnetization dynamics, the pump, while the other plays the role of the probe. Both powers are tunable with a half waveplate coupled to a polarizer and the probe power should be fixed. Most importantly, assuming both beams are focused on the sample, the spot corresponding to the probe should be significantly smaller than the one of the pump to guarantee a uniform power during the measurement.

During this thesis we developed a TR-MOKE microscopy technique involving a Yt laser to measure magnetization dynamics as sketched in Figure 5.21. This set-up can also work as a simple MOKE microscopy but unlike the first laser set-up mentioned, the probe consists of the laser source itself and we focus the MOKE images with a lens. In opposite to usual TR-MOKE technique, the probe beam spot must be significantly larger than the pump beam spot to be able to image the magnetic state on a CCD Camera. The insertion of two OPAs allows us to tune the wavelength of both the pump and probe beams. In practice both OPAs provide ultrafast laser pulses whose duration ranges from 100 fs and 200 fs depending on the wavelength.

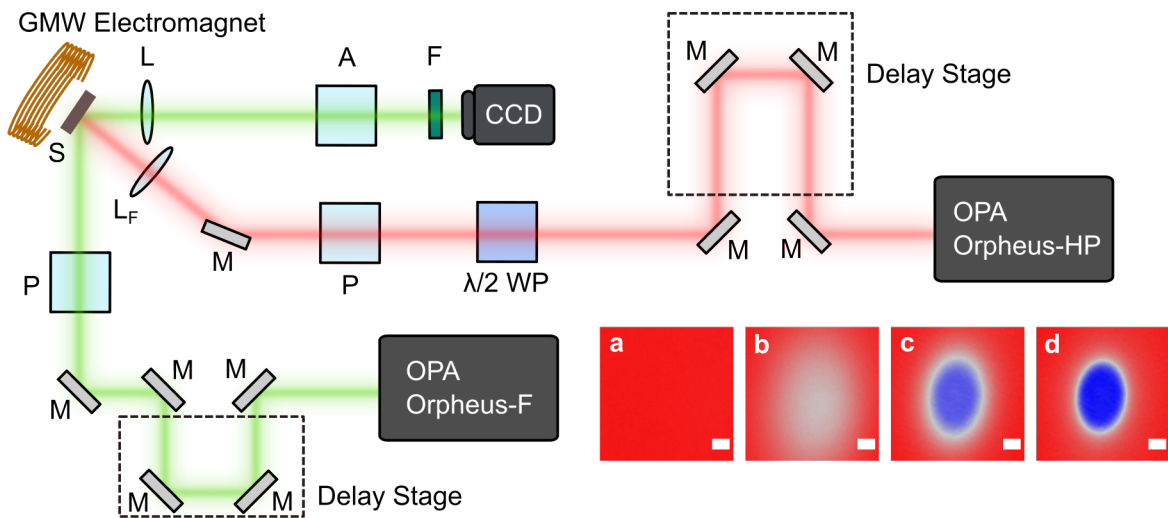


Figure 5.21: Time-resolved MOKE microscope Yt laser at *Institut Jean Lamour* with following elements: analyzer (A); charge coupled device (CCD); filter (F); lens (L); lens for focusing the laser beam ( $L_F$ ); mirror (M); polarizer (P); sample (S); half waveplate ( $\lambda/2$  WP). Processed MOKE images of a single GdFeCo layer subjected to an ultrafast laser pulse for a delay of (a) 0 ps, (b) 0.5 ps, (c) 5 ps, (d) 10 ps. The scale bars correspond to  $20 \mu m$ .

One of the main advantages of TR-MOKE microscopy is that images evidence directly the

impact of defects, dusts but also changes in coercive field in some areas, mostly due to an intense power which damaged magnetically the sample. This method allows a direct comparison with usual static microscopy images. Besides, due to the spatial resolution and the gaussian profile of the optical excitation, it is possible to study a consistent set of power for a given peak power.

An additional quarter waveplate on the path of the probe beam gives the opportunity to selectively measure magnetization dynamics of one magnetic system for samples consisting of two magnetic subsystems using complex MOKE<sup>411</sup>. The fundamental idea of using a quarter waveplate is that we add another degree of freedom that can suppress in principle the magnetic signal of one subsystem. This approach has been widely used already and is very powerful to extract intrinsic contributions<sup>306,412–416</sup>. The combination of several quarter waveplate angles allows to extract the magnetization dynamics of one magnetic subsystem<sup>306</sup>. The development of this experimental set up would not have been possible without the experience of J. Hohlfeld.

It is worth noting that the pump and probe light sources illuminate the sample with an incidence angle close to  $0^\circ$  and  $45^\circ$  respectively. This latter opens new perspectives of measurements of magnetization dynamics of systems with in-plane anisotropy or transition from out-of-plane to in-plane magnetic orientation<sup>417</sup>.

## 5.5 Simulations

We supported some of the experimental results of this work with numerical simulations. For that we considered the finite element method (FEM) implemented in the software COMSOL Multiphysics<sup>®</sup>. The idea of this kind of approach is to discretize a complex system into small 3D elements. This approach is based on a mesh of tetrahedral elements that is very convenient for curved geometries such as a disk or a sphere. Maxwell's equations are approximated by a set of basic functions so that linear equations are solved in each singular element. In this context boundary conditions are necessary at the interface of neighboring elements.

We considered the module `Wave Optics` to first calculate the total reflection, transmission and absorption of periodic arrays of [Co/Gd/Pt] nanodisks on glass substrate and embedded in index matching liquid so that the plasmonic structures are surrounded by a homogeneous medium of refractive index of 1.5. We used different geometries with the nanodisk diameter  $D = 100, 150, 200$  and  $250$  nm and the lattice period  $P = 400, 450, 500$  and  $550$  nm. All the systems have been subjected to the same input power. We assumed a single layer system with an effective refractive index for the entire multilayer stack. This allowed us to simplify the COMSOL simulations.

## CHAPTER 5. METHODOLOGY

---

We detail in Chapter 6 how we measured the effective refractive index. This numerical approach considers one unit cell that is why we applied periodic boundary conditions (Floquet periodicity) on its side to calculate the EM field distribution in periodic arrays of magnetic nanodisks. The light arrives in the cell from the air superstrate at normal incidence and comes out from the glass substrate. We also considered perfect matched layer (PML) domains on top of the air domain and at the bottom of the glass substrate to mimic an open and nonreflecting infinite domain in order to avoid unrealistic reflections in the system. The source was a monochromatic linearly polarized plane wave with  $p$  polarization and we swept its wavelength over a large range.

The mesh involved free triangular elements whose maximum size was 2 nm. The FEM provides the total reflection, transmission and absorption of the system (air+periodic arrays of nanodisks+glass). It is also possible to define a cut plane to obtain the near field distribution of optical fields within and out of the nanodisks. We used this approach for estimating the near field enhancement induced by the excitation of SLRs.

### 5.6 Conclusion

This chapter explained the methodology that conducted this work. We first explained how we grew and patterned the samples. Then we described the different experimental characterizations. After discussing the strategies to induce single ultrafast laser pulses, we detailed the MOKE experiments including the one we developed to tune the pump and probe wavelengths. Finally we emphasized the importance of numerical simulations to support certain experimental results.

## Chapter 6

# Energy efficient single pulse all optical switching

*In this chapter, we experimentally demonstrate energy efficient single pulse switching of  $[\text{Co}/\text{Gd}/\text{Pt}]_N$  multilayer nanodisks by measuring the magneto-optical response of different metasurfaces to different optical excitations. In particular, we show, at the resonance, a fivefold enhancement of optical absorption combined to an improvement of the magneto-optical Faraday effect by a factor of more than 50. The position, width and amplitude of the collective resonances strongly depend on the design of the periodic arrays of magnetic nanodisks. This opens the way to the development of all-optical magnetic recording considering metasurfaces whose energy efficient information writing and read-back sensitivity are modulated by the pump wavelength.*

### 6.1 Motivations

The ability to control magnetization with arbitrary polarized ultrafast laser pulses and its potential applicability paved the path for energy efficient ultrafast magnetic recording<sup>8,123</sup>. In particular Radu *et al.* showed that magnetization of GdFeCo alloys could be deterministically reversed with linearly polarized single laser pulse leading to the class of AOS so-called AO-HIS<sup>8</sup>. This latter is believed to be driven by a pure thermal effect. This phenomenon has been also observed in Co/Gd multilayers<sup>10</sup> as well as Tb/Co multilayers<sup>134</sup> and Mn<sub>2</sub>Ru<sub>x</sub>Ga alloys<sup>132</sup>. Co/Gd is a system of primary interest since AO-HIS can be observed without any composition restrictions<sup>10,136</sup>, promising for wafers manufacturing. Besides magnetic properties remain unchanged after annealing making easier the production of nanostructures of opto-controllable magnetic tunnel junctions<sup>418–420</sup>.

To compete with areal density of current HDDs in the market, AO-HIS needs to be achievable in nanostructures whose writing resolution is not bounded by the diffraction limit. In this perspective, we aim in this chapter to provide a new approach for energy efficient ultrafast all-optical magnetic recording in nanoobjects<sup>421</sup>. After showing that we can reduce the minimum laser fluence by 400 % in [Co/Gd/Pt] metasurfaces for performing AO-HIS, we point out that these nanostructures exhibit a stochastic switching. Also, we highlight that the excitation of SLRs in such geometries can lead to strong enhancement of MO activity with a Faraday readout sensitivity increased by 5000 % compared to the unpatterned film.

### 6.2 Energy efficient all-optical magnetization switching with plasmonics

We studied the samples Pt(1)/[Pt(3)/Gd(2)/Co(1)]<sub>N</sub>/Pt(5)/Ta(5)//glass with  $N$  varying from 1 to 6 and the numbers in parenthesis in nm. From the continuous films we prepared square arrays of nanodisks through a top-down approach as detailed in Figure 5.6. Figure 6.1 presents the magnetic properties of the [Co/Gd/Pt]<sub>N</sub> unpatterned continuous films and corresponding metasurfaces using the polar MOKE and MOFE, respectively. The coercive field of the thin films ranges from 3.2 mT to 9.5 mT for  $N = 1, 2, 3$  and 4. From  $N = 5$  and 6 the remanence approaches 0 due to domain formation as shown in magnetic force microscopy (MFM) images. In parallel, all [Co/Gd/Pt]<sub>N</sub> disks exhibit perpendicular magnetic anisotropy but require significantly higher magnetic field to be magnetically switched. We attribute this behaviour to lower probability of domain nucleation within the disks. We could not perform MFM on periodic ar-



## CHAPTER 6. ENERGY EFFICIENT SINGLE PULSE ALL OPTICAL SWITCHING

rays of  $[\text{Co}/\text{Gd}/\text{Pt}]_{N=5,6}$  nanodisks to confirm maximal remanence in such systems but domain sizes extracted from MFM images of the corresponding continuous films suggest that even the largest disks for  $N = 5$  and  $6$  are still single domain. Figures 6.1(g-j) prove that Co/Gd multilayer can overcome annealing. This material is ideal in a sense it is not strongly sensitive to its thermal history while other systems such as GdFeCo can lose enough remanence even after a soft baking so that AO-HIS can not be observed.

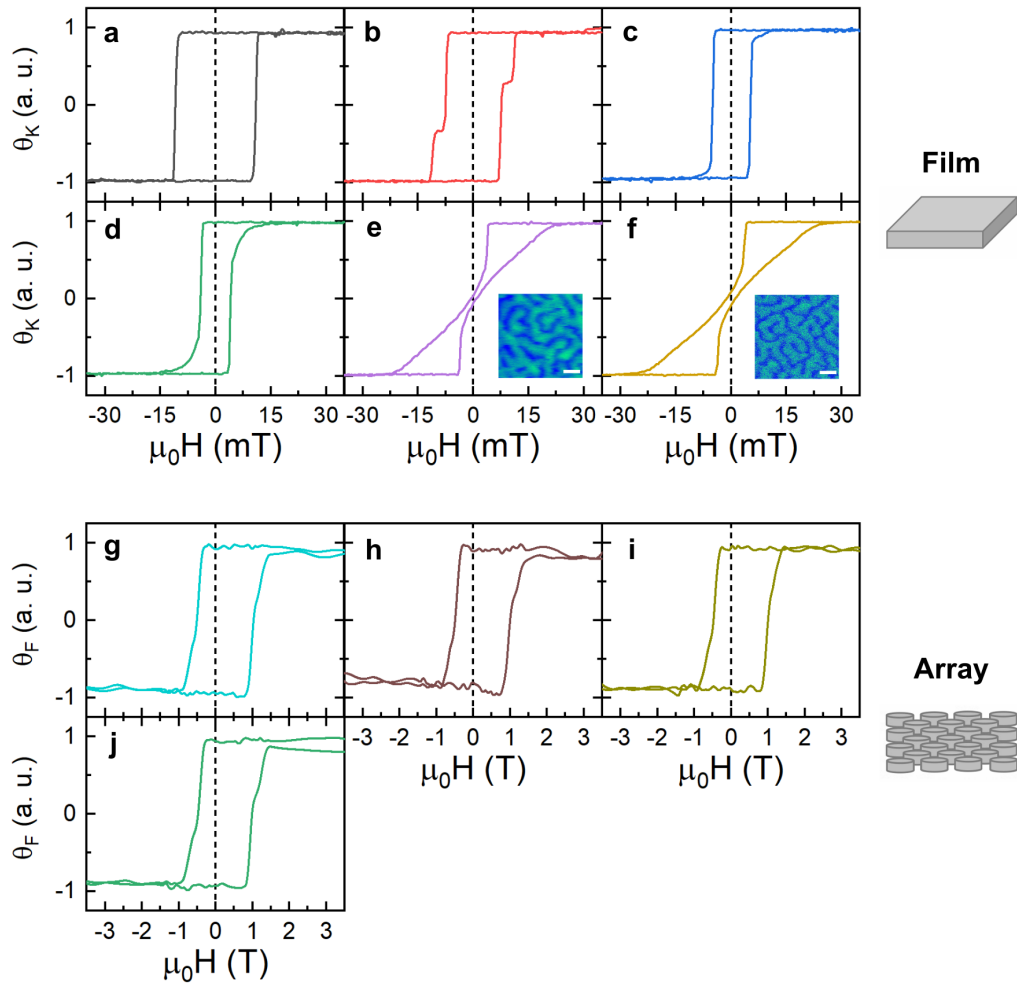


Figure 6.1: Hysteresis loops (Kerr rotation) of  $[\text{Co}/\text{Gd}/\text{Pt}]_N$  continuous films for (a)  $N = 1$ , (b)  $N = 2$ , (c)  $N = 3$ , (d)  $N = 4$ , (e)  $N = 5$  and (f)  $N = 6$ . Hysteresis loops (Faraday rotation) of periodic arrays of  $[\text{Co}/\text{Gd}/\text{Pt}]_N$  nanodisks with g)  $D = 100$  nm, (h)  $D = 150$  nm, (i)  $D = 200$  nm, (j)  $D = 250$  nm. Insets show MFM images of  $[\text{Co}/\text{Gd}/\text{Pt}]_N$  thin films for (e)  $N = 5$  and (f)  $N = 6$ . The images were recorded under zero magnetic field. The scale bars correspond to 1000 nm.

Recent work from Kools<sup>422</sup> and further discussions with the group of TU Eindhoven lead

## CHAPTER 6. ENERGY EFFICIENT SINGLE PULSE ALL OPTICAL SWITCHING

to the conclusion that capping layer can give a complete different story. In particular Pt tends to induce intermixing with Gd layer that is why the group of TU Eindhoven prefers to use TaN capping layer instead<sup>422–424</sup>. Our main argument for using Pt in our stack is to strengthen PMA and then to preserve it during and after clean room preparation.

We chose the sample with  $N = 2$  to investigate the influence of plasmon excitation on AO-HIS. We justify this decision by a good compromise between achievable toggle switching in the thin continuous film for the whole wavelength range of study for AO-HIS and strong MO activity since all the data analysis to state for light-induced magnetization reversal or not is based on MOKE images analysis. We led the AO-HIS experiments using 216 fs laser pulses induced by a Yt fiber laser with regenerative amplifier at wavelengths varying from 650 nm to 1000 nm. We considered four different nanodisk diameters as well as four different array periods. This allowed us to strengthen or weaken the SLRs by aligning more or less LSPRs of single nanodisks with the resonance of the arrays as shown in Figure 6.2.

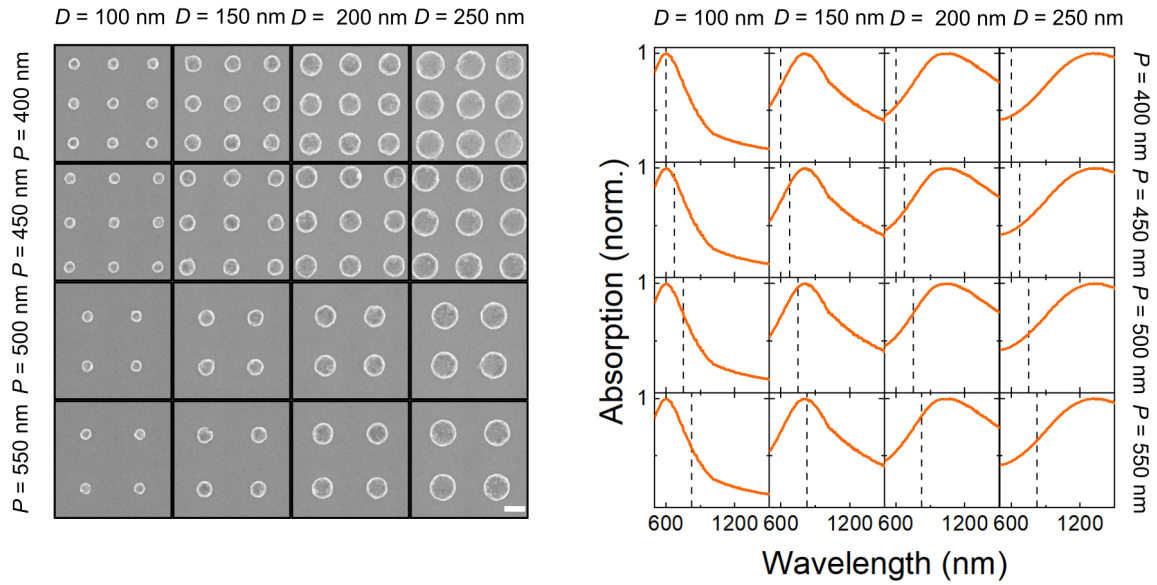


Figure 6.2: SEM images of  $[\text{Co}/\text{Gd}/\text{Pt}]_5$  nanodisk arrays with corresponding simulated normalized absorption of a single nanodisk embedded in an homogeneous medium of refractive index 1.5. The dashed lines represent the different array resonances. The scale bar corresponds to 200 nm.

We simulated by means of the FEM the optical behaviour of single disk with  $D = 100, 150, 200$  and  $250$  nm embedded in a homogeneous surrounding medium of refractive index of 1.5. In particular, each peak of absorption corresponds to the spectral position of the LSPR. The ideal system has its LSPR aligned with the array resonance. One can notice that the LSPR redshifts when  $D$  increases while the array resonance reshifts when the lattice period  $P$  increases. The

## CHAPTER 6. ENERGY EFFICIENT SINGLE PULSE ALL OPTICAL SWITCHING

16 different conditions of  $D$  and  $P$  then lead to 16 different SLRs. We prepared the six samples, corresponding to the six number of repetitions, during the same period and we provide the SEM images for all of them in Appendix C. For instance, for  $P = 500$  nm, if we consider the diameters  $D = 150, 200$  and  $250$  nm, we would expect a weaker coupling when  $D$  increases as suggested by Figure 6.2. We investigated the 16 conditions and the six samples by measuring the extinction (absorption and reflection) as function of the wavelength at *Aalto University*. Since the SLR mode absorbs light more than it scatters<sup>425,426</sup>, the extinction measurement is a good measure of the light absorption by the magnetic metasurface. We expect the enhancement of this latter on resonance to support the AO-HIS so that the threshold fluence for observing light-induced magnetization reversal should be lower than the one for the continuous film.

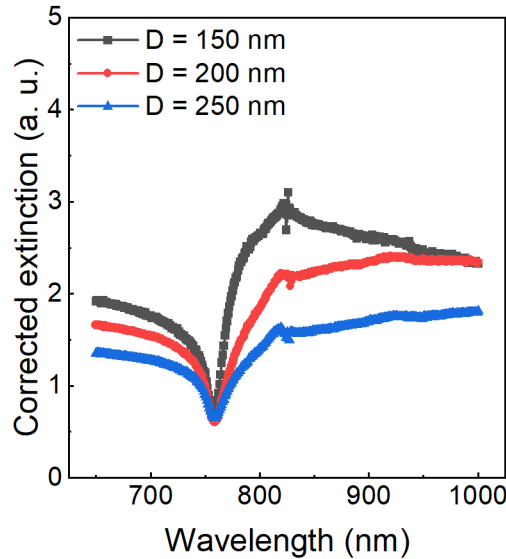


Figure 6.3: Corrected extinction spectra of  $[\text{Co/Gd/Pt}]_2$  nanodisk arrays with  $D = 150, 200$  and  $250$  nm and  $P = 500$  nm. We define his quantity by the ratio between the raw extinction and the filling factor of the array.

Figure 6.3 presents extinction spectra of  $[\text{Co/Gd/Pt}]_2$  nanodisk arrays with  $D = 150, 200$  and  $250$  nm and  $P = 500$  nm. We scaled the three spectra by the corresponding filling factor of each periodic array. The filling factor is the ratio between the area covered by the nanodisks and the total area. In this way we noticed that the system that should lead to the greatest radiative coupling according to Figure 6.2 actually exhibit the narrowest SLR combined with the largest local absorption enhancement. Thus this kind of system seems promising for energy efficient AO-HIS since it is driven by a pure thermal effect. We provide the raw extinction spectra of all

## CHAPTER 6. ENERGY EFFICIENT SINGLE PULSE ALL OPTICAL SWITCHING

the systems in Appendix D. We summarize in Table 6.1 the filling factors for all the metasurfaces studied in this work.

	$D = 100 \text{ nm}$	$D = 150 \text{ nm}$	$D = 200 \text{ nm}$	$D = 250 \text{ nm}$
$P = 400 \text{ nm}$	4.89 %	11.0 %	19.6 %	30.6 %
$P = 450 \text{ nm}$	3.87 %	8.71 %	15.5 %	24.1 %
$P = 500 \text{ nm}$	3.13 %	7.03 %	12.5 %	19.5 %
$P = 550 \text{ nm}$	2.59 %	5.82 %	10.4 %	16.2 %

Table 6.1: Filling factors of the metasurfaces studied in this thesis.

Then we conducted AOS experiments with a pump wavelength ranging from 650 nm to 1000 nm with a 25 nm step. MOKE images of light-induced magnetization reversal for both the  $[\text{Co}/\text{Gd}/\text{Pt}]_2$  film and a  $[\text{Co}/\text{Gd}/\text{Pt}]_2$  metasurface with  $D = 150 \text{ nm}$  and  $P = 500 \text{ nm}$  are shown in Figure 6.4 for different laser fluences and two wavelengths 650 (off resonance) and 825 nm (on resonance). We noticed that the metasurface switches at considerably smaller energy than the unpatterned film, even off resonance. We define the gain of energy as the ratio between the AO-HIS threshold fluence of the continuous film and the AO-HIS threshold of the magnetoplasmonic metasurface.

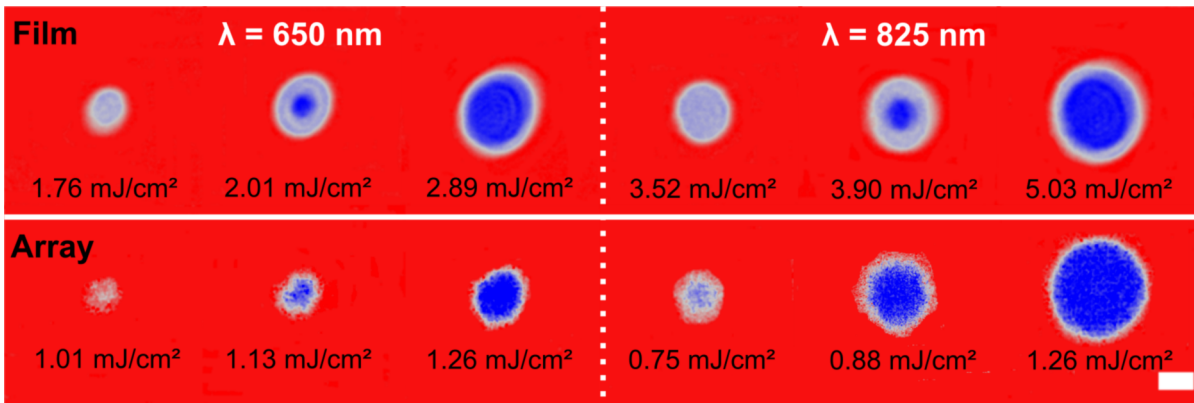


Figure 6.4: Single-pulse AO-HIS for a continuous  $[\text{Co}/\text{Gd}/\text{Pt}]_2$  film (top panels) and for a patterned  $[\text{Co}/\text{Gd}/\text{Pt}]_2$  metasurface with  $D = 150 \text{ nm}$  and  $P = 500 \text{ nm}$  (bottom panels) at  $\lambda = 650 \text{ nm}$ , and  $\lambda = 825 \text{ nm}$ . Red and blue colors indicate magnetization pointing up and down, respectively. The laser fluence is indicated in the figure. The scale bar corresponds to  $50 \mu\text{m}$ . Figure and caption from reference 421.

This quantity reaches  $1.77 \pm 0.14$  at 650 nm and this effect is significantly stronger at 825 nm

## CHAPTER 6. ENERGY EFFICIENT SINGLE PULSE ALL OPTICAL SWITCHING

since we excited SLR leading to humongous absorption enhancement. This way the excitation of a collective resonance gives a gain of energy of  $4.43 \pm 0.39$  so that the switching threshold fluence is reduced by more than 75 % in the periodic array of nanodisks.

We further investigated the wavelength dependence of single pulse AO-HIS in metasurfaces with  $D = 150, 200$  and  $250$  nm and  $P = 500$  nm and the unpatterned film as depicted in Figure 6.5. We plot the gain of energy that we just defined as function of the laser pump wavelength. We notice that at almost all the wavelengths single pulse AO-HIS is more energy efficient in the plasmonic structure than in the continuous film and the largest reduction of switching threshold fluence of the metasurface corresponds to the excitation of the SLR as suggested by Figure 6.5(b).

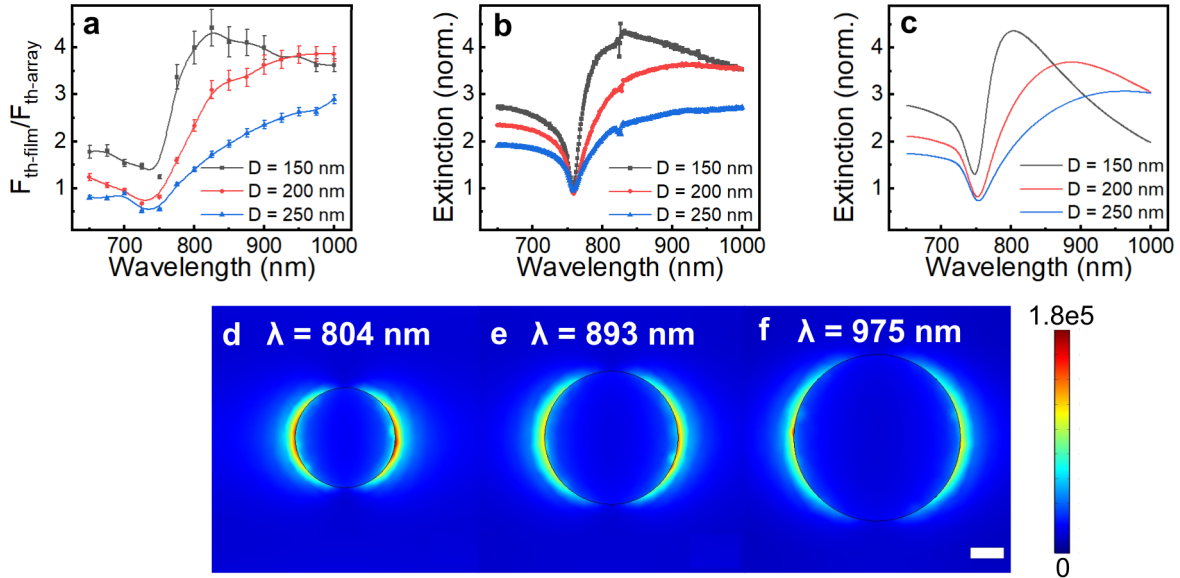


Figure 6.5: (a) Gain of energy as function of the wavelength for  $[\text{Co/Gd/Pt}]_2$  metasurfaces. (b) Extinction spectra of the same structures scaled by their filling factor and normalized by the extinction spectrum of the corresponding continuous film. (c) Simulated normalized extinction spectra for the same metasurfaces. (d-f) Electric field intensity ( $|E|/|E_0|$ ) distribution near a nanostructure in a periodic arrangement of nanodisks with  $P = 500$  nm at the SLR wavelength. The disk diameter takes the values (d) 150, (e) 200, and (f) 250 nm. The scale bar corresponds to 50 nm.

The extinction spectra shape is determined by the DO of the array (sharp minimum  $\approx 760$  nm) and a broader collective resonance (maximum of extinction following the DO) due to hybridization between the LSPR of each singular nanodisk and the DO<sup>270,273,279,282</sup>. As we explained already, the SLR leads more to absorption enhancement within the plasmonic system than to strong scattering so this measurement is a good estimation of the metasurfaces absorption. In particular, we scaled this raw quantity by the filling factors of the periodic arrays and

## CHAPTER 6. ENERGY EFFICIENT SINGLE PULSE ALL OPTICAL SWITCHING

normalized it by the extinction spectra of the corresponding continuous film. Thus we can deduce the local absorption enhancement within the metasurface in comparison to the unpatterned film. The normalized extinction, measured with CW laser, clearly resembles the shape of the energy gain spectra. More than that the amplitudes almost coincide. This correspondence provides a powerful tool for designing magnetoplasmonic metasurfaces in order to lower the switching threshold fluence as much as possible in comparison to unpatterned systems. More than that, a precise estimation of the gain of energy can be deduced from straightforward extinction measurements involving a simple CW laser. These results support the statement that AO-HIS is driven by a pure thermal effect since making the system absorb more light leads to a reduction of the minimum energy required to perform AO-HIS.

We support this trend with numerical simulations by means of FEM. Indeed for the periodic arrays that we mention here ( $P = 500$  nm), the most efficient AO-HIS is reached for nanodisks with  $D = 150$  nm because of the strongest optical absorption per unit area, as further confirmed by the simulated intensity of the optical near fields presented in Figure 6.5(d–f). We obtained the same behaviour for a lattice period of 550 nm as depicted in Figure 6.6.

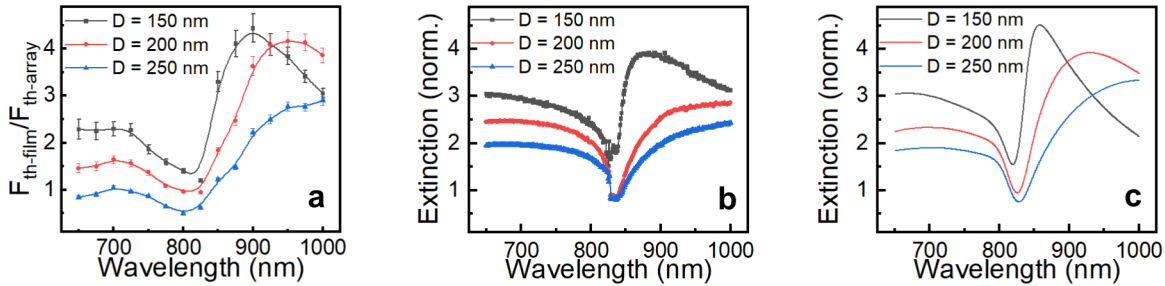


Figure 6.6: (a) Gain of energy as function of the wavelength for  $[\text{Co}/\text{Gd}/\text{Pt}]_2$  metasurfaces. (b) Extinction spectra of the same structures scaled by their filling factor and normalized by the extinction spectrum of the corresponding continuous film. (c) Simulated normalized extinction spectra for the same metasurfaces. (d–f) Electric field intensity ( $|E|/|E_0|$ ) distribution near a nanostructure in a periodic arrangement of nanodisks with  $P = 550$  nm at the SLR wavelength. The disk diameter takes the values (d) 150, (e) 200, and (f) 250 nm. The scale bar corresponds to 50 nm.

We were not able to study the systems with  $D = 100$  nm because the filling factors were so small that we could not have a good SNR to analyze the images. We optimize the SNR through an optimum of the MO contrast that we detail in Chapter 7. All simulations involved a linearly polarized incident light coming to the sample at normal incidence with a wavelength ranging from 650 to 1000 nm. We considered a uniform embedding medium with a dielectric constant of 1.5. In fact we used an index matching liquid with the same refractive index of the substrate to

avoid refractive index mismatch that would weaken the radiative coupling that should lead to the excitation of the SLR<sup>300</sup>. We measured the refractive index of the system as detailed in Figure 6.7. We used this data sets as inputs for the simulations.

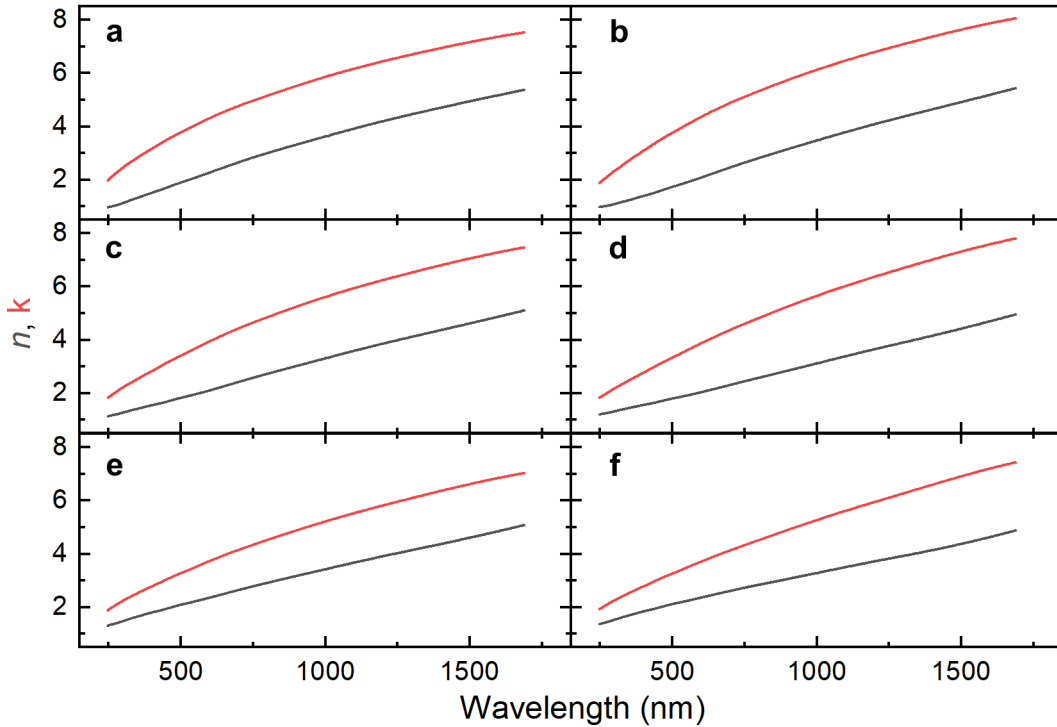


Figure 6.7: Measured refractive index of  $[\text{Co/Gd/Pt}]_N$  metasurfaces for (a)  $N = 1$ , (b)  $N = 2$ , (c)  $N = 3$ , (d)  $N = 4$ , (e)  $N = 5$  and (f)  $N = 6$ .

Yann Le Guen performed these measurements at *Aalto University*. The optical constants were extracted from the ellipsometry measurements using CompleteEASE software and considering the whole multilayer as a single layer system. The CompleteEASE software utilizes a Bruggeman effective medium approach to minimize the mean-square deviation between measured and calculated ellipsometry parameters. We want to point out that assuming the whole system as a single layer system is good thing because it allowed us to simplify considerably the numerical simulations, especially for the meshing step. For example, in case of  $N = 2$ , we patterned in COMSOL a periodic arrangement of 23 nm-thick nanodisks with the measured effective refractive index. After demonstrating the opportunity to achieve energy efficient AO-HIS we investigated the switching endurance of the magnetic nanodisks, i. e. if we can perform millions of writing cycles in these systems.



### 6.3 Switching endurance of magnetic nanodisks

We showed that we could control the gain of energy related to AO-HIS with SLRs. One remaining question is the switching endurance of magnetic nanodisks. In other terms, can we reverse back and forth magnetization of nanodisks with light ? We observed deterministic switching in the continuous film as presented in Figure 6.8.

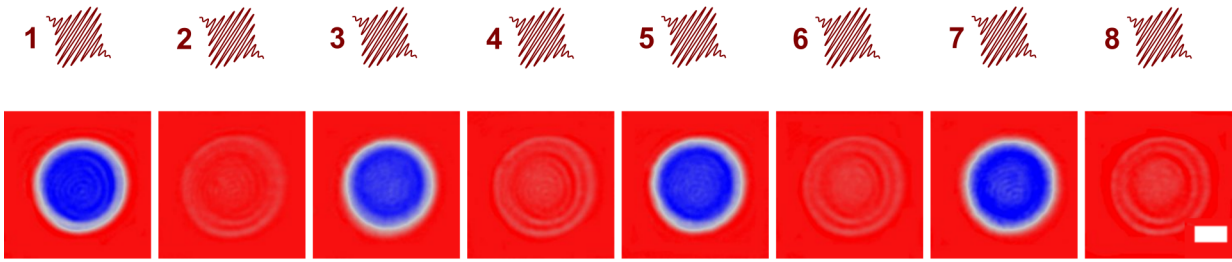


Figure 6.8: Toggle switching on  $[\text{Co/Gd/Pt}]_2$  continuous film with a fluence  $F = 3.02 \text{ mJ/cm}^2$  at 650 nm. Red and blue colors indicate magnetization pointing up and down, respectively. The scale bar corresponds to  $50 \mu\text{m}$ .

However, metasurfaces do not exhibit toggle switching as evidenced in Figure 6.9 for  $D = 150 \text{ nm}$  and  $P = 500 \text{ nm}$ . We notice that an increasing even number of pulses leads to lighter and lighter blue color while an increasing odd number of pulses gives lighter and lighter red color. This means that we did not observe toggle switching on the periodic arrays of nanodisks so that the magnetic amplitude gets closer to zero when the number of pulses increases. In conclusion, the lighting of magnetic contrasts related to both perpendicular orientations is due to a loss of magnetization.

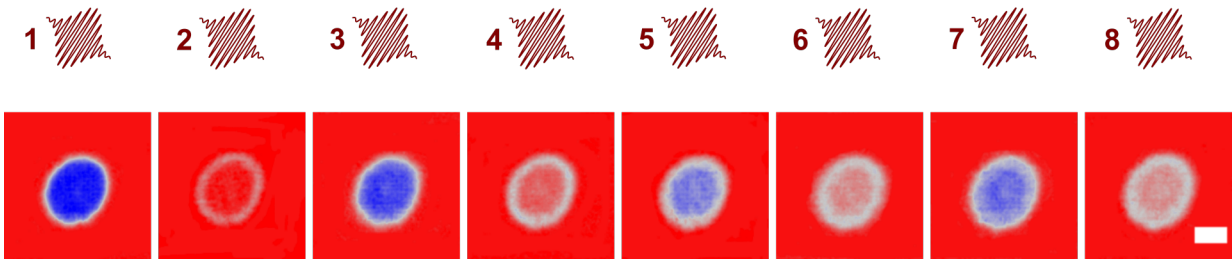


Figure 6.9: Repetitive switching of single-pulse AO-HIS in a  $[\text{Co/Gd/Pt}]_2$  metasurface with  $D = 150 \text{ nm}$  and  $P = 500 \text{ nm}$  for a fluence of  $1.26 \text{ mJ/cm}^2$  at 650 nm. Red and blue colors indicate magnetization pointing up and down, respectively. The scale bar corresponds to  $50 \mu\text{m}$ .



## CHAPTER 6. ENERGY EFFICIENT SINGLE PULSE ALL OPTICAL SWITCHING

In order to quantify this loss of magnetization, we checked the magnetic contrast along a line on MOKE images from Figure 6.9 from 1 to 8 consecutive light pulses. As usually, we define the normalized magnetization amplitude as  $m = \frac{M}{M_0}$ . Here we rather refer to normalized switching rate. Figure 6.10(b) then shows normalized radial switching rate profiles and supports the statement that a given fraction of magnetization is lost after each pulse that is sent.

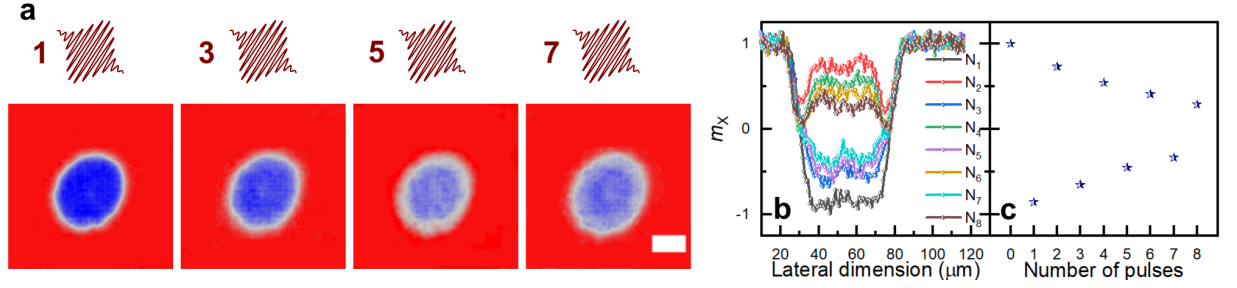


Figure 6.10: Repetitive switching of single-pulse AO-HIS in a  $[\text{Co/Gd/Pt}]_2$  metasurface with  $D = 150$  nm and  $P = 500$  nm for a fluence of  $1.26$  mJ/cm<sup>2</sup> at  $650$  nm. (a) MOKE images for 1, 3, 5 and 7 consecutive pulses. (b) Corresponding switching rates line profiles across the reversed areas after each single ultrafast laser pulse was sent. (c) Switching rate at metasurface center a a function of pulse number.  $N_X$  denotes the event "The system has been subjected to  $X$  light pulses". The scale bar corresponds to  $50$   $\mu\text{m}$ .

In order to explain the incomplete switching of the nanodisks, we used the simplest model. Indeed, we assumed that every single disk has a switching probability  $P_{SW}$  that is independent of its magnetization state but also of the magnetic orientation of surrounding nanodisks. Thus each nanodisk is treated as a macrospin and we neglected any magnetic interaction. We note  $n_{\uparrow}$  ( $n_{\downarrow}$ ) the number of nanodisks pointing up (down), leading to the total normalized magnetization  $m = \frac{n_{\uparrow} - n_{\downarrow}}{n}$  where  $n$  is the total number of nanodisks. Before the first laser pulse, we note  $n_{\uparrow,0}$  and  $n_{\downarrow,0}$  the initial number of nanodisks pointing up and down, respectively. We note  $m_X$  the normalized magnetization amplitude, or the normalized switching rate, after  $X$  consecutive ultrafast laser pulses. Then, after one laser pulse, one can obtain

$$n_{\uparrow,1} = n_{\uparrow,0} - n_{\uparrow,0} \times P_{SW} + n_{\downarrow,0} \times P_{SW} \quad (6.1a)$$

$$n_{\downarrow,1} = n_{\downarrow,0} - n_{\downarrow,0} \times P_{SW} + n_{\uparrow,0} \times P_{SW} \quad (6.1b)$$

$$m_1 = m_0 \times (1 - 2P_{SW}) \quad (6.1c)$$

One can notice that from  $n_{\uparrow,0}$  to  $n_{\uparrow,1}$ , a fraction  $n_{\uparrow,0}P_{SW}$  is lost while a fraction  $n_{\downarrow,0}P_{SW}$  is

## CHAPTER 6. ENERGY EFFICIENT SINGLE PULSE ALL OPTICAL SWITCHING

gained. This works the other way around with  $n_{\downarrow,1}$ . The next iterations gives

$$n_{\uparrow,2} = n_{\uparrow,1} - n_{\uparrow,1} \times P_{SW} + n_{\downarrow,1} \times P_{SW} \quad (6.2a)$$

$$n_{\downarrow,2} = n_{\downarrow,1} - n_{\downarrow,1} \times P_{SW} + n_{\uparrow,1} \times P_{SW} \quad (6.2b)$$

$$m_2 = m_1 \times (1 - 2P_{SW}) \quad (6.2c)$$

Then, we deduced the final equations giving the switching rate  $m_X$  depending only on the initial configuration  $m_0$ , the switching probability and the number of pulses  $X$

$$m_X = m_0 \times |1 - 2P_{SW}|^X \quad (6.3a)$$

$$m_X = \prod_i m_i \text{ with } \sum_i i = X \quad (6.3b)$$

If this holds true, then we should be able to reproduce a given state  $m_X$  from Figure 6.10(b) with the product of previous states. Figure 6.11 shows that it is in fact possible to predict a given magnetization state knowing the previous ones, validating the assumption that the magnetic metasurfaces experience a stochastic switching.

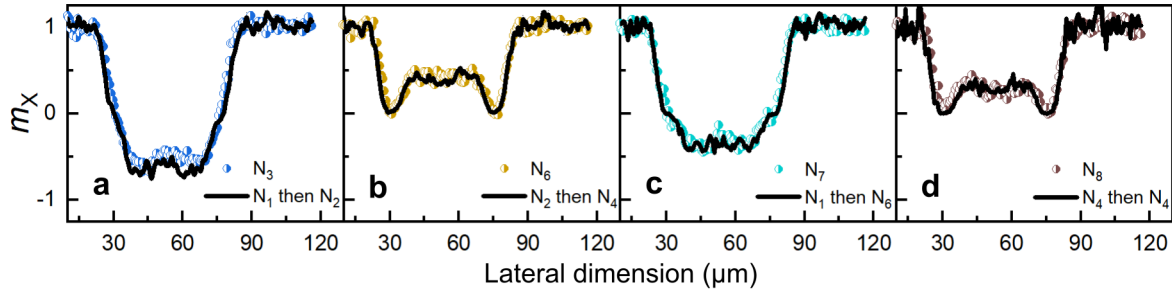


Figure 6.11: Non-complete switching in a  $[\text{Co/Gd/Pt}]_2$  metasurface with  $D = 150$  nm and  $P = 500$  nm for a fluence of  $1.26$  mJ/cm<sup>2</sup> at  $650$  nm. Reproduction of switching rates (a)  $m_3$ , (b)  $m_6$ , (c)  $m_7$  and (d)  $m_8$  with a combination of previous states.

We also observed stochastic switching for other subwavelength-sized disks as shown in Figure 6.12. We further studied the intrinsic switching probability related to each nanodisk disk.

Along the same idea, we also determined the switching rates from 1 to 8 consecutive pulses for  $D = 200$  and  $250$  nm as presented in Figure 6.13. We described our systems assuming all the

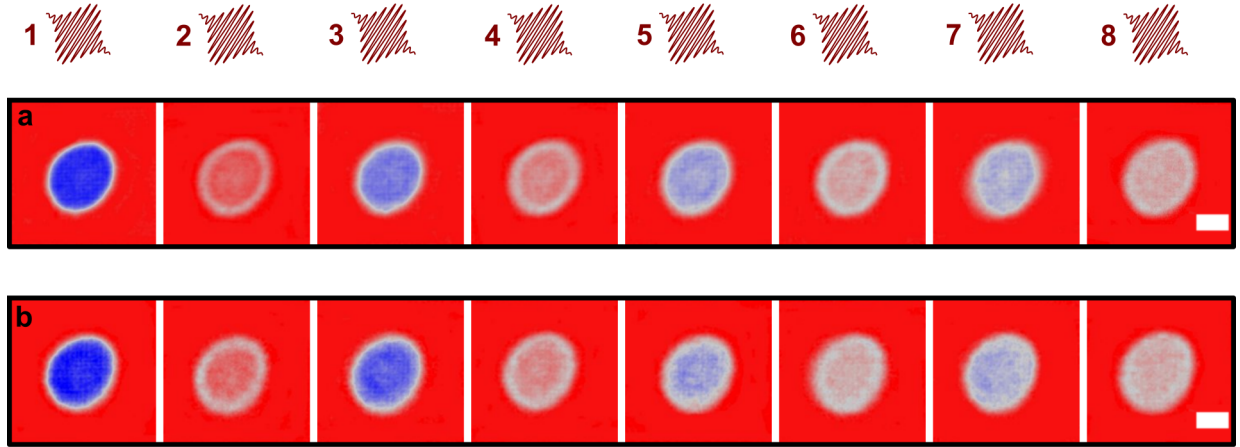


Figure 6.12: Repetitive switching of single-pulse AO-HIS in a  $[\text{Co/Gd/Pt}]_2$  metasurface with (a)  $D = 200$  nm and  $P = 500$  nm for a fluence of  $1.89$  mJ/cm<sup>2</sup> at 650 nm, (b)  $D = 250$  nm and  $P = 500$  nm for a fluence of  $2.77$  mJ/cm<sup>2</sup> at 650 nm. The scale bar corresponds to  $50$   $\mu\text{m}$ .

nanodisks react to a given optical excitation. One could also consider the case in which most of them react. Noting the amount of nanodisks not reacting  $n_{\uparrow,NS}$ , the normalized switching rate should be rewritten  $m = \frac{n_{\uparrow,NS} + n_{\uparrow} - n_{\downarrow}}{n}$ . This gives the final equation describing the stochastic switching of most of the nanodisks reacting to the excitation

$$m_X = m_{NS} + (1 - m_{NS}) \times |1 - 2P_{SW}|^X \quad (6.4)$$

We find back Equation (6.3a) when all the disks react to any laser pulse during the switching endurance investigation as in this case  $m_{NS} = 0$ . From the switching rates  $m_X$  in case all the nanodisks respond to the excitation, one can deduce the switching probability through the equation

$$P_{SW} = \frac{1 - \left(\frac{m_N}{m_0}\right)^{\frac{1}{X}}}{2} \quad (6.5)$$

From this we can investigate the dependence of  $P_{SW}$  on the disk diameter but also on the lateral dimension so that the laser fluence. We present in Figure 6.14 this analysis for all the diameters. In particular, starting from the center of the profiles, we noticed a plateau then a decrease in  $P_{SW}$  until it reaches zero since the light did not illuminate these areas. The transition between the plateau and 0 depicts the dependence of  $P_{SW}$  with incoming laser fluence since the laser exhibits a spatial gaussian profiles. It should be noted that an optimum can be found for  $P_{SW}$  for a given laser fluence and increasing this surface energy would lead to a reduction of the

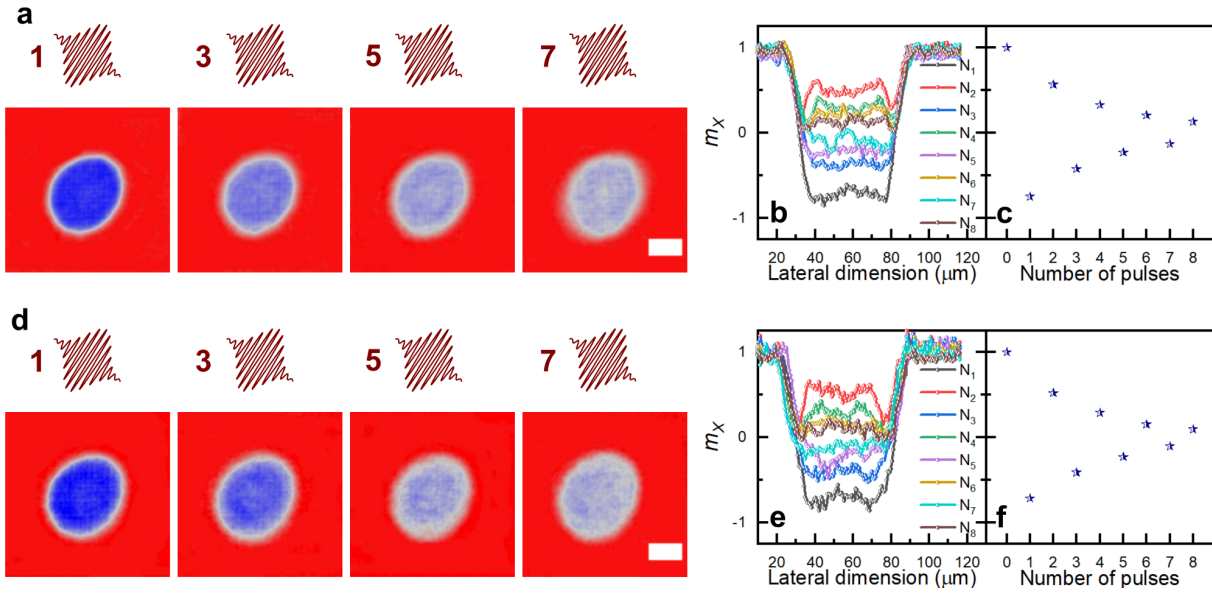


Figure 6.13: Repetitive switching of single-pulse AO-HIS in a  $[\text{Co}/\text{Gd}/\text{Pt}]_2$  metasurface with (a)  $D = 200$  nm and  $P = 500$  nm for a fluence of  $1.89$  mJ/cm<sup>2</sup> at  $650$  nm, (b)  $D = 250$  nm and  $P = 500$  nm for a fluence of  $2.77$  mJ/cm<sup>2</sup> at  $650$  nm. (a,d) MOKE images for 1, 3, 5 and 7 consecutive pulses. (b,e) Corresponding switching rates line profiles across the reversed areas after each single ultrafast laser pulse was sent. (c,f) Switching rate at metasurface center as a function of pulse number. The scale bars correspond to  $50 \mu\text{m}$ .

switching rate since it would favor a multidomain state. In other terms, if the system is subjected to a fluence that is too high,  $P_{SW}$  should decrease.

Figure 6.14 also stresses that we have a great agreement between the measured switching rates (estimated, for a given pulse number  $X$ , by an average of all the  $m_X$  on the plateau) and the ones predicted by our simple macrospin model. These agreements for all the diameters validate once again the stochastic behavior of subwavelength-sized magnetic disks. In particular, as presented in Figure 6.15, one can notice that the smallest nanodisks exhibit the largest switching probability. We attribute this trend to a non-homogeneous absorption in the largest nanodisks while going smaller and smaller favors an absorption more homogeneously distributed within the nanodisks. This way we identified a path to achieve a reliable switching of individual nanodisks. Here  $P_{SW}$ , for a given nanodisk size, is the maximum switching probability we could obtain. Since this quantity also depends on the applied laser fluence, the maximum  $P_{SW}$  have been observed for different applied fluences for the three different nanodisk sizes.

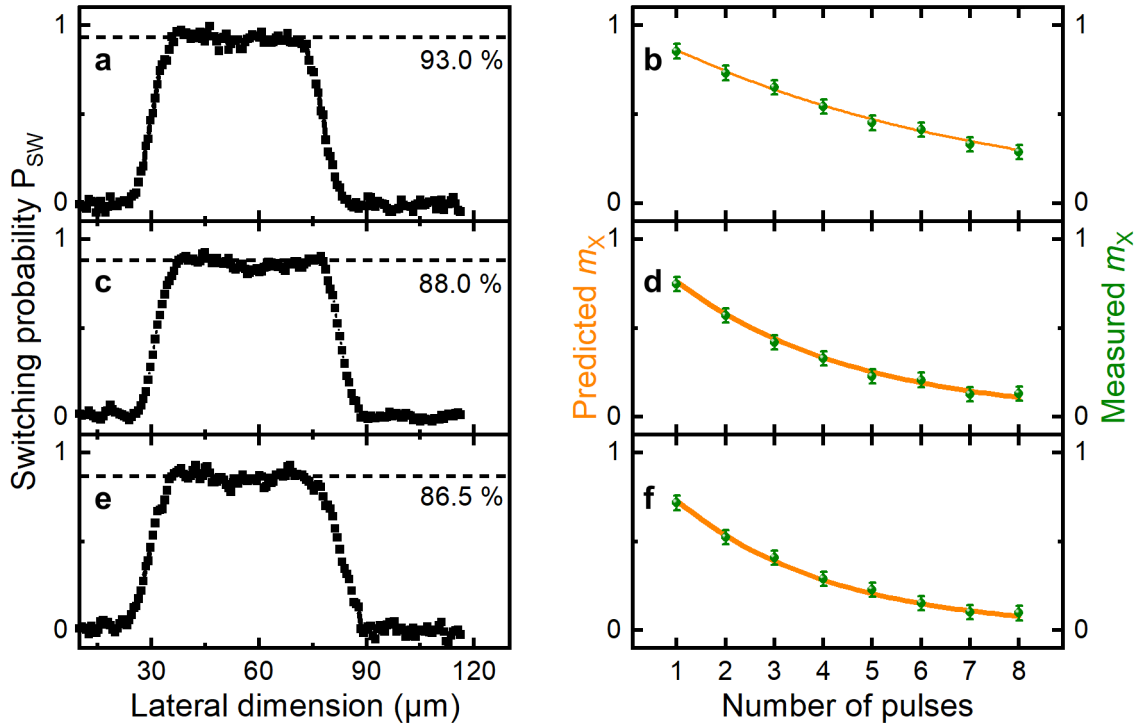


Figure 6.14: Switching probability profile in a  $[\text{Co}/\text{Gd}/\text{Pt}]_2$  metasurface with a)  $D = 150$  nm and  $P = 500$  nm for a fluence of  $1.26$   $\text{mJ}/\text{cm}^2$  at  $650$  nm, c)  $D = 200$  nm and  $P = 500$  nm for a fluence of  $1.89$   $\text{mJ}/\text{cm}^2$  at  $650$  nm, e)  $D = 250$  nm and  $P = 500$  nm for a fluence of  $2.77$   $\text{mJ}/\text{cm}^2$  at  $650$  nm. Comparison between measured and predicted switching rates  $m_x$  for b)  $D = 150$  nm, d)  $D = 200$  nm, f)  $D = 250$  nm.

## 6.4 Collective resonances enhance magneto-optical response

So far we presented how SLR excitations can improve the writing step in all-optical magnetic recording. We also studied how SLRs monitor MO activity since readout sensitivity is another key ingredient for this kind of data storage technologies. For this investigation, we measured the MO Faraday angle  $\Phi_F$  in  $[\text{Co}/\text{Gd}/\text{Pt}]_N$  as function of nanodisk diameter  $D$ , array period  $P$  and repetition number  $N$ . Faraday angle is linked to rotation and ellipticity via  $\Phi_F = \theta_F + \eta_F$  with  $\theta$  and  $\eta$  the rotation and the ellipticity, respectively. Depending if the incoming light is  $s$  or  $p$  polarized, we note the corresponding Faraday angle  $\Phi_{F,s}$  or  $\Phi_{F,p}$ . These two terms depend on complex transmission spectra through

$$\Phi_{F,s} = \frac{t_{ps}}{t_{ss}} \quad (6.6a)$$

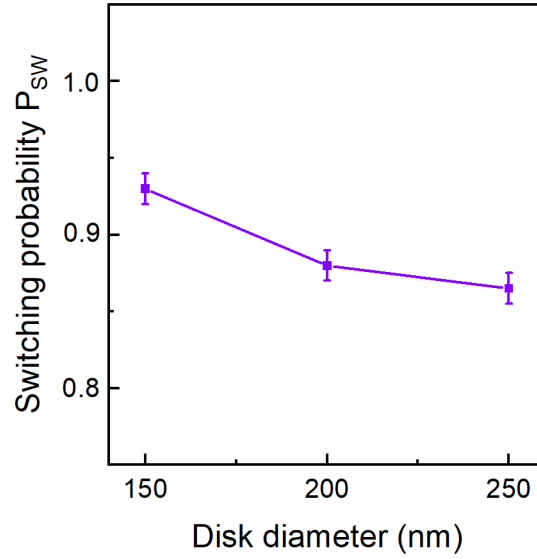


Figure 6.15: Switching probability as function of nanodisk diameter

$$\Phi_{F,p} = \frac{t_{sp}}{t_{pp}} \quad (6.6b)$$

Following these equations, one can already propose strategies to control the MO effect in periodic arrays of nanoparticles. In this context, Figure 6.16 allows to comment all of them. Regarding a [Co/Gd/Pt]<sub>5</sub> metasurface with  $D = 100$  nm and  $P = 400$  nm embedded in homogeneous media with refractive index of 1.5, a DO is expected at 600 nm. At this wavelength,  $|t_{ss/pp}|^2$  tends to 1 since all the light is scattered out from the array. Then, regarding Equations (5.6), only small MO effect should be observed that is in agreement with Figure 6.16(b). However, increasing  $|t_{ps/sp}|^2$  should provide a strong MO effect and this is exactly what we observed. Finally, another approach is to excite SLRs leading to a strong enhancement of local field within the nanodisk so that  $E_{loc} \gg E_{ext}$ . Regarding Figure 6.16, this should occur at 675 nm giving rise to strong MO activity.

We aimed to quantify the impact of such collective resonances on the MO readout sensitivity. For that we calculated the ratio of the Faraday angles of the [Co/Gd/Pt]<sub>N</sub> metasurfaces and of the corresponding continuous films at the resonance wavelengths. In addition we scaled these ratio with the filling factors of the periodic arrays of nanodisks in order to describe the local enhancement of MO activity. Figure 6.17 presents this ratio for any metasurface. In particular, when the reading process is performed locally, we observed a sensitivity enhancement by up to 15 for  $N = 2$ , even up to 50 for  $N = 6$ . Also, this improvement is even more impressive for the smallest disks since they experience the most intense optical near-field enhancement. We provide

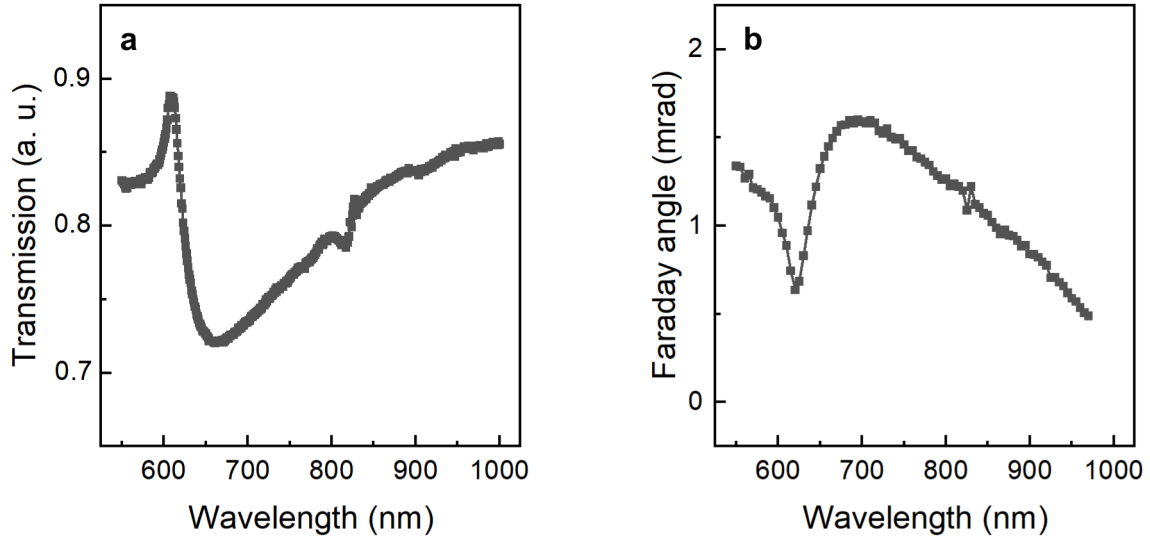


Figure 6.16: (a) Optical and (b) MO spectra of  $[\text{Co}/\text{Gd}/\text{Pt}]_5$  metasurface with  $D = 100$  nm and  $P = 400$  nm.

the raw MO spectra of all the metasurfaces and the corresponding unpatterned continuous films in Appendix E.

## 6.5 Comment on periodic arrays of GdFeCo nanodisks

Our first attempt considered periodic arrangements of GdFeCo nanodisks. However the nanostructures did not exhibit AO-HIS, even for the largest nanodisks with a diameter of 250 nm. We think this failure comes from two main causes. First, unlike the  $[\text{Co}/\text{Gd}/\text{Pt}]_N$  metasurfaces, the GdFeCo nanodisks experienced a loss of remanence of around 10 %. Indeed such amorphous alloy magnetic system is highly sensitive to its thermal history and even a soft annealing is able to damage its magnetic anisotropy. The second reason might be related to strong chemical inhomogeneities. This should not impact the AO-HIS in continuous thin films since the typical size of switched domains is around tens of micrometers but at nanoscale the story is completely different. Strong chemical inhomogeneities could provide some nanostructures whose atomic composition within the magnetic system is not close to the magnetic compensation so that AO-HIS is not observable. All these explanations are speculative but could explain why we observed AO-HIS in the crystalline multilayer  $[\text{Co}/\text{Gd}/\text{Pt}]_N$  nanostructures and not in the amorphous alloy GdFeCo.

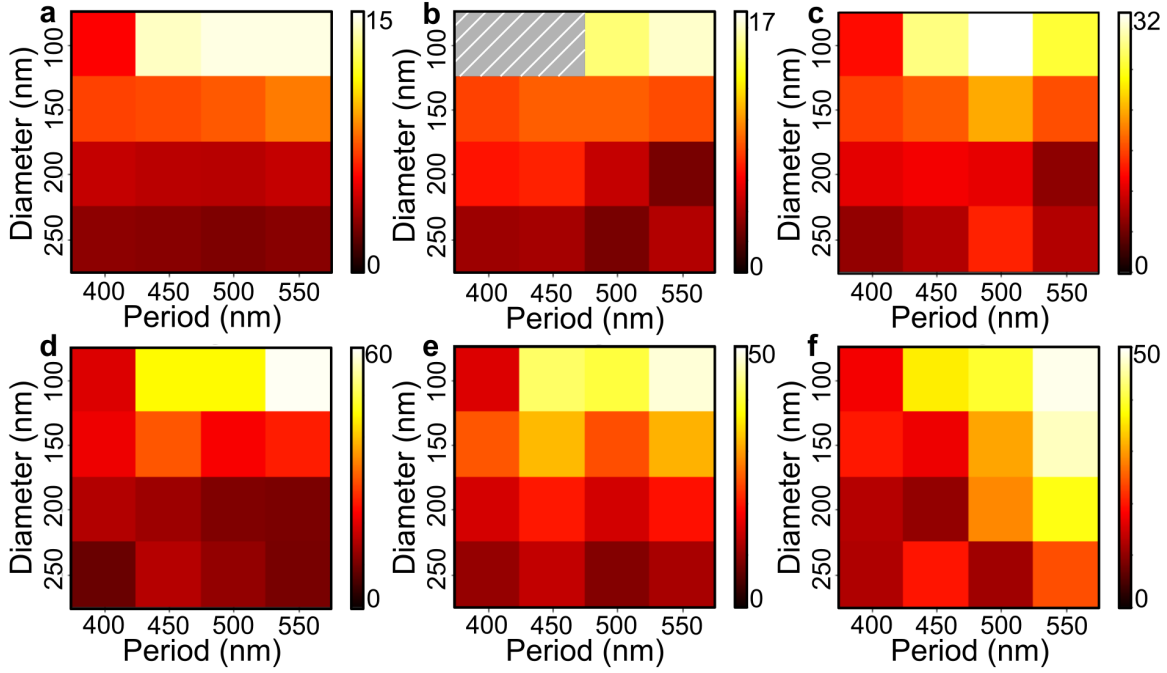


Figure 6.17: SLR enhanced Faraday readout sensitivity for  $[\text{Co/Gd/Pt}]_N$  metasurfaces with (a)  $N = 1$ , (b)  $N = 2$ , (c)  $N = 3$ , (d)  $N = 4$ , (e)  $N = 5$  and (f)  $N = 6$ .

## 6.6 Conclusion

In conclusion, SLRs reduce the minimum energy for AO-HIS by a factor of more than 4. We identified a path to perform reliable switching of individual nanodisks since the systems in our study provide a stochastic switching. From the other side, collective resonances significantly enhance MO readout sensitivity. In this perspective, a 50 times enhancement of the Faraday effect at SLR wavelength can be combined to a maximum energy efficiency for the writing process.



## Chapter 7

# Magnetism-induced surface lattice resonances

*In this chapter, we evidence the existence of magnetic surface lattice resonances induced by metasurfaces consisting of [Co/Gd/Pt]<sub>3</sub> multilayer nanodisk arrays. Exciting the system with a non normal angle of incidence leads to three collective resonances while only one or two are shown for regular arrays of Ta/Pt nanodisks depending of the polarization of the incoming light. Besides, playing with illumination polarization and experiment parameters, we can mimic this magnetic behaviour in non magnetic metallic metasurfaces..*

## 7.1 Motivations

In line with Chapter 6, a crucial parameter for the MO read-out is the SNR that is, in our methodology, related to the MO contrast, in other terms the difference in the light intensities reflected by the same sample magnetized up and down. This quantity has to be optimized to make the AO-HIS investigation more reliable, in particular to determine properly the switching probabilities for any nanodisk size. The MO contrast spectra measured on magnetic metasurfaces is related to its intrinsic MO rotation and ellipticity spectra. Since the magnetoplasmonic system was probed at a certain oblique incidence, this allowed us to decouple the contributions of the SLRs of pure optical origin and the other ones coming from the presence of magnetism in the system. Indeed, a given linearly polarized light gives rise within the nanodisks to two orthogonal electric dipoles coupled by spin-orbit coupling. Since we explained in Chapter 3 that the positions of SLRs can be changed with incoming light polarization, we expected to distinguish usual SLRs from magnetism-induced SLRs.

## 7.2 Surface lattice resonances and Kerr effect

We give an alternative definition of the complex Kerr angle for an  $s$ -polarized incoming wave

$$\Phi_{K,s} = \frac{\tilde{r}_{ps}}{\tilde{r}_{ss}} = \frac{mr_{ps}e^{\delta_{ps}}}{r_{ss}e^{\delta_{ss}}} = m(\theta_{K,s} + i\eta_{K,s}) \quad (7.1)$$

where  $\delta_{ps}$  and  $\delta_{ss}$  are phase angles. Here,  $m$  is an absolute quantity describing the normalized magnetization equals to 1 since we assume that the sample is always saturated. Then the magnetic states up and down correspond to  $+m$  and  $-m$ , respectively. Using this description and the Jones Formalism, one can deduce the reflected light intensity that depends on  $m$  and the analyzer angle  $\alpha$

$$\frac{I(\alpha, \pm m)}{I_0} = \frac{r_{ss}^2}{2}(\sin^2(\alpha)) + \frac{m^2 r_{ss}^2}{2}(|\theta_{K,s}|^2 + |\eta_{K,s}|^2)(\cos^2(\alpha)) \pm \frac{mr_{ss}^2}{2}(\theta_{K,s} \sin(2\alpha)) \quad (7.2)$$

where the reflected intensity has been scaled by the incoming light intensity  $I_0$ . To certify the validity of Equation (7.2) we first obtained a domain pattern on a [Co/Gd/Pt]<sub>3</sub> continuous film and varied the angle  $\alpha$  between the polarizer and the analyzer. Figure 7.1 provides a set of 35 images on which one can notice that for a "negative" analyzer angle  $\alpha^*$ , domains with

---

\* $\alpha$  is actually the angle between the analyzer and polarizer transmission axes. In this work we refer to the analyzer angle.

## CHAPTER 7. MAGNETISM-INDUCED SURFACE LATTICE RESONANCES

$-m$  orientation reflects more light than the one with  $+m$  orientation. The opposite trend is obtained for positive angles and the transition from both behaviours occurs, as expected, close to a configuration for which both transmission axis of the polarizer and the analyzer are crossed.

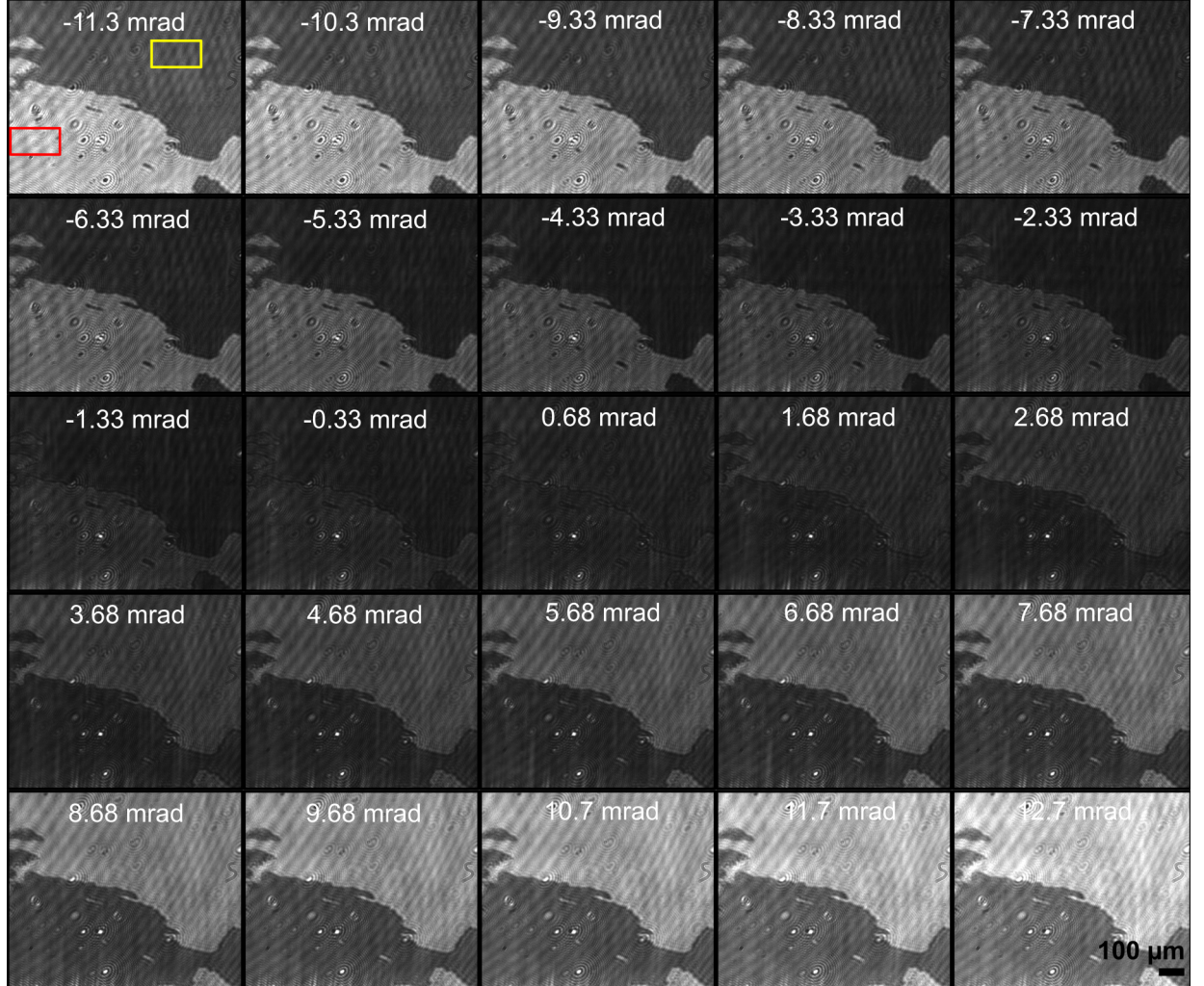


Figure 7.1: MOKE images of domain pattern measured for various  $\alpha$  indicated on each images. The MOKE images have been recorded at 800 nm.  $I(\alpha, +m)$  and  $I(\alpha, -m)$  are derived from averaged intensities within the two indicated regions, yellow and red respectively.

Using Equation (7.1), we deduced the quantities  $\Delta(\alpha)$  and  $\Sigma(\alpha)$  following

$$\Delta(\alpha) = \frac{I(\alpha, +m) - I(\alpha, -m)}{I_0} = mr_{ss}^2 \theta_{K,s} \sin(2\alpha) \quad (7.3a)$$

$$\Sigma(\alpha) = \frac{I(\alpha, +m) + I(\alpha, -m)}{I_0} = r_{ss}^2 \sin^2(\alpha) + m^2 r_{ss}^2 (|\theta_{K,s}|^2 + |\eta_{K,s}|^2) \cos^2(\alpha) \quad (7.3b)$$

## CHAPTER 7. MAGNETISM-INDUCED SURFACE LATTICE RESONANCES

It appears from Equations (7.3) that both terms are determined by pure optical but also MO effects and additional reflectivity measurements are requisite to extract the  $\theta_{K,s}$  from  $\Delta(\alpha)$  then  $\eta_{K,s}$  from  $\Sigma(\alpha)$ . Figure 7.2 presents a very good agreement between intensities extracted from Figure 7.1 and theory.

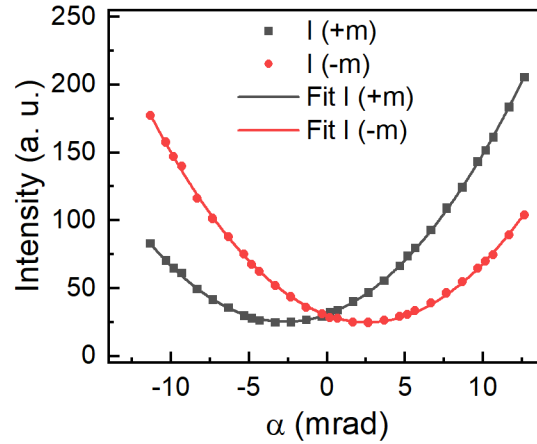


Figure 7.2: Experimental intensity measurements of both  $I(\alpha, +m)$  and  $I(\alpha, -m)$  fitted by Equation (7.2).

Then the MO contrast can be defined as

$$C(\alpha) = \frac{\Delta(\alpha)}{\Sigma(\alpha)} \quad (7.4)$$

We show in Figure 7.3 the resulting values of  $\Delta(\alpha)$  and  $\Sigma(\alpha)$  and subsequent MO contrast. We fitted the results but with Equations (7.3) and (7.4).

We still have a good agreement between what we measured and what the theory predicts. In particular, for fitting the results of the experimental MO contrast, we obtained a Kerr rotation  $\theta_{K,s}$  of 2.63 mrad, meaning that the optimum MO contrast is obtained for a rotation close to  $\alpha$ . In addition we estimated the extinction ratio (minimum intensity over maximum intensity) to be around  $3.10^{-5}$ , very close to the value announced by the optics provider, equals to  $1.10^{-5}$ . We obtained the minimum intensity from the minimum value from Figure 7.2 while the maximum value comes from one of the fitting parameters giving rise to the curve fits in Figure 7.2.

Since the magnetic metasurfaces exhibit low filling factors, the resulting MO contrast is significantly lower than the one observed in the corresponding continuous films. However, we thought that since we could control the MO response of these structures with the wavelength, then we should be able to tune the MO contrast with the wavelength. We present in Figure 7.4 the measured MO contrast for  $D = 150$  nm and  $P = 400, 450, 500,$  and  $550$  nm.

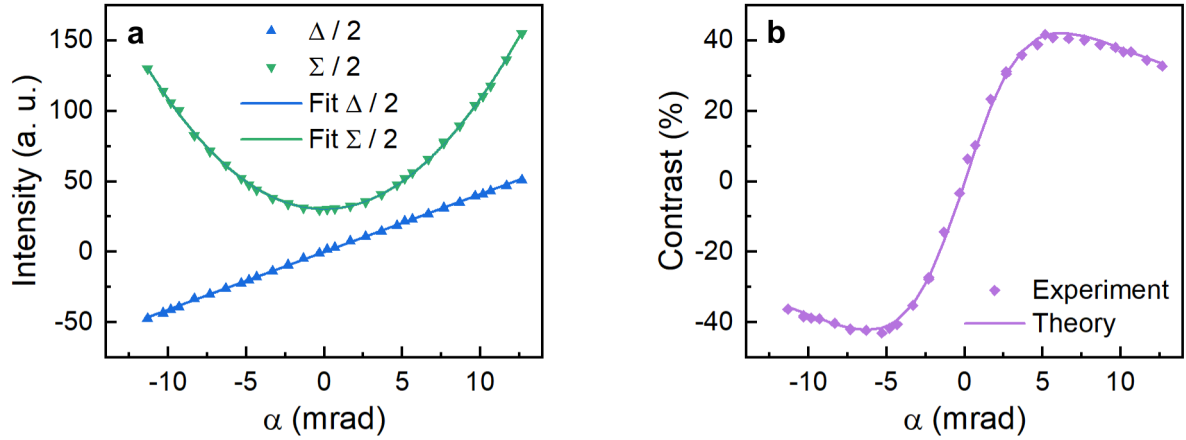


Figure 7.3: Experimental measurements of (a)  $\Delta(\alpha)/2$  and  $\Sigma(\alpha)/2$  and (b) MO contrast as function of  $\alpha$  compared to theory.

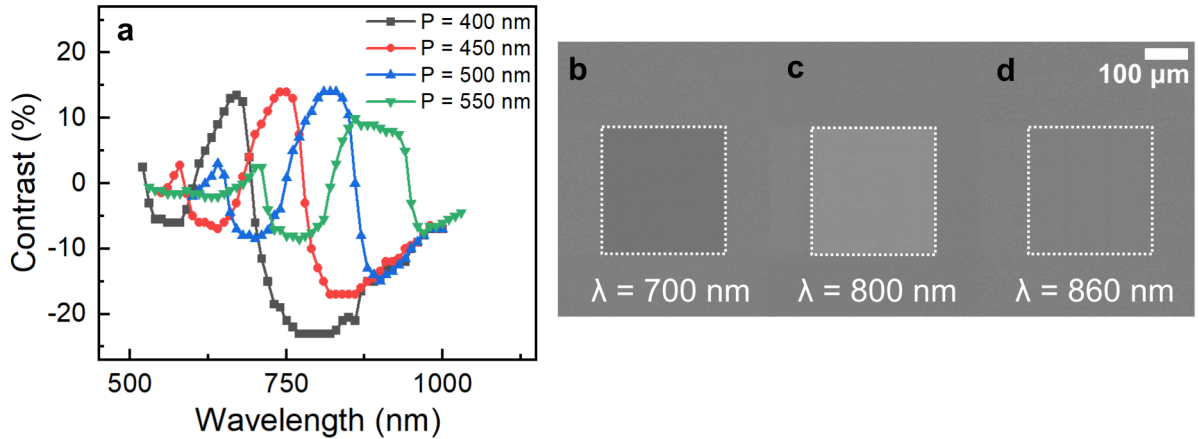


Figure 7.4: MO contrast of  $[\text{Co}/\text{Gd}/\text{Pt}]_3$  metasurfaces. (a) MO contrast for  $D = 150 \text{ nm}$  and  $P = 400, 450, 500,$  and  $550 \text{ nm}$ . (b–d) MO contrast for  $P = 500 \text{ nm}$  with highlights at  $700, 800,$  and  $860 \text{ nm}$ , respectively.

In particular, for  $P = 500 \text{ nm}$  that corresponds to one of the two lattice periods that we considered in Chapter 6 for AO-HIS experiments, we could obtain a MO contrast near 15 % if we would probe the magnetic system at  $800 \text{ nm}$ . Thus, when we considered the metasurface with same disk diameter but with a period of  $550 \text{ nm}$ , we had to use a probe wavelength even larger, at  $860 \text{ nm}$ , while probing the system at  $800 \text{ nm}$  would have resulted in a MO contrast close to zero synonym of low SNR. When we performed AO-HIS in this kind of nanostructures, we employed two OPAs whose one enables to explore the whole visible and near-IR ranges. The

second one is more restricted since we could not really reach wavelengths shorter than 790 nm. Since we had to pump the plasmonic system from 650 nm, we used the more restricted OPA for probing the magnetic state. For this only reason, regarding the trends of the MO contrast for the four systems, we only studied AO-HIS for  $P = 500$  and  $550$  nm. We obtained the behaviours for  $D = 200$  and  $250$  nm as presented in Figure 7.5.

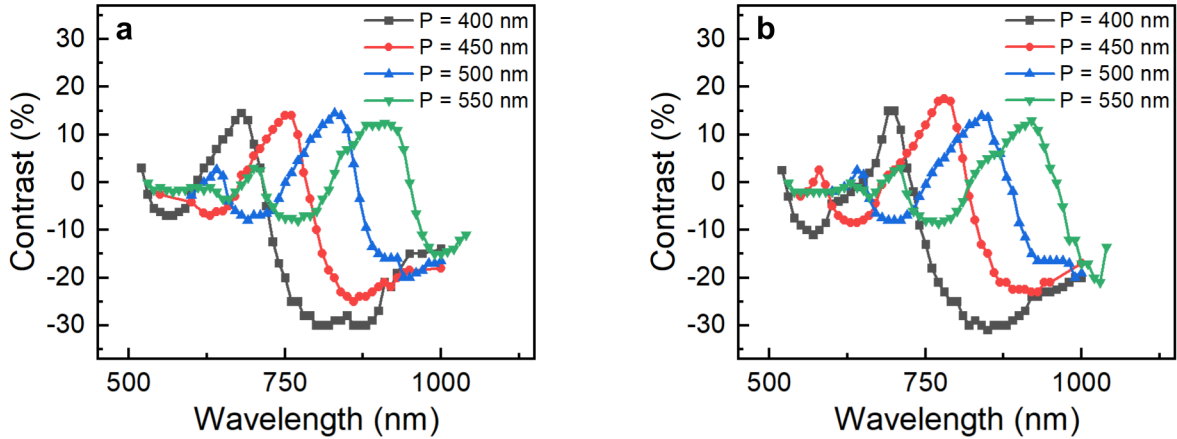


Figure 7.5: MO contrast of  $[\text{Co/Gd/Pt}]_3$  metasurfaces for  $P = 400, 450, 500,$  and  $550$  nm and (a)  $D = 200$  and (b)  $250$  nm.

We think that these features are of primary importance for the investigation of AOS in magneto-plasmonic nanostructures. These considerations must make the data analysis and subsequent conclusions even more reliable. Now we extract the intrinsic MO Kerr rotation and ellipticity spectra from the MO contrast spectra.

### **7.3 Evidence of magnetism-induced surface lattice resonances**

We show an example in Figure 7.6 of the MO spectra derived from the MO contrast spectra from Figure 7.4 for  $D = 150$  nm and  $P = 450$  nm. As far as we know, excitation of a SLR induces a phase change in reflection meaning in our case a sign change in the Kerr rotation. Since we probed the system with  $s$ -polarized light at oblique incidence (approx.  $12^\circ$ ), we would expect, regarding Chapter 3, two sign changes in Kerr rotation. In particular, as  $P = 450$  nm, we would expect two SLRs apparent around 580 and 770 nm. We actually noted 3 SLRs where the centered one would correspond to the one we would have expected if the sample would have

been subjected to  $p$ -polarized light.

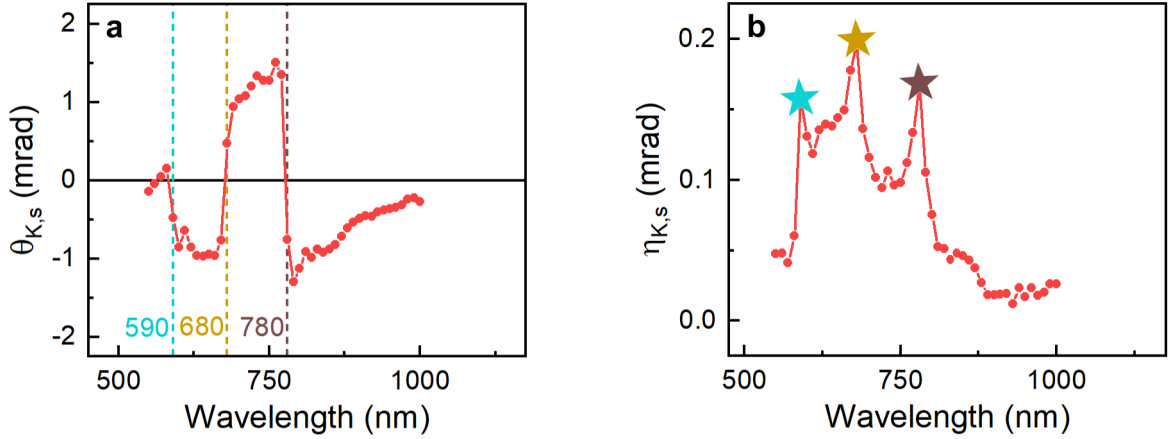


Figure 7.6: (a) Kerr rotation and (b) ellipticity spectra of  $[\text{Co/Gd/Pt}]_3$  metasurface with  $D = 150$  nm and  $P = 450$  nm for incoming  $s$ -polarized light. The vertical dotted lines in (a) highlight for which wavelength the rotation has been measured to be close to zero while the corresponding stars in (b) underline, for the same wavelengths, that ellipticity is maximum.

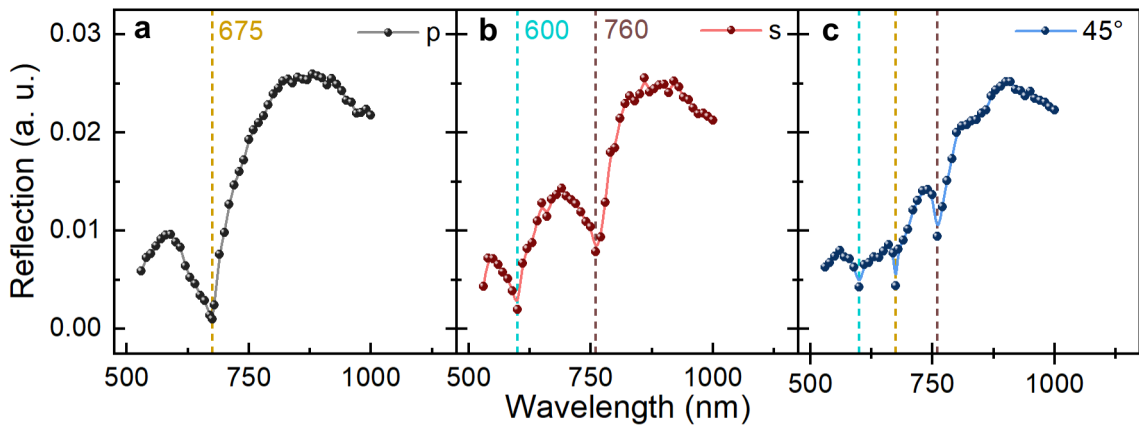


Figure 7.7: Reflection spectra of periodic arrays of Pt nanodisks with  $D = 200$  nm and  $P = 450$  nm. The incoming light was initially (a)  $p$ , (b)  $s$  and (c)  $45^\circ$ -polarized. The solid lines are guides for the eye. The dashed lines points the DO positions.

To understand these features, we came back to basics with the study of non magnetic systems made of noble metals. Similarly to the magnetic metasurfaces, we patterned a periodic array of Ta(5)/Pt(30) on glass substrate. We also employed index matching liquid as in Chapter 6 to embed the plasmonic system in homogeneous surrounding media. As detailed in Chapter 3,



## CHAPTER 7. MAGNETISM-INDUCED SURFACE LATTICE RESONANCES

for a fixed metasurface design, the use of oblique incidence combined with changes in light polarization is expected to change the position of the SLRs.

Then we probed the reflection of the non magnetic system with incoming light set in three configurations:  $p$ -polarized,  $s$ -polarized and  $45^\circ$ -polarized (half  $s$ , half  $p$ ). Since we measured pure optical behaviour, we aligned the transmission axis of the polarizer and the analyzer. Figure 7.7 presents results for  $D = 200$  nm and  $P = 450$  nm. As expected, we observed only one SLR for incoming  $p$ -polarized light and two SLRs for incoming  $s$ -polarized light because we probed the system at oblique incidence, around  $12^\circ$ . We were able to combine the first two curves into the third one because in this case the incoming light initially contained  $p$  and  $s$  components in its polarization. These straightforward results can qualitatively explain what is presented in Figure 7.6.

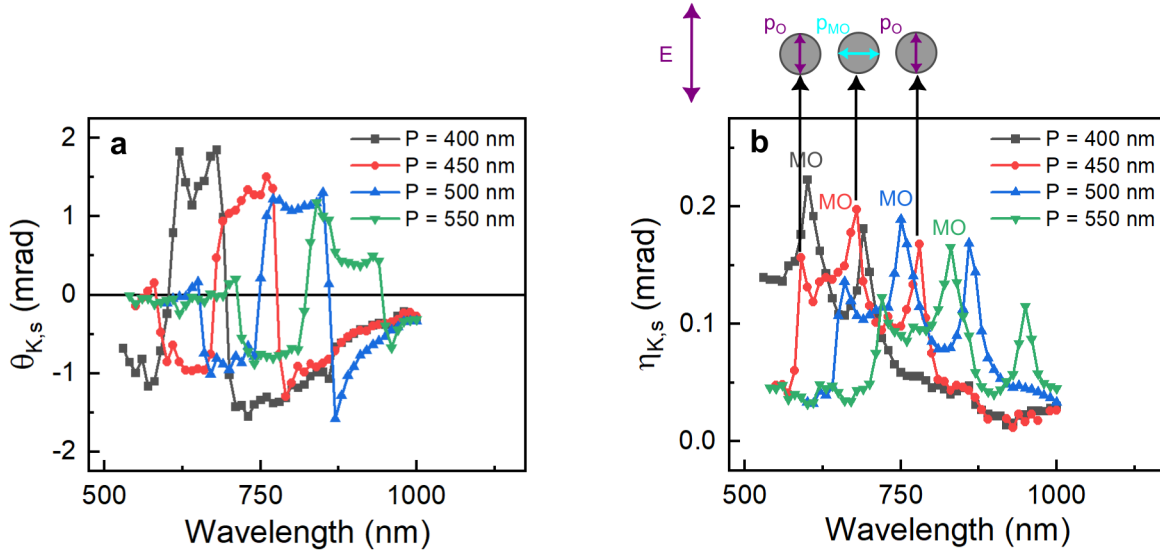


Figure 7.8: (a) Kerr rotation and (b) ellipticity spectra of  $[\text{Co}/\text{Gd}/\text{Pt}]_3$  metasurfaces with  $D = 150$  nm and  $P = 400, 450, 500$  and  $550$  nm for incoming  $s$ -polarized light. MO denotes the position of SLRs whose existence is possible due to the excitation of a MO electric dipole. For  $P = 450$  nm, we illustrate the orientation of the corresponding electric dipole for a given electric field direction. We distinguish the pure optical dipole (purple) from MO dipole (cyan).

In fact we highlighted in Chapter 3 that even if the incoming electric field would be polarized along one axis, like  $x$  axis, a magnetic nanodisk would exhibit two orthogonal electric dipoles. The first one,  $p_x$ , is induced in any metallic nanodisk and has a pure optical origin while the second one,  $p_y$ , exists because of the presence of magnetization within the nanostructure. Then, similar to this description, since we probed the magnetic metasurface with  $s$ -polarized light, we



would expect the polarization of the reflected to contain a non-zero  $p$  component because of the existence of a magnetism-induced electric dipole with the magnetic nanodisk. We concluded that the SLRs highlighted in cyan and brown in Figure 7.6 correspond to SLRs of pure optical origin while the one pointed in dark yellow stands for a magnetism-induced SLR due to an "artificial"  $p$  component in the light polarization induced by the induced MO dipole.

Figure 7.8 shows that this behaviour can be extended to other geometries keeping  $D = 150$  nm. For instance, extending the lattice period consistently redshifts the three resonances since the DO related to the lattice period increases with this parameter. We provide the resulting analysis for all the metasurface geometries in Appendix F. We want to stress that these data also emphasize the need to optimize the design of the magnetoplasmonic metasurface in order to induce a strong radiative coupling leading to a well-defined SLR with decent quality factor.

Figure 6.2 already points out that in  $[\text{Co/Gd/Pt}]_3$  metasurfaces with  $P = 450$  nm, a nanodisk diameter of 100 nm is preferred in comparison to a nanodisk diameter of 250 nm since the array resonance and the LSPR should be aligned to optimize the quality of the hybridization of the modes. Actually, Figure 7.9 expresses this statement in a different manner. We explained above that the first and third SLRs stand for SLRs of pure optical origin while the centered one exists due to the presence of magnetism. One can notice on Figure 7.9 that the first and third SLRs are pretty well defined for  $D = 100$  nm while it looks like a shoulder effect in case of  $D = 250$  nm. This proves that preliminary optimization of the metasurface geometry is crucial.

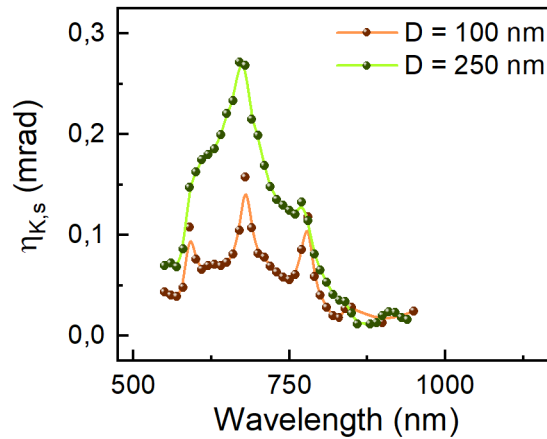


Figure 7.9: Kerr ellipticity spectra of  $[\text{Co/Gd/Pt}]_3$  metasurfaces with  $D = 100$  and  $250$  nm and  $P = 450$  nm for incoming  $s$ -polarized light. Solid lines are guides for the eye.

Finally, we aimed to reproduce 7.6(b) with non-magnetic system. For that, we probed the reflected intensity of the Pt metasurface ( $D = 200$  nm and  $P = 450$  nm) with incoming light

## CHAPTER 7. MAGNETISM-INDUCED SURFACE LATTICE RESONANCES

with 45°-polarization (half  $s$ , half  $p$ ). We almost crossed the transmission axis of the polarizer and analyzer, in the same configuration as when we measured the MO contrast in the magnetic systems. Then Figure 7.10 presents the spectra of intensity reflected by Pt metasurface with  $D = 200$  nm and  $P = 450$  nm and compares it with pure optical reflection spectra measured in Figure 7.7(c). This latter has been measured with polarizer and analyzer open. One can notice that the drops in intensity become rises, reproducing qualitatively what we observed in Figure 7.6(b) (but obtained for incoming  $s$ -polarized light). We explain this behaviour by the presence of two non zero  $s$  and  $p$  components in light polarization. For instance, when  $s$  component should lead to a drop in intensity (for instance at 600 nm), the  $p$  component rotates the light polarization, making it more aligned with analyzer transmission axis and finally leading to strong reflected signal.

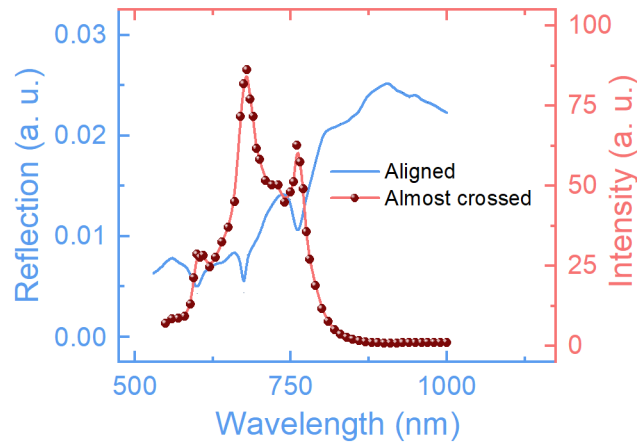


Figure 7.10: Spectra of intensity reflected by Pt metasurface with  $D = 200$  nm and  $P = 450$  nm for which polarizer and analyzer transmission axis are almost crossed as for the measurements of MO contrast (red circles). We compare this spectra with reflection spectra from Figure 7.7(c) (blue solid line). Solid lines are guides for the eyes.

## 7.4 Conclusion

Since the MO response enhanced of magnetic metasurfaces can be tuned by the incoming light wavelength, we showed that the MO contrast strongly depends on the wavelength. A good choice of light wavelength seems to be requisite for a reliable investigation of AO-HIS in such magnetoplasmonic platforms. After extracting the intrinsic Kerr rotation and ellipticity spectra from these metasurfaces, we explained how the use of an oblique incidence allows to distinguish

## **CHAPTER 7. MAGNETISM-INDUCED SURFACE LATTICE RESONANCES**

---

the SLRs of pure optical origin from magnetism-induced SLRs. We reproduced the observed trends in non-magnetic systems with a 45°-polarized light.



## Chapter 8

# Control of all-optical switching by means of Cu heat sinks

*In this chapter, we show that the maximum laser fluence and pulse length allowing all-optical magnetization reversal in thin continuous GdFeCo films strongly depend on the thickness of adjacent Cu heat sink layer. Varying this parameter from 5 nm to 900 nm almost does not affect the minimum fluence for observing light-induced magnetization switching but enlarges the fluence window for observing AOS. In addition, increasing heat sink thickness makes AOS possible above a laser pulse duration of 10 ps while 5 nm limits it at 4.5 ps. We claim that engineering the heat sink layer allows to quench the electron temperature below Curie temperature before magnetic order is completely lost.*

### 8.1 Motivations

Many aspects remain unclear regarding the underlying physics of AO-HIS in GdFeCo alloys induced by a single ultrafast arbitrary polarized laser pulse. AO-HIS, also known as temperature-induced magnetization switching (TIMS), is due to an out-of-equilibrium state between the electrons and the phonons in a ferrimagnetic system. It is believed that TIMS is a competition between exchange scattering and spin-orbit coupling in which gadolinium seems to be the best candidate since it exhibits zero net orbital momentum so that all the energy transferred from the laser pulse to the electrons is directly transferred to the spins that can exchange angular momentum resulting in AO-HIS. A direct demonstration of its exchange driven nature has been provided by Radu *et al.*<sup>8</sup>.

The more energy the electrons receive, the more spins can exchange angular momentum. In this context it is believed that the heat given by a single femtosecond laser pulse is required and sufficient to achieve magnetization reversal<sup>123</sup>. The recent demonstration of magnetization reversal induced by a transient joule heating coming from external picosecond current pulses confirms its thermal nature<sup>142</sup>. Also, the possibility to perform TIMS with picosecond light pulses addresses the questions whether the reversal mechanism occurs at femtosecond time scale or much later. Indeed, in Gd-based samples, TIMS exhibits mostly two steps of de- and remagnetization when the systems are subjected to ultrafast laser pulses. We aim to discuss these two contributions in this chapter.

A general trend shows that ferrimagnetic RE-TM alloys and multilayers experience TIMS when subjected to a single linearly polarized laser pulse when the applied fluence and laser pulse duration stay within mutually dependent bounds. For Gd-based samples, it is predicted that TIMS can not occur for pulse duration longer than 15 ps<sup>139,143</sup> but our results actually suggest that it could be performed until 25 ps. By studying a laser pulse length varying from 0.150 ps to 10 ps, we stress that increasing the adjacent Cu layer thickness from 5 nm to 900 nm extends the maximum fluence value for which TIMS can be achieved while the switching threshold fluence remains unchanged. A direct consequence is the increase of the maximal pulse length for which TIMS can be performed, up to 10 ps. Cu layer plays the role of a heat sink that allows to control the electronic temperature rise time, maximum value and decay in the magnetic layer. It is suggested that some of the key ingredients for TIMS are an initial electron temperature transient state that should overcome a certain threshold value, not necessarily the Curie point, followed by electronic system cooling below the Curie point before the magnetic order is completely lost.

## 8.2 Control of all-optical magnetization switching of GdFeCo with Cu heat sinks

Some theoretical studies concluded that an exchange scattering greater than angular momentum dissipation to the lattice through spin-orbit coupling is required for achieving TIMS<sup>136, 139, 153–166</sup>. They reproduced qualitatively the dependence of TIMS on Gd-concentration, applied fluence and initial temperature. However, the exact contribution of the transient electron temperature is still not fully understood raising the question of what electron temperature changes give rise to TIMS. The criteria displayed are definitely necessary and relevant but certainly not sufficient since they do not describe the interplay between heating and cooling rates resulting from temperature transients. That is why other key ingredients are needed for a better understanding of TIMS and further extension of TIMS for much larger laser pulse durations than the upper limit that was predicted at 15 ps.

In this context we varied the thickness of a Cu layer adjacent to a 10-nm thick  $\text{Gd}_{24}(\text{Fe}_{90}\text{Co}_{10})_{76}$ . This provided another degree of freedom for controlling the decay time of the transient electron dynamics for an applied laser fluence  $F_{las}$  while the pulse duration  $\tau_{las}$  determines the electron temperature rise time and maximum. We investigated thicknesses varying from 5 nm to 900 nm. Figure 8.1 presents an example of the impact of  $t_{Cu}$  and  $\tau_{las}$  for a fixed fluence on the electron temperature  $T_e$  on the GdFeCo layer. These dynamics have been calculated with the two-temperature model (2TM) whose parameters are detailed later.

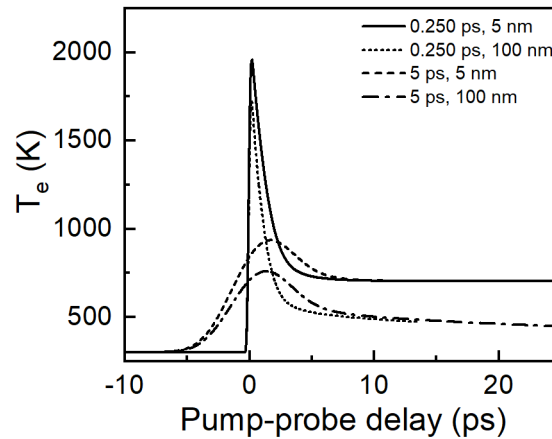


Figure 8.1: Transients dynamics of  $T_e$  within the GdFeCo layer in the studied samples calculated via the 2TM for  $F_{las} = 8 \text{ mJ/cm}^2$  and for combinations of  $t_{Cu}$  and  $\tau_{las}$  detailed in the legend.

We define  $F_{SW}$  and  $F_{max}$  as the minimum fluence to observe the appearance of a reversed

## CHAPTER 8. CONTROL OF ALL-OPTICAL SWITCHING BY MEANS OF CU HEAT SINKS

domain and stochastic multidomain formation, respectively. Then we studied the dependence of these factors on  $t_{Cu}$  and  $\tau_{las}$ . We deposited by DC magnetron sputtering the following heterostructures glass//Ta(3)/Cu(5)/Gd<sub>24</sub>(Fe<sub>90</sub>Co<sub>10</sub>)<sub>76</sub>(10)/Cu( $t_{Cu}$ )/Pt(5) where the numbers in parenthesis correspond to the layer thickness in nanometers. The first Ta and Cu are a requisite for the adhesion of the sample on the substrate and ensuring a perpendicularly magnetized sample<sup>427</sup>, respectively. We proceeded that way to make sure we could probe the magnetic state of the GdFeCo subjected to ultrafast laser pulses via MOKE images.

We relied on M. Hehn to provide heat sink wedges in which  $t_{Cu}$  varies linearly along the sample length over the following ranges in nanometers: [5,10], [10,15], [10, 20], [20, 30], [35, 70], [70, 105], [50, 100], [100, 150], [100, 200], [200, 300], [300, 600], and [600, 900]. All the samples were prepared at the same period with the same parameters in the PVD system to guarantee that all the GdFeCo layers exhibit identical composition, coercive field and  $F_{SW}$  for a fixed  $t_{Cu}$ .

### 8.2.1 Determination of threshold fluences and beam spot size

We extracted the thresholds  $F_{SW} / F_{max}$  from the dependence of the written domains / multidomain areas size  $r$  on the applied fluence  $F_{las}$ , the pulse duration  $\tau_{las}$  and  $t_{Cu}$  by means of MOKE images. In this work the wavelength on incoming light was fixed at 800 nm. First we want to point out that we used a consistent definition of the fluence derived from the spatial gaussian distribution of the laser beam. Indeed, let us propose three similar but not identical definitions from Liu's description<sup>144</sup> of a general threshold fluence  $F_{th}$

$$F_{th,0.5} = F_{0.5} \times e^{-\frac{1}{2}(\frac{r_{0.5}}{\sigma})^2} \quad (8.1a)$$

$$F_{th,1} = F_1 \times e^{-(\frac{r_1}{\sigma})^2} \quad (8.1b)$$

$$F_{th,2} = F_2 \times e^{-2(\frac{r_2}{\sigma})^2} \quad (8.1c)$$

where  $r$  is the radius of the area of interest. The fluence amplitudes  $F_{0.5}$ ,  $F_1$  and  $F_2$  are linked to the beam spot radius  $\sigma$  and the pulse energy  $E_p$  following

$$F_{0.5} = \frac{E_p}{2\pi\sigma^2} \quad (8.2a)$$



## CHAPTER 8. CONTROL OF ALL-OPTICAL SWITCHING BY MEANS OF CU HEAT SINKS

$$F_1 = \frac{E_p}{\pi\sigma^2} \quad (8.2b)$$

$$F_2 = \frac{2E_p}{\pi\sigma^2} \quad (8.2c)$$

From Equations (8.2) one can obtain the dependence of  $r_{SW}$  on the pulse energy

$$r_{0.5} = \sigma \sqrt{2 \times \ln\left(\frac{E_p}{2\pi\sigma^2 F_{th,0.5}}\right)} \quad (8.3a)$$

$$r_1 = \sigma \sqrt{\ln\left(\frac{E_p}{\pi\sigma^2 F_{th,1}}\right)} \quad (8.3b)$$

$$r_2 = \sigma \sqrt{\frac{1}{2} \times \ln\left(\frac{2E_p}{\pi\sigma^2 F_{th,2}}\right)} \quad (8.3c)$$

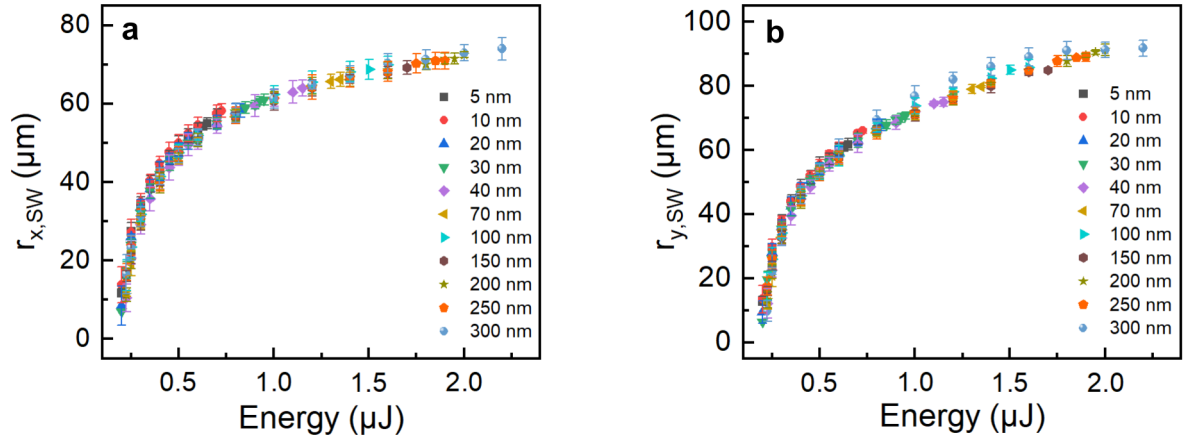


Figure 8.2: Written domain size  $r_{SW}$  as function of the pulse energy for various  $t_{Cu}$ . We distinguish the distributions of (a)  $r_{x,SW}$  and (b)  $r_{y,SW}$  to take into account that the beam spot is elliptical. Thus we can extract the beam spot radius along both in-plane directions  $x$  and  $y$  to properly convert any threshold energy into threshold fluence.

It appears from Equations (8.3) that calculating the written domains radius with one description while fitting their distribution with another would lead to wrong results. Then, fitting the experimental measurements with the inappropriate function does not affect neither the FWHM nor  $F_{th}$  but changes the estimation of the laser beam spot dimension. In this work we stuck to

## CHAPTER 8. CONTROL OF ALL-OPTICAL SWITCHING BY MEANS OF CU HEAT SINKS

the function from Equation (8.1b). Because the spot is never perfectly circular, we transformed Equation (8.3b) for general elliptical beams into

$$r_{x/y} = \sigma_{x/y} \sqrt{\ln\left(\frac{E_p}{\pi\sigma_x\sigma_y F_{th}}\right)} \quad (8.4)$$

where  $\sigma_x$  and  $\sigma_y$  correspond to the beam spot radius along  $x$  and  $y$  directions, respectively. Figure 8.2 presents the distribution of written domains size  $r_{SW}$  as function of the energy pulse for different  $t_{Cu}$ . The analysis reveals a beam spot radius around 48 micrometers and almost identical  $F_{SW}$  for any  $t_{Cu}$ .

### 8.2.2 Impact of heat sink thickness on TIMS

This preliminary analysis was necessary to transform any threshold energy into threshold fluence. This further allowed us to provide both  $F_{SW}$  and  $F_{max}$  as function of  $t_{Cu}$  as depicted in Figure 8.3. It points out that  $F_{SW}$  remains almost unaffected by an increasing  $t_{Cu}$  while the evolution of  $F_{max}$  with  $t_{Cu}$  mimics the dependence of the minimum ultrafast laser pulse fluence requested to melt gold films with the gold film thickness<sup>428</sup>.

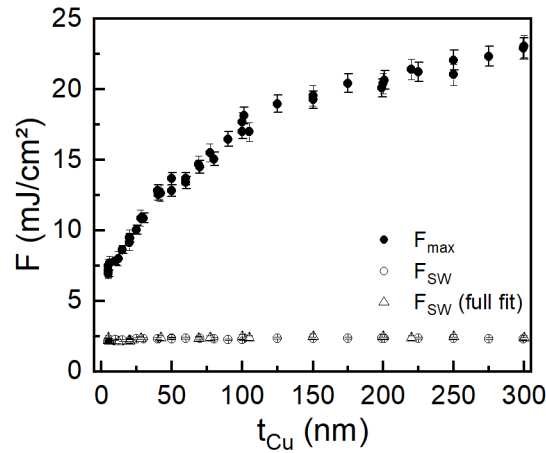


Figure 8.3: Evolution of  $F_{SW}$  and  $F_{max}$  with  $t_{Cu}$  for a single pulse length of 0.150 fs length with light coming with an incident angle of  $\approx 5$  deg. Open triangles represent results of the fits used to determine the beam size. Other threshold fluences for the appearance of magnetization reversal and multidomain state are described by open and closed circles, respectively

These results suggest that TIMS must requisite  $T_e$  transients to first overcome a certain critical value so that  $T_{e,max}(F_{SW}) \geq T_{e,crit}$ . This rise might be then followed by the cooling of the

## CHAPTER 8. CONTROL OF ALL-OPTICAL SWITCHING BY MEANS OF CU HEAT SINKS

electronic system below the Curie point  $T_C$  that should be performed fast enough to avoid demagnetization of the magnetic layer. Assuming this time limit is governed by the electron phonon thermalization time  $\tau_{e-ph}$ , then  $F_{max}$  is determined by the condition  $T_e(F_{max}, \tau_{e-ph}) \geq T_C$ . To address these questions, we studied the evolution of  $F_{SW}$  and  $F_{max}$  with  $t_{Cu}$  and  $\tau_{las}$ . The experimental configuration, for this investigation, involved an incidence angle of  $54^\circ$ .

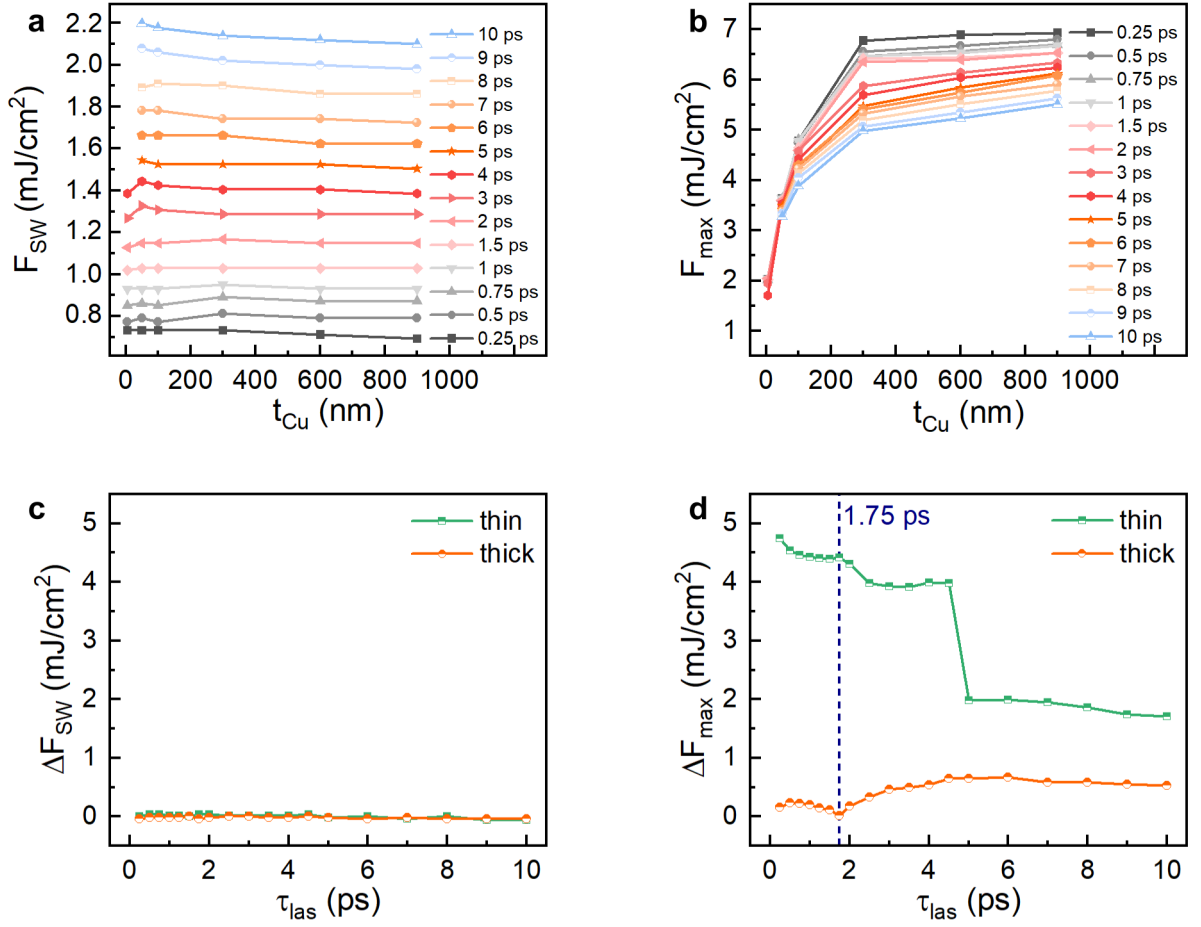


Figure 8.4: (a)  $F_{SW}$  and (b)  $F_{max}$  as function of  $t_{Cu}$  for several  $\tau_{las}$ . We detail the dependence of (c)  $\Delta F_{SW} = F_{SW}(300 \text{ nm}) - F_{SW}(5 \text{ nm})$  and (d)  $\Delta F_{max} = F_{max}(300 \text{ nm}) - F_{max}(5 \text{ nm})$  on  $\tau_{las}$ . Thin corresponds to  $\Delta F = F(300 \text{ nm}) - F(5 \text{ nm})$  for  $\tau_{las} \leq 4.5$  ps and  $F(300 \text{ nm}) - F(50 \text{ nm})$  for  $\tau_{las} \geq 5$  ps. Thick corresponds to  $\Delta F = F(900 \text{ nm}) - F(300 \text{ nm})$ .

In agreement with the 2TM calculations depicted in Figure 8.1 that point out that  $T_{e,max}$  is reduced for larger  $\tau_{las}$  but remains almost unaffected by variations of  $t_{Cu}$ , we observed experimentally on Figure 8.4(a) that  $F_{SW}$  tends to rise with the pulse duration  $\tau_{las}$  but seems to be almost independent of  $t_{Cu}$ . This means that TIMS, in a first step, is not determined by thermal

## CHAPTER 8. CONTROL OF ALL-OPTICAL SWITCHING BY MEANS OF CU HEAT SINKS

diffusion but by the capability of the electron bath to overcome a certain temperature leading to further enough exchange scattering. In this perspective, Figure 8.4(a) confirms that  $\tau_{las}$  tailors the heating rate, in other terms the rise of  $T_e$  transients. As expected, since longer pulse duration are associated to lower heating rate, then TIMS can only be achieved for larger  $F_{SW}$  compared to shorter pulse durations.

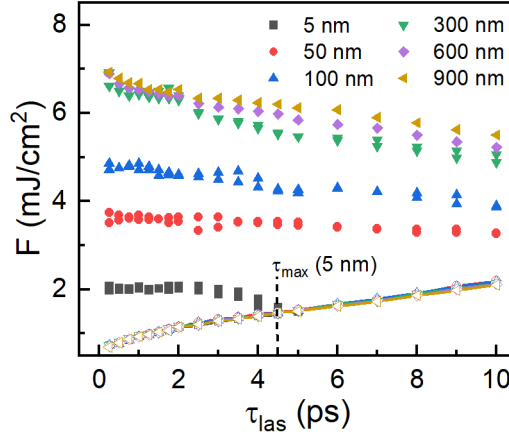


Figure 8.5:  $F_{SW}$  (open symbols with solid lines) and  $F_{max}$  (closed symbols) as function of  $\tau_{las}$  for various  $t_{Cu}$ . The dashed line gives the maximum pulse duration for the observation of TIMS with  $t_{Cu} = 5$  nm.

As we would have expected, Figure 8.4(b) shows that  $F_{max}$  consistently, for any  $\tau_{las}$ , rises with increasing heat sink thickness. We observed in Figure 8.4(d) that changes of  $F_{max}$ , for  $t_{Cu} \in [5, 300]$  nm is greater for short pulse durations, below 1.75ps, than for the longer ones. The opposite trend is given for thicker Cu layers. This finding might reflect the transition from fast, electron diffusivity dominated thermal transport to slow, phonon diffusivity dominated transport with increasing pulse length. We combined in Figure 8.5 both subfigures from Figure 8.4 to build the TIMS state diagram of the GdFeCo layer with 24% of Gd with different  $t_{Cu}$ .

We want to stress that the present state diagram, obtained in the same manner as in Wei's work<sup>141</sup>, emphasizes that the values of  $\tau_{las}$  reported for samples with  $t_{Cu} = 5$  nm does not reflect a weak exchange scattering but thermal erasure due to insufficiently cooled electrons. Indeed we performed TIMS on the same GdFeCo layer for  $\tau_{las}$  up to 10 ps but with adjacent Cu layer thicker than 50 nm. Figure 8.4 even suggests that longer pulse durations could also result in light-induced magnetization switching. We extrapolated linearly the data for  $t_{Cu} = 900$  nm according to Wei's work<sup>141</sup> and estimated that TIMS must be achievable for a maximum pulse length of 25 ps, much better than the upper limit predicted in the literature. Also, for a fixed value of  $\tau_{las}$ ,

making the heat sink thicker expands the fluence window where TIMS can be performed. This is a proof that the heat sinks play their role by cooling faster the electronic system below the Curie point so that a stochastic multidomain state is not observed. This effect becomes limited from  $t_{Cu} = 300$  nm since heat diffusion has a certain finite speed. These results support the statement that observing a stochastic multidomain state comes from an insufficient electron cooling, not a weak exchange scattering amplitude.

## 8.3 Theoretical approach

In an attempt to reproduce at least qualitatively our measurements, we combined a 2TM with the ultrafast spin dynamics model in ferrimagnets developed by Gridnev<sup>150–152</sup>. This theoretical framework has been computed by Q. Remy<sup>429</sup> and we now discuss the underlying methodology. We firstly detail the implementation of the 2TM.

### 8.3.1 First step : 2TM

We explain of the first step of the complete model has been implemented. Assuming that the electron specific heat  $C_e$  is proportional to  $T_e$  following  $C_e = \gamma T_e$ , we considered the set of equations

$$\gamma T_e \frac{\partial T_e}{\partial t} = \frac{\partial}{\partial z} \left( \kappa_e \frac{T_e}{T_p} \frac{\partial T_e}{\partial z} \right) - g_{e-p}(T_e - T_p) + S \quad (8.5a)$$

$$C_p \frac{\partial T_p}{\partial t} = \kappa_p \frac{\partial^2 T_p}{\partial z^2} + g_{e-p}(T_e - T_p) \quad (8.5b)$$

where  $C_e$  ( $C_p$ ),  $\kappa_e$  ( $\kappa_p$ ) and  $T_e$  ( $T_p$ ) is the electron specific heat, thermal conductivity and temperature, respectively.  $S$  stands for a source term. We assumed a non zero interfacial thermal conductance at Ta/glass interface only and we fixed it at  $100.10^6$  W.m<sup>-2</sup>.K<sup>-1</sup>. We also fixed  $T_e$  at 0 K in the substrate to take into account that electrons do not carry heat in insulators. Also initial  $T_e$  is defined at 300 K. We detail the parameters we used in Table 8.1.

Besides, the time and spatial steps have been chosen to be 0.01 fs and 0.25 nm, respectively, in order to converge the calculations. We refer to the Ph.D. thesis of Q. Remy for more technical details about the implementation<sup>429</sup>.

## CHAPTER 8. CONTROL OF ALL-OPTICAL SWITCHING BY MEANS OF CU HEAT SINKS

Material	$\gamma$ (JK <sup>-2</sup> m <sup>-3</sup> )	$\kappa_e$ (WK <sup>-1</sup> m <sup>-1</sup> )	$g_{e-p}$ (10 <sup>16</sup> WK <sup>-1</sup> m <sup>-3</sup> )	$C_p$ (10 <sup>6</sup> JK <sup>-1</sup> m <sup>-3</sup> )	$\kappa_p$ (WK <sup>-1</sup> m <sup>-1</sup> )
Cu <sup>28,430,431</sup>	98	300	7.5	3.43	5
Pt <sup>28,430,431</sup>	749	45	110	3.45	5
Ta	543	58	100	2.23	5
GdFeCo <sup>28,139</sup>	781	10.5	60	2.3	5
Glass	0	0	0	2	2

Table 8.1: Material parameters used for the 2TM implementation.

### 8.3.2 Second step : Spin dynamics

The model developed by Gridnev uses  $T_e$  calculated in the first step as an input. We neglected the dependence of  $T_e$  on magnetization<sup>151</sup>. Indeed we observed that this effect gives rise to unphysical electronic temperature raises, for specific fluences, due to the presence of a plateau (both magnetization amplitudes are close to zero) followed by a sudden rise of both sublattices magnetizations. This is a general feature of mean-field models of longitudinal magnetization dynamics<sup>136</sup>. It is however possible to overcome this issue by making all the parameters in use in the 2TM temperature-dependent<sup>432</sup>. It should be noted that the  $T_e$  used as an input in the spin dynamics model is an average along the magnetic layer thickness since the model of Gridnev assumes that any magnetic is homogeneously excited within its depth. Next we introduce the parameters requisite for the implementation of the spin dynamics model with the same notations as in Q. Remy's Ph.D. thesis<sup>429</sup>.

First, since the localized electrons exchange energy and angular momentum via the itinerant electrons, we need the observable of the average spin polarizations of each sublattice for the localized and itinerant electrons. Also, the dynamics is longitudinal along  $z$  axis, leading first to the average spin polarization  $\bar{S}_\nu^z$  of each sublattice  $\nu \in [A = \text{Gd}, B = \text{FeCo}]$

$$\bar{S}_\nu^z = S_\nu B_{S_\nu}(-\beta_e \Delta_\nu S_\nu) \quad (8.6)$$

where  $S_\nu$ ,  $B_{S_\nu}$  and  $\Delta_\nu = -J_\nu \bar{S}_\nu^z$  are the spin quantum number for any sublattice  $\nu$ , the Brillouin function related to  $S_\nu$  and the exchange splitting for any sublattice  $\nu$ , respectively. In particular, the exchange splitting depends on the exchange coupling  $J_\nu$  and the average spin polarization

## CHAPTER 8. CONTROL OF ALL-OPTICAL SWITCHING BY MEANS OF CU HEAT SINKS

of itinerant spins  $\bar{s}_\nu^z$ . Also  $\beta_e = 1/(k_B T_e)$ . Equation (8.6) holds true at equilibrium. Noting  $x$  the concentration of atom A, the spatially averaged conduction electrons spin polarization can be written as

$$\bar{s}^z = x\bar{s}_A^z + (1-x)\bar{s}_B^z \quad (8.7)$$

The terms  $\bar{s}_\nu^z$  are the average spin polarizations of each sublattice associated to the itinerant electrons. This latter depend on  $\bar{S}_\nu^z$ , the composition  $x$  and parameters  $\chi_{\mu\nu}$  following

$$\bar{s}_A^z = x\chi_{AA}\bar{S}_A^z + (1-x)\chi_{AB}\bar{S}_B^z \quad (8.8a)$$

$$\bar{s}_B^z = x\chi_{BA}\bar{S}_A^z + (1-x)\chi_{BB}\bar{S}_B^z \quad (8.8b)$$

This set of equations remains valid even in an out-of-equilibrium regime in opposite to Equations (8.6) and (8.7). Then the dynamics of  $\bar{S}_\nu^z = \sum_m m\rho_m^\nu / \sum_m \rho_m^\nu$  is determined by the diagonal terms of the localized spin density matrix since we deal by longitudinal dynamics. As in Q. Remy's Ph.D. thesis,  $m$  indexes one of the  $2S_\nu + 1$  localized spin states  $|\nu m\rangle$ <sup>429</sup>. The master rate equations that describes the localized spin density matrix dynamics is given by

$$\frac{d\rho_m^\nu}{dt} = W_{m,m+1}^\nu \rho_{m+1}^\nu + W_{m,m-1}^\nu \rho_{m-1}^\nu - (W_{m+1,m}^\nu + W_{m-1,m}^\nu) \rho_m^\nu \quad (8.9)$$

Here, the terms  $W_{m\pm 1,m}^\nu$  stand for transition rates, that Q. Remy, assuming any spin orientation transition to occur near the Fermi energy level, simplified into

$$W_{m\pm 1,m}^\nu = C_\nu S_m^{\nu\pm} (\Delta_\nu - \Delta\mu) \frac{e^{\mp\beta_e(\Delta_\nu - \Delta\mu)/2}}{2 \sinh(\beta_e(\Delta_\nu - \Delta\mu)/2)} \quad (8.10)$$

where  $\Delta\mu$  is the spin accumulation and  $S_m^{\nu\pm} = S_\nu(S_\nu + 1) - m(m \pm 1)$ . Q. Remy pointed out that Equation (8.10) softly differs from references<sup>150–152</sup> but is line with the work proposed by Beens *et al.*<sup>433</sup>. Also, in the same manner as Gridnev, Q. Remy defined its own  $C_\nu$  following

$$C_\nu = \frac{\pi}{2\hbar} J_\nu^2 \lambda_\nu^2 D_\uparrow(\epsilon_F) D_\downarrow(\epsilon_F) \quad (8.11)$$

where  $D_\downarrow(E_F)$  denotes the itinerant electrons density of state per atom at the Fermi level for spin up and down. Since we assumed in the 2TM that  $C_e = \gamma T_e$ , we could further calculate  $D_\downarrow(\epsilon_F) = 3\gamma / (\pi k_B^2 \rho)$  with  $\rho$  the number of atoms per unit volume that we estimated from the literature. Also the parameters  $\lambda_\nu$  have been intensively discussed in Q. Remy's work<sup>429</sup>. At equilibrium,  $\mu_\uparrow = \mu_\downarrow = \mu$ . Noting the number of conduction electrons  $N = N_\uparrow + N_\downarrow$ , one can

## CHAPTER 8. CONTROL OF ALL-OPTICAL SWITCHING BY MEANS OF CU HEAT SINKS

deduce the average spin polarization of itinerant electrons  $\bar{s}_{ie}^z = (N_\uparrow + N_\downarrow)\mu/(2N)$ . Then the spin accumulation can be rewritten following

$$\Delta\mu = (\bar{s}^z - \bar{s}_{ie}^z) \frac{D_\uparrow(\epsilon_F) + D_\downarrow(\epsilon_F)}{D_\uparrow(\epsilon_F)D_\downarrow(\epsilon_F)} \quad (8.12)$$

We deduced the final average itinerant spin dynamics that is governed by exchange scattering and spin-lattice relaxation according to

$$\frac{d\bar{s}^z}{dt} = -x \frac{d\bar{S}_A^z}{dt} - (1-x) \frac{d\bar{S}_B^z}{dt} - \frac{\bar{s}^z - \bar{s}_{ie}^z}{\tau_s} \quad (8.13)$$

where  $\tau_s$  stands for itinerant electrons spin relaxation time. According to the description of Gridnev, we considered a spin quantum number of 1 for the TM while we fixed it at 7/2 for the RE. We used the same exchange parameters as in his works. Q. Remy tuned  $\chi_{AA}$  and  $\chi_{BB}$  to fit with the corresponding  $T_C$  of Gd and FeCo while  $\chi_{AB}$  and  $\chi_{BA}$  have been adjusted to make  $T_M$  at room temperature for  $x = 25\%$  but also to make the itinerant electrons spin polarization near  $T_M$  small enough. We detail in Table 8.2 the parameters we considered to define the magnetic properties of the GdFeCo layer. We fixed the composition at 24% in the simulations and the Curie point at 635 K.

$\nu$	$A = \text{Gd}$	$B = \text{FeCo}$
$S_\nu$	7/2	1
$J_\nu$ (eV)	0.01	0.10
$\chi_{A\nu}$	0.48	-2.60
$\chi_{B\nu}$	0.40	1.35

Table 8.2: Equilibrium parameters for the implementation of the spin dynamics model.

Also the implementation of spin dynamics requisite other specific parameters that we itemize in Table 8.3. One could argue that the value of the spin relaxation time we considered is pretty low, however with the same order of magnitude as what is used in the literature<sup>433</sup>. There is no widely used value for  $\lambda_\nu$  so we fixed it at 1 for Gd and figured out that 0.04 for FeCo gives rise to qualitatively good dynamics.



$\nu$	$A = \text{Gd}$	$B = \text{FeCo}$
$\rho \text{ (m}^{-3}\text{)}$	$2.5 \cdot 10^{28}$	$2.5 \cdot 10^{28}$
$\tau_s \text{ (fs)}$	10	10
$\lambda_\nu$	1	0.04

Table 8.3: Other parameters for the implementation of the spin dynamics model.

### 8.3.3 Results

The implementation of such model allowed us to predict  $F_{SW}$  and  $F_{max}$  for the combinations of  $t_{Cu}$  and  $\tau_{las}$  that we used experimentally. For a given heat sink thickness and pulse duration, we increased progressively the applied fluence until we noticed that both sublattice spin orientations have been reversed. The transition from no spin orientation reversal to spin orientation switching is the signature of the threshold for performing TIMS. In this way we obtained  $F_{SW}$  and we illustrated this criteria in Figure 8.6.

Figures 8.6(a-d) detail the criterion for the transition no-TIMS/TIMS for  $t_{Cu} = 100$  nm and  $\tau_{las} = 0.25$  and 5 ps. For the longest (shortest) pulse duration,  $F_{SW}$  equals 5.0 (1.2) mJ/m<sup>2</sup> while the spin dynamics of both sublattices exhibit no-TIMS at 4.8 (1.1) mJ/m<sup>2</sup>. As we would expect, the maximum temperature attained in both configurations is higher for the largest fluence meaning that overcoming a critical value  $T_{e,crit}$  is requisite to observe TIMS. Interestingly, we noted for  $\tau_{las} = 5$  ps that  $T_e$  does not have to reach  $T_C$  to observe magnetization reversal meaning that reaching the Curie point does not seem to be a key ingredient for TIMS.

For a given heat sink thickness and pulse duration, we determined also  $F_{max}$  by exploring a wide range of fluences, starting from an applied from which TIMS can be achieved, until both spin sublattices do not change their magnetic orientations. As well as Figures 8.6(a-d), Figures 8.7(a-d) emphasize how we obtained  $F_{max}$  for  $t_{Cu} = 100$  nm. Then, we identified  $F_{max}$  at 16.0 and 12.8 mJ/cm<sup>2</sup> for  $\tau_{las} = 0.25$  and 5 ps, respectively. We noted that in the four configurations, the electronic bath cools down below the Curie point. However, Figures 8.7(e-h) highlight that  $T_e$  has to be lower than  $T_C$  before a certain characteristic time  $\tau_{lim}$  to prevent the formation of a stochastic multidomain state. Then, Figure 8.7 supports the statement that  $F_{max}$  is reached when the electronic system is not cooled well enough within a restricted period  $\tau_{lim}$ .

Figure 8.8 details reveals the dependence of  $F_{SW}$  (squares) and  $F_{max}$  (stars) on heat sink thickness for  $\tau_{las} = 0.25$  (black) and 5 ps (red). We qualitatively reproduced the experimental

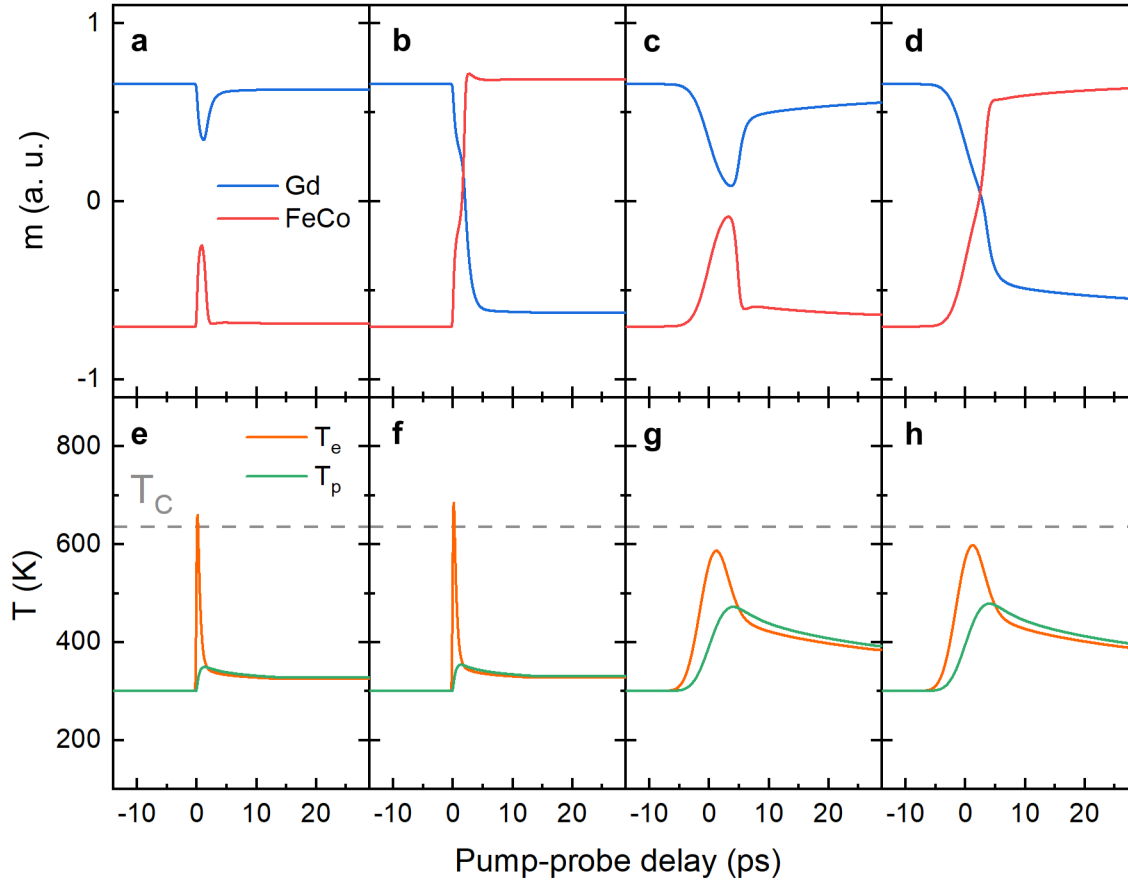


Figure 8.6: Spin dynamics simulation of both Gd and FeCo sublattices with  $t_{Cu} = 100$  nm and  $\tau_{las} =$  (a,b) 0.25 and (c,d) 5 ps. The applied fluence has been fixed to (a) 1.1, (b) 1.2, (c) 4.8 and (d) 5.0 mJ/cm<sup>2</sup>. Corresponding electron and phonon temperature dynamics in the GdFeCo layer for  $\tau_{las} =$  (e,f) 0.25 and (g,h) 5 ps. The applied fluence has been fixed to (e) 1.1, (f) 1.2, (g) 4.8 and (h) 5.0 mJ/cm<sup>2</sup>.

trend of Figure 8.4(a) since we observed that  $F_{SW}$  almost does not depend on the heat sink thickness and has been shown to rise with increasing  $\tau_{las}$  for a fixed  $t_{Cu}$ . Also, we noted a more pronounced increase of  $F_{max}$  for  $t_{Cu} \leq 300$  nm until it flattens for thicker heat sink layers, similar to what we obtained in Figure 8.4(b).

## 8.4 Conclusion

Our experimental results, supported by analytical calculations based on the implementation of a 2TM combined with a spin dynamics model, enable to identify a strategy to control TMS by

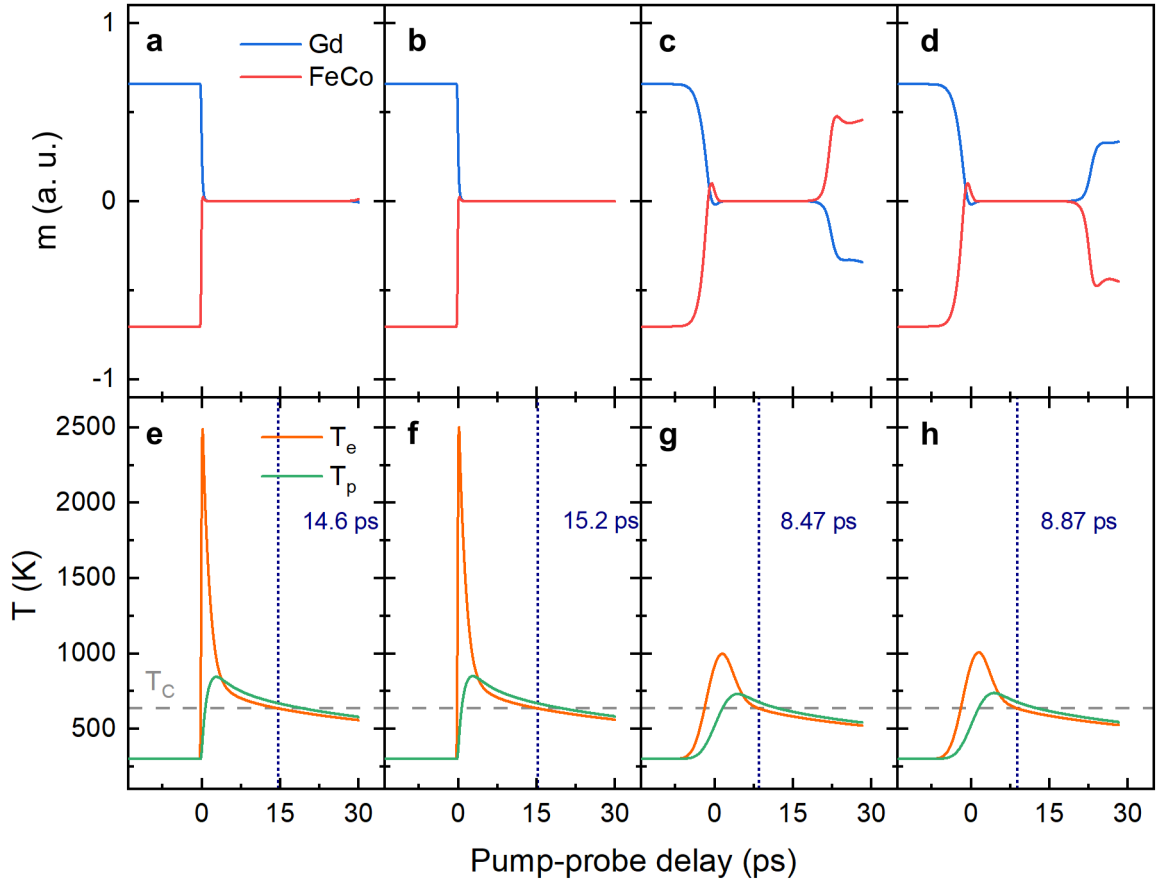


Figure 8.7: Spin dynamics simulation of both Gd and FeCo sublattices with  $t_{Cu} = 100$  nm and  $\tau_{las} =$  (a,b) 0.25 and (c,d) 5 ps. The applied fluence has been fixed to (a) 16.0, (b) 16.2, (c) 12.8 and (d) 13.0  $\text{mJ}/\text{cm}^2$ . Corresponding electron and phonon temperature dynamics in the GdFeCo layer for  $\tau_{las} =$  (e,f) 0.25 and (g,h) 5 ps. The applied fluence has been fixed to (e) 16.0, (f) 16.2, (g) 12.8 and (h) 13.0  $\text{mJ}/\text{cm}^2$ .

means of Cu heat sinks. In particular, the data suggest that TIMS could be performed for laser pulse duration of tens of picoseconds, for the considered concentration. We point out that only temperature erasure, due to unefficient cooling of the electronic system, is responsible for the formation of a stochastic multidomain state. Increasing  $t_{Cu}$  allows, for a given  $\tau_{las}$ , to achieve TIMS for a wider range of fluences. In this perspective, TIMS can be extended to longer  $\tau_{las}$ . We think that our results are promising for the integration of laser diodes producing long light pulses in the development of all-optical magnetic recording devices.

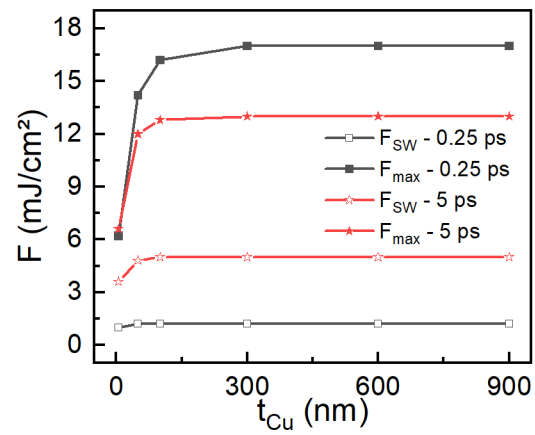


Figure 8.8: Threshold fluences  $F_{SW}$  and  $F_{max}$  as a function of  $t_{Cu}$  for light wavelength of 800 nm and pulse durations of 0.25 and 5 ps. The incidence angle has been fixed at 5°.

# Chapter 9

## Conclusion

The thesis focused on controlling the thermal nature of all-optical helicity-independent switching by means of plasmonics and heat sinks. We started by describing the magnetic properties of the materials we used and pointed out that these materials can have their magnetization deterministically reversed by an ultrafast arbitrary polarized single laser pulse. In particular, we discussed the underlying mechanism and stressed that all-optical helicity-independent switching is possible once exchange scattering is greater than spin-orbit coupling. In this context, Gd-based materials are ideal candidates since Gd exhibits zero net orbital momentum so that neither energy nor angular momentum can be dissipated from the electron system to the lattice. Then the angular momentum transfer from electrons to spins depends on how much energy is sent to the system. That is why this type of light-induced magnetization reversal is also called temperature-induced magnetization switching. We proposed in this thesis to use plasmonics to make all-optical helicity-independent switching more energy efficient since the excitation of a plasmonic mode leads to absorption enhancement within the target system. Plasmonics also provides the tools to manipulate light at nanoscale. This capability sounds of particular interest since the smallest written domains obtained by all-optical helicity-independent switching reach micrometer scale and we aim to combine plasmonics and AO-HIS to be more competitive in terms of areal density.

Thus we dedicated the next parts to the different strategies provided by plasmonics to enhance locally absorption. We finally decided to use the excitation of SLRs in periodic arrays of  $[\text{Co}/\text{Gd}/\text{Pt}]_N$  nanodisks. After reviewing the recent advancements in magnetoplasmonics related to its integration in future HAMR technologies but also the enhancement of all-optical helicity-independent switching and magneto-optical effects, we pointed out why this work is the next step towards the integration of plasmonics in future all-optical magnetic recording platforms.

## CHAPTER 9. CONCLUSION

Next we presented the experimental and numerical methods that were requisite to lead properly this thesis. After shortly introducing the thin film deposition techniques, we explained carefully how we obtained the nanostructures and how we characterized them with optical and magneto-optical characterizations. Since we worked on ultrafast magnetism, we considered the use of ultrafast lasers and we had the opportunity to install, under the watchful eye of J. Hohlfeld, our own laser system to perform MOKE microscopy whose pump and probe wavelengths were tunable. Also we pointed out that the design of magnetic metasurface is critical for obtaining a strong radiative coupling leading to a well-defined SLR. For this reason we simulated the optical behaviour of various systems with a finite element method to select sixteen metasurface geometries.

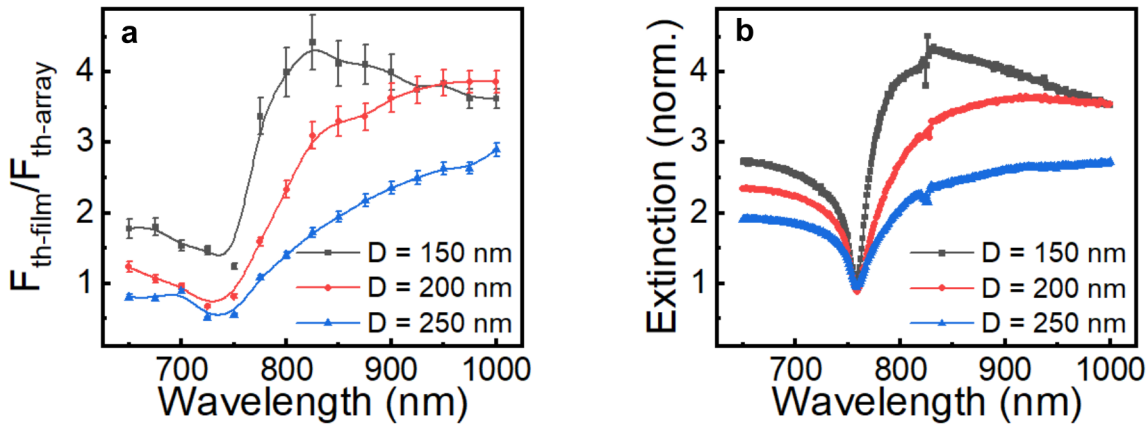


Figure 9.1: (a) Gain of energy as function of the wavelength for [Co/Gd/Pt]<sub>2</sub> metasurfaces with  $P = 500$  nm. The nanodisk diameters are indicated in the legend. (b) Extinction spectra of the same structures scaled by their filling factor and normalized by the extinction spectrum of the corresponding continuous film.

The remaining parts of this thesis have been dedicated to the experimental results that have been in some cases supported either by numerical simulations or by analytical calculations. This latter involved the implementation a two temperature model combined with a spin dynamics model developed initially by Gridnev<sup>150</sup>. This complete analytical approach has been computed by Q. Remy during his Ph.D. and has been applied in one of our projects<sup>429</sup>. First we considered periodic arrays of [Co/Gd/Pt]<sub>N</sub> nanodisks and we showed that, once we excited a SLR, we could achieve single pulse all-optical helicity-independent switching with a threshold switching fluence reduced by more than 4. A figure of merit is presented IN Figure 9.1. We pointed out that, for any wavelength, the reduction of threshold switching fluence for all-optical helicity-

independent switching for a given metasurface design can be determined by simple extinction measurements performed with a continuous wave laser.

While the continuous film exhibited toggle switching we revealed, after sending from one to eight consecutive laser pulses, that the metasurfaces experienced stochastic switching. Each nanodisk has been shown to own its proper switching probability and this latter depends only on nanodisk diameter. In particular we emphasized that the probability increases when the diameter reduces. We attributed this trend to a more homogeneous absorption distributed within the nanodisk when it gets smaller. In this way we identified a path for deterministic magnetization reversal in magnetoplasmonic metasurfaces.

In parallel, we showed that the excitation of collective resonances gives rise to magneto-optical activity enhancement due to a local electric field much greater than the incident one. Then we indicated that  $[\text{Co/Gd/Pt}]_N$  metasurfaces experienced a fivefold enhancement of the magneto-optical Faraday effect at the resonance condition. This observation led to the optimization of the magneto-optical contrast with the wavelength. This latter was absolutely required for having the greater SNR, allowing the best reliability of our analysis. Further processing of the magneto-optical contrast spectra gave us intrinsic Kerr rotation and ellipticity spectra. Since we probed the system at oblique incidence we revealed the existence of magnetism-induced surface lattice resonances. Since we broke the symmetry with a non normal angle of incidence, we could distinguish the surface lattice resonances of pure optical origin from the one induced by the hybridization of magneto-optical dipoles. A figure of merit of magnetism-induced surface lattice resonances is given in Figure 9.2.

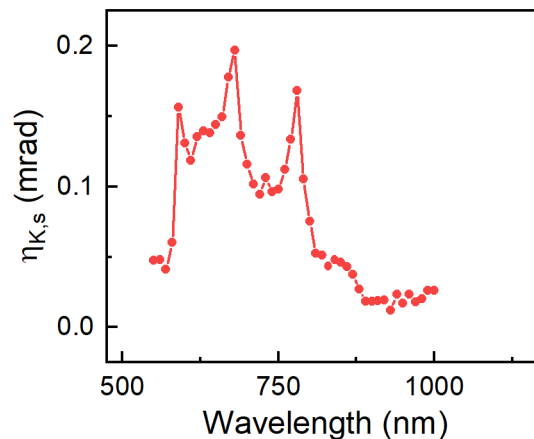


Figure 9.2: Kerr ellipticity spectra of  $[\text{Co/Gd/Pt}]_3$  metasurface with  $D = 150$  nm and  $P = 450$  nm.

We also investigated how all-optical helicity-independent switching depends on pulse du-

## CHAPTER 9. CONCLUSION

ration and applied fluence in GdFeCo continuous films. For that we added another degree of freedom by varying the thickness of an adjacent Cu layer from 5 to 900 nm, playing the role of a heat sink, while the pulse duration ranged from 0.150 ps to 10 ps. The results showed that the switching threshold fluence almost does not depend on heat sink thickness while the minimum fluence for the appearance of a stochastic multidomain state tends to be enlarged with increasing heat sink thickness. This enlargement opens the fluence window for achieving all-optical helicity-independent switching for longer pulse duration and our data suggests that all-optical helicity-independent switching could be performed at 25 ps. The last figure of merit of this thesis is presented in Figure 9.3.

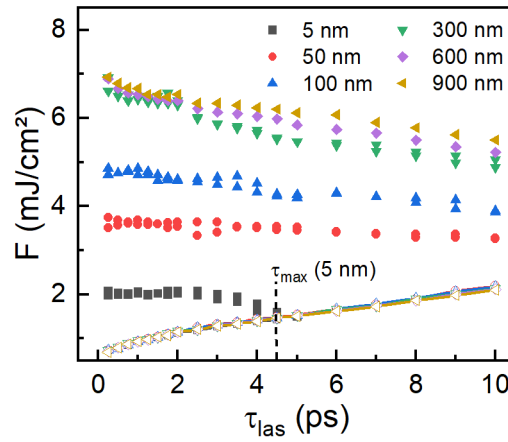


Figure 9.3:  $F_{SW}$  (open symbols with solid lines) and  $F_{max}$  (closed symbols) as function of  $\tau_{las}$  for various  $t_{Cu}$ . The dashed line gives the maximum pulse duration for the observation of TIMS with  $t_{Cu} = 5$  nm.

Theoretical calculations addressed the questions around the competition between the de- and remagnetization rates to explain our experimental results. The results highlighted that all-optical helicity-independent switching is observable once the transient electron temperature rises above a certain critical temperature (not necessarily the Curie point) followed by the cooling of the electron temperature below the Curie temperature that should occur before a certain characteristic time. In this context we highlighted that the breakdown of all-optical helicity-independent switching for longer pulse duration is not due to weak exchange scattering but unefficient electron bath cooling. We made it possible by means of heat sinks that allow to chill the electronic system efficiently.

Now we aim to propose new perspectives for further developments of magnetoplasmonic platforms. The integration of plasmonics in future HAMR technologies requires three key in-



gradients : a near field transducer<sup>5</sup>, a granular media and a heat sink. We focused on the last two aspects and we believed that an external plasmonic near field transducer could be useful to excite a surface lattice resonance. Due to the gaussian distribution of energy for an ultrafast laser pulse, one could reverse only one nanodisk located in the area of highest energy while the magnetization of the other would remain unaffected.

Hybrid systems involving non magnetic structures sound also of particular interest since they must, through the inverse Faraday effect, induce opto-magnetic field that might change the magnetic orientation in subsequent continuous thin films. In this context Hurst *et al.* described by means of a quantum hydrodynamic model the magnetic behaviour of small Au spherical nanoparticles subjected to circularly polarized light<sup>434</sup>. They found out that such light source can induce orbital magnetism density since electrons circulate around the particle. However they did not really address the transfer of angular momentum between the opto-magnetic field and the electron gas. Fortunately, Cheng *et al.* evidenced light-induced magnetism in Au nanoparticles colloids. They carefully distinguished the contributions of both the inverse Faraday effect and the optical Kerr effect and concluded, regarding the Kerr rotation dynamics, that the underlying mechanism creating light-induced magnetic moment in non-magnetic Au nanoparticles is different from the one driving the ultrafast spin dynamics in magnetic materials<sup>435</sup>. The connection between orbital momentum and the spin should be well addressed to include this kind of geometry.

Also, Bonod *et al.* proposed in 2019 a method based on genetic algorithm to optimize a Si antenna in order to induce a magnetic power density that is five times larger than widely used dielectric nanoantennas. This method is very powerful since it can optimize any plasmonic antenna based on simple criteria such as the material, the ratio magnetic power density over the electric power density or the resonance wavelength<sup>436</sup>. The same research group also designed in 2022 with the same method a plasmonic gold structure to induce an intense magnetic field pulse of 1.5 T over tens of femtoseconds<sup>437</sup>. Plasmonics-induced magnetic field, under the condition this latter lasts long enough to impact the magnetization of subsequent magnetic layer, seems to be a nice way to explore.



# Bibliography

- [1] Baibich, M. N. *et al.* Giant Magnetoresistance of (001)Fe/(001)Cr Magnetic Superlattices. *Physical Review Letters* **61**, 2472–2475 (1988). URL <https://doi.org/10.1103/PhysRevLett.61.2472>.
- [2] Binasch, G., Grünberg, P., Saurenbach, F. & Zinn, W. Enhanced magnetoresistance in layered magnetic structures with antiferromagnetic interlayer exchange. *Physical Review B* **39**, 4828–4830 (1989). URL <https://doi.org/10.1103/PhysRevB.39.4828>.
- [3] Rottmayer, R. E. *et al.* Heat-Assisted Magnetic Recording. *IEEE Transactions on Magnetics* **42**, 2417–2421 (2006). URL <https://doi.org/10.1109/TMAG.2006.879572>.
- [4] Kryder, M. H. *et al.* Heat Assisted Magnetic Recording. *Proceedings of the IEEE* **96**, 1810–1835 (2008). URL <https://doi.org/10.1109/JPROC.2008.2004315>.
- [5] Challener, W. A. *et al.* Heat-assisted magnetic recording by a near-field transducer with efficient optical energy transfer. *Nature Photonics* **3**, 220–224 (2009). URL <https://doi.org/10.1038/nphoton.2009.26>.
- [6] Beaurepaire, E., Merle, J. C., Daunois, A. & Bigot, J. Y. Ultrafast spin dynamics in ferromagnetic nickel. *Physical Review Letters* **76**, 4250–4253 (1996). URL <https://doi.org/10.1103/PhysRevLett.76.4250>.
- [7] Stanciu, C. D. *et al.* All-Optical Magnetic Recording with Circularly Polarized Light. *Physical Review Letters* **99**, 047601 (2007). URL <https://doi.org/10.1103/PhysRevLett.99.047601>.
- [8] Radu, I. *et al.* Transient ferromagnetic-like state mediating ultrafast reversal of antiferromagnetically coupled spins. *Nature* **472**, 205–209 (2011). URL <https://doi.org/10.1038/nature09901>.

## BIBLIOGRAPHY

---

- [9] Lambert, C. H. *et al.* All-optical control of ferromagnetic thin films and nanostructures. *Science* **345**, 1337–1340 (2014). URL <https://doi.org/10.1126/science.1253493>.
- [10] Lalieu, M. L., Peeters, M. J., Haenen, S. R., Lavrijsen, R. & Koopmans, B. Deterministic all-optical switching of synthetic ferrimagnets using single femtosecond laser pulses. *Physical Review B* **96**, 220411(R) (2017). URL <https://doi.org/10.1103/PhysRevB.96.220411>.
- [11] Lalieu, M. L., Lavrijsen, R. & Koopmans, B. Integrating all-optical switching with spintronics. *Nature Communications* **10**, 1–6 (2019). URL <https://doi.org/10.1038/s41467-018-08062-4>.
- [12] Li, P., Kools, T. J., Koopmans, B. & Lavrijsen, R. Ultrafast Racetrack Based on Compensated Co/Gd-Based Synthetic Ferrimagnet with All-Optical Switching. *Advanced Electronic Materials* **9**, 2200613 (2022). URL <https://doi.org/10.1002/aelm.202200613>.
- [13] Kent, A. D. & Worledge, D. C. A new spin on magnetic memories. *Nature Nanotechnology* **10**, 187–191 (2015). URL <https://doi.org/10.1038/nnano.2015.24>.
- [14] Parkin, S. & Yang, S. H. Memory on the racetrack. *Nature Nanotechnology* **10**, 195–198 (2015). URL <https://doi.org/10.1038/nnano.2015.41>.
- [15] Emori, S., Bono, D. C. & Beach, G. S. D. Interfacial current-induced torques in Pt / Co / GdOx. *Applied Physics Letters* **101**, 042405 (2012). URL <https://doi.org/10.1063/1.4737899>.
- [16] Emori, S., Bauer, U., Ahn, S. M., Martinez, E. & Beach, G. S. Current-driven dynamics of chiral ferromagnetic domain walls. *Nature Materials* **12**, 611–616 (2013). URL <https://doi.org/10.1038/nmat3675>.
- [17] Ryu, K. S., Thomas, L., Yang, S. H. & Parkin, S. Chiral spin torque at magnetic domain walls. *Nature Nanotechnology* **8**, 527–533 (2013). URL <https://doi.org/10.1038/nnano.2013.102>.
- [18] Kimel, A. *et al.* The 2022 magneto-optics roadmap. *Journal of Physics D: Applied Physics* **55**, 463003 (2022). URL <https://doi.org/10.1088/1361-6463/ac8da0>.

- [19] Walford, J. N., Porto, J.-A., Carminati, R. & Greffet, J.-J. Theory of near-field magneto-optical imaging. *Journal of the Optical Society of America A* **19**, 572–583 (2002). URL <https://doi.org/10.1364/josaa.19.000572>.
- [20] Gramotnev, D. K. & Bozhevolnyi, S. I. Plasmonics beyond the diffraction limit. *Nature Photonics* **4**, 83–91 (2010). URL <https://doi.org/10.1038/nphoton.2009.282>.
- [21] Stockman, M. I. *et al.* Roadmap on plasmonics. *Journal of Optics* **20**, 043001 (2018). URL <https://doi.org/10.1088/2040-8986/aaa114>.
- [22] Zheng, Y. B., Kiraly, B., Weiss, P. S. & Huang, T. J. Molecular plasmonics for biology and nanomedicine. *Nanomedicine* **7**, 751–770 (2012). URL <https://doi.org/10.2217/nmm.12.30>.
- [23] Zograf, G. P. *et al.* All-Optical Nanoscale Heating and Thermometry with Resonant Dielectric Nanoparticles for Controllable Drug Release in Living Cells. *Laser and Photonics Reviews* **14**, 1900082 (2020). URL <https://doi.org/10.1002/lpor.201900082>.
- [24] Atwater, H. A. & Polman, A. Plasmonics for improved photovoltaic devices. *Nature Materials* **9**, 205–213 (2010). URL <https://doi.org/10.1038/nmat2629>.
- [25] Linic, S., Christopher, P. & Ingram, D. B. Plasmonic-metal nanostructures for efficient conversion of solar to chemical energy. *Nature Materials* **10**, 911–921 (2011). URL <https://doi.org/10.1038/nmat3151>.
- [26] Landau, L. & Lifshitz, E. On the theory of the dispersion of magnetic permeability in ferromagnetic bodies. *Physikalische Zeitschrift der Sowjetunion* **8**, 153–169 (1935). URL <https://doi.org/10.1016/b978-0-08-036364-6.50008-9>.
- [27] du Trémollet, E. *Magnétisme, I- Fondements* (EDP Sciences, 2000).
- [28] Kittel, C. *Introduction to Solid State Physics* (John Wiley & Sons, 2004), 8th edn. URL <https://www.wiley.com/en-us/Introduction+to+Solid+State+Physics%2C+8th+Edition-p-9780471415268>.
- [29] Gilbert, T. L. A Phenomenological Theory of Damping in Ferromagnetic Materials. *IEEE Transactions on Magnetics* **40**, 3443–3449 (2004). URL <https://doi.org/10.1109/TMAG.2004.836740>.

## BIBLIOGRAPHY

---

- [30] Heinrich, B., Urban, R. & Woltersdorf, G. Magnetic relaxation in metallic films: Single and multilayer structures. *Journal of Applied Physics* **91**, 7523–7525 (2002). URL <https://doi.org/10.1063/1.1447215>.
- [31] Suhl, H. Theory of the magnetic damping constant. *IEEE Transactions on Magnetics* **34**, 1834 (1998). URL <https://doi.org/10.1109/20.706720>.
- [32] Arias, R. & Mills, D. L. Extrinsic contributions to the ferromagnetic resonance response of ultrathin films. *Physical Review B - Condensed Matter and Materials Physics* **60**, 7395–7409 (1999). URL <https://doi.org/10.1103/PhysRevB.60.7395>.
- [33] Pati, S. P. Influence on the Gilbert damping of yttrium-iron-garnet films by the spin-pumping effect. *Materials Science in Semiconductor Processing* **107**, 104821 (2020). URL <https://doi.org/10.1016/j.mssp.2019.104821>.
- [34] Tserkovnyak, Y., Brataas, A. & Bauer, G. E. Spin pumping and magnetization dynamics in metallic multilayers. *Physical Review B - Condensed Matter and Materials Physics* **66**, 224403 (2002). URL <https://doi.org/10.1103/PhysRevB.66.224403>.
- [35] Tserkovnyak, Y., Brataas, A., Bauer, G. E. & Halperin, B. I. Nonlocal magnetization dynamics in ferromagnetic heterostructures. *Reviews of Modern Physics* **77**, 1375–1421 (2005). URL <https://doi.org/10.1103/RevModPhys.77.1375>.
- [36] Moorjani, K. & Coey, J. M. D. *Magnetic Glasses* (Amsterdam, 1984).
- [37] Campbell, I. A. Indirect exchange for rare earths in metals. *Journal of Physics F: Metal Physics* **2**, L47 (1972). URL <https://doi.org/10.1088/0305-4608/2/3/004>.
- [38] Kirchmayr, H. *et al.* Magnetic Order of the Compound Series RE<sub>6</sub> (M<sub>x</sub>Fe<sub>1-x</sub>)<sub>23</sub> (RE = Y, Gd). *Journal de Physique Colloques* **32**, C1 665 (1971). URL <https://doi.org/10.1051/jphyscol:19711231>.
- [39] Harris, R., Plischke, M. & Zuckermann, M. J. New Model for Amorphous Magnetism. *Physical Review Letters* **31**, 160–162 (1973). URL <https://doi.org/10.1103/PhysRevLett.31.160>.
- [40] Coey, J. M. Amorphous magnetic order. *Journal of Applied Physics* **49**, 1646–1652 (1978). URL <https://doi.org/10.1063/1.324880>.

- [41] Spano, M. L. & Rhyne, J. J. Suppression of long-range order by random fields in Tb<sub>x</sub>Fe<sub>1-x</sub> alloys. *Journal of Applied Physics* **57**, 3303–3305 (1985). URL <https://doi.org/10.1063/1.335129>.
- [42] Hadjipanayis, G., Sellmyer, D. J. & Brandt, B. Rare-earth-rich metallic glasses. I. Magnetic hysteresis. *Physical Review B* **23**, 3349–3354 (1981). URL <https://doi.org/10.1103/PhysRevB.23.3349>.
- [43] Rebouillat, J. P., Lienard, A., Coey, J. M., Arrese-Boggiano, R. & Chappert, J. Magnetic structures and properties of the amorphous alloys DyT<sub>3</sub>; T = Fe, Co, Ni. *Physica B+C* **86-88**, 773–774 (1977). URL [https://doi.org/10.1016/0378-4363\(77\)90680-5](https://doi.org/10.1016/0378-4363(77)90680-5).
- [44] Pickart, S. J., Rhyne, J. J. & Alperin, H. A. Anomalous Small-Angle Magnetic Scattering from Amorphous TbFe<sub>2</sub> and YFe<sub>2</sub>. *Physical Review Letters* **33**, 424–427 (1974). URL <https://doi.org/10.1103/PhysRevLett.33.424>.
- [45] Rhyne, J. J., Schelleng, J. H. & Koon, N. C. Anomalous magnetization of amorphous TbFe<sub>2</sub>, GdFe<sub>2</sub>, and YFe<sub>2</sub>. *Physical Review B* **10**, 4672–4679 (1974). URL <https://doi.org/10.1103/PhysRevB.10.4672>.
- [46] Coey, J. M. D., McGuire, T. R. & Tissier, B. Amorphous Dy-Cu: Random spin freezing in the presence of strong local anisotropy. *Physical Review B* **24**, 1261–1273 (1981). URL <https://doi.org/10.1103/PhysRevB.24.1261>.
- [47] Gambino, R. J., Chaudhari, P. & Cuomo, J. J. Amorphous Magnetic Materials. *AIP Conference Proceedings* **18**, 578–591 (1974). URL <https://doi.org/10.1063/1.3141775>.
- [48] Chaudhari, P., Cuomo, J. J. & Gambino, R. J. Amorphous metallic films for magneto-optic applications. *Applied Physics Letters* **22**, 337–339 (1973). URL <https://doi.org/10.1063/1.1654662>.
- [49] Gambino, R. J. & Cuomo, J. J. Selective resputtering-induced anisotropy in amorphous films. *Journal of Vacuum Science and technology* **15**, 296–301 (1978). URL <https://doi.org/10.1116/1.569574>.
- [50] Taylor, R. C. & Gangulee, A. Magnetization and magnetic anisotropy in evaporated GdCo amorphous films. *Journal of Applied Physics* **47**, 4666–4668 (1976). URL <https://doi.org/10.1063/1.322397>.

## BIBLIOGRAPHY

---

- [51] Rehr, J. J., Mustre de Leon, J., Zabinsky, S. I. & Albers, R. C. Theoretical X-ray Absorption Fine Structure Standards. *Journal of the American Chemical Society* **113**, 5135–5140 (1991). URL <https://doi.org/10.1021/ja00014a001>.
- [52] Rehr, J. J., Albers, R. C. & Zabinsky, S. I. High-order multiple-scattering calculations of x-ray-absorption fine structure. *Physical Review Letters* **69**, 3397–3400 (1992). URL <https://doi.org/10.1103/PhysRevLett.69.3397>.
- [53] Erbil, A., Cargill, G. S., Frahm, R. & Boehme, R. F. Total-electron-yield current measurements for near-surface extended x-ray-absorption fine structure. *Physical Review B* **37**, 2450–2464 (1988). URL <https://doi.org/10.1103/PhysRevB.37.2450>.
- [54] Harris, V. G., Aylesworth, K. D., Das, B. N., Elam, W. T. & Koon, N. C. Structural Origins of Magnetic Anisotropy in Sputtered Amorphous Tb-Fe Films. *Physical Review Letters* **69**, 1939–1942 (1992). URL <https://doi.org/10.1103/PhysRevLett.69.1939>.
- [55] Harris, V. G., Elam, W. T. & Koon, N. C. Deposition-temperature dependence of structural anisotropy in amorphous Tb-Fe films. *Physical Review B* **49**, 3637(R) (1994). URL <https://doi.org/10.1103/PhysRevB.49.3637>.
- [56] Hellman, F. & Gyorgy, E. M. Growth-induced magnetic anisotropy in amorphous Tb-Fe. *Physical Review Letters* **68**, 1391–1394 (1992). URL <https://doi.org/10.1103/PhysRevLett.68.1391>.
- [57] Harris, V. G. & Pokhil, T. Selective-resputtering-induced perpendicular magnetic anisotropy in amorphous TbFe films. *Physical Review Letters* **87**, 672071–672074 (2001). URL <https://doi.org/10.1103/PhysRevLett.87.067207>.
- [58] Hansen, P., Klahn, S., Clausen, C., Much, G. & Witter, K. Magnetic and magneto-optical properties of rare-earth transition-metal alloys containing Gd, Tb, Fe, Co. *Journal of Applied Physics* **66**, 756–767 (1989). URL <https://doi.org/10.1063/1.343551>.
- [59] Zhang, W., Li, C., Su, X. & Han, K. An Updated Evaluation of the Fe-Gd (Iron-Gadolinium) System. *Journal of Phase Equilibria* **19**, 56–63 (1998). URL <https://doi.org/10.1361/105497198770342751>.
- [60] Ding, M. & Poon, S. J. Tunable perpendicular magnetic anisotropy in GdFeCo amorphous films. *Journal of Magnetism and Magnetic Materials* **339**, 51–55 (2013). URL <http://dx.doi.org/10.1016/j.jmmm.2013.03.007>.



- [61] Chimata, R. *et al.* All-thermal switching of amorphous Gd-Fe alloys: Analysis of structural properties and magnetization dynamics. *Physical Review B - Condensed Matter and Materials Physics* **92**, 094411 (2015). URL <https://doi.org/10.1103/PhysRevB.92.094411>. 1508.05972.
- [62] Ostler, T. A. *et al.* Crystallographically amorphous ferrimagnetic alloys: Comparing a localized atomistic spin model with experiments. *Physical Review B - Condensed Matter and Materials Physics* **84**, 024407 (2011). URL <https://doi.org/10.1103/PhysRevB.84.024407>.
- [63] Hansen, P., Klahn, S., Clausen, C., Much, G. & Witter, K. Magnetic and magneto-optical properties of rare-earth transition-metal alloys containing Dy, Ho, Fe, Co. *Journal of Applied Physics* **69**, 3194–3207 (1991). URL <https://doi.org/10.1063/1.348561>.
- [64] Stanciu, C. D. *et al.* Ultrafast spin dynamics across compensation points in ferrimagnetic GdFeCo: The role of angular momentum compensation. *Physical Review B - Condensed Matter and Materials Physics* **73**, 220402(R) (2006). URL <https://doi.org/10.1103/PhysRevB.73.220402>.
- [65] Jensen, J. & Mackintosh, A. *Rare Earth Magnetism* (Clarendon Press, Oxford, 1991). URL [http://www.fys.ku.dk/~sim\\$jjensen/Book/Ebook.pdf](http://www.fys.ku.dk/~sim$jjensen/Book/Ebook.pdf).
- [66] Binder, M. *et al.* Magnetization dynamics of the ferrimagnet CoGd near the compensation of magnetization and angular momentum. *Physical Review B - Condensed Matter and Materials Physics* **74**, 134404 (2006). URL <https://doi.org/10.1103/PhysRevB.74.134404>.
- [67] Kim, K. J. *et al.* Fast domain wall motion in the vicinity of the angular momentum compensation temperature of ferrimagnets. *Nature Materials* **16**, 1187–1192 (2017). URL <https://doi.org/10.1038/nmat4990>.
- [68] Hirata, Y. *et al.* Correlation between compensation temperatures of magnetization and angular momentum in GdFeCo ferrimagnets. *Physical Review B* **97**, 2203403(R) (2018). URL <https://doi.org/10.1103/PhysRevB.97.220403>.
- [69] Anisimov, S. I., Kapeliovich, B. L. & Perel'man, T. L. Electron emission from metal surfaces exposed to ultrashort laser pulses. *Zhurnal Eksperimentalnoi i Teoreticheskooi Fiziki* **66**, 776–781 (1974). URL <https://ui.adsabs.harvard.edu/abs/1974ZhETF.66..776A>.

## BIBLIOGRAPHY

---

- [70] G. L. Eesley. Observation of Nonequilibrium Electron Heating in Copper. *Phys. Rev. Lett.* **25**, 2140 (1970). URL <https://doi.org/10.1103/PhysRevLett.51.2140>.
- [71] Brorson, S. D., Fujimoto, J. G. & Ippen, E. P. Femtosecond Electronic Heat-Transport Dynamics in Thin Gold Films. *Physical Review Letters* **59**, 1962–1965 (1987). URL <https://doi.org/10.1103/PhysRevLett.59.1962>.
- [72] Elsayed-Ali, H. E., Juhasz, T., Smith, G. O. & Bron, W. E. Femtosecond thermorefectivity and thermotransmissivity of polycrystalline and single-crystalline gold films. *Physical Review B* **43**, 4488–4491 (1991). URL <https://doi.org/10.1103/PhysRevB.43.4488>.
- [73] Schoenlein, R. W., Lin, W. Z., Fujimoto, J. G. & Eesley, G. L. Femtosecond Studies of Nonequilibrium Electronic Processes in Metals. *Physical Review Letters* **58**, 1680–1683 (1987). URL <https://doi.org/10.1103/PhysRevLett.58.1680>.
- [74] Hohlfeld, J., Müller, J. G., Wellershoff, S. S. & Matthias, E. Time-resolved thermorefectivity of thin gold films and its dependence on film thickness. *Applied Physics B: Lasers and Optics* **64**, 387–390 (1997). URL <https://doi.org/10.1007/s003400050189>.
- [75] Hicks, J. M., Urbach, L. E., Plummer, E. W. & Dai, H.-I. Can Pulsed Laser Excitation of Surfaces Be Described by a Thermal Model ? *Physical Review Letters* **61**, 2588–2591 (1988). URL <https://doi.org/10.1103/PhysRevLett.61.2588>.
- [76] Elsayed-Ali, H. E., Norris, T. B., Pessot, M. A. & Mourou, G. A. Time-Resolved Observation of Electron-Phonon Relaxation in Copper. *Physical Review Letters* **58**, 1212–1215 (1987). URL <https://doi.org/10.1103/PhysRevLett.58.1212>.
- [77] Hohlfeld, J., Grosenick, D., Conrad, U. & Matthias, E. Femtosecond time-resolved reflection second-harmonic generation on polycrystalline copper. *Applied Physics A Materials Science and Processing* **60**, 137–142 (1995). URL <https://doi.org/10.1007/BF01538238>.
- [78] Juhasz, T., Elsayed-Ali, H. E., Smith, G. O., Suáez, C. & Bron, W. E. Direct measurements of the transport of nonequilibrium electrons in gold films with different crystal structures. *Physical Review B* **48**, 488–491 (1993). URL <https://doi.org/10.1103/PhysRevB.48.15488>.

- [79] Hohlfeld, J. *et al.* Electron and lattice dynamics following optical excitation of metals. *Chemical Physics* **251**, 237–258 (2000). URL [https://doi.org/10.1016/S0301-0104\(99\)00330-4](https://doi.org/10.1016/S0301-0104(99)00330-4).
- [80] Knorren, R., Bennemann, K. H., Burgermeister, R. & Aeschlimann, M. Dynamics of excited electrons in copper and ferromagnetic transition metals: Theory and experiment. *Physical Review B* **61**, 9427–9440 (2000). URL <https://doi.org/10.1103/PhysRevB.61.9427>.
- [81] Aeschlimann, M. *et al.* Transport and dynamics of optically excited electrons in metals. *Applied Physics A: Materials Science and Processing* **71**, 485–491 (2000). URL <https://doi.org/10.1007/s00339000070>.
- [82] Vaterlaus, A., Beutler, T. & Meier, F. Spin-lattice relaxation time of ferromagnetic gadolinium determined with time-resolved spin-polarized photoemission. *Physical Review Letters* **67**, 3314–3317 (1991). URL <https://doi.org/10.1103/PhysRevLett.67.3314>.
- [83] Hübner, W. & Bennemann, K. Simple theory for spin-lattice relaxation in metallic rare-earth ferromagnets. *Physical Review B - Condensed Matter and Materials Physics* **53**, 3422–3427 (1996). URL <https://doi.org/10.1103/PhysRevB.53.3422>.
- [84] Koopmans, B., Van Kampen, M., Kohlhepp, J. T. & De Jonge, W. J. Ultrafast magneto-optics in nickel: magnetism or optics? *Physical Review Letters* **85**, 844–847 (2000). URL <https://doi.org/10.1103/PhysRevLett.85.844>.
- [85] Hohlfeld, J., Matthias, E., Knorren, R. & Bennemann, K. H. Nonequilibrium Magnetization Dynamics of Nickel. *Physical Review Letters* **78**, 4861–4864 (1997). URL <https://doi.org/10.1103/PhysRevLett.78.4861>.
- [86] Conrad, U., Güdde, J., Jähnke, V. & Matthias, E. Ultrafast electron and magnetization dynamics of thin Ni and Co films on Cu(001) observed by time-resolved SHG. *Applied Physics B: Lasers and Optics* **68**, 511–517 (1999). URL <https://doi.org/10.1007/s003400050658>.
- [87] Scholl, A., Baumgarten, L., Jacquemin, R. & Eberhardt, W. Ultrafast spin dynamics of ferromagnetic thin films observed by fs spin-resolved two-photon photoemission. *Physical Review Letters* **79**, 5146–5149 (1997). URL <https://doi.org/10.1103/PhysRevLett.79.5146>.

## BIBLIOGRAPHY

---

- [88] Stamm, C. *et al.* Femtosecond modification of electron localization and transfer of angular momentum in nickel. *Nature Materials* **6**, 740–743 (2007). URL <https://doi.org/10.1038/nmat1985>.
- [89] Koopmans, B., Ruigrok, J. J., Dalla Longa, F. & De Jonge, W. J. Unifying ultrafast magnetization dynamics. *Physical Review Letters* **95**, 267207 (2005).
- [90] Cinchetti, M. *et al.* Spin-Flip Processes and Ultrafast Magnetization Dynamics in Co: Unifying the Microscopic and Macroscopic View of Femtosecond Magnetism. *Physical Review Letters* **97**, 177201 (2006). URL <https://doi.org/10.1103/PhysRevLett.97.177201>. 0605272.
- [91] Carpena, E. *et al.* Dynamics of electron-magnon interaction and ultrafast demagnetization in thin iron films. *Physical Review B - Condensed Matter and Materials Physics* **78**, 174422 (2008). URL <https://doi.org/10.1103/PhysRevB.78.174422>.
- [92] Krauß, M. *et al.* Ultrafast demagnetization of ferromagnetic transition metals: The role of the Coulomb interaction. *Physical Review B - Condensed Matter and Materials Physics* **80**, 180407(R) (2009). URL <https://doi.org/10.1103/PhysRevB.80.180407>.
- [93] Koopmans, B. *et al.* Explaining the paradoxical diversity of ultrafast laser-induced demagnetization. *Nature Materials* **9**, 259–265 (2010). URL <https://doi.org/10.1038/nmat2593>.
- [94] Schmidt, A. B. *et al.* Ultrafast Magnon Generation in an Fe Film on Cu(100). *Physical Review Letters* **105**, 197401 (2010). URL <https://doi.org/10.1103/PhysRevLett.105.197401>.
- [95] Mueller, B. Y. *et al.* Feedback Effect during Ultrafast Demagnetization Dynamics in Ferromagnets. *Physical Review Letters* **111**, 167204 (2013). URL <https://doi.org/10.1103/PhysRevLett.111.167204>.
- [96] Carva, K., Battiato, M., Legut, D. & Oppeneer, P. M. Ab initio theory of electron-phonon mediated ultrafast spin relaxation of laser-excited hot electrons in transition-metal ferromagnets. *Physical Review B - Condensed Matter and Materials Physics* **87**, 184425 (2013). URL <https://doi.org/10.1103/PhysRevB.87.184425>. 1305.3511.
- [97] Weiss, P. & Forrer, R. Aimantation et phénomène magnéto-calorique du nickel. *Ann. Phys.* 153–213 (1926). URL <https://doi.org/10.1051/anphys/192610050153>.

- [98] Fähnle, M. Comparison of theories of fast and ultrafast magnetization dynamics. *Journal of Magnetism and Magnetic Materials* **469**, 28–29 (2019). URL <https://doi.org/10.1016/j.jmmm.2018.08.015>.
- [99] Kaganov, M. I., Lifschitz, I. M. & Tanatrov, L. V. Relaxation between Electrons and the Crystalline Lattice. *Soviet Physics JETP* **4**, 173–178 (1957). URL <http://www.jetp.ac.ru/cgi-bin/e/index/e/4/2/p173?a=list>.
- [100] Fann, W. S., Storz, R., Tom, H. W. & Bokor, J. Direct Measurement of Nonequilibrium Electron-Energy Distributions in Subpicosecond Laser-Heated Gold Films. *Physical Review Letters* **68**, 2834–2837 (1992). URL <https://doi.org/10.1103/PhysRevLett.68.2834>.
- [101] Agranat, M. B., Ashitkov, S. I., Granovskii, A. B. & Rukman, G. I. interaction of picosecond laser pulses with the electron, spin, and phonon subsystems of nickel. *Zhurnal Éksperimental'noĭ i Teoreticheskoi Fiziki* **86**, 804–806 (1984). URL <http://www.jetp.ac.ru/cgi-bin/e/index/e/59/4/p804?a=list>.
- [102] Melnikov, A. *et al.* Nonequilibrium Magnetization Dynamics of Gadolinium Studied by Magnetic Linear Dichroism in Time-Resolved 4f Core-Level Photoemission. *Physical Review Letters* **100**, 107202 (2008). URL <https://doi.org/10.1103/PhysRevLett.100.107202>.
- [103] Wietstruk, M. *et al.* Hot-electron-driven enhancement of spin-lattice coupling in Gd and Tb 4f ferromagnets observed by femtosecond x-ray magnetic circular dichroism. *Physical Review Letters* **106**, 3–6 (2011). URL <https://doi.org/10.1103/PhysRevLett.106.127401>.
- [104] Alebrand, S. *et al.* Light-induced magnetization reversal of high-anisotropy TbCo alloy films. *Applied Physics Letters* **101**, 162408 (2012). URL <https://doi.org/10.1063/1.4759109>.
- [105] Hassdenteufel, A. *et al.* Thermally Assisted All-Optical Helicity Dependent Magnetic Switching in Amorphous Fe<sub>100-x</sub>Tb<sub>x</sub> Alloy Films. *Advanced Materials* **25**, 3122–3128 (2013). URL <https://doi.org/10.1002/adma.201300176>.
- [106] Mangin, S. *et al.* Engineered materials for all-optical helicity-dependent magnetic switching. *Nature Materials* **13**, 286–292 (2014). URL <https://doi.org/10.1038/nmat3864>.

## BIBLIOGRAPHY

---

- [107] Schubert, C. *et al.* All-optical helicity dependent magnetic switching in an artificial zero moment magnet. *Applied Physics Letters* **104**, 082406 (2014). URL <https://doi.org/10.1063/1.4866803>.
- [108] Gorchon, J., Yang, Y. & Bokor, J. Model for multishot all-thermal all-optical switching in ferromagnets. *Physical Review B* **94**, 020409(R) (2016). URL <https://doi.org/10.1103/PhysRevB.94.020409>. 1604.06441.
- [109] Ellis, M. O., Fullerton, E. E. & Chantrell, R. W. All-optical switching in granular ferromagnets caused by magnetic circular dichroism. *Scientific Reports* **6**, 30522 (2016). URL <https://doi.org/10.1038/srep30522>. 1605.00835.
- [110] Quessab, Y. *et al.* Helicity-dependent all-optical domain wall motion in ferromagnetic thin films. *Physical Review B* **97**, 054419 (2018). URL <https://doi.org/10.1103/PhysRevB.97.054419>. 1709.07645.
- [111] Pitaevskii, L. P. Electric Forces in a Transparent Dispersive Medium. *J. Exptl. Theoret. Phys. (U.S.S.R.)* **12**, 1450 (1961). URL <http://www.jetp.ac.ru/cgi-bin/e/index/e/12/5/p1008?a=list>.
- [112] Du, Z., Chen, C., Cheng, F., Liu, Y. & Pan, L. Prediction of Deterministic All-Optical Switching of Ferromagnetic Thin Film by Ultrafast Optothermal and Optomagnetic Couplings. *Scientific Reports* **7**, 13513 (2017). URL <http://doi.org/10.1038/s41598-017-13568-w>.
- [113] Cornelissen, T. D., Córdoba, R. & Koopmans, B. Microscopic model for all optical switching in ferromagnets. *Applied Physics Letters* **108**, 142405 (2016). URL <https://doi.org/10.1063/1.4945660>.
- [114] Scheid, P., Malinowski, G., Mangin, S. & Lebègue, S. Ab initio theory of magnetization induced by light absorption in ferromagnets. *Physical Review B* **100**, 214402 (2019). URL <https://doi.org/10.1103/PhysRevB.100.214402>.
- [115] Scheid, P., Sharma, S., Malinowski, G., Mangin, S. & Lebègue, S. Ab Initio Study of Helicity-Dependent Light-Induced Demagnetization: From the Optical Regime to the Extreme Ultraviolet Regime. *Nano Letters* **21**, 1943–1947 (2021). URL <https://doi.org/10.1021/acs.nanolett.0c04166>.

- [116] Kichin, G. *et al.* From Multiple- to Single-Pulse All-Optical Helicity-Dependent Switching in Ferromagnetic Co/Pt Multilayers. *Physical Review Applied* **12**, 1 (2019). URL <https://doi.org/10.1103/PhysRevApplied.12.024019>.
- [117] Li, G. *et al.* Timescales and contribution of heating and helicity effect in helicity-dependent all-optical switching. *arXiv* (2020). URL <https://arxiv.org/abs/2009.12816>.
- [118] Ali, S., Davies, J. R. & Mendonca, J. T. Inverse Faraday Effect with Linearly Polarized Laser Pulses. *Physical Review Letters* **105**, 035001 (2010). URL <https://doi.org/10.1103/PhysRevLett.105.035001>.
- [119] Khrapko, R. I. Question 79. Does plane wave not carry a spin? *American Journal of Physics* **69**, 405–405 (2001). URL <https://doi.org/10.1119/1.1352719>.
- [120] Yurchenko, V. B. Answer to Question 79. Does plane wave not carry a spin? *American Journal of Physics* **70**, 568–569 (2002). URL <https://doi.org/10.1119/1.1463741>.
- [121] Tudosa, I. *et al.* The ultimate speed of magnetic switching in granular recording media. *Nature* **428**, 831–833 (2004). URL <https://doi.org/10.1038/nature02438>.
- [122] Wang, S. *et al.* Dual-shot dynamics and ultimate frequency of all-optical magnetic recording on GdFeCo. *Light: Science and Applications* **10**, 1–8 (2021). URL <https://doi.org/10.1038/s41377-020-00451-z>.
- [123] Ostler, T. A. *et al.* Ultrafast heating as a sufficient stimulus for magnetization reversal in a ferrimagnet. *Nature Communications* **3**, 1–6 (2012). URL <https://doi.org/10.1038/ncomms1666>.
- [124] Xu, Y. *et al.* From single to multiple pulse all-optical switching in GdFeCo thin films. *Physical Review B* **100**, 064424 (2019). URL <https://doi.org/10.1103/PhysRevB.100.064424>.
- [125] Khorsand, A. R. *et al.* Role of magnetic circular dichroism in all-optical magnetic recording. *Physical Review Letters* **108**, 1–5 (2012). URL <https://doi.org/10.1103/PhysRevLett.108.127205>.
- [126] El-Ghazaly, A. *et al.* Ultrafast magnetization switching in nanoscale magnetic dots. *Applied Physics Letters* **114**, 232407 (2019). URL <https://doi.org/10.1063/1.5098453>.



## BIBLIOGRAPHY

---

- [127] Ceballos, A. *et al.* Role of element-specific damping in ultrafast, helicity-independent, all-optical switching dynamics in amorphous (Gd,Tb)Co thin films. *Physical Review B* **103**, 024438 (2021). URL <https://doi.org/10.1103/PhysRevB.103.024438>.
- [128] Zhang, W. *et al.* Role of spin-lattice coupling in ultrafast demagnetization and all optical helicity-independent single-shot switching in Gd<sub>1-x</sub>yTb<sub>y</sub>Co<sub>x</sub> alloys. *Physical Review B* **105**, 054410 (2022). URL <https://doi.org/10.1103/PhysRevB.105.054410>.
- [129] Ciuciulkaite, A. *et al.* Magnetic and all-optical switching properties of amorphous Tb<sub>x</sub>Co<sub>100-x</sub> alloys. *Physical Review Materials* **4**, 104418 (2020). URL <https://doi.org/10.1103/PhysRevMaterials.4.104418>.
- [130] Hu, Z. *et al.* Single-pulse all-optical partial switching in amorphous Dy<sub>x</sub>Co<sub>1-x</sub> and Tb<sub>x</sub>Co<sub>1-x</sub> with random anisotropy. *Applied Physics Letters* **120**, 112401 (2022). URL <https://doi.org/10.1063/5.0077226>.
- [131] Liu, Y. *et al.* Ultrafast single-pulse switching of Tb-dominant CoTb alloy. *Applied Physics Letters* **122**, 022401 (2023). URL <https://doi.org/10.1063/5.0131716>.
- [132] Banerjee, C. *et al.* Single pulse all-optical toggle switching of magnetization without gadolinium in the ferrimagnet Mn<sub>2</sub>Ru<sub>x</sub>Ga. *Nature Communications* **11**, 1–6 (2020). URL <https://doi.org/10.1038/s41467-020-18340-9>.
- [133] Avilés-Félix, L. *et al.* Integration of Tb/Co multilayers within optically switchable perpendicular magnetic tunnel junctions. *AIP Advances* **9**, 125328 (2019). URL <https://doi.org/10.1063/1.5129821>.
- [134] Avilés-Félix, L. *et al.* Single-shot all-optical switching of magnetization in Tb/Co multilayer-based electrodes. *Scientific Reports* **10**, 1–8 (2020). URL <https://doi.org/10.1038/s41598-020-62104-w>.
- [135] Peng, Y. *et al.* In plane reorientation induced single laser pulse magnetization reversal in rare-earth based multilayer. *arXiv* 1–27 (2023). URL <https://doi.org/10.48550/arXiv.2212.13279>.
- [136] Beens, M., Laliou, M. L., Deenen, A. J., Duine, R. A. & Koopmans, B. Comparing all-optical switching in synthetic-ferrimagnetic multilayers and alloys. *Physical Review B* **100**, 220409(R) (2019). URL <https://doi.org/10.1103/PhysRevB.100.220409>.



- [137] Steil, D., Alebrand, S., Hassdenteufel, A., Cinchetti, M. & Aeschlimann, M. All-optical magnetization recording by tailoring optical excitation parameters. *Physical Review B - Condensed Matter and Materials Physics* **84**, 224408 (2011). URL <https://doi.org/10.1103/PhysRevB.84.224408>.
- [138] Vahaplar, K. *et al.* All-optical magnetization reversal by circularly polarized laser pulses: Experiment and multiscale modeling. *Physical Review B - Condensed Matter and Materials Physics* **85**, 104402 (2012). URL <https://doi.org/10.1103/PhysRevB.85.104402>.
- [139] Gorchon, J. *et al.* Role of electron and phonon temperatures in the helicity-independent all-optical switching of GdFeCo. *Physical Review B* **94**, 184406 (2016). URL <https://doi.org/10.1103/PhysRevB.94.184406>.
- [140] Davies, C. S. *et al.* Pathways for Single-Shot All-Optical Switching of Magnetization in Ferrimagnets. *Physical Review Applied* **13**, 024064 (2020). URL <https://doi.org/10.1103/PhysRevApplied.13.024064>.
- [141] Wei, J. *et al.* All-optical Helicity-Independent Switching State Diagram in Gd - Fe - Co Alloys. *Physical Review Applied* **15**, 054065 (2021). URL <https://doi.org/10.1103/PhysRevApplied.15.054065>.
- [142] Yang, Y. *et al.* Ultrafast magnetization reversal by picosecond electrical pulses. *Science Advances* **3**, e1603117 (2017). URL <https://doi.org/10.1126/sciadv.1603117>.
- [143] Jakobs, F. *et al.* Unifying femtosecond and picosecond single-pulse magnetic switching in Gd-Fe-Co. *Physical Review B* **103**, 104422 (2021). URL <https://doi.org/10.1103/PhysRevB.103.104422>.
- [144] Liu, J. M. Simple technique for measurements of pulsed Gaussian-beam spot sizes. *Optics Letters* **7**, 196–198 (1982). URL <https://doi.org/10.1364/OL.7.000196>.
- [145] Steinbach, F. *et al.* Accelerating double pulse all-optical write/erase cycles in metallic ferrimagnets. *Applied Physics Letters* **120**, 112406 (2022). URL <https://doi.org/10.1063/5.0080351>.
- [146] Bonfiglio, G. *et al.* Sub-picosecond exchange-relaxation in the compensated ferrimagnet Mn<sub>2</sub>Ru<sub>x</sub>Ga. *Journal of Physics: Condensed Matter* **33**, 135804 (2021). URL <https://doi.org/10.1088/1361-648X/abda7c>.

## BIBLIOGRAPHY

---

- [147] Bergeard, N. *et al.* Ultrafast angular momentum transfer in multisublattice ferrimagnets. *Nature Communications* **5**, 1–7 (2014). URL <https://doi.org/10.1038/ncomms4466>.
- [148] Hennecke, M. *et al.* Angular Momentum Flow during Ultrafast Demagnetization of a Ferrimagnet. *Physical Review Letters* **122**, 157202 (2019). URL <https://doi.org/10.1103/PhysRevLett.122.157202>.
- [149] Graves, C. E. *et al.* Nanoscale spin reversal by non-local angular momentum transfer following ultrafast laser excitation in ferrimagnetic GdFeCo. *Nature Materials* **12**, 293–298 (2013). URL <https://doi.org/10.1038/nmat3597>.
- [150] Gridnev, V. N. Ultrafast heating-induced magnetization switching in ferrimagnets. *Journal of Physics: Condensed Matter* **28**, 476007 (2016). URL <https://doi.org/10.1088/0953-8984/28/47/476007>.
- [151] Gridnev, V. N. Ferromagneticlike states and all-optical magnetization switching in ferrimagnets. *Physical Review B* **98**, 014427 (2018). URL <https://doi.org/10.1103/PhysRevB.98.014427>.
- [152] Gridnev, V. N. Role of compensation points in all-optical magnetization switching. *Physical Review B* **100**, 174405 (2019). URL <https://doi.org/10.1103/PhysRevB.100.174405>.
- [153] Vahaplar, K. *et al.* Ultrafast Path for Optical Magnetization Reversal via a Strongly Nonequilibrium State. *Physical Review Letters* **103**, 117201 (2009). URL <https://doi.org/10.1103/PhysRevLett.103.117201>.
- [154] Atxitia, U., Nieves, P. & Chubykalo-Fesenko, O. Landau-Lifshitz-Bloch equation for ferrimagnetic materials. *Physical Review B - Condensed Matter and Materials Physics* **86**, 104414 (2012). URL <https://doi.org/10.1103/PhysRevB.86.104414>. 1206.6672.
- [155] Mentink, J. H. *et al.* Ultrafast Spin Dynamics in Multisublattice Magnets. *Physical Review Letters* **108**, 057202 (2012). URL <https://doi.org/10.1103/PhysRevLett.108.057202>.
- [156] Atxitia, U. *et al.* Ultrafast dynamical path for the switching of a ferrimagnet after femtosecond heating. *Physical Review B - Condensed Matter and Materials Physics* **87**,

- 224417 (2013). URL <https://doi.org/10.1103/PhysRevB.87.224417>. 1207.4092.
- [157] Schellekens, A. J. & Koopmans, B. Microscopic model for ultrafast magnetization dynamics of multisublattice magnets. *Physical Review B - Condensed Matter and Materials Physics* **87**, 020407(R) (2013). URL <https://doi.org/10.1103/PhysRevB.87.020407>.
- [158] Wienholdt, S., Hinzke, D., Carva, K., Oppeneer, P. M. & Nowak, U. Orbital-resolved spin model for thermal magnetization switching in rare-earth-based ferrimagnets. *Physical Review B - Condensed Matter and Materials Physics* **88**, 020406(R) (2013). URL <https://doi.org/10.1103/PhysRevB.88.020406>.
- [159] Atxitia, U., Barker, J., Chantrell, R. W. & Chubykalo-Fesenko, O. Controlling the polarity of the transient ferromagneticlike state in ferrimagnets. *Physical Review B - Condensed Matter and Materials Physics* **89**, 224421 (2014). URL <https://doi.org/10.1103/PhysRevB.89.224421>. 1308.0993.
- [160] Evans, R. F., Ostler, T. A., Chantrell, R. W., Radu, I. & Rasing, T. Ultrafast thermally induced magnetic switching in synthetic ferrimagnets. *Applied Physics Letters* **104**, 082410 (2014). URL <https://doi.org/10.1063/1.4867015>.
- [161] Baral, A. & Schneider, H. C. Magnetic switching dynamics due to ultrafast exchange scattering: A model study. *Physical Review B - Condensed Matter and Materials Physics* **91**, 100402(R) (2015). URL <https://doi.org/10.1103/PhysRevB.91.100402>.
- [162] Kalashnikova, A. M. & Kozub, V. I. Exchange scattering as the driving force for ultrafast all-optical and bias-controlled reversal in ferrimagnetic metallic structures. *Physical Review B* **93**, 054424 (2016). URL <https://doi.org/10.1103/PhysRevB.93.054424>. 1506.06585.
- [163] Gerlach, S. *et al.* Modeling ultrafast all-optical switching in synthetic ferrimagnets. *Physical Review B* **95**, 224435 (2017). URL <https://doi.org/10.1103/PhysRevB.95.224435>.
- [164] Dewhurst, J. K., Elliott, P., Shallcross, S., Gross, E. K. U. & Sharma, S. Laser-Induced Intersite Spin Transfer. *Nano Letters* **18**, 1842–1848 (2018). URL <https://doi.org/10.1021/acs.nanolett.7b05118>.

## BIBLIOGRAPHY

---

- [165] Vogler, C., Abert, C., Bruckner, F. & Suess, D. Stochastic ferrimagnetic Landau-Lifshitz-Bloch equation for finite magnetic structures. *Physical Review B* **100**, 054401 (2019). URL <https://doi.org/10.1103/PhysRevB.100.054401>.
- [166] Skubic, B., Hellsvik, J., Nordström, L. & Eriksson, O. A method for atomistic spin dynamics simulations: Implementation and examples. *Journal of Physics: Condensed Matter* **20**, 315203 (2008). URL <https://doi.org/10.1088/0953-8984/20/31/315203>.
- [167] Barker, J. *et al.* Two-magnon bound state causes ultrafast thermally induced magnetisation switching. *Scientific Reports* **3**, 3262 (2013). URL <https://doi.org/10.1038/srep03262>.
- [168] Liu, T. M. *et al.* Nanoscale Confinement of All-Optical Magnetic Switching in TbFeCo - Competition with Nanoscale Heterogeneity. *Nano Letters* **15**, 6862–6868 (2015). URL <https://doi.org/10.1021/acs.nanolett.5b02743>.
- [169] Jackson, J. D. *Classical Electrodynamics* (John Wiley & Sons, 1999), 3rd edn. URL <https://www.wiley.com/en-us/Classical+Electrodynamics%2C+3rd+Edition-p-9780471309321>.
- [170] Landau, L. & Lifshitz, E. *Electrodynamics of Continuous Media* (Elsevier, 1984), 2nd edn. URL <https://www.elsevier.com/books/electrodynamics-of-continuous-media/landau/978-0-08-057060-0>.
- [171] Johnson, P. B. & Christy, R. W. Optical Constant of the Nobel Metals. *Physical Review B* **6**, 4370–4379 (1972). URL <https://doi.org/10.1103/PhysRevB.6.4370>.
- [172] Ginzburg, P. & Zayats, A. V. Localized surface plasmon resonances in spatially dispersive nano-objects: Phenomenological treatise. *ACS Nano* **7**, 4334–4342 (2013). URL <https://pubs.acs.org/doi/10.1021/nn400842m>.
- [173] Drude, P. Zur Elektronentheorie der Metalle. *Annalen der Physik* **306**, 566–613 (1900). URL <https://doi.org/10.1002/andp.19003060312>.
- [174] Ashcroft, N. W. & Mermin, N. D. *Physique des solides* (EDP Sciences, 2002).
- [175] Khurgin, J. B. & Sun, G. Scaling of losses with size and wavelength in nanoplasmonics and metamaterials. *Applied Physics Letters* **99**, 211106 (2011). URL <https://doi.org/10.1063/1.3664105>.

- [176] Boriskina, S. V. *et al.* Losses in plasmonics: from mitigating energy dissipation to embracing loss-enabled functionalities. *Advances in Optics and Photonics* **9**, 775 (2017). URL <https://doi.org/10.1364/AOP.9.000775>.
- [177] Caldwell, J. D. *et al.* Low-loss, infrared and terahertz nanophotonics using surface phonon polaritons. *Nanophotonics* **4**, 44–68 (2015). URL <https://doi.org/10.1515/nanoph-2014-0003>.
- [178] Stockman, M. I. Nanoplasmonics: past, present, and glimpse into future. *Optics Express* **19**, 22029 (2011). URL <https://doi.org/10.1364/OE.19.022029>.
- [179] Ehrenreich, H. & Philipp, H. R. Optical properties of Ag and Cu. *Physical Review* **128**, 1622–1629 (1962). URL <https://doi.org/10.1103/PhysRev.128.1622>.
- [180] Ehrenreich, H., Philipp, H. R. & Segall, B. Optical Properties of Aluminium. *Physical Review* **132**, 1918 – 1928 (1963). URL <https://doi.org/10.1103/PhysRev.132.1918>.
- [181] Vial, A. & Laroche, T. Description of dispersion properties of metals by means of the critical points model and application to the study of resonant structures using the FDTD method. *Journal of Physics D: Applied Physics* **40**, 7152–7158 (2007). URL <https://doi.org/10.1088/0022-3727/40/22/043>.
- [182] Vial, A. & Laroche, T. Comparison of gold and silver dispersion laws suitable for FDTD simulations. *Applied Physics B: Lasers and Optics* **93**, 139–143 (2008). URL <https://doi.org/10.1007/s00340-008-3202-4>.
- [183] Vial, A., Laroche, T., Dridi, M. & Le Cunff, L. A new model of dispersion for metals leading to a more accurate modeling of plasmonic structures using the FDTD method. *Applied Physics A: Materials Science and Processing* **103**, 849–853 (2011). URL <https://doi.org/10.1007/s00339-010-6224-9>.
- [184] Etchegoin, P. G., Le Ru, E. C. & Meyer, M. An analytic model for the optical properties of gold. *Journal of Chemical Physics* **125**, 164705 (2006). URL <https://doi.org/10.1063/1.2360270>.
- [185] Etchegoin, P. G., Le Ru, E. C. & Meyer, M. Erratum: “An analytic model for the optical properties of gold” [J. Chem. Phys. 125, 164705 (2006)]. *The Journal of Chemical Physics* **127**, 189901 (2007).

## BIBLIOGRAPHY

---

- [186] Sehmi, H. S., Langbein, W. & Muljarov, E. A. Optimizing the Drude-Lorentz model for material permittivity: Method, program, and examples for gold, silver, and copper. *Physical Review B* **95**, 1–8 (2017). URL <https://doi.org/10.1103/PhysRevB.95.115444>. 1612.06925.
- [187] Kim, C. C., Garland, J. W., Abad, H. & Raccah, P. M. Modeling the optical dielectric function of semiconductors: Extension of the critical-point parabolic-band approximation. *Physical Review B* **45**, 11749–11767 (1992). URL <https://doi.org/10.1103/PhysRevB.45.11749>.
- [188] Brendel, R. & Bormann, D. An infrared dielectric function model for amorphous solids. *Journal of Applied Physics* **71**, 1–6 (1992). URL <https://doi.org/10.1063/1.350737>.
- [189] Kim, C. C., Garland, J. W. & Raccah, P. M. Modeling the optical dielectric function of the alloy system  $\text{Al}_x\text{Ga}_{1-x}\text{As}$ . *Physical Review B* **47**, 1876–1888 (1993). URL <https://doi.org/10.1103/PhysRevB.47.1876>.
- [190] Rakić, A. D., Djurišić, A. B., Elazar, J. M. & Majewski, M. L. Optical properties of metallic films for vertical-cavity optoelectronic devices. *Applied Optics* **37**, 5271–5283 (1998). URL <https://doi.org/10.1364/AO.37.005271>.
- [191] Grosso, G. & Parravicini, G. P. *Solid State Physics* (Academic Press, 2013), 2nd edn. URL <https://doi.org/10.1016/B978-0-12-304460-0.X5000-2>.
- [192] Mahan, G. D. *Many-Particle Physics* (Springer New York, NY, 2000), 3rd edn. URL <https://doi.org/10.1007/978-1-4757-5714-9>.
- [193] Burke, K., Werschnik, J. & Gross, E. K. Time-dependent density functional theory: Past, present, and future. *Journal of Chemical Physics* **123**, 062206 (2005). URL <https://doi.org/10.1063/1.1904586>.
- [194] Kohanoff, J. *Electronic structure calculations for solids and molecules: theory and computational methods* (Cambridge University Press, 2006). URL <https://doi.org/10.1017/CB09780511755613>.
- [195] Maier, S. A. *Plasmonics : fundamentals and applications* (Springer US, New York, 2007). URL <https://www.springer.com/gp/book/9780387331508>.

- [196] Martín-Cano, D., Haakh, H. R. & Agio, M. Quadrature-Squeezed Light from Emitters in Optical Nanostructures. In *Quantum Plasmonics*, chap. 2, 25–46 (Springer Series in Solid-State Sciences, 2017). URL [https://doi.org/10.1007/978-3-319-45820-5\\_2](https://doi.org/10.1007/978-3-319-45820-5_2).
- [197] Raether, H. *Surface Plasmons on Smooth and Rough Surfaces and on Gratings* (Springer Berlin, Heidelberg, 1988), 1st edn. URL <https://doi.org/10.1007/BFb0048317>.
- [198] Maradudin, A. A., Sambles, J. R. & Barnes, W. L. *Modern Plasmonics*, vol. 4 (Elsevier Science, 2014), 1st edn. URL <https://www.elsevier.com/books/modern-plasmonics/maradudin/978-0-444-59526-3>.
- [199] Hartstein, A., Burstein, E., Maradudin, A. A., Brewer, R. & Wallis, R. F. Surface polaritons on semi-infinite gyromagnetic media. *Journal of Physics C: Solid State Physics* **6**, 1266–1276 (1973). URL <https://doi.org/10.1088/0022-3719/6/7/016>.
- [200] Barnes, W. L., Dereux, A. & Ebbesen, T. W. Surface plasmon subwavelength optics. *Nature* **424**, 824 (2003). URL <https://doi.org/10.1038/nature01937>.
- [201] Kretschmann, E. & Raether, H. Radiative Decay of Non Radiative Surface Plasmons Excited by Light. *Zeitschrift fur Naturforschung - Section A Journal of Physical Sciences* **23**, 2135–2136 (1968). URL <https://doi.org/10.1515/zna-1968-1247>.
- [202] Sinev, I. *et al.* Polarization control over electric and magnetic dipole resonances of dielectric nanoparticles on metallic films. *Laser and Photonics Reviews* **10**, 799–806 (2016). URL <https://doi.org/10.1002/lpor.201600055>.
- [203] Sinev, I. S. *et al.* Chirality Driven by Magnetic Dipole Response for Demultiplexing of Surface Waves. *Laser and Photonics Reviews* **11**, 1700168 (2017). URL <https://doi.org/10.1002/lpor.201700168>.
- [204] Sinev, I. *et al.* Steering of Guided Light with Dielectric Nanoantennas. *ACS Photonics* **7**, 680–686 (2020). URL <https://dx.doi.org/10.1021/acsp Photonics.9b01515>.
- [205] Wolff, C., Busch, K. & Mortensen, N. A. Modal expansions in periodic photonic systems with material loss and dispersion. *Physical Review B* **97**, 104203 (2018). URL <https://doi.org/10.1103/PhysRevB.97.104203>.



## BIBLIOGRAPHY

---

- [206] Giannini, V., Fernández-Domínguez, A. I., Heck, S. C. & Maier, S. A. Plasmonic nanoantennas: Fundamentals and their use in controlling the radiative properties of nanoemitters. *Chemical Reviews* **111**, 3888–3912 (2011). URL <https://dx.doi.org/10.1021/cr1002672>.
- [207] Agranovich, V. M. & Mills, D. L. *Surface polaritons: Electromagnetic Waves at Surfaces and Interfaces* (North Holland, 1982), 1st edn.
- [208] Maier, S. A. & Atwater, H. A. Plasmonics: Localization and guiding of electromagnetic energy in metal/dielectric structures. *Journal of Applied Physics* **98**, 011101 (2005). URL <https://doi.org/10.1063/1.1951057>.
- [209] Weber, W. H. & Ford, G. W. Optical electric-field enhancement at a metal surface arising from surface-plasmon excitation. *Optics Letters* **6**, 122 (1981). URL <https://doi.org/10.1364/OL.6.000122>.
- [210] Nagpal, P., Lindquist, N. C., Oh, S. H. & Norris, D. J. Ultrasmooth patterned metals for plasmonics and metamaterials. *Science* **325**, 594–597 (2009). URL <https://doi.org/10.1126/science.1174655>.
- [211] Berini, P. Long-range surface plasmon polaritons. *Advances in Optics and Photonics* **1**, 484 (2009). URL <https://doi.org/10.1364/AOP.1.000484>.
- [212] Otto, A. Excitation of nonradiative surface plasma waves in silver by the method of frustrated total reflection. *Zeitschrift für Physik* **216**, 398–410 (1968). URL <https://doi.org/10.1007/BF01391532>.
- [213] Ignatyeva, D. O. *et al.* Plasmonic layer-selective all-optical switching of magnetization with nanometer resolution. *Nature Communications* **10**, 1–7 (2019). URL <https://doi.org/10.1038/s41467-019-12699-0>.
- [214] Wood, R. W. XLII. On a remarkable case of uneven distribution of light in a diffraction grating spectrum. *Proceedings of the Physical Society of London* **6**, 396 (1902). URL <https://doi.org/10.1080/14786440209462857>.
- [215] Van Mechelen, T. & Jacob, Z. Universal spin-momentum locking of evanescent waves. *Optica* **3**, 118 (2016). URL <http://dx.doi.org/10.1364/OPTICA.3.000118>.



- [216] Chekhov, A. L. *et al.* Surface Plasmon-Mediated Nanoscale Localization of Laser-Driven sub-Terahertz Spin Dynamics in Magnetic Dielectrics. *Nano Letters* **18**, 2970–2975 (2018). URL <https://doi.org/10.1021/acs.nanolett.8b00416>. 1712.01617.
- [217] Gazzola, E. *et al.* Coupled SPP Modes on 1D Plasmonic Gratings in Conical Mounting. *Plasmonics* **9**, 867–876 (2014). URL <https://doi.org/10.1007/s11468-013-9624-9>.
- [218] Gazzola, E., Ruffato, G. & Romanato, F. Propagation of grating-coupled surface plasmon polaritons and cosine–Gauss beam generation. *Journal of the Optical Society of America B* **32**, 1564 (2015). URL <https://doi.org/10.1364/JOSAB.32.001564>.
- [219] Papanikolaou, N. Optical properties of metallic nanoparticle arrays on a thin metallic film. *Physical Review B - Condensed Matter and Materials Physics* **75**, 1–7 (2007). URL <https://doi.org/10.1103/PhysRevB.75.235426>.
- [220] Pourjamal, S., Kataja, M., Maccaferri, N., Vavassori, P. & van Dijken, S. Tunable magnetoplasmonics in lattices of Ni/SiO<sub>2</sub>/Au dimers. *Scientific Reports* **9**, 9907 (2019). URL <https://doi.org/10.1038/s41598-019-46058-2>.
- [221] Freire-Fernández, F., Kataja, M. & Van Dijken, S. Surface-plasmon-polariton-driven narrow-linewidth magneto-optics in ni nanodisk arrays. *Nanophotonics* **9**, 113–121 (2020). URL <https://doi.org/10.1515/nanoph-2019-0331>.
- [222] Freire-Fernández, F., Mansell, R. & Van Dijken, S. Magnetoplasmonic properties of perpendicularly magnetized [Co/Pt]N nanodots. *Physical Review B* **101**, 054416 (2020). URL <https://doi.org/10.1103/PhysRevB.101.054416>.
- [223] Born, M. & Wolf, E. *Principles of Optics* (Cambridge University Press, 2019), 7th edn.
- [224] Mie, G. Beitrage zur optic truber medien, speziell kolloidaller metallosungen. *Annalen der Physik* **330**, 337 (1908). URL <https://doi.org/10.1002/andp.19083300302>.
- [225] Bohren, C. F. & Huffman, D. R. *Absorption and scattering of light by small particles* (Wiley, 1998).
- [226] Hergert, W. & Wriedt, T. *The Mie theory: basics and applications*, vol. 169 (Springer Berlin, Heidelberg, 2012), 1st edn. URL <https://doi.org/10.1007/978-3-642-28738-1>.

## BIBLIOGRAPHY

---

- [227] van de Hulst, H. C. *Light scattering by small particles* (Dover Publications, Inc., 1981), 1st edn.
- [228] Stratton, J. A. *Electromagnetic theory* (McGraw-Hill, New York, 1941), 1st edn.
- [229] Kreibig, U. & Vollmer, M. *Optical Properties of Metal Clusters* (Springer Berlin Heidelberg, 1995).
- [230] Christensen, T. *et al.* Nonlocal Response of Metallic Nanospheres Probed by Light, Electrons, and Atoms. *ACS Nano* **8**, 1745–1758 (2014). URL <https://doi.org/10.1021/nm406153k>.
- [231] Wokaun, A., Gordon, J. P. & Liao, P. F. Radiation damping in surface-enhanced Raman scattering. *Physical Review Letters* **48**, 957–960 (1982). URL <https://doi.org/10.1103/PhysRevLett.48.957>.
- [232] Jensen, T., Kelly, L., Lazarides, A. & Schatz, G. C. Electrodynamics of Noble Metal Nanoparticles and Nanoparticle Clusters. *Journal of Cluster Science* **10**, 295–317 (1999). URL <https://doi.org/10.1023/A:1021977613319>.
- [233] Kelly, K. L., Coronado, E., Zhao, L. L. & Schatz, G. C. The Optical Properties of Metal Nanoparticles: The Influence of Size, Shape, and Dielectric Environment. *The Journal of physical Chemistry B* **107**, 668 (2003). URL <https://doi.org/10.1021/jp026731y>.
- [234] Myroshnychenko, V. *et al.* Modelling the optical response of gold nanoparticles. *Chemical Society Reviews* **37**, 1792–1805 (2008). URL <https://doi.org/10.1039/B711486A>.
- [235] Barnes, W. L. Particle plasmons: Why shape matters. *American Journal of Physics* **84**, 593–601 (2016). URL <https://doi.org/10.1119/1.4948402>.
- [236] Liu, M. & Guyot-Sionnest, P. Mechanism of Silver(I)-Assisted Growth of Gold Nanorods and Bipyramids. *Journal of Physical Chemistry B* **109**, 22192–22200 (2005). URL <https://doi.org/10.1021/jp054808n>.
- [237] Sherry, L. J., Chang, S.-H., Schatz, G. C. & Van Duyne, R. P. Localized Surface Plasmon Resonance Spectroscopy of Single Silver Nanocubes. *Nano Letters* **5**, 2034–2038 (2005). URL <https://doi.org/10.1021/nl0515753>.

- [238] Nehl, C. L., Liao, H. & Hafner, J. H. Optical Properties of Star-Shaped Gold Nanoparticles. *Nano Letters* **6**, 683–688 (2006). URL <https://doi.org/10.1021/nl052409y>.
- [239] Bukasov, R. & Shumaker-Parry, J. S. Highly Tunable Infrared Extinction Properties of Gold Nanocrescents. *Nano Letters* **7**, 1113–1118 (2007). URL <https://doi.org/10.1021/nl062317o>.
- [240] Murray, W. A. & Barnes, W. L. Plasmonic Materials. *Advanced Materials* **19**, 3771–3782 (2007). URL <https://doi.org/10.1002/adma.200700678>.
- [241] Muskens, O. L., Giannini, V., Sánchez-Gil, J. A. & Gómez Rivas, J. Optical scattering resonances of single and coupled dimer plasmonic nanoantennas. *Optics Express* **15**, 17736 (2007). URL <https://doi.org/10.1364/oe.15.017736>.
- [242] Chen, H., Kou, X., Yang, Z., Ni, W. & Wang, J. Shape- and Size-Dependent Refractive Index Sensitivity of Gold Nanoparticles. *Langmuir* **24**, 5233–5237 (2008). URL <https://doi.org/10.1021/la800305j>.
- [243] Mayer, K. M. & Hafner, J. H. Localized Surface Plasmon Resonance Sensors. *Chemical Reviews* **111**, 3828–3857 (2011). URL <https://doi.org/10.1021/cr100313v>.
- [244] Fang, Z. *et al.* Plasmonic Coupling of Bow Tie Antennas with Ag Nanowire. *Nano Letters* **11**, 1676–1680 (2011). URL <https://doi.org/10.1021/nl200179y>.
- [245] Balezin, M., Baryshnikova, K. V., Kapitanova, P. & Evlyukhin, A. B. Electromagnetic properties of the Great Pyramid: First multipole resonances and energy concentration. *Journal of Applied Physics* **124**, 034903 (2018). URL <https://doi.org/10.1063/1.5026556>.
- [246] Fujiwara, H. *et al.* Spin-Orbit Angular-Momentum Transfer from a Nanogap Surface Plasmon to a Trapped Nanodiamond. *Nano Letters* **21**, 6268–6273 (2021). URL <https://doi.org/10.1021/acs.nanolett.1c02083>.
- [247] Jin, R. *et al.* Photoinduced conversion of silver nanospheres to nanoprisms. *Science* **294**, 1901–1903 (2001). URL <https://doi.org/10.1126/science.1066541>.
- [248] Kataja, M. *et al.* Surface lattice resonances and magneto-optical response in magnetic nanoparticle arrays. *Nature Communications* **6**, 7072 (2015). URL <https://doi.org/10.1038/ncomms8072>.

## BIBLIOGRAPHY

---

- [249] Pourjamal, S. *et al.* Lasing in Ni Nanodisk Arrays. *ACS Nano* **13**, 5686–5692 (2019). URL <https://doi.org/10.1021/acsnano.9b01006>.
- [250] Kuzmichev, A. N. *et al.* Influence of the Plasmonic Nanodisk Positions Inside a Magnetic Medium on the Faraday Effect Enhancement. *Physica Status Solidi - Rapid Research Letters* **14**, 1900682 (2020). URL <https://doi.org/10.1002/pssr.201900682>.
- [251] Fang, Z. *et al.* Plasmonic coupling of bow tie antennas with Ag nanowire. *Nano Letters* **11**, 1676–1680 (2011). URL <https://doi.org/10.1021/nl200179y>.
- [252] Lee, B. *et al.* Fano resonance and spectrally modified photoluminescence enhancement in monolayer MoS<sub>2</sub> integrated with plasmonic nanoantenna array. *Nano Letters* **15**, 3646–3653 (2015). URL <https://doi.org/10.1021/acs.nanolett.5b01563>.
- [253] Fujiwara, H. *et al.* Spin–Orbit Angular-Momentum Transfer from a Nanogap Surface Plasmon to a Trapped Nanodiamond. *Nano Letters* **21**, 6268–6273 (2021). URL <https://doi.org/10.1021/acs.nanolett.1c02083>.
- [254] Ctistis, G. *et al.* Optical and magnetic properties of hexagonal arrays of subwavelength holes in optically thin cobalt films. *Nano Letters* **9**, 1–6 (2009). URL <https://doi.org/10.1021/nl801811t>.
- [255] Rollinger, M. *et al.* Light Localization and Magneto-Optic Enhancement in Ni Antidot Arrays. *Nano Letters* **16**, 2432–2438 (2016). URL <https://doi.org/10.1021/acs.nanolett.5b05279>. 1507.05538.
- [256] Martín-Moreno, L. *et al.* Theory of extraordinary optical transmission through sub-wavelength hole arrays. *Physical Review Letters* **86**, 1114–1117 (2001). URL <https://doi.org/10.1103/PhysRevLett.86.1114>. 0008204.
- [257] Lee, K. G. & Park, Q. H. Coupling of surface plasmon polaritons and light in metallic nanoslits. *Physical Review Letters* **95**, 1–4 (2005). URL <https://doi.org/10.1103/PhysRevLett.95.103902>.
- [258] Ropers, C. *et al.* Femtosecond light transmission and subradiant damping in plasmonic crystals. *Physical Review Letters* **94**, 1–4 (2005). URL <https://doi.org/10.1103/PhysRevLett.94.113901>.

- [259] Kumar, S., Doi, Y., Namura, K. & Suzuki, M. Plasmonic Nanoslit Arrays Fabricated by Serial Bideposition: Optical and Surface-Enhanced Raman Scattering Study. *ACS Applied Bio Materials* **3**, 3226–3235 (2020). URL <https://doi.org/10.1021/acscabm.0c00215>. 2002.04738.
- [260] Clark, A. W., Glidle, A., Cumming, D. R. & Cooper, J. M. Plasmonic split-ring resonators as dichroic nanophotonic DNA biosensors. *Journal of the American Chemical Society* **131**, 17615–17619 (2009). URL <https://doi.org/10.1021/ja905910q>.
- [261] Sersic, I., Frimmer, M., Verhagen, E. & Koenderink, A. F. Electric and Magnetic Dipole Coupling in Near-Infrared Split-Ring Metamaterial Arrays. *Physical Review Letters* **103**, 1–4 (2009). URL <https://doi.org/10.1103/PhysRevLett.103.213902>. 0907.3026.
- [262] Wu, P. C. *et al.* Plasmon coupling in vertical split-ring resonator metamolecules. *Scientific Reports* **5**, 1–5 (2015). URL <https://doi.org/10.1038/srep09726>.
- [263] DeVoe, H. Optical Properties of Molecular Aggregates. I. Classical Model of Electronic Absorption and Refraction. *The Journal of Chemical Physics* **41**, 393–400 (1964). URL <https://doi.org/10.1063/1.1725879>.
- [264] DeVoe, H. Optical Properties of Molecular Aggregates. II. Classical Theory of the Refraction, Absorption, and Optical Activity of Solutions and Crystals. *The Journal of Chemical Physics* **43**, 3199–3208 (1965). URL <https://doi.org/10.1063/1.1697294>.
- [265] Purcell, Edward, M. & Pennypacker, Carlton, R. Scattering and Absorption of Light by Nonspherical Dielectric Grains. *The Astrophysical Journal* **186**, 705–714 (1973). URL <https://ui.adsabs.harvard.edu/abs/1973ApJ...186..705P/abstract>.
- [266] Laor, U. & Schatz, G. C. The role of surface roughness in surface enhanced raman spectroscopy (SERS): the importance of multiple plasmon resonances. *Chemical Physics Letters* **82**, 566–570 (1981). URL [https://doi.org/10.1016/0009-2614\(81\)85442-5](https://doi.org/10.1016/0009-2614(81)85442-5).
- [267] Meier, M., Liao, P. F. & Wokaun, A. Enhanced fields on rough surfaces: dipolar interactions among particles of sizes exceeding the Rayleigh limit. *Journal of the Optical Society of America B* **2**, 931 (1985). URL <https://doi.org/10.1364/JOSAB.2.000931>.
- [268] Carron, K. T., Lehmann, H. W., Fluhr, W., Meier, M. & Wokaun, A. Resonances of two-dimensional particle gratings in surface-enhanced Raman scattering. *Journal of the*

## BIBLIOGRAPHY

---

- Optical Society of America B* **3**, 430 (1986). URL <https://doi.org/10.1364/josab.3.000430>.
- [269] Zou, S., Janel, N. & Schatz, G. C. Silver nanoparticle array structures that produce remarkably narrow plasmon lineshapes. *Journal of Chemical Physics* **120**, 10871–10875 (2004). URL <https://doi.org/10.1063/1.1760740>.
- [270] Zou, S. & Schatz, G. C. Narrow plasmonic/photonic extinction and scattering line shapes for one and two dimensional silver nanoparticle arrays. *Journal of Chemical Physics* **121**, 12606–12612 (2004). URL <https://doi.org/10.1063/1.1826036>.
- [271] Markel, V. A. Coupled-dipole approach to scattering of light from a onedimensional periodic dipole structure. *Journal of Modern Optics* **40**, 2281–2291 (1993). URL <https://doi.org/10.1080/09500349314552291>.
- [272] Markel, V. A. Divergence of dipole sums and the nature of non-Lorentzian exponentially narrow resonances in one-dimensional periodic arrays of nanospheres. *Journal of Physics B: Atomic, Molecular and Optical Physics* **38** (2005). URL <https://doi.org/10.1088/0953-4075/38/7/L02>.
- [273] Kravets, V. G., Kabashin, A. V., Barnes, W. L. & Grigorenko, A. N. Plasmonic Surface Lattice Resonances: A Review of Properties and Applications. *Chemical Reviews* **118**, 5912–5951 (2018). URL <https://doi.org/10.1021/acs.chemrev.8b00243>.
- [274] Yurkin, M. A. & Hoekstra, A. G. The discrete dipole approximation: An overview and recent developments. *Journal of Quantitative Spectroscopy and Radiative Transfer* **106**, 558–589 (2007). URL <https://doi.org/10.1016/j.jqsrt.2007.01.034>.
- [275] Lamprecht, B. *et al.* Metal Nanoparticle Gratings: Influence of Dipolar Particle Interaction on the Plasmon Resonance. *Physical Review Letters* **84**, 4721–4724 (2000). URL <https://doi.org/10.1103/PhysRevLett.84.4721>.
- [276] Haynes, C. L. *et al.* Nanoparticle Optics: The Importance of Radiative Dipole Coupling in Two-Dimensional Nanoparticle Arrays. *Journal of Physical Chemistry B* **107**, 7337–7342 (2003). URL <https://doi.org/10.1021/jp034234r>.
- [277] Hicks, E. M. *et al.* Controlling plasmon line shapes through diffractive coupling in linear arrays of cylindrical nanoparticles fabricated by electron beam lithography. *Nano Letters* **5**, 1065–1070 (2005). URL <https://doi.org/10.1021/nl0505492>.

- [278] Sung, J., Hicks, E. M., Van Duyne, R. P. & Spears, K. Nanoparticle Spectroscopy: Plasmon Coupling in Finite-Sized Two-Dimensional Arrays of Cylindrical Silver Nanoparticles. *Journal of Physical Chemistry C* **112**, 4091–4096 (2008). URL <https://doi.org/10.1021/jp077332b>.
- [279] Kravets, V. G., Schedin, F. & Grigorenko, A. N. Extremely narrow plasmon resonances based on diffraction coupling of localized plasmons in arrays of metallic nanoparticles. *Physical Review Letters* **101**, 1–4 (2008). URL <https://doi.org/10.1103/PhysRevLett.101.087403>.
- [280] Azzam, R. M. A. & Bashara, N. M. *Ellipsometry and Polarized Light* (North-Holland, 1977).
- [281] Chu, Y., Schonbrun, E., Yang, T. & Crozier, K. B. Experimental observation of narrow surface plasmon resonances in gold nanoparticle arrays. *Applied Physics Letters* **93**, 1–3 (2008). URL <https://doi.org/10.1063/1.3012365>.
- [282] Auguié, B. & Barnes, W. L. Collective resonances in gold nanoparticle arrays. *Physical Review Letters* **101**, 1–4 (2008). URL <https://doi.org/10.1103/PhysRevLett.101.143902>.
- [283] Vecchi, G., Giannini, V. & Gómez Rivas, J. Surface modes in plasmonic crystals induced by diffractive coupling of nanoantennas. *Physical Review B - Condensed Matter and Materials Physics* **80**, 1–4 (2009). URL <https://doi.org/10.1103/PhysRevB.80.201401>.
- [284] Rodriguez, S. R. *et al.* Coupling Bright and Dark Plasmonic Lattice Resonances. *Physical Review X* **1**, 1–7 (2011). URL <https://doi.org/10.1103/PhysRevX.1.021019>. 1108.1620.
- [285] Teperik, T. V. & Degiron, A. Design strategies to tailor the narrow plasmon-photonic resonances in arrays of metallic nanoparticles. *Physical Review B - Condensed Matter and Materials Physics* **86**, 1–5 (2012). URL <https://doi.org/10.1103/PhysRevB.86.245425>.
- [286] Weick, G., Woollacott, C., Barnes, W. L., Hess, O. & Mariani, E. Dirac-like plasmons in honeycomb lattices of metallic nanoparticles. *Physical Review Letters* **110**, 1–6 (2013). URL <https://doi.org/10.1103/PhysRevLett.110.106801>. 1209.5005.



## BIBLIOGRAPHY

---

- [287] Vitrey, A., Aigouy, L., Prieto, P., García-Martín, J. M. & González, M. U. Parallel collective resonances in arrays of gold nanorods. *Nano Letters* **14**, 2079–2085 (2014). URL <https://doi.org/10.1021/nl500238h>.
- [288] Kravets, V. G., Schedin, F., Kabashin, A. V. & Grigorenko, A. N. Sensitivity of collective plasmon modes of gold nanoresonators to local environment. *Optics Letters* **35**, 956 (2010). URL <https://doi.org/10.1364/ol.35.000956>.
- [289] Yang, A. *et al.* Real-time tunable lasing from plasmonic nanocavity arrays. *Nature Communications* **6** (2015). URL <https://doi.org/10.1038/ncomms7939>.
- [290] Thackray, B. D. *et al.* Super-narrow, extremely high quality collective plasmon resonances at telecom wavelengths and their application in a hybrid graphene-plasmonic modulator. *Nano Letters* **15**, 3519–3523 (2015). URL <https://doi.org/10.1021/acs.nanolett.5b00930>.
- [291] Le-Van, Q. *et al.* Enhanced Quality Factors of Surface Lattice Resonances in Plasmonic Arrays of Nanoparticles. *Advanced Optical Materials* **7** (2019). URL <https://doi.org/10.1002/adom.201801451>.
- [292] Deng, S. *et al.* Ultranarrow plasmon resonances from annealed nanoparticle lattices. *Proceedings of the National Academy of Sciences of the United States of America* **117**, 23380–23384 (2020). URL <https://doi.org/10.1073/pnas.2008818117>.
- [293] Bin-Alam, M. S. *et al.* Ultra-high-Q resonances in plasmonic metasurfaces. *Nature Communications* **12**, 1–8 (2021). URL <http://dx.doi.org/10.1038/s41467-021-21196-2>. 2004.05202.
- [294] Vecchi, G., Giannini, V. & Gómez Rivas, J. Shaping the fluorescent emission by lattice resonances in plasmonic crystals of nanoantennas. *Physical Review Letters* **102**, 2–5 (2009). URL <https://doi.org/10.1103/PhysRevLett.102.146807>. 0901.1817.
- [295] Rodriguez, S. R. *et al.* Quantum rod emission coupled to plasmonic lattice resonances: A collective directional source of polarized light. *Applied Physics Letters* **100**, 1–3 (2012). URL <https://doi.org/10.1063/1.3693397>.
- [296] Teperik, T. V. & Degiron, A. Superradiant optical emitters coupled to an array of nanosize metallic antennas. *Physical Review Letters* **108**, 1–5 (2012). URL <https://doi.org/10.1103/PhysRevLett.108.147401>.



- [297] Zhou, W. *et al.* Lasing action in strongly coupled plasmonic nanocavity arrays. *Nature Nanotechnology* **8**, 506–511 (2013). URL <https://doi.org/10.1038/nnano.2013.99>.
- [298] Wang, X. Y. *et al.* Lasing Enhanced Surface Plasmon Resonance Sensing. *Nanophotonics* **6**, 472–478 (2017). URL <https://doi.org/10.1515/nanoph-2016-0006>.
- [299] Freire-Fernández, F. *et al.* Magnetic on–off switching of a plasmonic laser. *Nature Photonics* **16**, 27–32 (2022). URL <https://doi.org/10.1038/s41566-021-00922-8.2104.14321>.
- [300] Auguié, B., Bendaña, X. M., Barnes, W. L. & García De Abajo, F. J. Diffractive arrays of gold nanoparticles near an interface: Critical role of the substrate. *Physical Review B - Condensed Matter and Materials Physics* **82**, 1–7 (2010). URL <https://doi.org/10.1103/PhysRevB.82.155447.1007.4428>.
- [301] Faraday, M. *On the magnetization of light and the illumination of magnetic lines of force* (The Royal Society, 1846). URL <https://doi.org/10.5479/sil.389644.mq591299>.
- [302] Kerr, J. XLIII. On rotation of the plane of polarization by reflection from the pole of a magnet. *The London, Edinburgh, and Dublin Philosophical Magazine and Journal of Science* **3**, 321–343 (1877).
- [303] Ferré, J., Jamet, J. P. & Meyer, P. Magneto-Optical Studies of Magnetic Ultrathin Film Structures. *Physica Status Solidi (A) Applied Research* **175**, 213–223 (1999). URL [https://doi.org/10.1002/\(SICI\)1521-396X\(199909\)175:1%3C213::AID-PSSA213%3E3.0.CO;2-5](https://doi.org/10.1002/(SICI)1521-396X(199909)175:1%3C213::AID-PSSA213%3E3.0.CO;2-5).
- [304] Pommier, J. *et al.* Magnetization Reversal in Ultrathin Ferromagnetic Films with Perpendicular Anisotropy: Domain Observations. *Physical Review Letters* **65**, 2054–2058 (1990). URL <https://doi.org/10.1103/PhysRevLett.65.2054>.
- [305] Aign, T. *et al.* Magnetization Reversal in Arrays of Perpendicularly Magnetized Ultrathin Dots Coupled by Dipolar Interaction. *Physical Review Letters* **81**, 5656–5659 (1998). URL <https://doi.org/10.1103/PhysRevLett.81.5656>.
- [306] Remy, Q. *et al.* Accelerating ultrafast magnetization reversal by non-local spin transfer. *Nature Communications* **14**, 445 (2022). URL <https://doi.org/10.1038/s41467-023-36164-1>.

## BIBLIOGRAPHY

---

- [307] Igarashi, J. *et al.* Optically induced ultrafast magnetization switching in ferromagnetic spin valves. *Nature Materials* 1–6 (2023). URL <https://doi.org/10.1038/s41563-023-01499-z>.
- [308] Sepúlveda, B., González-Díaz, J. B., García-Martín, A., Lechuga, L. M. & Armelles, G. Plasmon-Induced Magneto-Optical Activity in Nanosized Gold Disks. *Physical Review Letters* **104**, 147401 (2010). URL <https://doi.org/10.1103/PhysRevLett.104.147401>.
- [309] Bonanni, V. *et al.* Designer magnetoplasmonics with nickel nanoferrromagnets. *Nano Letters* **11**, 5333–5338 (2011). URL <https://doi.org/10.1021/nl2028443>.
- [310] Maccaferri, N. *et al.* Tuning the Magneto-Optical Response of Nanosize Ferromagnetic Ni Disks Using the Phase of Localized Plasmons. *Physical Review Letters* **111**, 167401 (2013). URL <https://doi.org/10.1103/PhysRevLett.111.167401>.
- [311] Maccaferri, N. *et al.* Effects of a non-absorbing substrate on the magneto-optical Kerr response of plasmonic ferromagnetic nanodisks. *Physica Status Solidi (A) Applications and Materials Science* **211**, 1067–1075 (2014).
- [312] Armelles, G., Cebollada, A., García-Martín, A. & González, M. U. Magnetoplasmonics: Combining Magnetic and Plasmonic Functionalities. *Advanced Optical Materials* **1**, 10–35 (2013). URL <https://doi.org/10.1002/adom.201200011>.
- [313] Toshiba Leads Industry in Bringing Perpendicular Data Recording to HDD - Sets New Record for Storage Capacity with Two New HDDs (2004). URL <https://www.global.toshiba/ww/news/corporate/2004/12/pr1401.html>.
- [314] Sharrock, M. P. Time-dependent magnetic phenomena and particle-size effects in recording media. *IEEE Transactions on Magnetics* **26**, 193–197 (1990). URL <https://doi.org/10.1109/20.50532>.
- [315] Wood, R. The Feasibility of Magnetic Recording at 1 Terabit per Square Inch. *IEEE Transactions on Magnetics* **36**, 36–42 (2000). URL <https://doi.org/10.1109/20.824422>.
- [316] Pan, L. & Bogy, D. B. Heat-assisted magnetic recording. *Nature Photonics* **3**, 189–190 (2009). URL <https://doi.org/10.1038/nphoton.2009.40>.

- [317] Weller, D. *et al.* Review Article: FePt heat assisted magnetic recording media. *Journal of Vacuum Science and Technology B* **34**, 060801 (2016). URL <https://doi.org/10.1116/1.4965980>.
- [318] Chen, J. S. *et al.* Low temperature deposited L 10 FePt-C (001) films with high coercivity and small grain size. *Applied Physics Letters* **91**, 132506 (2007). URL <https://doi.org/10.1063/1.2789790>.
- [319] Perumal, A., Takahashi, Y. K. & Hono, K. L10 FePt-C Nanogranular Perpendicular Anisotropy Films with Narrow Size Distribution. *Applied Physics Express* **1**, 1013011–1013013 (2008). URL <https://doi.org/10.1143/APEX.1.101301>.
- [320] Klemmer, T., Peng, Y., Wu, X. & Ju, G. Materials Processing for High Anisotropy L10 Granular Media. *IEEE Transactions on Magnetics* **45**, 845–849 (2009). URL <https://doi.org/10.1109/TMAG.2008.2010649>.
- [321] Zhang, L. *et al.* L10-ordered FePtAg-C granular thin film for thermally assisted magnetic recording media (invited). *Journal of Applied Physics* **109**, 07B703 (2011). URL <https://doi.org/10.1063/1.3536794>.
- [322] Stipe, B. C. *et al.* Magnetic recording at 1.5 Pb m<sup>-2</sup> using an integrated plasmonic antenna. *Nature Photonics* **4**, 484–488 (2010). URL <https://doi.org/10.1038/nphoton.2010.90>.
- [323] Matsumoto, T., Akagi, F., Mochizuki, M., Miyamoto, H. & Stipe, B. Integrated head design using a nanobeak antenna for thermally assisted magnetic recording. *Optics Express* **20**, 18946 (2012). URL <https://doi.org/10.1364/OE.20.018946>.
- [324] Kautzky, M. C. & Blaber, M. G. Materials for heat-assisted magnetic recording heads. *MRS Bulletin* **43**, 100–105 (2018). URL <https://doi.org/10.1557/mrs.2018.1>.
- [325] Kief, M. T. & Victora, R. H. Materials for heat-assisted magnetic recording. *MRS Bulletin* **43**, 87–92 (2018). URL <https://doi.org/10.1557/mrs.2018.2>.
- [326] Hu, Y., Wu, H., Meng, Y. & Bogy, D. A Numerical Investigation of the Nanoscale Heat Transfer in Heat Assisted Magnetic Recording. *ASME 2017 Conference on Information Storage and Processing Systems, ISPS 2017* 1–5 (2017). URL <https://doi.org/10.1115/ISPS2017-5411>.

## BIBLIOGRAPHY

---

- [327] Le Guyader, L. *et al.* Demonstration of laser induced magnetization reversal in GdFeCo nanostructures. *Applied Physics Letters* **101**, 022410 (2012). URL <https://doi.org/10.1063/1.4733965>.
- [328] Le Guyader, L. *et al.* Nanoscale sub-100 picosecond all-optical magnetization switching in GdFeCo microstructures. *Nature Communications* **6**, 1–6 (2015). URL <https://doi.org/10.1038/ncomms6839>.
- [329] Savoini, M. *et al.* Highly efficient all-optical switching of magnetization in GdFeCo microstructures by interference-enhanced absorption of light. *Physical Review B - Condensed Matter and Materials Physics* **86**, 140404(R) (2012). URL <https://doi.org/10.1103/PhysRevB.86.140404>.
- [330] Xun, X., Peng, C. & Mansuripur, M. Estimation of thermal coefficients of magneto-optical media. *Applied Optics* **41**, 4596 (2002). URL <https://doi.org/10.1364/AO.41.004596>.
- [331] Fert, A., Cros, V. & Sampaio, J. Skyrmions on the track. *Nature Nanotechnology* **8**, 152–156 (2013). URL <https://doi.org/10.1038/nnano.2013.29>.
- [332] Mühlischlegel, P., Eisler, H. J., Martin, O. J., Hecht, B. & Pohl, D. W. Resonant Optical Antennas. *Science* **308**, 1607–1609 (2005). URL <https://doi.org/10.1126/science.1111886>.
- [333] Koene, B., Savoini, M., Kimel, A. V., Kirilyuk, A. & Rasing, T. Optical energy optimization at the nanoscale by near-field interference. *Applied Physics Letters* **101**, 013115 (2012). URL <https://doi.org/10.1063/1.4733292>.
- [334] Sala, G. *et al.* Asynchronous current-induced switching of rare-earth and transition-metal sublattices in ferrimagnetic alloys. *Nature Materials* **21**, 640–646 (2022). URL <https://doi.org/10.1038/s41563-022-01248-8>.
- [335] Li, P., Kools, T. J., Lavrijsen, R. & Koopmans, B. Ultrafast Racetrack Based on Compensated Co/Gd-Based Synthetic Ferrimagnet with All-Optical Switching. *Advanced Electronic materials* 2200613 (2022). URL <https://doi.org/10.1002/aelm.202200613>. 2204.11595.
- [336] Granitzka, P. W. *et al.* Magnetic Switching in Granular FePt Layers Promoted by Near-Field Laser Enhancement. *Nano Letters* **17**, 2426–2432 (2017). URL <https://doi.org/10.1021/acs.nanolett.7b00052>.

- [337] Mishra, K. *et al.* Ultrafast demagnetization in a ferrimagnet under electromagnetic field funneling. *Nanoscale* **13**, 19367–19375 (2021). URL <https://doi.org/10.1039/D1NR04308K>. 2103.05365.
- [338] Mishra, K. *et al.* Ultrafast Demagnetization Control in Magnetophotonic Surface Crystals. *Nano Letters* **22**, 9773–9780 (2022). URL <https://doi.org/10.1021/acs.nanolett.2c00769>.
- [339] Kataja, M. *et al.* Plasmon-induced demagnetization and magnetic switching in nickel nanoparticle arrays. *Applied Physics Letters* **112**, 072406 (2018). URL <https://doi.org/10.1063/1.5012857>.
- [340] Cheng, F. *et al.* All-Optical Manipulation of Magnetization in Ferromagnetic Thin Films Enhanced by Plasmonic Resonances. *Nano Letters* **20**, 6437–6443 (2020). URL <https://doi.org/10.1021/acs.nanolett.0c02089>.
- [341] Jiang, Y., Li, X. & Gu, M. Generation of sub-diffraction-limited pure longitudinal magnetization by the inverse Faraday effect by tightly focusing an azimuthally polarized vortex beam. *Optics Letters* **38**, 2957 (2013). URL <https://doi.org/10.1364/OL.38.002957>.
- [342] Hao, C. *et al.* Three-dimensional supercritical resolved light-induced magnetic holography. *Science Advances* **3**, e1701398 (2017). URL <https://doi.org/10.1126/sciadv.1701398>.
- [343] Borovkova, O. V., Ignatyeva, D. O. & Belotelov, V. I. Layer-selective magnetization switching in the chirped photonic crystal with GdFeCo. *Scientific Reports* **11**, 2239 (2021). URL <https://doi.org/10.1038/s41598-021-81887-0>.
- [344] Dutta, A., Kildishev, A. V., Shalaev, V. M., Boltasseva, A. & Marinero, E. E. Surface-plasmon opto-magnetic field enhancement for all-optical magnetization switching. *Optical Materials Express* **7**, 4316 (2017). URL <https://doi.org/10.1364/OME.7.004316>.
- [345] Pezeshki, H., Li, P., Lavrijsen, R., Van Der Tol, J. J. & Koopmans, B. Optical Reading of Nanoscale Magnetic Bits in an Integrated Photonic Platform. *IEEE Journal of Quantum Electronics* 1–8 (2022). URL <https://doi.org/10.1109/JQE.2022.3224782>.

## BIBLIOGRAPHY

---

- [346] Pezeshki, H. *et al.* Design of an integrated hybrid plasmonic-photonic device for all-optical switching and reading of spintronic memory. *arXiv* (2022). URL <http://arxiv.org/abs/2209.15556>. 2209.15556.
- [347] Pezeshki, H., Koopmans, B. & van der Tol, J. J. G. M. Broadband Multifunctional Plasmonic Polarization Converter based on Multimode Interference Coupler. *arXiv* (2022). URL <http://arxiv.org/abs/2210.11353>. 2210.11353.
- [348] Abendroth, J. M. *et al.* Helicity-Preserving Metasurfaces for Magneto-Optical Enhancement in Ferromagnetic [Pt/Co]N Films. *Advanced Optical Materials* **8**, 2001420 (2020). URL <https://doi.org/10.1002/adom.202001420>.
- [349] Maksymov, I. S. Magneto-Plasmonics and Resonant Interaction of Light with Dynamic Magnetisation in Metallic and All-Magneto-Dielectric Nanostructures. *Nanomaterials* **5**, 577–613 (2015). URL <https://doi.org/10.3390/nano5020577>.
- [350] Maccaferri, N. *et al.* Nanoscale magnetophotonics. *Journal of Applied Physics* **127**, 080903 (2020). URL <https://doi.org/10.1063/1.5100826>. 1904.11846.
- [351] Chen, J. *et al.* Plasmonic Nickel Nanoantennas. *Small* **7**, 2341–2347 (2011). URL <https://doi.org/10.1002/sml1.201100640>.
- [352] Floess, D., Weiss, T., Tikhodeev, S. & Giessen, H. Lorentz Nonreciprocal Model for Hybrid Magnetoplasmonics. *Physical Review Letters* **117**, 063901 (2016). URL <https://doi.org/10.1103/PhysRevLett.117.063901>.
- [353] Temnov, V. V. *et al.* Active magneto-plasmonics in hybrid metal-ferromagnet structures. *Nature Photonics* **4**, 107–111 (2010). URL <https://doi.org/10.1038/nphoton.2009.265>.
- [354] Caballero, B., García-Martín, A. & Cuevas, J. C. Faraday effect in hybrid magneto-plasmonic photonic crystals. *Optics Express* **23**, 22238 (2015). URL <https://doi.org/10.1364/OE.23.022238>.
- [355] Caballero, B., García-Martín, A. & Cuevas, J. C. Hybrid Magnetoplasmonic Crystals Boost the Performance of Nanohole Arrays as Plasmonic Sensors. *ACS Photonics* **3**, 203–208 (2016). URL <https://doi.org/10.1021/acsphotonics.5b00658>.

- [356] González-Díaz, J. B. *et al.* Plasmonic Au/Co/Au Nanosandwiches with Enhanced Magneto-optical Activity. *Small* **4**, 202–205 (2008). URL <https://doi.org/10.1002/sml1.200700594>.
- [357] Armelles, G., Cebollada, A., García, F., García-Martín, A. & De Sousa, N. Far- and Near-Field Broad-Band Magneto-Optical Functionalities Using Magnetoplasmonic Nanorods. *ACS Photonics* **3**, 2427–2433 (2016). URL <https://doi.org/10.1021/acsp Photonics.6b00670>.
- [358] Wang, L. *et al.* Plasmonics and Enhanced Magneto-Optics in Core-Shell Co-Ag Nanoparticles. *Nano Letters* **11**, 1237–1240 (2011). URL <https://doi.org/10.1021/nl1042243>.
- [359] Song, Y., Ding, J. & Wang, Y. Shell-Dependent Evolution of Optical and Magnetic Properties of Co@Au Core-Shell Nanoparticles. *Journal of Physical Chemistry C* **116**, 11343–11350 (2012). URL <https://doi.org/10.1021/jp300118z>.
- [360] Barsukova, M. G., Musorin, A. I., Shorokhov, A. S. & Fedyanin, A. A. Enhanced magneto-optical effects in hybrid Ni-Si metasurfaces. *APL Photonics* **4**, 016102 (2019). URL <https://doi.org/10.1063/1.5066307>.
- [361] Belotelov, V. I. *et al.* Enhanced magneto-optical effects in magnetoplasmonic crystals. *Nature Nanotechnology* **6**, 370–376 (2011). URL <https://doi.org/10.1038/nnano.2011.54>.
- [362] Belotelov, V. I. *et al.* Magnetophotonic intensity effects in hybrid metal-dielectric structures. *Physical Review B - Condensed Matter and Materials Physics* **89**, 045118 (2014). URL <https://doi.org/10.1103/PhysRevB.89.045118>.
- [363] Belotelov, V. I. *et al.* Plasmon-mediated magneto-optical transparency. *Nature Communications* **4**, 2128 (2013). URL <https://doi.org/10.1038/ncomms3128>.
- [364] Chekhov, A. L. *et al.* Magnetoplasmonic crystal waveguide. *Optics Express* **26**, 21086 (2018). URL <https://doi.org/10.1364/OE.26.021086>.
- [365] Maccaferri, N. *et al.* Anisotropic Nanoantenna-Based Magnetoplasmonic Crystals for Highly Enhanced and Tunable Magneto-Optical Activity. *Nano Letters* **16**, 2533–2542 (2016). URL <https://doi.org/10.1021/acs.nanolett.6b00084>.



## BIBLIOGRAPHY

---

- [366] Lodewijks, K. *et al.* Magnetoplasmonic design rules for active magneto-optics. *Nano Letters* **14**, 7207–7214 (2014). URL <https://doi.org/10.1021/nl504166n>. 1411. 7143.
- [367] Sotiriou, G. A. *et al.* Hybrid , Silica-Coated , Janus-Like Plasmonic-Magnetic Nanoparticles. *Chemistry of Materials* **23**, 1985–1992 (2011). URL <https://doi.org/10.1021/cm200399t>.
- [368] Passarelli, N., Pérez, L. A. & Coronado, E. A. Plasmonic Interactions: From Molecular Plasmonics and Fano Resonances to Ferroplasmons. *ACS Nano* **8**, 9723–9728 (2014). URL <https://doi.org/10.1021/nn505145v>.
- [369] Zubritskaya, I. *et al.* Active Magnetoplasmonic Ruler. *Nano Letters* **15**, 3204–3211 (2015). URL <https://doi.org/10.1021/acs.nanolett.5b00372>.
- [370] Feng, H. Y. *et al.* Active magnetoplasmonic split-ring/ring nanoantennas. *Nanoscale* **9**, 37–44 (2017). URL <https://doi.org/10.1039/c6nr07864h>.
- [371] Newman, D. M., Wears, M. L., Matelon, R. J. & Hooper, I. R. Magneto-optic behaviour in the presence of surface plasmons. *Journal of Physics Condensed Matter* **20**, 345230 (2008). URL <https://doi.org/10.1088/0953-8984/20/34/345230>.
- [372] Grunin, A. A., Zhdanov, A. G., Ezhov, A. A., Ganshina, E. A. & Fedyanin, A. A. Surface-plasmon-induced enhancement of magneto-optical Kerr effect in all-nickel subwavelength nanogratings. *Applied Physics Letters* **97**, 261908 (2010). URL <https://doi.org/10.1063/1.3533260>.
- [373] Grunin, A. A., Mukha, I. R., Chetvertukhin, A. V. & Fedyanin, A. A. Refractive index sensor based on magnetoplasmonic crystals. *Journal of Magnetism and Magnetic Materials* **415**, 72–76 (2016). URL <https://doi.org/10.1016/j.jmmm.2016.03.069>.
- [374] Clavero, C., Yang, K., Skuza, J. R. & Lukaszew, R. A. Magnetic-field modulation of surface plasmon polaritons on gratings. *Optics Letters* **35**, 1557 (2010). URL <https://doi.org/10.1364/OL.35.001557>.
- [375] Torrado, J. F., González-Díaz, J. B., González, M. U., García-Martín, A. & Armelles, G. Magneto-optical effects in interacting localized and propagating surface plasmon modes. *Optics Express* **18**, 15635 (2010). URL <https://doi.org/10.1364/OE.18.015635>.



- [376] Armelles, G. *et al.* Localized surface plasmon resonance effects on the magneto-optical activity of continuous Au/Co/Au trilayers. *Optics Express* **16**, 16104 (2008). URL <https://doi.org/10.1364/OE.16.016104>.
- [377] Torrado, J. F. *et al.* Tunable magneto-photonic response of nickel nanostructures. *Applied Physics Letters* **99**, 193109 (2011). URL <https://doi.org/10.1063/1.3660587>.
- [378] Sapozhnikov, M. V., Gusev, S. A., Troitskii, B. B. & Khokhlova, L. V. Optical and magneto-optical resonances in nanocorrugated ferromagnetic films. *Optics Letters* **36**, 4197 (2011). URL <https://doi.org/10.1364/OL.36.004197>.
- [379] Maccaferri, N. *et al.* Resonant Enhancement of Magneto-Optical Activity Induced by Surface Plasmon Polariton Modes Coupling in 2D Magnetoplasmonic Crystals. *ACS Photonics* **2**, 1769–1779 (2015). URL <https://doi.org/10.1021/acsphotonics.5b00490>.
- [380] Kalish, A. N. *et al.* Magnetoplasmonic quasicrystals: an approach for multiband magneto-optical response. *Optica* **5**, 617 (2018). URL <https://doi.org/10.1364/OPTICA.5.000617>.
- [381] Ctistis, G. *et al.* Optical and magnetic properties of hexagonal arrays of subwavelength holes in optically thin cobalt films. *Nano Letters* **9**, 1–6 (2009). URL <https://doi.org/10.1021/nl801811t>.
- [382] Papaioannou, E. T. *et al.* Magneto-optic enhancement and magnetic properties in Fe antidot films with hexagonal symmetry. *Physical Review B - Condensed Matter and Materials Physics* **81**, 054424 (2010). URL <https://doi.org/10.1103/PhysRevB.81.054424>.
- [383] Papaioannou, E. T. *et al.* Surface plasmons and magneto-optic activity in hexagonal Ni anti-dot arrays. *Optics Express* **19**, 23867 (2011). URL <https://doi.org/10.1364/OE.19.023867>.
- [384] Sepúlveda, B., Calle, A., Lechuga, L. M. & Armelles, G. Highly sensitive detection of biomolecules with the magneto-optic surface-plasmon-resonance sensor. *Optics Letters* **31**, 1085–1087 (2006). URL <https://doi.org/10.1364/OL.31.001085>.
- [385] Liu, N., Tang, M. L., Hentschel, M., Giessen, H. & Alivisatos, A. P. Nanoantenna-enhanced gas sensing in a single tailored nanofocus. *Nature Materials* **10**, 631–636 (2011). URL <https://doi.org/10.1038/nmat3029>.

## BIBLIOGRAPHY

---

- [386] Chou, K.-H. *et al.* Application of strong transverse magneto-optical Kerr effect on high sensitive surface plasmon grating sensors. *Optics Express* **22**, 19794 (2014). URL <https://doi.org/10.1364/OE.22.019794>.
- [387] Manera, M. G., Ferreiro-Vila, E., Garcia-Martin, J. M., Garcia-Martin, A. & Rella, R. Enhanced antibody recognition with a magneto-optic surface plasmon resonance (MO-SPR) sensor. *Biosensors and Bioelectronics* **58**, 114–120 (2014). URL <https://doi.org/10.1016/j.bios.2014.02.003>.
- [388] David, S. *et al.* Magneto-plasmonic biosensor with enhanced analytical response and stability. *Biosensors and Bioelectronics* **63**, 525–532 (2015). URL <https://doi.org/10.1016/j.bios.2014.08.004>.
- [389] Ignatyeva, D. O. *et al.* Magneto-optical plasmonic heterostructure with ultranarrow resonance for sensing applications. *Scientific Reports* **6**, 28077 (2016). URL <https://doi.org/10.1038/srep28077>.
- [390] Diaz-Valencia, B. F., Mejía-Salazar, J. R., Oliveira, O. N., Porrás-Montenegro, N. & Al-bella, P. Enhanced Transverse Magneto-Optical Kerr Effect in Magnetoplasmonic Crystals for the Design of Highly Sensitive Plasmonic (Bio)sensing Platforms. *ACS Omega* **2**, 7682–7685 (2017). URL <https://doi.org/10.1021/acsomega.7b01458>.
- [391] Garoli, D., Yamazaki, H., MacCafferri, N. & Wanunu, M. Plasmonic Nanopores for Single-Molecule Detection and Manipulation: Toward Sequencing Applications. *Nano Letters* **19**, 7553–7562 (2019). URL <https://doi.org/10.1021/acs.nanolett.9b02759>.
- [392] Zambrana-Puyalto, X. *et al.* A hybrid metal-dielectric zero mode waveguide for enhanced single molecule detection. *Chemical Communications* **55**, 9725–9728 (2019). URL <https://doi.org/10.1039/c9cc04118d>.
- [393] van Genuchten, H. C. M. *Installing and optimizing the MOKE setup*. Ph.D. thesis, Eindhoven University of Technology (2004). URL <https://research.tue.nl/nl/studentTheses/installing-and-optimizing-the-moke-setup>.
- [394] Polisetty, S. *et al.* Optimization of magneto-optical Kerr setup: Analyzing experimental assemblies using Jones matrix formalism. *Review of Scientific Instruments* **79**, 055107 (2008). URL <https://doi.org/10.1063/1.2932445>.

- [395] Badoz, J., Silverman, M. P. & Canit, J. C. Wave propagation through a medium with static and dynamic birefringence: theory of the photoelastic modulator. *Journal of the Optical Society of America A* **7**, 672 (1990). URL <https://doi.org/10.1364/JOSAA.7.000672>.
- [396] Wang, S., Han, X., Wang, Y. & Li, K. Dispersion of the Retardation of a Photoelastic Modulator. *Applied Sciences* **9**, 341 (2019). URL <https://doi.org/10.3390/app9020341>.
- [397] BV, P.-W. Different Types of SEM Imaging – BSE and Secondary Electron Imaging (2017). URL <https://www.azom.com/article.aspx?ArticleID=14309>.
- [398] Rullière, C. & Alfano, R. R. *Femtosecond Laser Pulses* (Springer, 2004), 2nd edn. URL [https://www.google.com/url?sa=t&rct=j&q=&esrc=s&source=web&cd=&cad=rja&uact=8&ved=2ahUKEwi0z8-TscT8AhUOVqQEHUeJB5AQFnoECBMQAQ&url=http%3A%2F%2Ffulviofrisone.com%2Fattachments%2Farticle%2F466%2FRulliere%2520C.%2520\(ed\)%2520Femtosecond%2520laser%2520pulses](https://www.google.com/url?sa=t&rct=j&q=&esrc=s&source=web&cd=&cad=rja&uact=8&ved=2ahUKEwi0z8-TscT8AhUOVqQEHUeJB5AQFnoECBMQAQ&url=http%3A%2F%2Ffulviofrisone.com%2Fattachments%2Farticle%2F466%2FRulliere%2520C.%2520(ed)%2520Femtosecond%2520laser%2520pulses).
- [399] Treacy, E. B. Optical Pulse Compression With Diffraction Gratings. *IEEE Journal of Quantum Electronics* **4**, 454–458 (1969). URL <https://doi.org/10.1109/JQE.1969.1076303>.
- [400] Shank, C. V., Fork, R. L., Yen, R., Stolen, R. H. & Tomlinson, W. J. Compression of femtosecond optical pulses. *Applied Physics B: Lasers and Optics* **40**, 1982 (1982). URL <https://doi.org/10.1063/1.93276>.
- [401] Fork, R. L., Martinez, E. & Gordon, J. P. Negative dispersion using pairs of prisms. *Optics Letters* **9**, 150–152 (1984). URL <https://doi.org/10.1364/OL.9.000150>.
- [402] Proctor, B. & Wise, F. Quartz prism sequence for reduction of cubic phase in a mode-locked Ti:Al<sub>2</sub>O<sub>3</sub> laser. *Optics Letters* **17**, 1295–1297 (1992). URL <https://doi.org/10.1364/OL.17.001295>.
- [403] Cheng, Z., Krausz, F. & Spielmann, C. Compression of 2 mJ kilohertz laser pulses to 17.5 fs by pairing double-prism compressor: Analysis and performance. *Optics Communications* **201**, 145–155 (2002). URL [https://doi.org/10.1016/S0030-4018\(01\)01675-3](https://doi.org/10.1016/S0030-4018(01)01675-3).
- [404] Szipöcs, R., Spielmann, C., Krausz, F. & Ferencz, K. Chirped multilayer coatings for broadband dispersion control in femtosecond lasers. *Optics Letters* **19**, 201 (1994). URL <https://doi.org/10.1364/OL.19.000201>.

## BIBLIOGRAPHY

---

- [405] Kartner, F. X. *et al.* Design and fabrication of double chirped mirrors. *Optics Letters* **22**, 831–833 (1997). URL <https://doi.org/10.1364/OL.22.000831>.
- [406] Matuschek, N., Kärtner, F. X. & Keller, U. Theory of double-chirped mirrors. *IEEE Journal on Selected Topics in Quantum Electronics* **4**, 197–208 (1998). URL <https://doi.org/10.1109/2944.686724>.
- [407] Steinmeyer, G., Sutter, D. H., Gallmann, L., Matuschek, N. & Keller, U. Frontiers in Ultra-short Pulse Generation: Pushing the Limits in Linear and Nonlinear Optics. *Science* **286**, 1507–1512 (1999). URL <https://doi.org/10.1126/science.286.5444.1507>.
- [408] Moulton, P. F. Spectroscopic and laser characteristics of Ti:Al<sub>2</sub>O<sub>3</sub>. *Journal of the Optical Society of America B* **3**, 125–133 (1986). URL <https://doi.org/10.1364/JOSAB.3.000125>.
- [409] Strickland, D. & Mourou, G. Compression of amplified chirped optical pulses. *Optics Communications* **56**, 219–221 (1985). URL [https://doi.org/10.1016/0030-4018\(85\)90120-8](https://doi.org/10.1016/0030-4018(85)90120-8).
- [410] Hentschel, M., Cheng, Z., Krausz, F. & Spielmann, C. Generation of 0.1-TW optical pulses with a single-stage Ti:sapphire amplifier at a 1-kHz repetition rate. *Applied Physics B: Lasers and Optics* **70**, S161–S164 (2000). URL <https://doi.org/10.1007/s003400000327>.
- [411] Hamrle, J. *Magneto-optical determination of the in-depth magnetization profile in magnetic multilayers*. Ph.D. thesis, University Paris XI UFR Scientifique d'Orsay and Faculty of Mathematics and Physics Charles University in Prague (2003). URL <https://theses.hal.science/tel-00002948>.
- [412] Schellekens, A. J., De Vries, N., Lucassen, J. & Koopmans, B. Exploring laser-induced interlayer spin transfer by an all-optical method. *Physical Review B - Condensed Matter and Materials Physics* **90**, 104429 (2014). URL <https://doi.org/10.1103/PhysRevB.90.104429>.
- [413] Wieczorek, J. *et al.* Separation of ultrafast spin currents and spin-flip scattering in Co/Cu(001) driven by femtosecond laser excitation employing the complex magneto-optical Kerr effect. *Physical Review B - Condensed Matter and Materials Physics* **92**, 174410 (2015). URL <https://doi.org/10.1103/PhysRevB.92.174410>.

- [414] Gorchon, J. *et al.* Single shot ultrafast all optical magnetization switching of ferromagnetic Co/Pt multilayers. *Applied Physics Letters* **111**, 042401 (2017). URL <https://doi.org/10.1063/1.4994802>.
- [415] Hofherr, M. *et al.* Speed and efficiency of femtosecond spin current injection into a nonmagnetic material. *Physical Review B* **96**, 100403(R) (2017). URL <https://doi.org/10.1103/PhysRevB.96.100403>.
- [416] Lichtenberg, T., Beens, M., Jansen, M. H., Koopmans, B. & Duine, R. A. Probing optically induced spin currents using terahertz spin waves in noncollinear magnetic bilayers. *Physical Review B* **105**, 144416 (2022). URL <https://doi.org/10.1103/PhysRevB.105.144416>.
- [417] Zhang, W. *et al.* Optical Creation of Skyrmions by Spin Reorientation Transition in Ferrimagnetic CoHo Alloys. *ACS Applied Materials and Interfaces* (2023). URL <https://doi.org/10.1021/acscami.2c19411>.
- [418] Chen, J. Y., He, L., Wang, J. P. & Li, M. All-Optical Switching of Magnetic Tunnel Junctions with Single Subpicosecond Laser Pulses. *Physical Review Applied* **7**, 021001 (2017). URL <https://doi.org/10.1103/PhysRevApplied.7.021001>.
- [419] Wang, L., Van Hees, Y. L., Lavrijsen, R., Zhao, W. & Koopmans, B. Enhanced all-optical switching and domain wall velocity in annealed synthetic-ferrimagnetic multilayers. *Applied Physics Letters* **117**, 022408 (2020). URL <https://doi.org/10.1063/5.0012269>.
- [420] Wang, L. *et al.* Picosecond optospintronic tunnel junctions. *Proceedings of the National Academy of Sciences* **119**, e2204732119 (2022). URL <https://doi.org/10.1073/pnas.2204732119>.
- [421] Vergès, M. *et al.* Energy Efficient Single Pulse Switching of [ Co / Gd / Pt ] N Nanodisks Using Surface Lattice Resonances. *Advanced Science* **10**, 2204683 (2022). URL <https://doi.org/10.1002/advs.202204683>.
- [422] Kools, T. J., van Gorp, M. C., Koopmans, B. & Lavrijsen, R. Magnetostatics of Room Temperature Compensated Co/Gd/Co/Gd-based Synthetic Ferrimagnets. *Applied Physics Letters* **121**, 242405 (2022). URL <https://doi.org/10.1063/5.0127694>.

## BIBLIOGRAPHY

---

- [423] Van Hees, Y. L., Koopmans, B. & Lavrijsen, R. Toward high all-optical data writing rates in synthetic ferrimagnets. *Applied Physics Letters* **120**, 252401 (2022). URL <https://doi.org/10.1063/5.0094540>.
- [424] Li, P. *et al.* Enhancing all-optical switching of magnetization by He ion irradiation. *Applied Physics Letters* **121**, 172404 (2022). URL <https://doi.org/10.1063/5.0111466>.
- [425] Kataja, M. *et al.* Hybrid plasmonic lattices with tunable magneto-optical activity. *Optics Express* **24**, 3652–3662 (2016). URL <https://doi.org/10.1364/OE.24.003652>.
- [426] Kataja, M., Pourjamal, S. & van Dijken, S. Magnetic circular dichroism of non-local surface lattice resonances in magnetic nanoparticle arrays. *Optics Express* **24**, 3562–3571 (2016). URL <https://doi.org/10.1364/OE.24.003562>.
- [427] Bello, J.-L. *et al.* Impact of interfaces on magnetic properties of Gdx(Fe90Co10)1-x alloys. *Applied Physics Letters* **121**, 212402 (2022). URL <https://doi.org/10.1063/5.0125011>.
- [428] Güdde, J., Hohlfeld, J., Müller, J. G. & Matthias, E. Damage threshold dependence on electron-phonon coupling in Au and Ni films. *Applied Surface Science* **127-129**, 40–45 (1998). URL [https://doi.org/10.1016/S0169-4332\(98\)00002-6](https://doi.org/10.1016/S0169-4332(98)00002-6).
- [429] Remy, Q. *Ultrafast spin dynamics and transport in magnetic metallic heterostructures*. Ph.D. thesis, Institut Jean Lamour - UMR 7198 - Université de Lorraine (2021). URL <https://hal.univ-lorraine.fr/tel-03560783>.
- [430] Bergeard, N. *et al.* Hot-Electron-Induced Ultrafast Demagnetization in Co/Pt Multilayers. *Physical Review Letters* **117**, 1–5 (2016). URL <https://doi.org/10.1103/PhysRevLett.117.147203>.
- [431] Kimling, J. & Cahill, D. G. Spin diffusion induced by pulsed-laser heating and the role of spin heat accumulation. *Physical Review B* **95**, 014402 (2017). URL <https://doi.org/10.1103/PhysRevB.95.014402>.
- [432] Griepe, T. & Atxitia, U. Electron-phonon mediated spin-flip as driving mechanism for ultrafast magnetization dynamics in 3d ferromagnets. *arXiv* 1–7 (2022). URL <https://doi.org/10.48550/arXiv.2210.15269%0A>.

- [433] Beens, M., Duine, R. A. & Koopmans, B. s-d model for local and nonlocal spin dynamics in laser-excited magnetic heterostructures. *Physical Review B* **102**, 054442 (2020). URL <https://doi.org/10.1103/PhysRevB.102.054442>.
- [434] Hurst, J., Oppeneer, P. M., Manfredi, G. & Hervieux, P. A. Magnetic moment generation in small gold nanoparticles via the plasmonic inverse Faraday effect. *Physical Review B* **94**, 134439 (2018). URL <https://doi.org/10.1103/PhysRevB.98.134439>.
- [435] Cheng, O. H. C., Son, D. H. & Sheldon, M. Light-induced magnetism in plasmonic gold nanoparticles. *Nature Photonics* **14**, 365–368 (2020). URL <https://doi.org/10.1038/s41566-020-0603-3>.
- [436] Bonod, N., Bidault, S., Burr, G. W. & Mivelle, M. Evolutionary Optimization of All-Dielectric Magnetic Nanoantennas. *Advanced Optical Materials* **7**, 1900121 (2019). URL <https://doi.org/10.1002/adom.201900121>.
- [437] Yang, X. *et al.* Tesla-Range Femtosecond Pulses of Stationary Magnetic Field, Optically Generated at the Nanoscale in a Plasmonic Antenna. *ACS Nano* **16**, 386–393 (2022). URL <https://doi.org/10.1021/acsnano.1c06922>.





# Appendix A

## Matlab code for Mie theory

In this appendix we aim to provide the code we used for calculating scattering and absorption behaviour of single spherical particles in homogenous media. First of all we needed a function to extract refractive indices from a data set. We called this function `RF_material` where  $n_1$  and  $n_2$  are the real and imaginary parts of the total refractive index, respectively.

```
function [n1,n2] = RF_material(lambda0)

    n_input = load('nRefractiveIndex.txt');
    n_input(:,1) = n_input(:,1)*1000;
    lambda = 200:1:1500;
    n_output = interp1(n_input(:,1),n_input(:,2),lambda,'spline');

    k_input = load('kRefractiveIndex.txt');
    k_input(:,1) = k_input(:,1)*1000;
    k_output = interp1(k_input(:,1),k_input(:,2),lambda,'spline');

    index = find (lambda == lambda0);
    n1 = n_output(index);
    n2 = k_output(index);

end
```

Initial data sets come from [refractiveindex.info](http://refractiveindex.info) and each initial data set dedicate its first column for the wavelength of incoming light while the second column is either for  $n$  or  $k$ . Since the wavelength is given in  $\mu\text{m}$ , we multiply the terms related to this quantity by 1000. This first

## APPENDIX A. MATLAB CODE FOR MIE THEORY

---

function aims to interpolate any measured data to estimate carefully the refractive indices for any wavelength of interest.

Next we apply the Mie theory. We called this function `Mie` and it requires as inputs the incident wavelength, the particle size `r_0` and the refractive index of the surrounding homogenous media `n_d`. This program provides the calculated scattering and extinction cross sections `Qsca` and `Qext`.

```
function [Qsca , Qext] = Mie(lambda0 , r_0 , n_d)

[n1 , n2] = RF_material(lambda0);
n = n1 + 1i*n2;
m = n/n_d;
f = 2*pi*n_d/(lambda0*1e-9);
x = f*r_0*1e-9;
z = m*x;
N = round(2+x+4*x^(1/3));

j=(1:N);
sqr = sqrt(pi*x/2);
sqrM = sqrt(pi*z/2);

phi = sqr.*besselj(j+0.5,x);
xi = sqr.*(besselj(j+0.5,x) + 1i*bessely(j+0.5,x));
phim = sqrM.*besselj(j+0.5,z);
phi1 = [sin(x), phi(1:N-1)];
phi1M = [sin(z), phim(1:N-1)];
y = sqr.*bessely(j+0.5,x);
y1 = [-cos(x), y(1:N-1)];

phip = (phi1-j/x.*phi);
phimp = (phi1M-j/z.*phim);
xip = (phi1 + 1i*y1) - j/x.*(phi+1i*y);

aj = (m*phim.*phip - phi.*phimp)./(m*phim.*xip-xi.*phimp);
```

## APPENDIX A. MATLAB CODE FOR MIE THEORY

```
bj = (phim.* phip - m*phi.* phimp) ./ (phim.* xip - m*xi.* phimp);

Qsca = sum( (2*j+1).*(abs(aj).*abs(aj) + abs(bj).*abs(bj)) );
Qsca = Qsca*2*pi/(f*f);
Qext = sum( (2*j+1).*(real(aj + bj)) );
Qext = Qext*2*pi/(f*f);
%
end
```

Since we calculated the scattering and extinction cross sections from the Mie theory for a given wavelength and for a single particle size, we can further calculate them for any condition in order to obtain the maps in Figure 3.12. This representation is very convenient to point out any optical resonance (but the Mie theory remains more adequate for particles whose size is of the order of the incident light wavelength). IN this perspective, we developed a last program namely Maps. It should be noted that we plot in this program the scattering and extinction efficiencies by dividing the outputs of Mie by the geometric cross section of the particle of size  $r_0$

```
tic
lambda = 300:1:1000;
n_d = 1;
R = 5:1:400;
Qsca = zeros(length(lambda),length(R));
Qext = zeros(length(lambda),length(R));
Qabs = zeros(length(lambda),length(R));

Qsca_prime = 300:1:1000;
Qext_prime = 300:1:1000;
z = 0;

for j=1:length(R)
    for p = 1:length(lambda)
        [Qsca_prime(p),Qext_prime(p)]= Mie(lambda(p),R(j),n_d);
        Qsca_prime(p) = Qsca_prime(p)/(pi*R(j)*1e-9)^2;
        Qext_prime(p) = Qext_prime(p)/(pi*R(j)*1e-9)^2;
    end
end
```

## APPENDIX A. MATLAB CODE FOR MIE THEORY

---

```
    Qsca(:,j) = Qsca_prime;
    Qext(:,j) = Qext_prime;
    Qabs(:,j) = Qext(:,j)-Qsca(:,j);
    z = R(j);
end
toc

T1 = table(lambda.',Qsca)
T2 = table(lambda.',Qext)
T3 = table(lambda.',Qabs)

surfc(lambda,R,Qsca.', 'LineStyle', 'none');
ylabel('Nanosphere Radius (nm)');
xlabel(['Light Wavelength (nm)']);
colormap(jet(256));
colorbar;
view([0 0 1]);
title('Scattering Efficiency of single nanosphere, a.u.');
```

# Appendix B

## Jones formalism

The Jones formalism depicts how the light polarization is impacted after being reflected or transmitted by optical components such as a photoelastic modulator (PEM), a waveplate, a polarizer (P), an analyzer (A) (that is actually a polarizer), a compensator (C), the sample (S) etc. This description is very convenient to explain the measurements of first and second harmonic MOKE hysteresis loops. In this work we consider the basis with  $p$  and  $s$  components so that the optical elements used in Kerr magnetometer set-up can be described with the following matrices<sup>280</sup>

Optical component	Notation	General case
Polarizer	$\overline{\overline{P}}$	$\begin{pmatrix} \cos(\beta)^2 & \cos(\beta) \sin(\beta) \\ \cos(\beta) \sin(\beta) & \sin(\beta)^2 \end{pmatrix}$
Sample	$\overline{\overline{S}}$	$\begin{pmatrix} \tilde{r}_{pp} & \tilde{r}_{ps} \\ \tilde{r}_{sp} & \tilde{r}_{ss} \end{pmatrix}$
Photoelastic modulator	$\overline{\overline{\overline{PEM}}}$	$\begin{pmatrix} e^{\frac{\phi}{2}} & 0 \\ 0 & e^{-\frac{\phi}{2}} \end{pmatrix}$
Analyzer	$\overline{\overline{A}}$	$\begin{pmatrix} \cos(\alpha)^2 & \cos(\alpha) \sin(\alpha) \\ \cos(\alpha) \sin(\alpha) & \sin(\alpha)^2 \end{pmatrix}$

Table B.1: Magneto-optical response of optics involved in MOKE magnetometer set-up expressed in the Jones formalism in the most general case. The angles  $\alpha$  and  $\beta$  denotes the angle between the plane of incidence and the main axis of the analyzer and polarizer, respectively.  $\phi$  and  $f$  correspond to the amplitude and modulation frequency of the photoelastic modulator, respectively.

## APPENDIX B. JONES FORMALISM

---

Table B.1 has been written with the following conventions for incident and reflected electric field

$$E^i = \begin{pmatrix} E_p^i \\ E_s^i \end{pmatrix} \quad (\text{B.1a})$$

$$E^r = \begin{pmatrix} E_p^r \\ E_s^r \end{pmatrix} \quad (\text{B.1b})$$

As stressed in Chapter 2, the terms  $\tilde{r}_{ss} = r_{ss}e^{i\delta_{ss}}$  and  $\tilde{r}_{pp} = r_{pp}e^{i\delta_{pp}}$  are pure optical terms while the terms  $\tilde{r}_{ps} = r_{ps}e^{i\delta_{ps}}$  and  $\tilde{r}_{sp} = r_{sp}e^{i\delta_{sp}}$  contain the MOKE. The terms  $\delta_{ij}$  stand for phase angles. As explained in chapter 4, the PEM provides a phase retardation  $\phi = \phi_0 \sin(2\pi ft)$ . According to Polisetty *et al.*, the configuration for the highest signal-to-noise ratio (SNR) for P-MOKE and L-MOKE measurements requires the polarizer oriented at  $90^\circ$  followed by the sample then the PEM and finally the analyzer oriented either at  $45^\circ$  or  $135^\circ$ . Then the reflected electric field can be expressed as

$$E^r = \overline{\overline{A}} \times \overline{\overline{PEM}} \times \overline{\overline{S}} \times \overline{\overline{P}} \times E^i \quad (\text{B.2})$$

In this context, the general expression, in case of polarizer transmission axis at  $90^\circ$ , for the measured intensity is given for any angle  $\alpha$  by

$$\begin{aligned} I \propto |E^r|^2 &= r_{ss}^2 \sin(\alpha)^2 + r_{ps}^2 \cos(\alpha)^2 + 2J_0(\phi_0)r_{ss}r_{ps} \cos(\delta_{ss} - \delta_{ps}) \sin(\alpha) \cos(\alpha) \\ &+ 4J_1(\phi_0)\sin(2\pi ft)r_{ss}r_{ps} \sin(\delta_{ss} - \delta_{ps}) \sin(\alpha) \cos(\alpha) \\ &+ 4J_2(\phi_0) \cos(4\pi ft)r_{ss}r_{ps} \cos(\delta_{ss} - \delta_{ps}) \sin(\alpha) \cos(\alpha) \\ &+ \dots \end{aligned} \quad (\text{B.3})$$

Both  $\cos(\phi_0)$  and  $\sin(\phi_0)$  have been expanded into Bessel functions of order  $n$  noted  $J_n$ .

## **Appendix C**

# **Scanning electron microscopy of magnetic metasurfaces**

We supply SEM images of  $[\text{Co/Gd/Pt}]_N$  metasurfaces with  $N = 1, 2, 3, 4, 5$  and  $6$ .

## APPENDIX C. SCANNING ELECTRON MICROSCOPY OF MAGNETIC METASURFACES

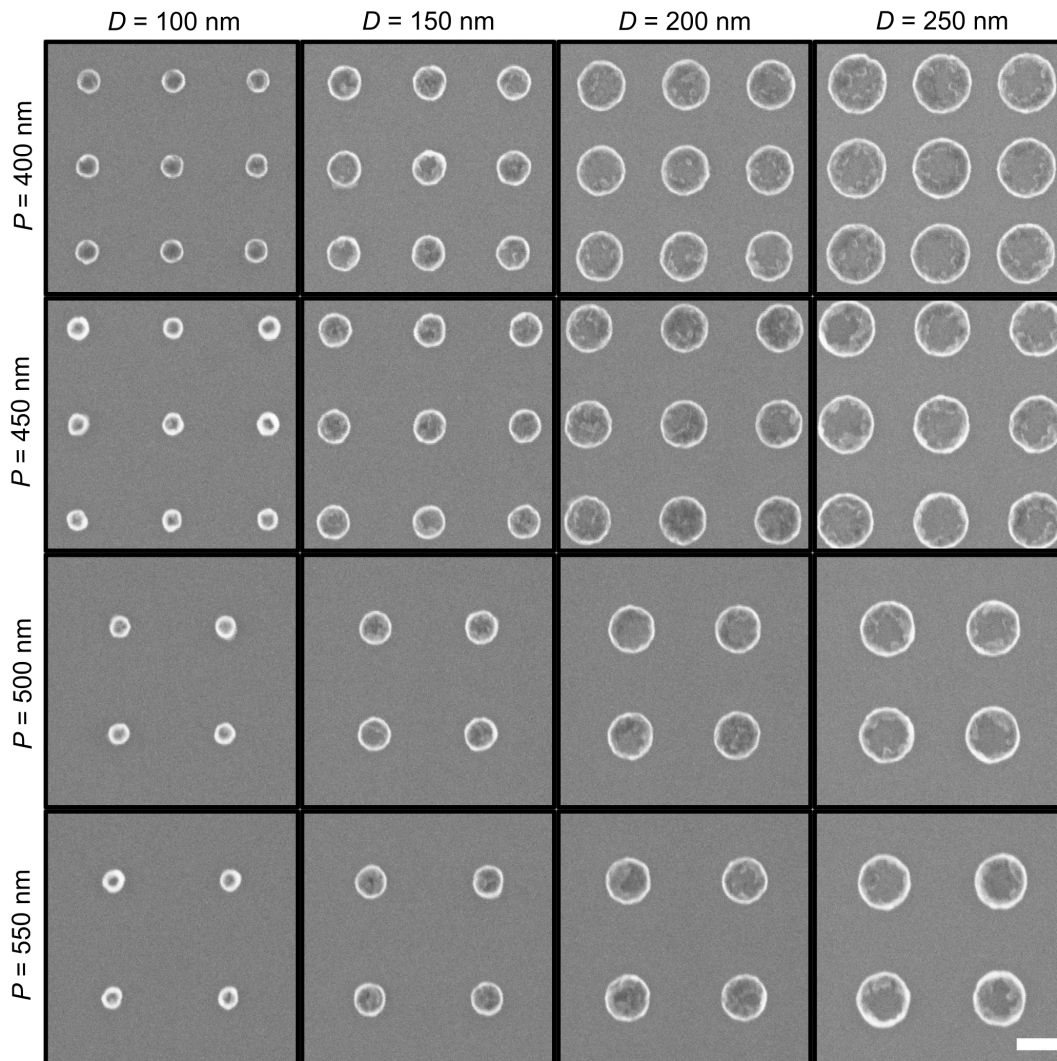


Figure C.1: SEM images of [Co/Gd/Pt]<sub>1</sub> nanodisk arrays. The scale bar corresponds to 200 nm.



## APPENDIX C. SCANNING ELECTRON MICROSCOPY OF MAGNETIC METASURFACES

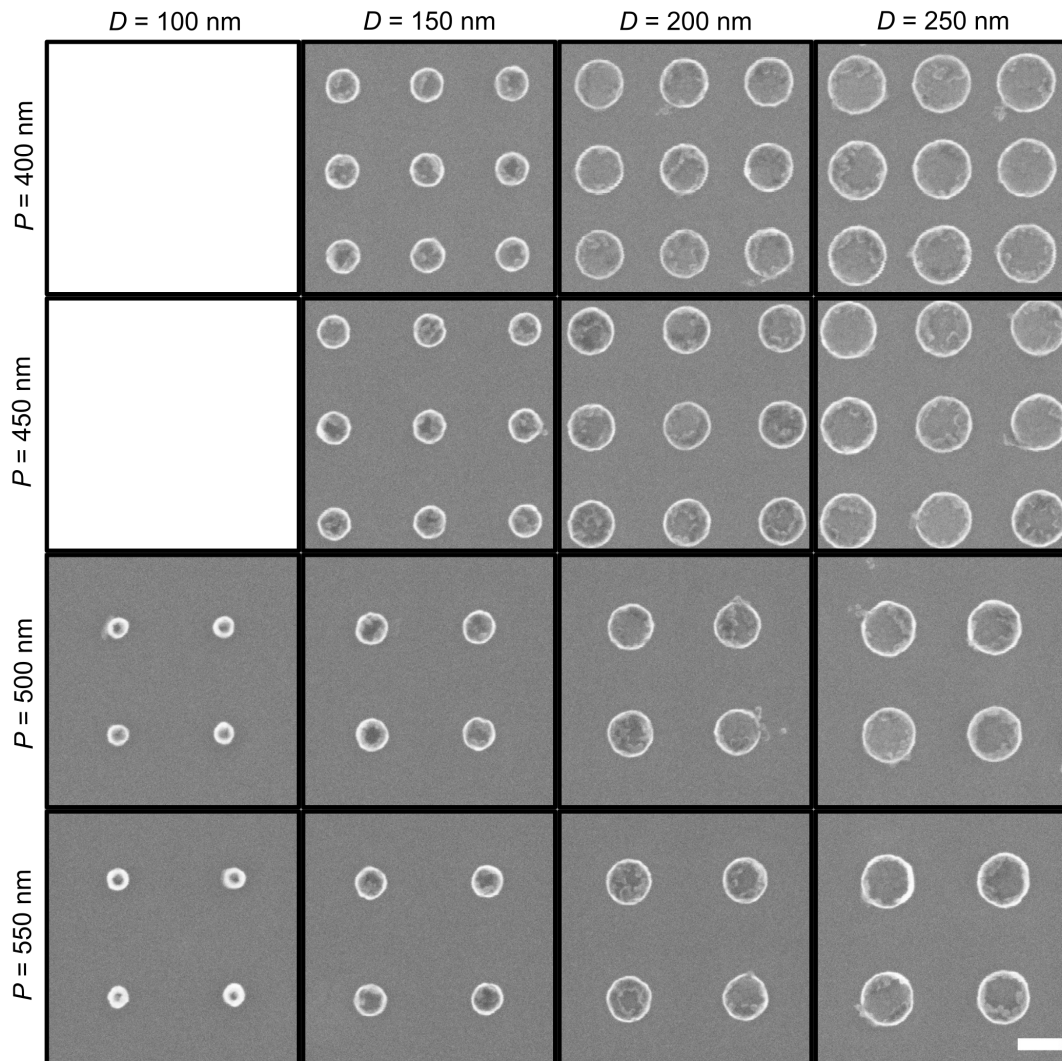


Figure C.2: SEM images of [Co/Gd/Pt]<sub>2</sub> nanodisk arrays. The scale bar corresponds to 200 nm.

## APPENDIX C. SCANNING ELECTRON MICROSCOPY OF MAGNETIC METASURFACES

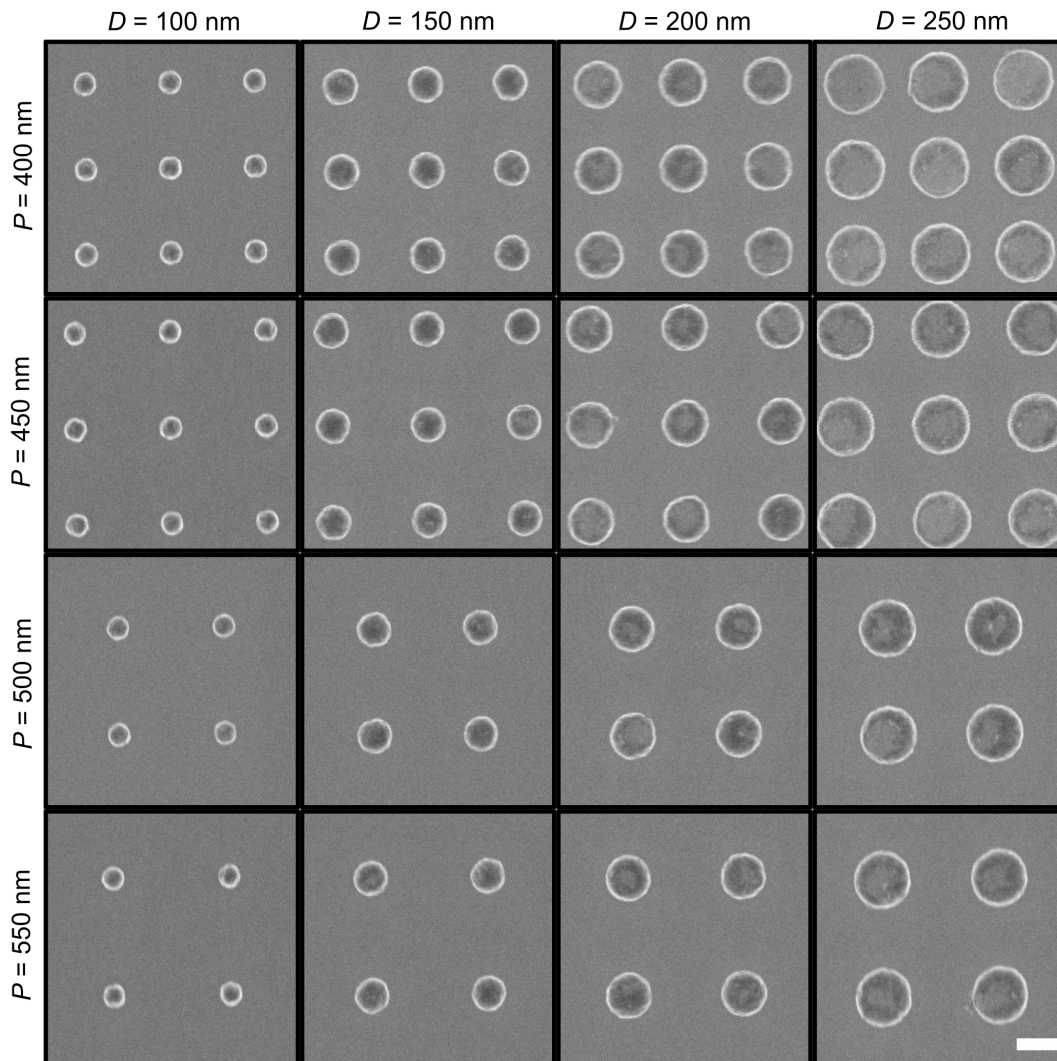


Figure C.3: SEM images of [Co/Gd/Pt]<sub>3</sub> nanodisk arrays. The scale bar corresponds to 200 nm.

## APPENDIX C. SCANNING ELECTRON MICROSCOPY OF MAGNETIC METASURFACES

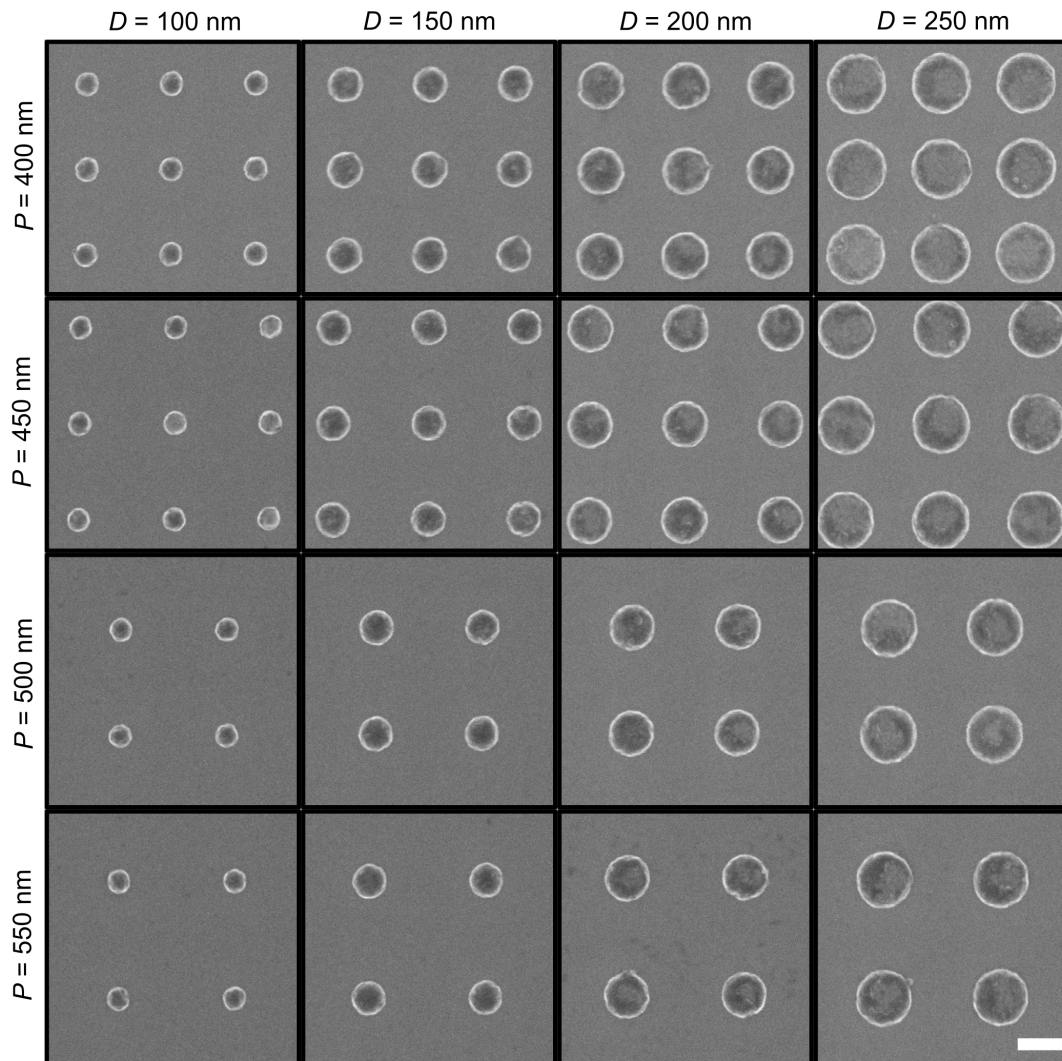


Figure C.4: SEM images of [Co/Gd/Pt]<sub>4</sub> nanodisk arrays. The scale bar corresponds to 200 nm.

## APPENDIX C. SCANNING ELECTRON MICROSCOPY OF MAGNETIC METASURFACES

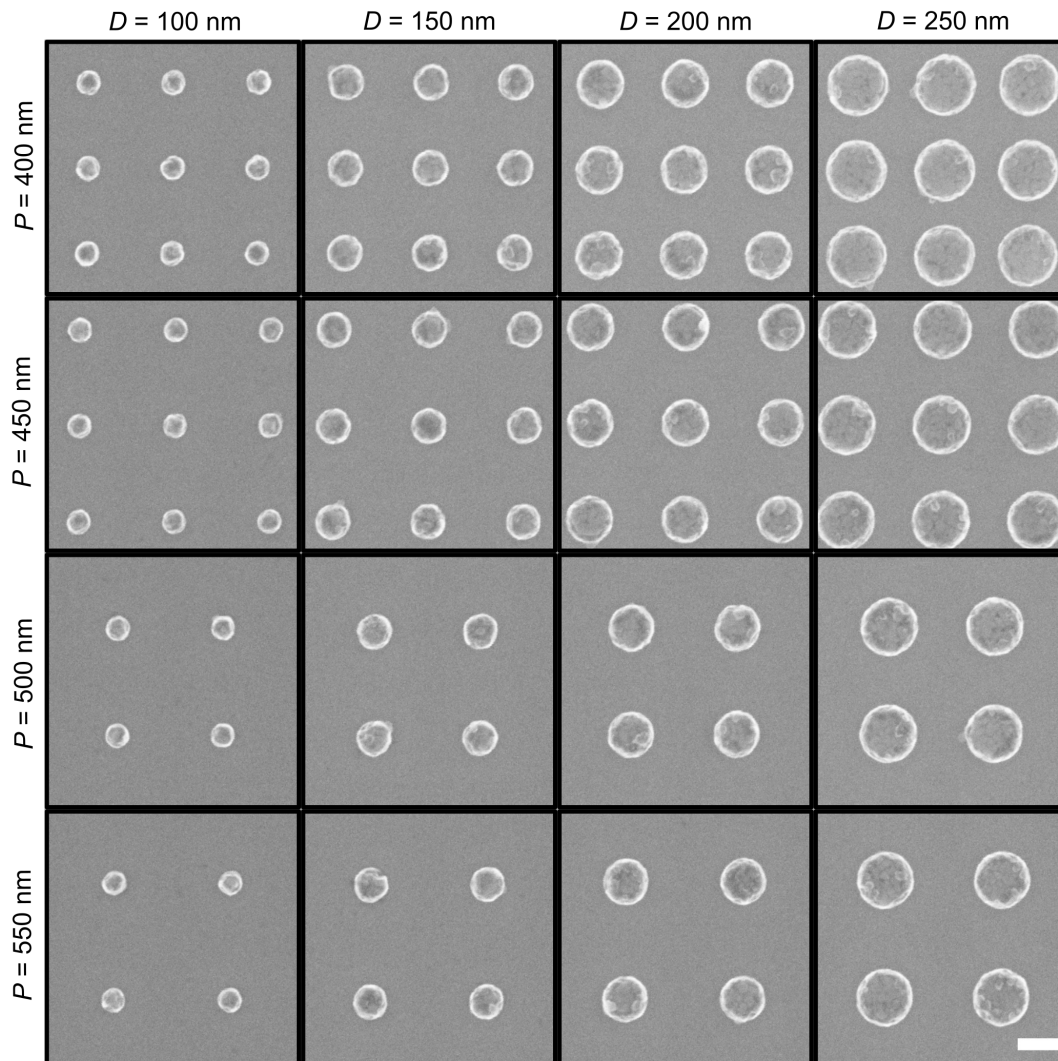


Figure C.5: SEM images of [Co/Gd/Pt]<sub>5</sub> nanodisk arrays. The scale bar corresponds to 200 nm.

## APPENDIX C. SCANNING ELECTRON MICROSCOPY OF MAGNETIC METASURFACES

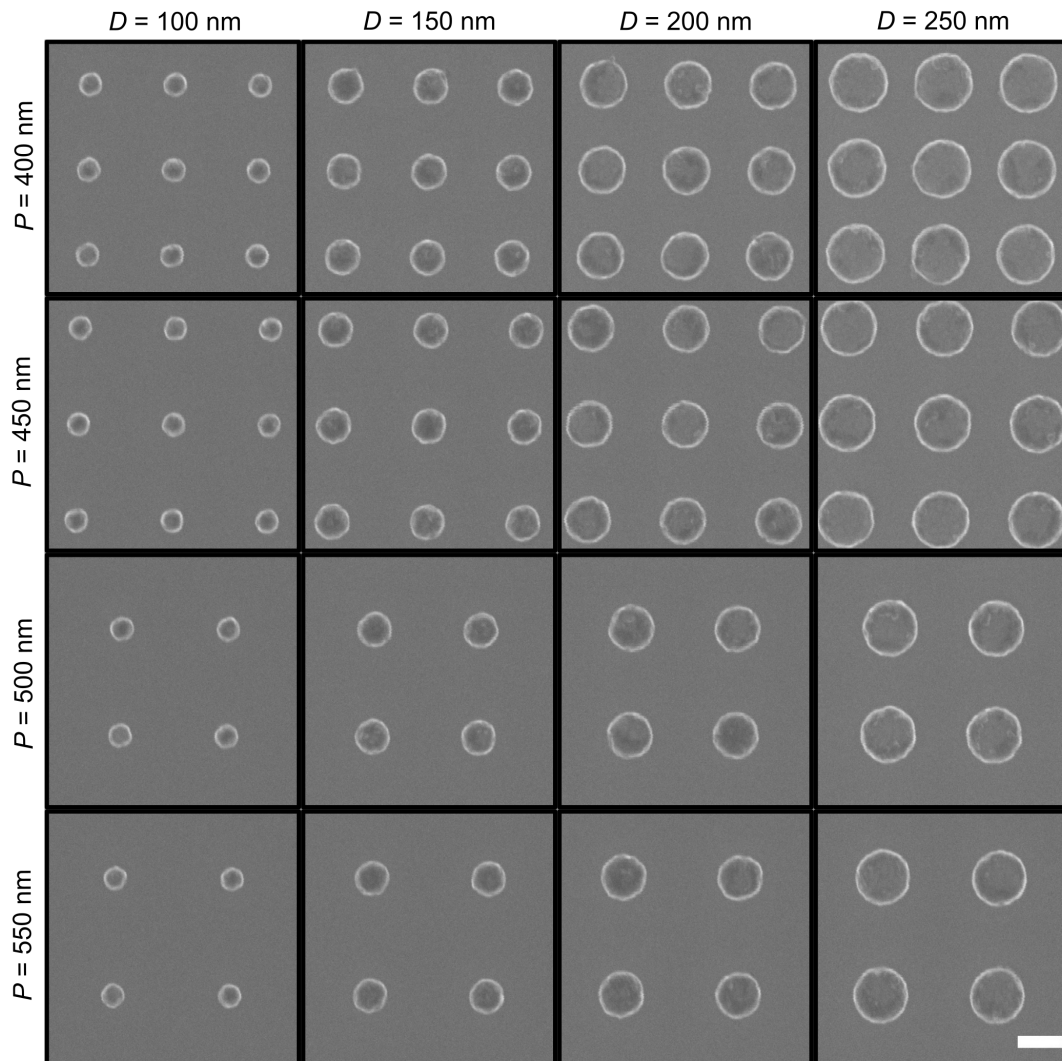


Figure C.6: SEM images of  $[\text{Co}/\text{Gd}/\text{Pt}]_6$  nanodisk arrays. The scale bar corresponds to 200 nm.



## **Appendix D**

# **Extinction spectra of magnetic metasurfaces**

We supply raw extinction spectra of  $[\text{Co/Gd/Pt}]_N$  metasurfaces  $N = 1, 2, 3, 4, 5$  and  $6$  and the corresponding continuous films.

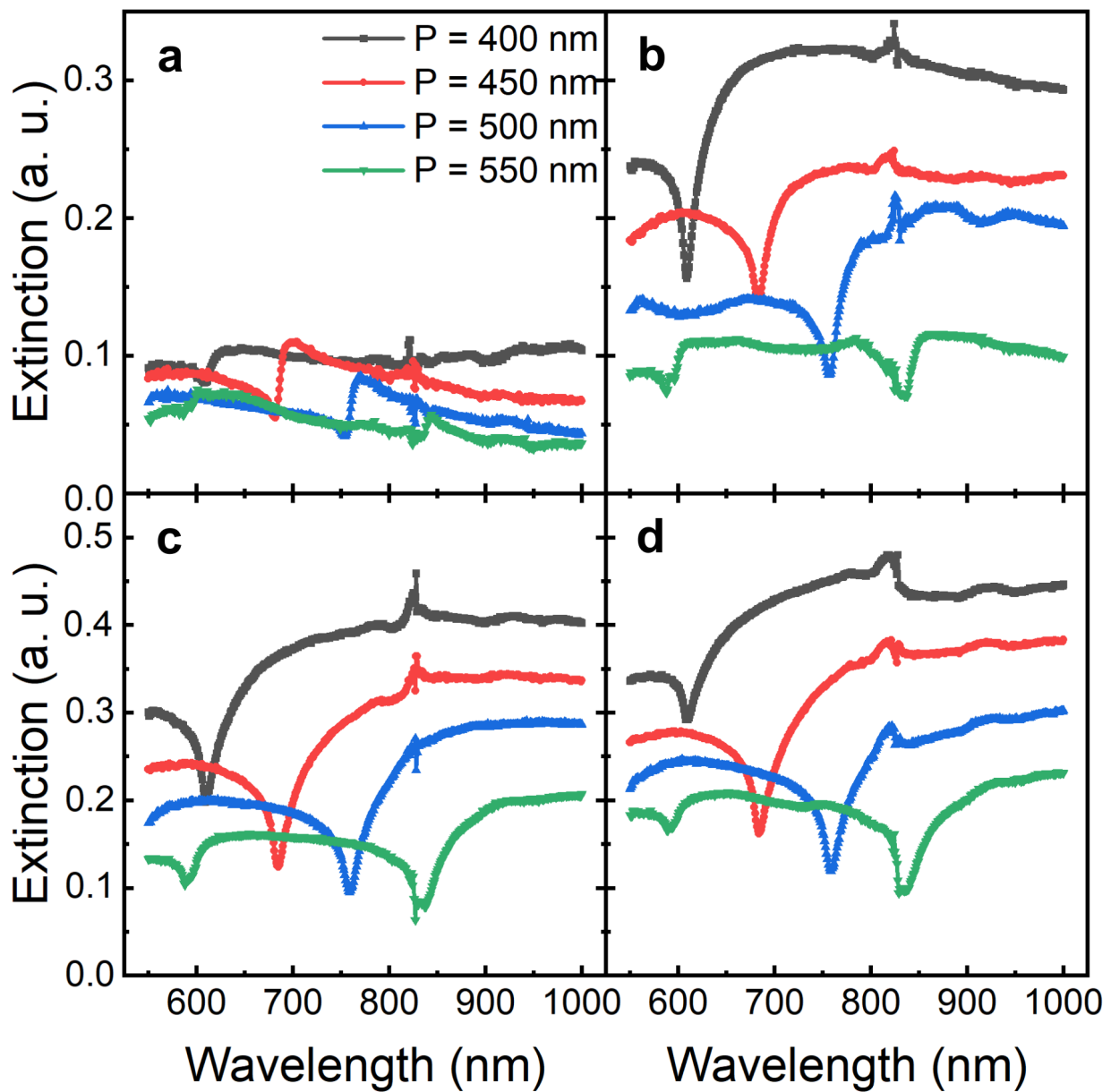


Figure D.1: Extinction spectra of  $[\text{Co/Gd/Pt}]_1$  nanodisk arrays with (a)  $D = 100$  nm, (b)  $D = 150$  nm, (c)  $D = 200$  nm and (d)  $D = 250$  nm.



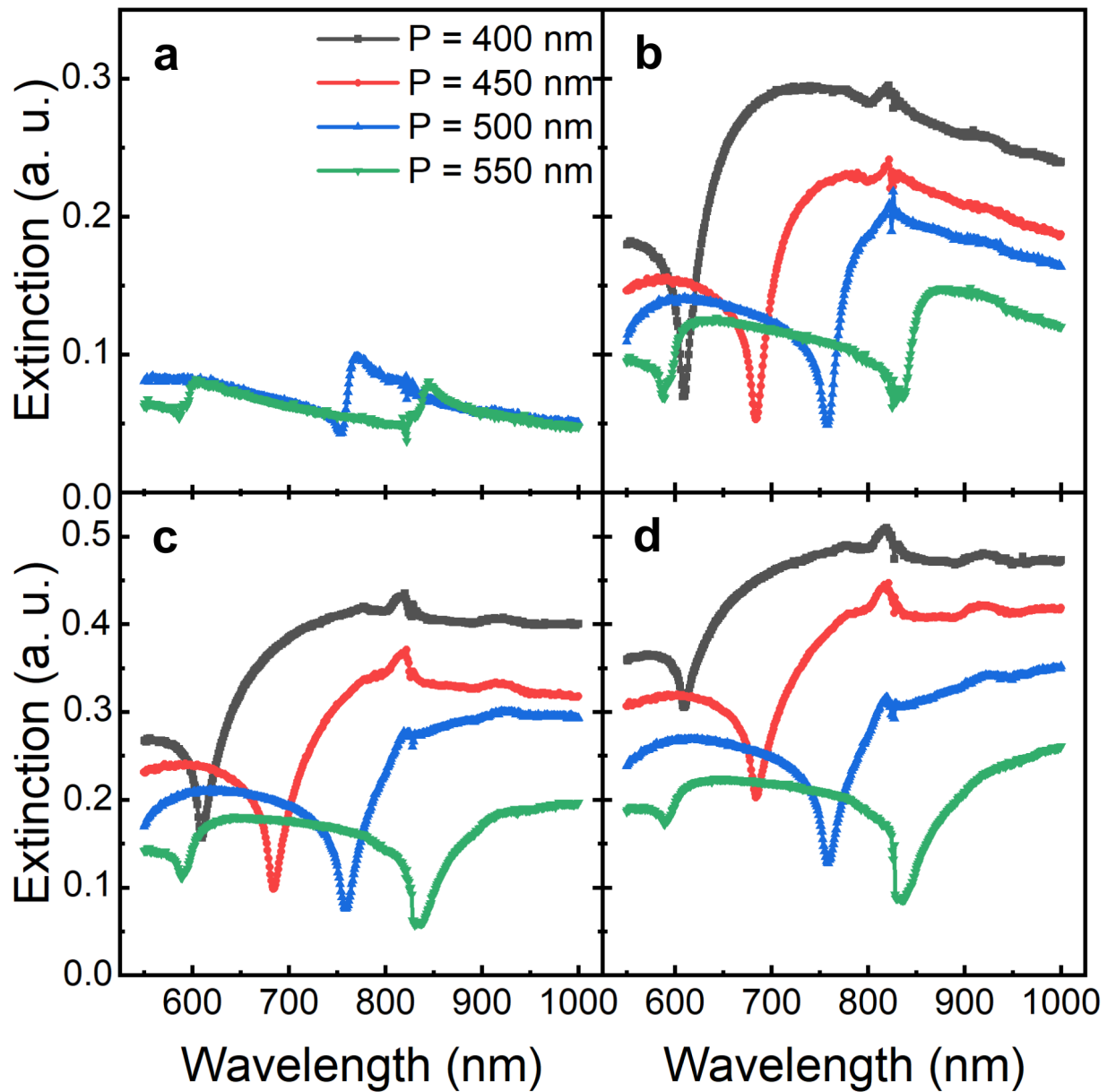


Figure D.2: Extinction spectra of  $[\text{Co}/\text{Gd}/\text{Pt}]_2$  nanodisk arrays with (a)  $D = 100$  nm, (b)  $D = 150$  nm, (c)  $D = 200$  nm and (d)  $D = 250$  nm.

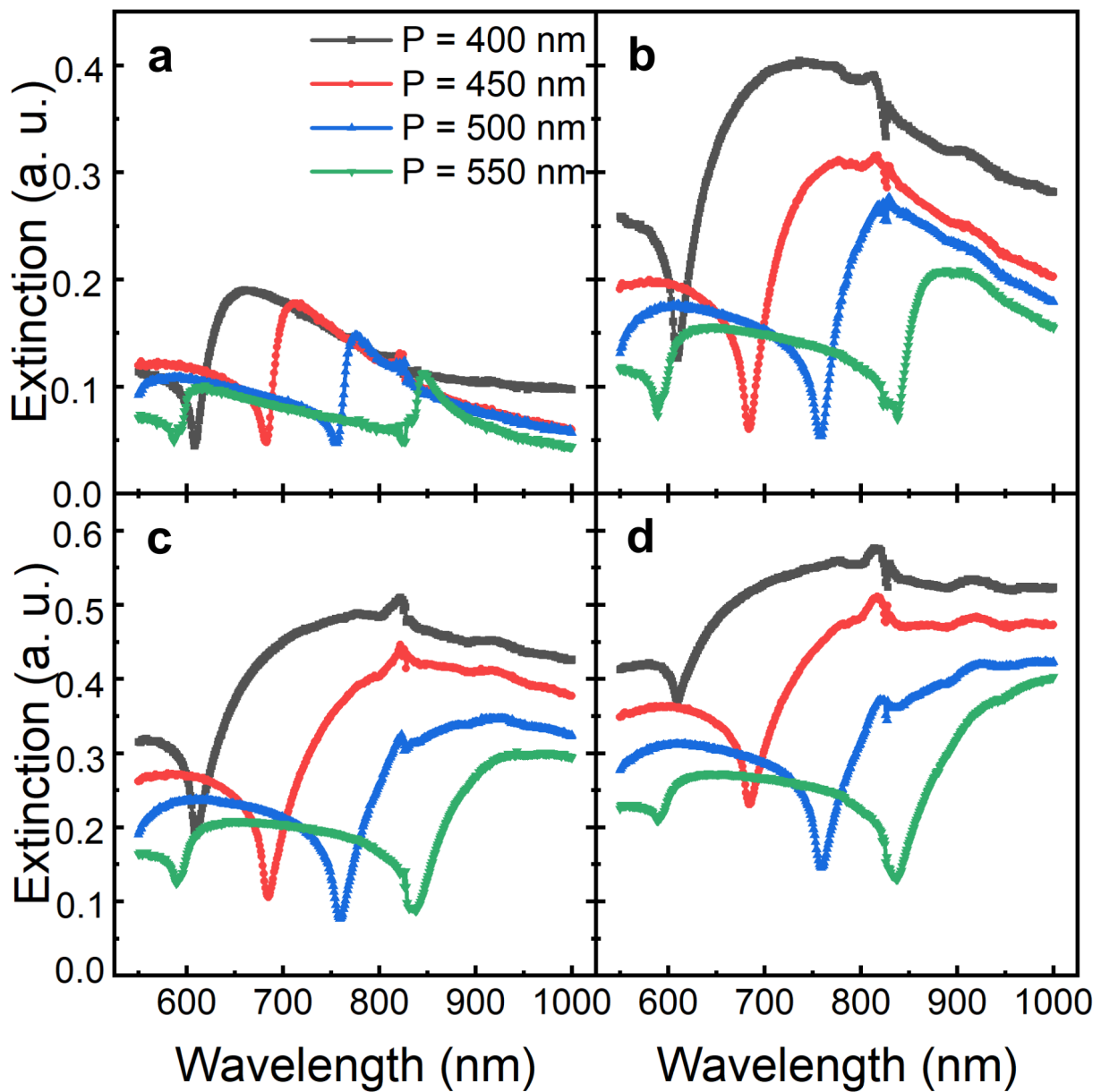


Figure D.3: Extinction spectra of  $[\text{Co/Gd/Pt}]_3$  nanodisk arrays with (a)  $D = 100$  nm, (b)  $D = 150$  nm, (c)  $D = 200$  nm and (d)  $D = 250$  nm.

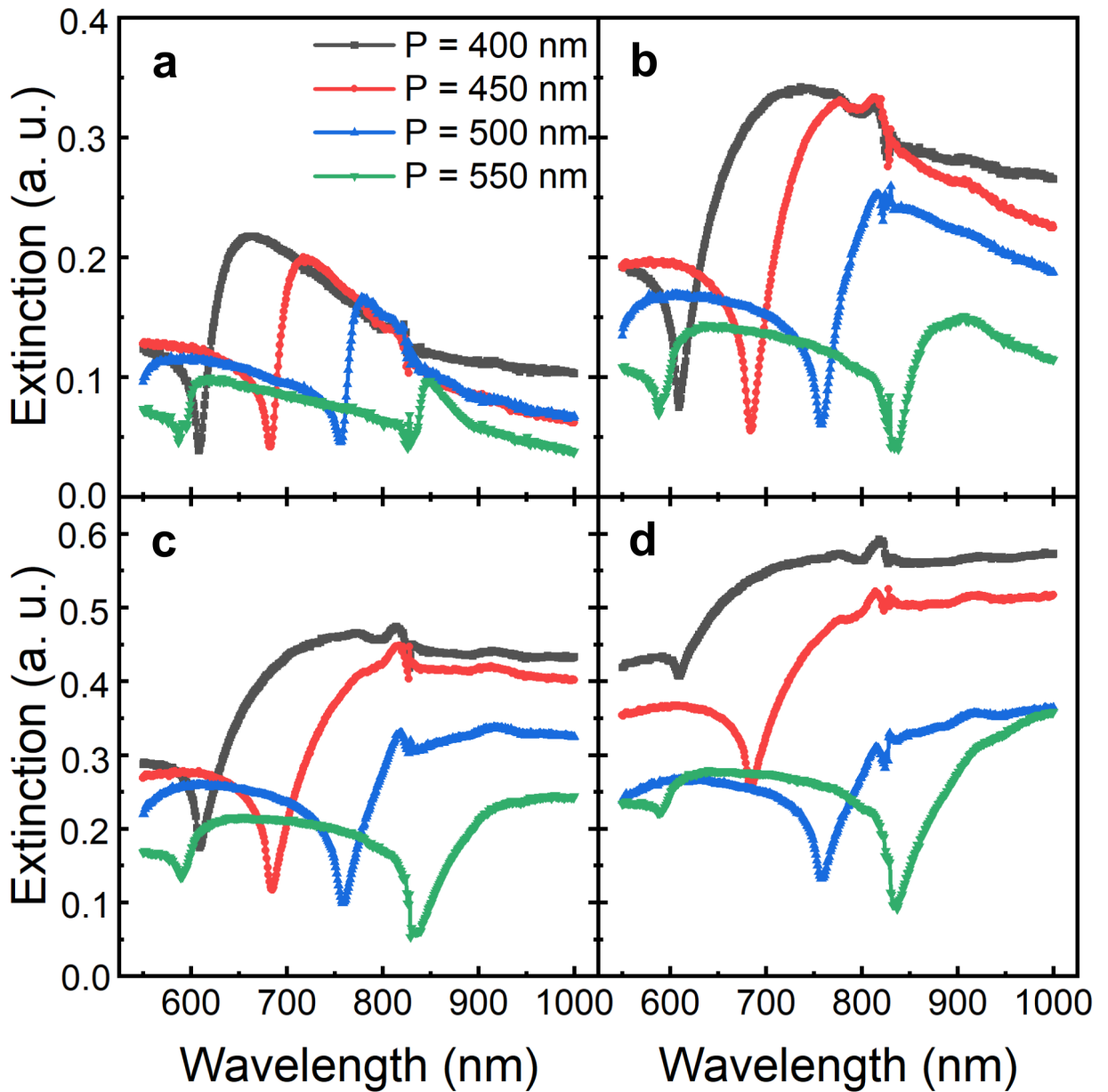


Figure D.4: Extinction spectra of  $[\text{Co/Gd/Pt}]_4$  nanodisk arrays with (a)  $D = 100$  nm, (b)  $D = 150$  nm, (c)  $D = 200$  nm and (d)  $D = 250$  nm.

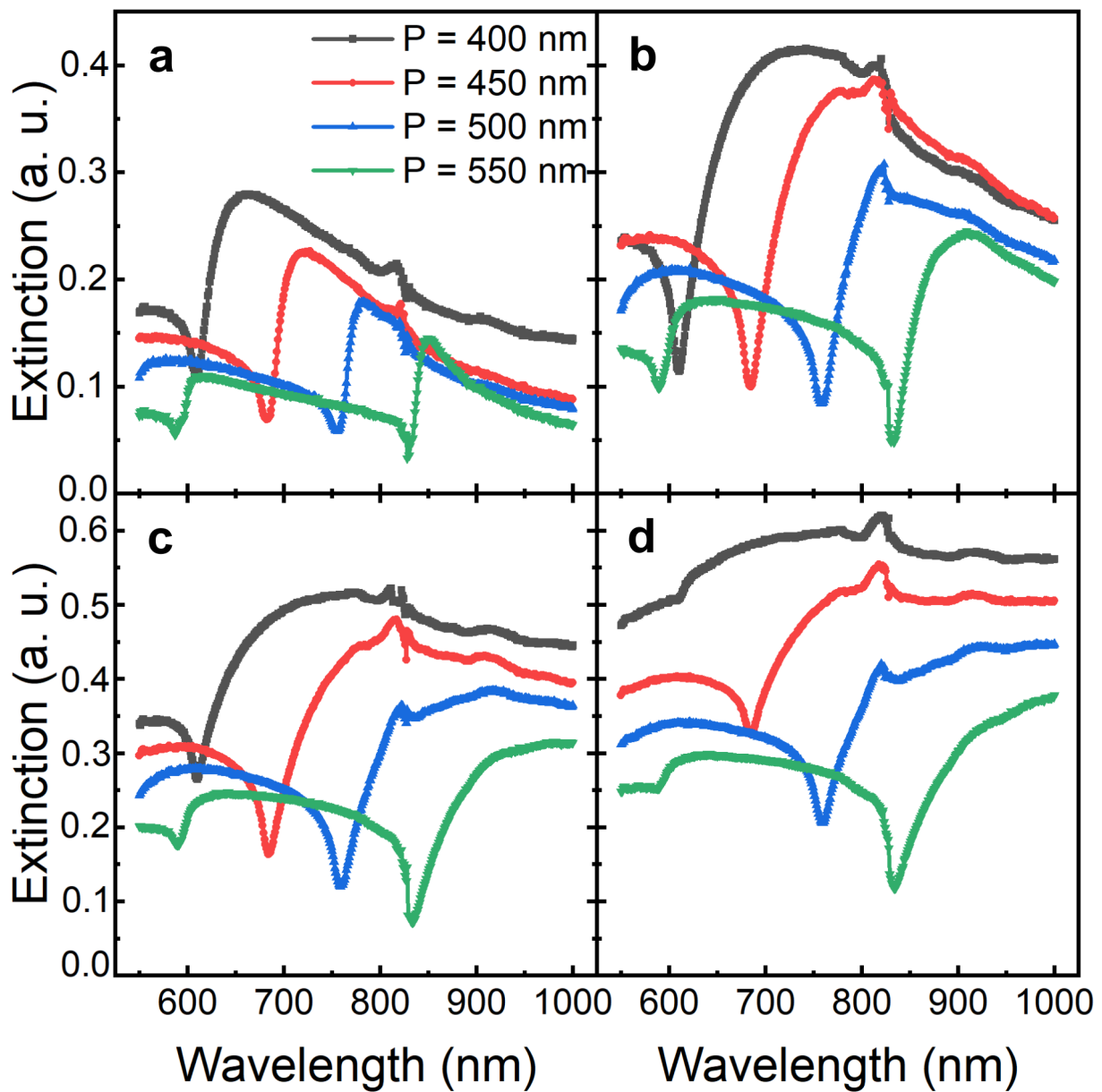


Figure D.5: Extinction spectra of  $[\text{Co/Gd/Pt}]_5$  nanodisk arrays with (a)  $D = 100$  nm, (b)  $D = 150$  nm, (c)  $D = 200$  nm and (d)  $D = 250$  nm.

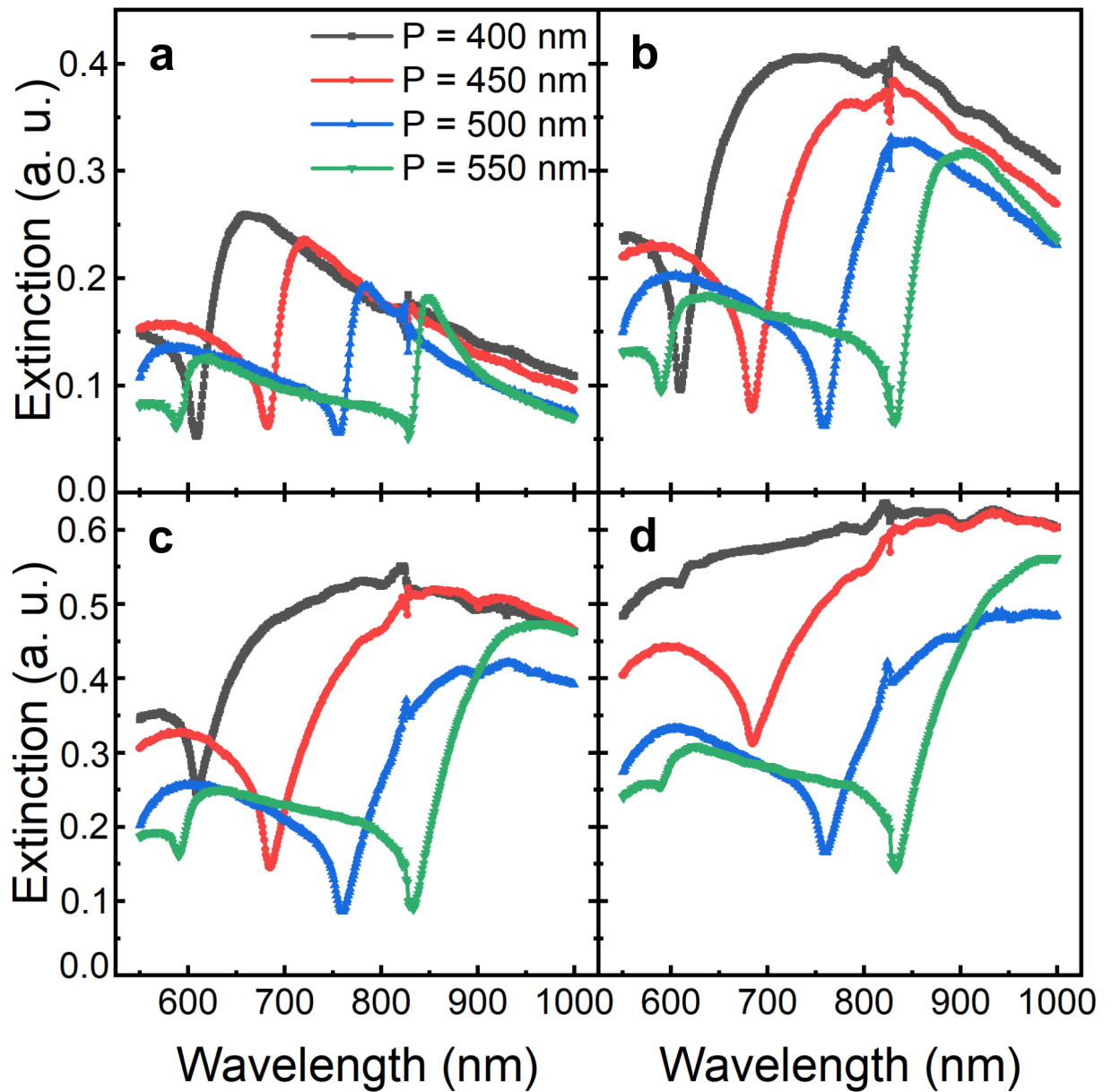


Figure D.6: Extinction spectra of  $[\text{Co}/\text{Gd}/\text{Pt}]_6$  nanodisk arrays with (a)  $D = 100$  nm, (b)  $D = 150$  nm, (c)  $D = 200$  nm and (d)  $D = 250$  nm.

## APPENDIX D. EXTINCTION SPECTRA OF MAGNETIC METASURFACES

---

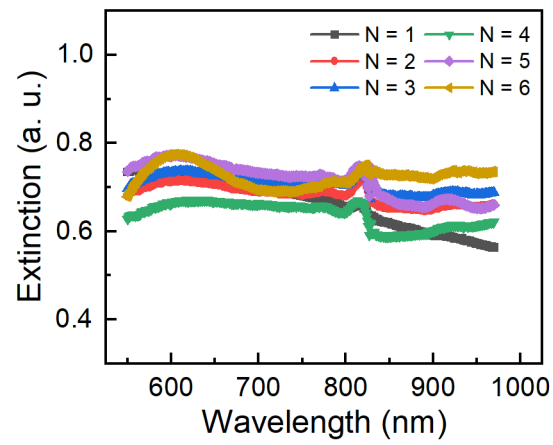


Figure D.7: Extinction spectra of  $[\text{Co}/\text{Gd}/\text{Pt}]_N$  continuous films.

## **Appendix E**

# **Magneto-optical spectra of magnetic metasurfaces**

We supply raw MO spectra of  $[\text{Co/Gd/Pt}]_N$  metasurfaces  $N = 1, 2, 3, 4, 5$  and  $6$  and the corresponding continuous films.

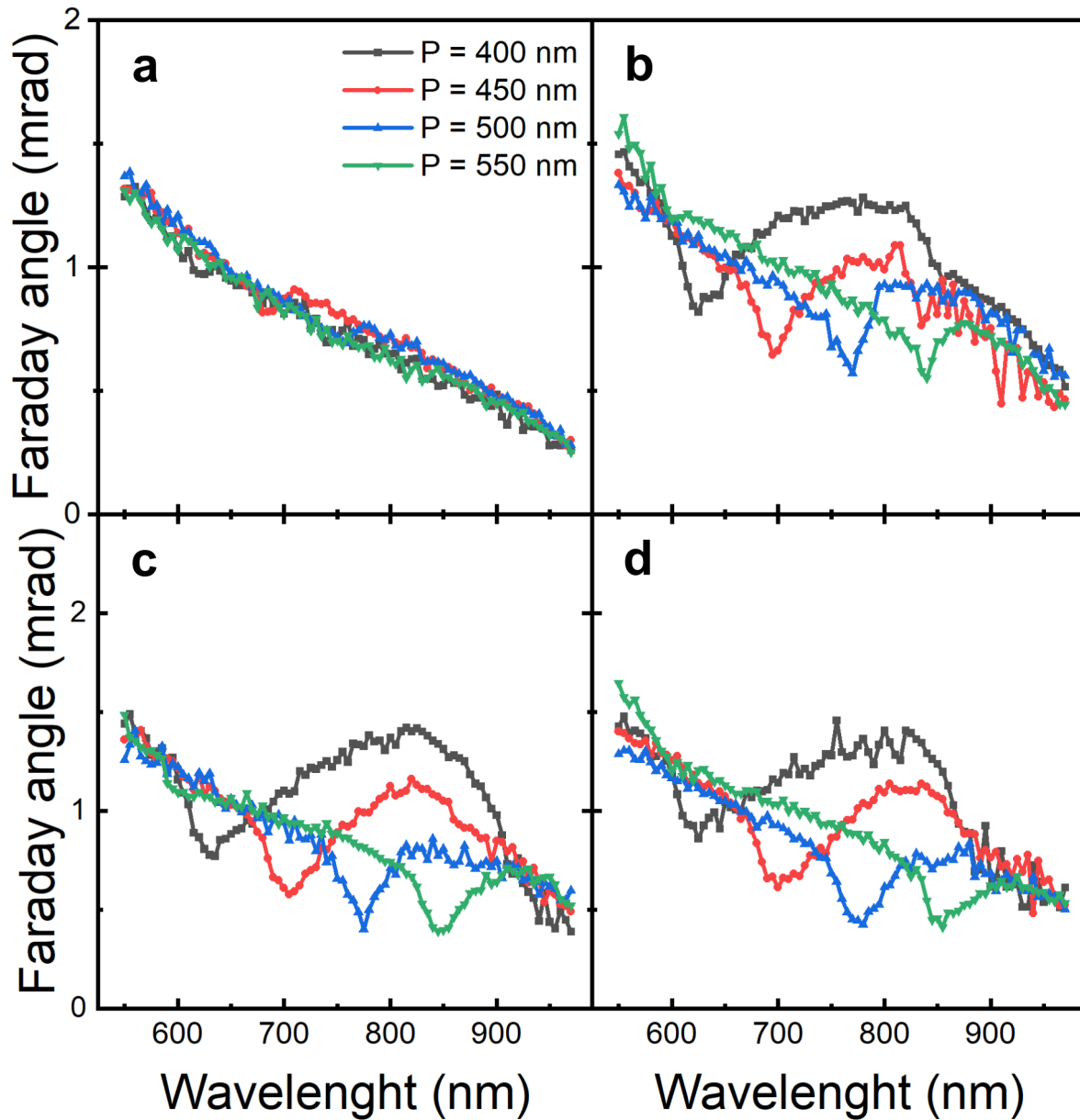


Figure E.1: Faraday angle spectra of  $[\text{Co}/\text{Gd}/\text{Pt}]_1$  nanodisk arrays with (a)  $D = 100$  nm, (b)  $D = 150$  nm, (c)  $D = 200$  nm and (d)  $D = 250$  nm.



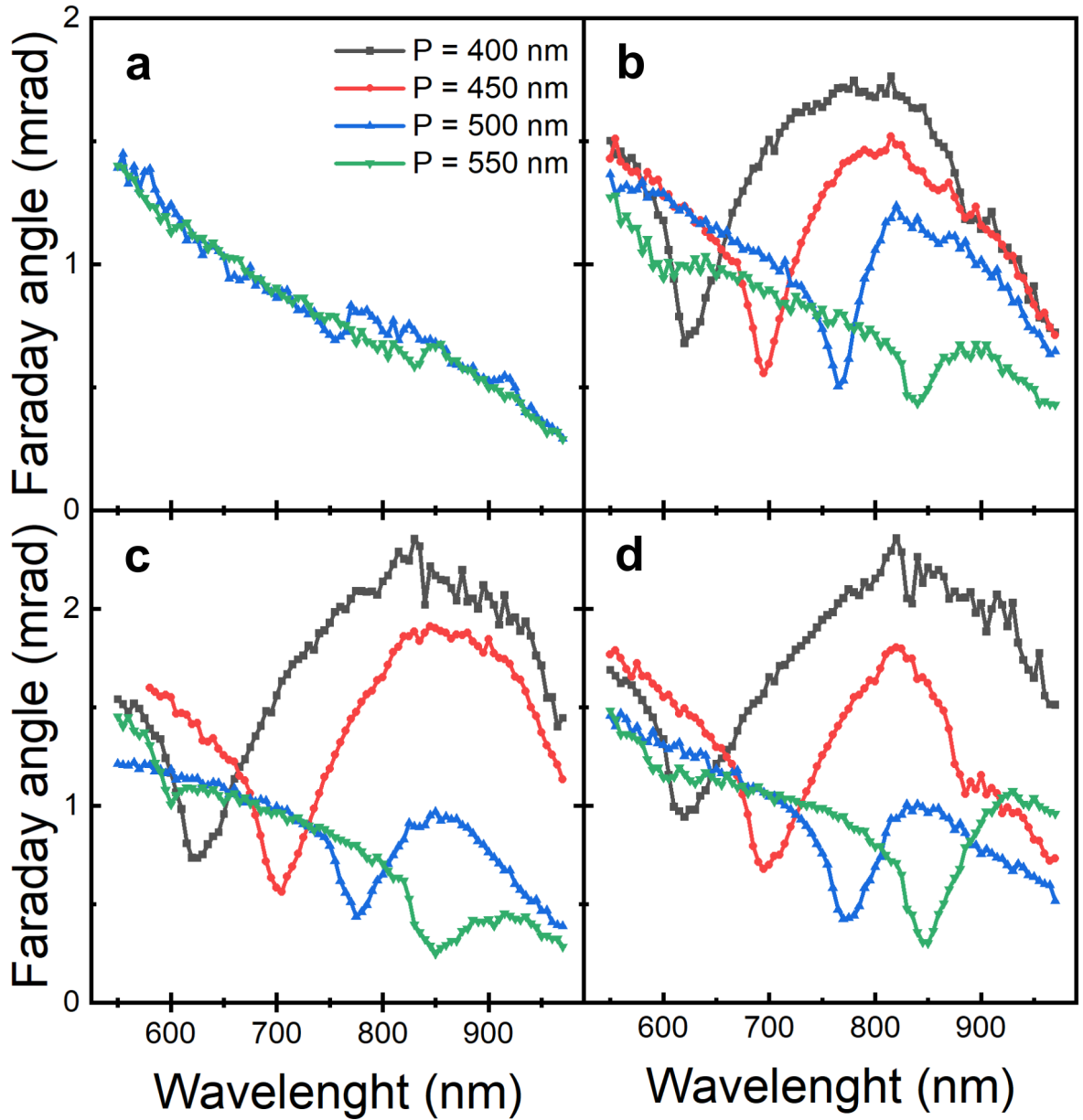


Figure E.2: Faraday angle spectra of  $[\text{Co}/\text{Gd}/\text{Pt}]_2$  nanodisk arrays with (a)  $D = 100$  nm, (b)  $D = 150$  nm, (c)  $D = 200$  nm and (d)  $D = 250$  nm.

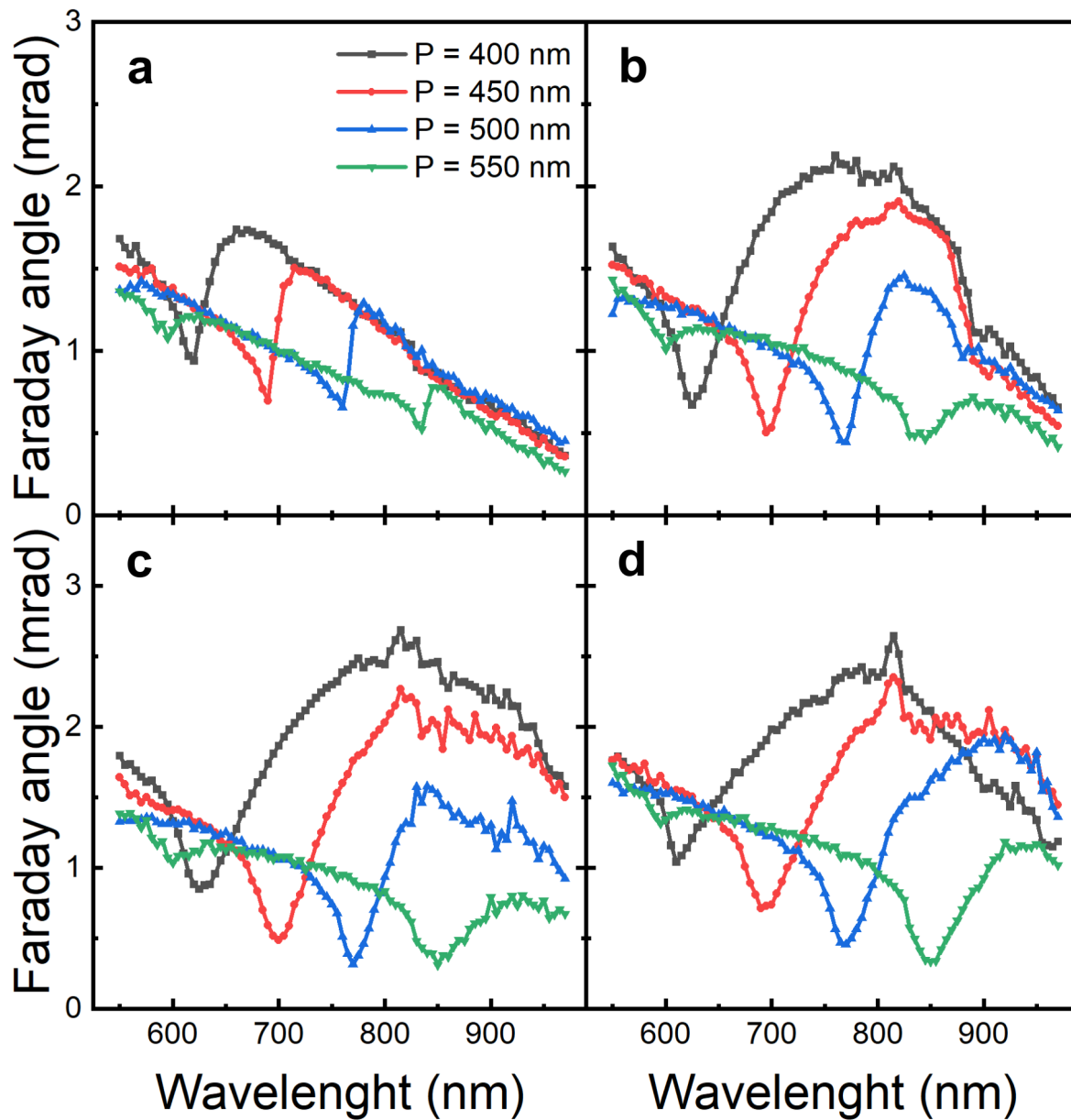


Figure E.3: Faraday angle spectra of  $[\text{Co}/\text{Gd}/\text{Pt}]_3$  nanodisk arrays with (a)  $D = 100$  nm, (b)  $D = 150$  nm, (c)  $D = 200$  nm and (d)  $D = 250$  nm.

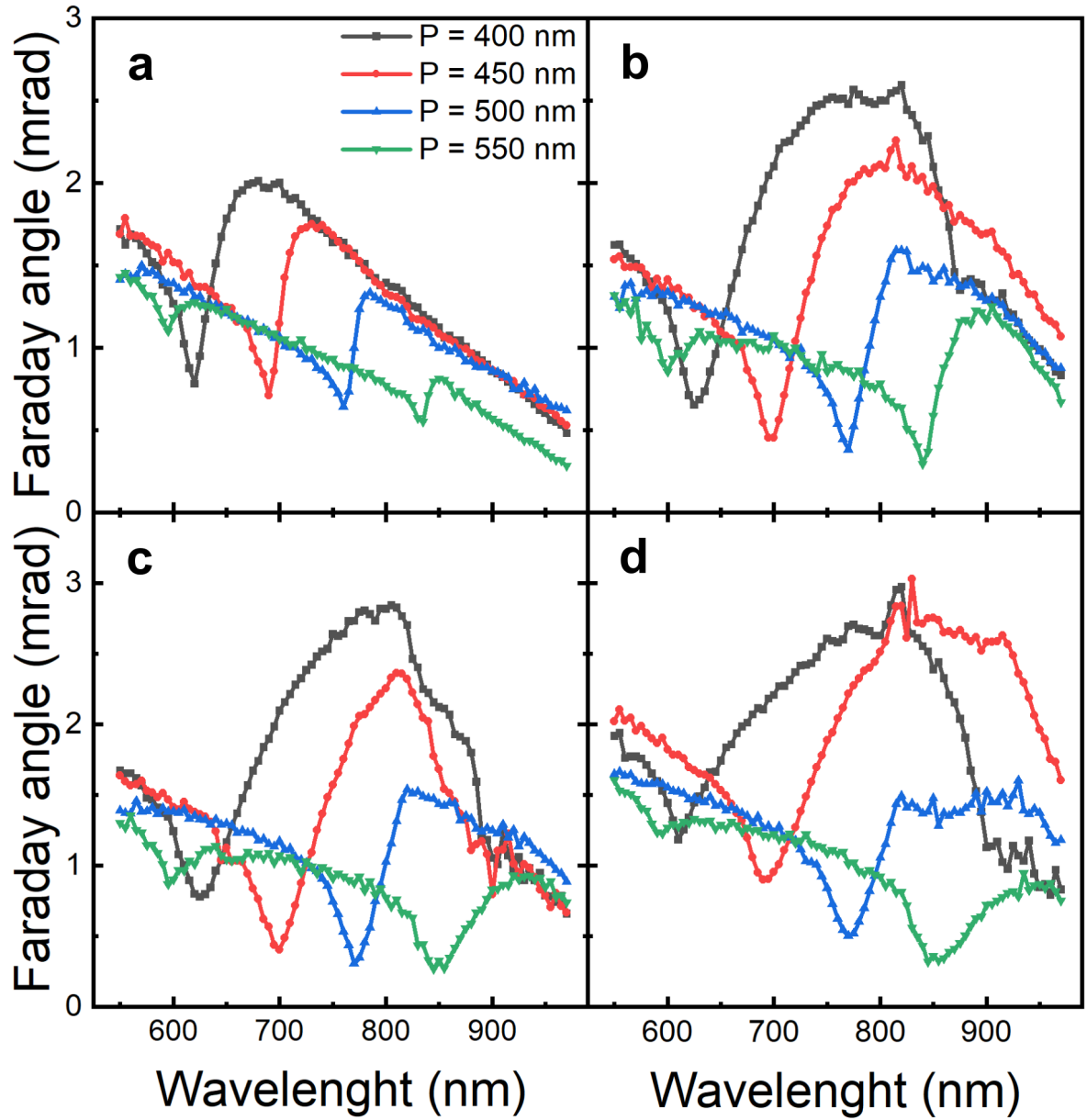


Figure E.4: Faraday angle spectra of  $[\text{Co/Gd/Pt}]_4$  nanodisk arrays with (a)  $D = 100$  nm, (b)  $D = 150$  nm, (c)  $D = 200$  nm and (d)  $D = 250$  nm.

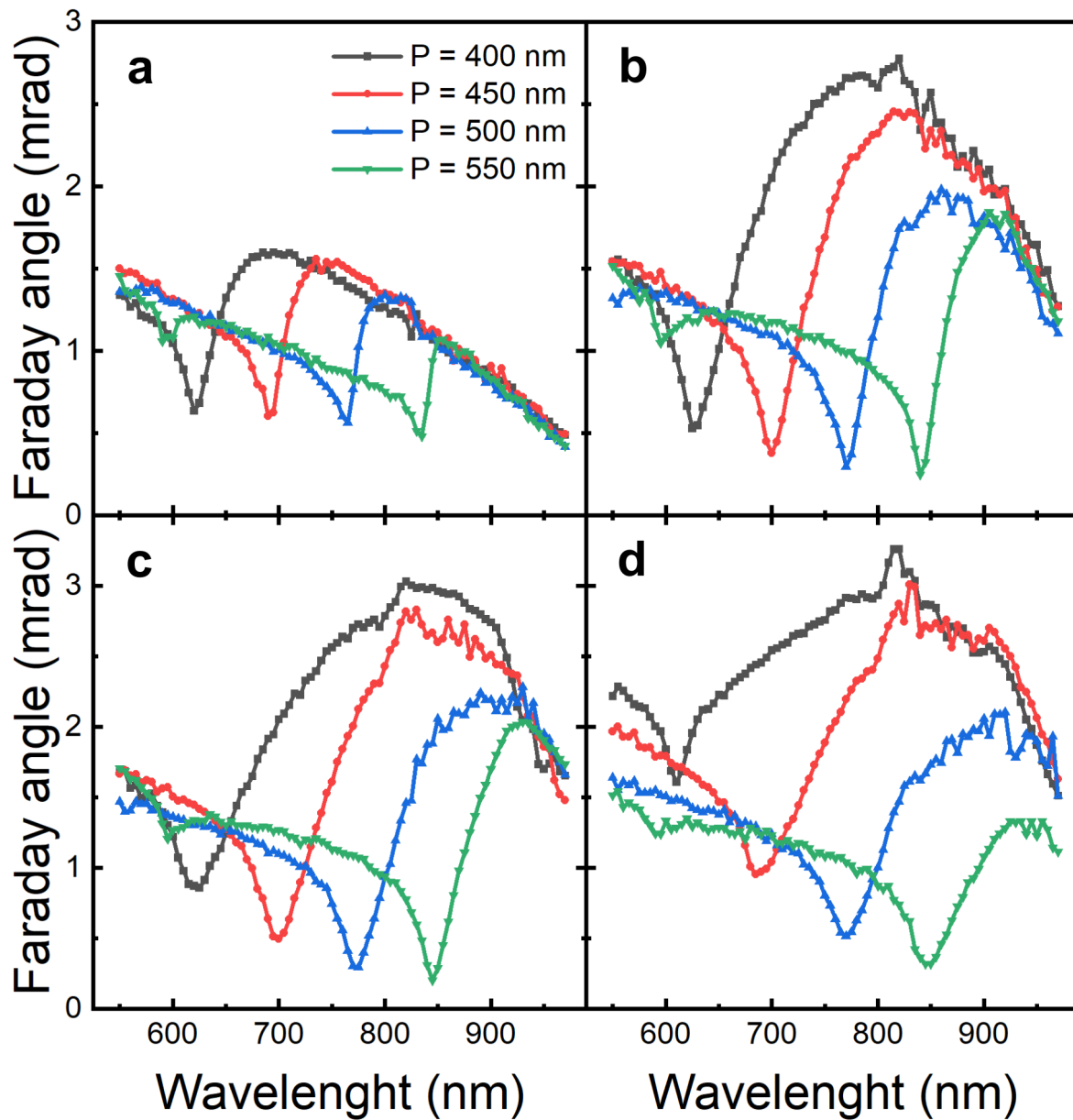


Figure E.5: Faraday angle spectra of  $[\text{Co}/\text{Gd}/\text{Pt}]_5$  nanodisk arrays with (a)  $D = 100$  nm, (b)  $D = 150$  nm, (c)  $D = 200$  nm and (d)  $D = 250$  nm.

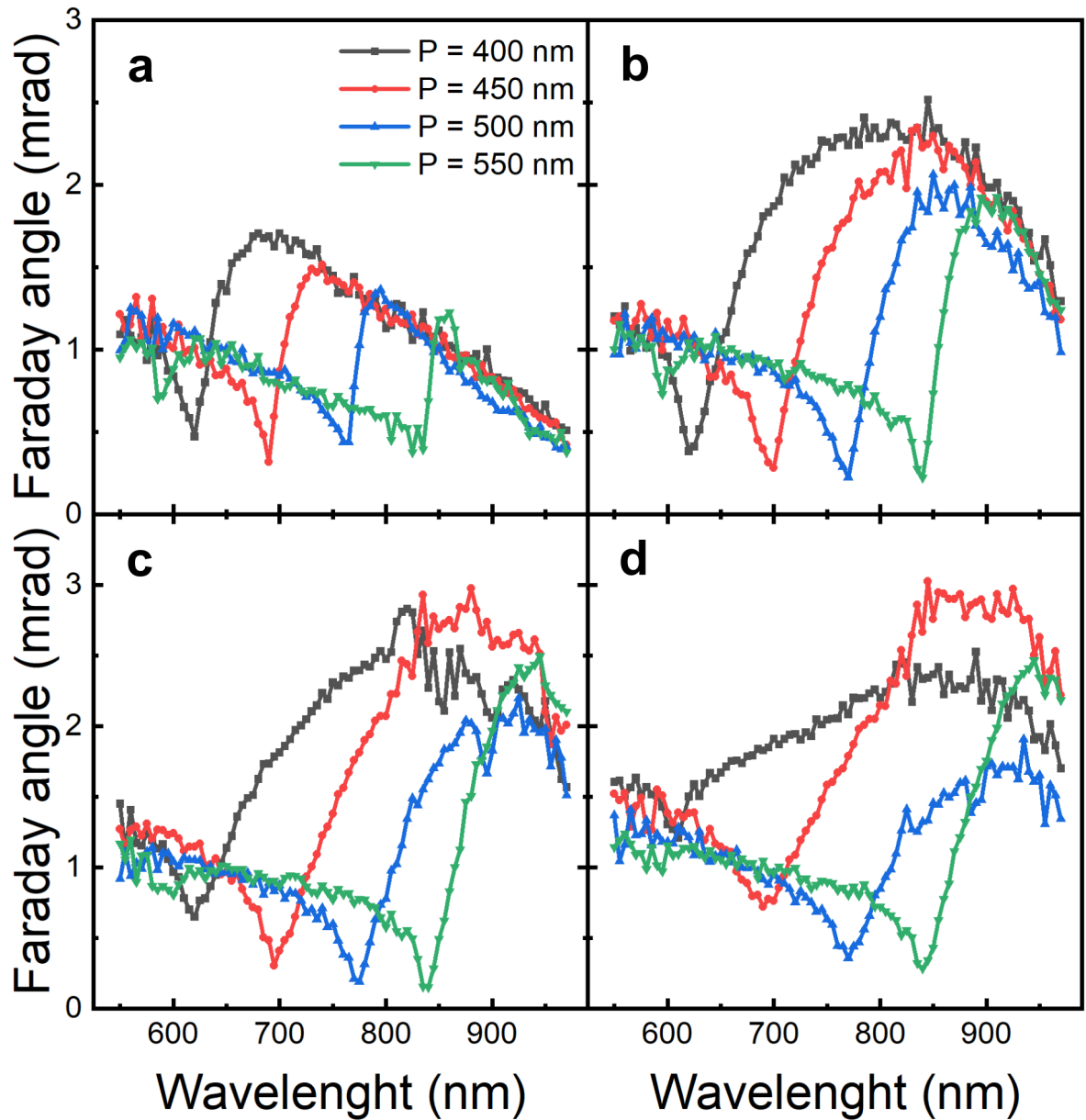


Figure E.6: Faraday angle spectra of  $[\text{Co/Gd/Pt}]_6$  nanodisk arrays with (a)  $D = 100$  nm, (b)  $D = 150$  nm, (c)  $D = 200$  nm and (d)  $D = 250$  nm.

## APPENDIX E. MAGNETO-OPTICAL SPECTRA OF MAGNETIC METASURFACES

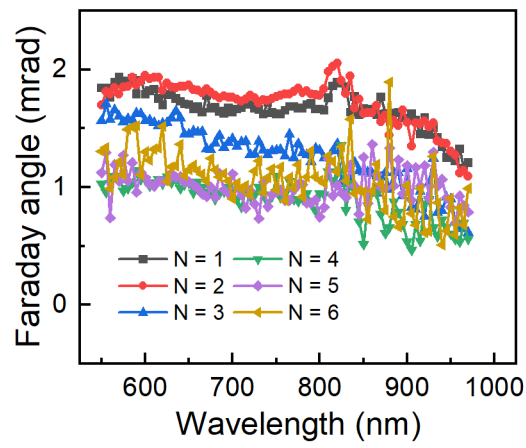


Figure E.7: Faraday angle spectra of  $[\text{Co/Gd/Pt}]_N$  continuous films.

## Appendix F

# Demonstration of magnetism-induced surface lattice resonances in magnetic metasurfaces

We supply MO spectra of  $[\text{Co}/\text{Gd}/\text{Pt}]_3$  metasurfaces measured at oblique angle of incidence.

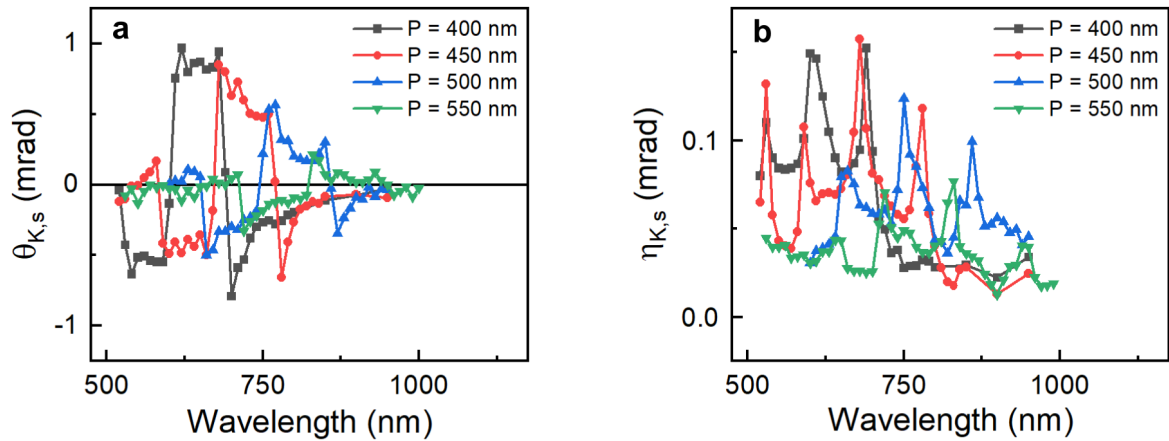


Figure F.1: (a) Kerr rotation and (b) ellipticity spectra of  $[\text{Co}/\text{Gd}/\text{Pt}]_3$  metasurfaces with  $D = 100$  nm and  $P = 400, 450, 500$  and  $550$  nm for incoming s-polarized light.

**APPENDIX F. DEMONSTRATION OF MAGNETISM-INDUCED SURFACE LATTICE RESONANCES**

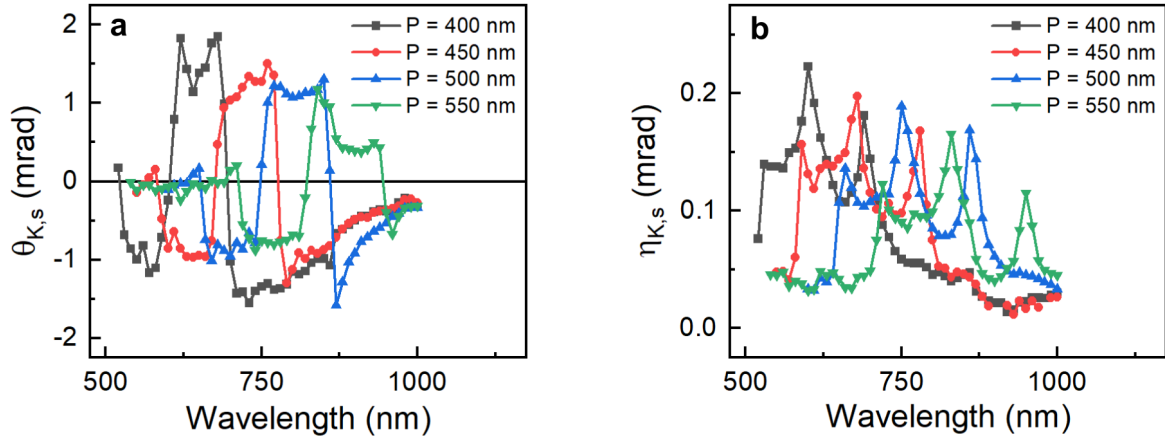


Figure F.2: (a) Kerr rotation and (b) ellipticity spectra of  $[\text{Co}/\text{Gd}/\text{Pt}]_3$  metasurfaces with  $D = 150$  nm and  $P = 400, 450, 500$  and  $550$  nm for incoming s-polarized light.

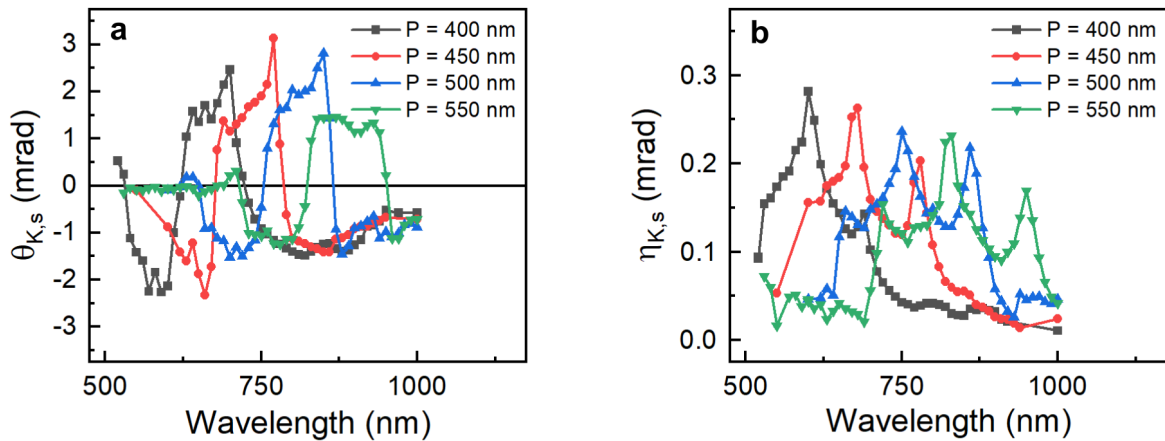


Figure F.3: (a) Kerr rotation and (b) ellipticity spectra of  $[\text{Co}/\text{Gd}/\text{Pt}]_3$  metasurfaces with  $D = 200$  nm and  $P = 400, 450, 500$  and  $550$  nm for incoming s-polarized light.



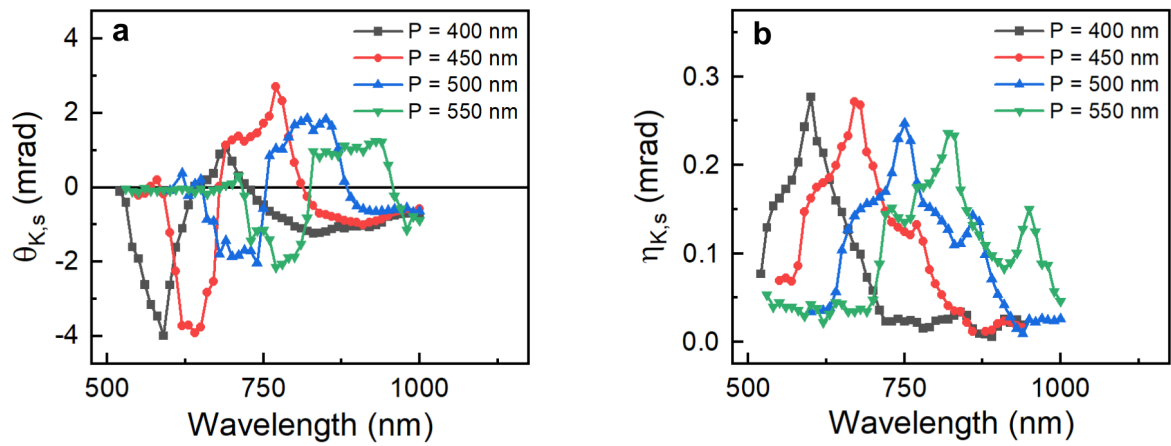
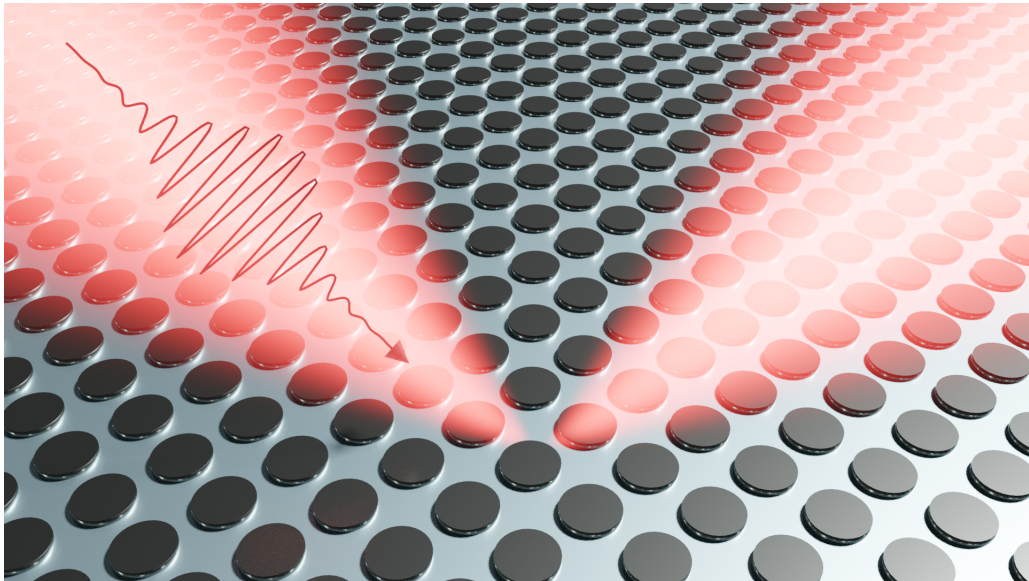


Figure F.4: (a) Kerr rotation and (b) ellipticity spectra of [Co/Gd/Pt]<sub>3</sub> metasurfaces with  $D = 250$  nm and  $P = 400, 450, 500$  and  $550$  nm for incoming s-polarized light.



## Résumé de la thèse



Représentation schématique d'une métasurface magnétique étudiée dans cette thèse.

Nous accordons de plus en plus de place au digital dans notre vie quotidienne. En effet, la quantité de données générées et consultées ne fait qu'augmenter au cours des années. La société est ainsi en pleine mutation dans laquelle les objets les plus utilisés sont amenés à être connectés donnant naissance à l'Internet des Objets. Ainsi l'industrie de stockage de données a besoin de nouvelles stratégies pour stocker plus d'information, plus vite et avec un coût énergétique moindre. A ce jour le moyen le plus rapide d'effectuer un retournement complet de l'aimantation requiert uniquement une impulsion laser ultrarapide. En effet, certains matériaux ferrimagnétiques, caractérisés par deux sous réseaux magnétiques, peuvent voir leur aimantation changer d'orientation sous l'action d'une impulsion laser ultrarapide dont la polarisation peut être linéaire<sup>8,123</sup>. Ce phénomène est communément appelé *All Optical Helicity Independent Switching* (AO-HIS). Ce retournement local d'aimantation peut être induit par une impulsion laser unique qui irradie le système magnétique dont la durée est généralement de l'ordre

## RÉSUMÉ DE LA THÈSE

---

de quelques dizaines voir centaines de femtosecondes. Principalement observé dans l'alliage amorphe  $\text{GdFeCo}$ <sup>8,123</sup>, l'AO-HIS a été étendu à d'autres systèmes tels que  $\text{Mn}_2\text{Ru}_x\text{Ga}$ <sup>132, 126</sup>,  $\text{GdTbCo}$ <sup>127,128</sup>,  $\text{TbCo}$ <sup>129–131</sup> mais aussi dans des systèmes ferrimagnétiques de synthèse, en particulier les arrangements multicouches  $\text{Tb/Co}$ <sup>133–135</sup>,  $\text{Tb/Fe}$ <sup>135</sup> and  $\text{Co/Gd}$ <sup>10,11,136</sup>.

Les phénomènes en jeu sont issus d'un état hors équilibre transitoire comme l'ont suggéré les premiers travaux pionniers sur la désaimantation ultrarapide<sup>6,85</sup>. En effet le système n'est pas thermalisé, en d'autres termes il n'est pas à l'équilibre thermodynamique. Il a été montré dans le cas de l'alliage amorphe  $\text{GdFeCo}$ , matériau qui est au coeur de ces études, que l'irradiation par une impulsion laser ultrarapide donne lieu à une différence de température entre le système électronique (électrons de conduction), le réseau cristallin (les phonons) et les spins. Puisque l'état de non-équilibre peut être caractérisé par une différence de potentiel chimique entre deux sous-systèmes qui interagissent entre eux, les électrons portant un spin up et down ne possèdent pas eux-mêmes le même potentiel chimique. Les différents acteurs ne sont donc pas à l'équilibre entre eux. Cependant ils sont interdépendants donnant lieu à des transferts d'énergie et de moment angulaire pour retrouver un état d'équilibre global. Par exemple, les électrons localisés du Gd, qui portent l'aimantation, transfèrent ce moment angulaire via les électrons de conduction, plus mobiles, vers l'autre sous réseau magnétique FeCo. Ceci donne lieu naissance à un état transitoire ferromagnétique puis c'est le sous système FeCo qui permet par la suite de renverser l'orientation magnétique du Gd. Il est important de souligner que le Gd ne peut pas dissiper ni d'énergie ni de moment angulaire avec le réseau cristallin, permettant de consacrer toute l'énergie de l'impulsion laser absorbée au retournement d'aimantation.

Le mécanisme sous-jacent de ce type de retournement d'aimantation tout optique est un effet thermique puisque l'ingrédient clé est la quantité d'énergie reçue par le système ferrimagnétique par l'impulsion laser ultrarapide. Dans cette perspective nous employons la plasmonique pour que le processus soit moins demandeur en énergie puisque l'excitation d'un mode plasmonique implique que le système visé va absorber plus d'énergie que si aucun mode n'était excité. Par exemple, dans le cas d'une nanoparticule faite de métal noble, le nuage d'électrons va répondre à un champ électrique oscillant externe tout comme un ressort répondrait à une sollicitation externe. Il existe ainsi une fréquence, la fréquence plasmon, pour laquelle les oscillations du nuage d'électrons sont extrêmement prononcées menant à une forte absorption d'énergie par la nanoparticule. On parle de résonance de plasmon de surface localisée (LSPR) lorsqu'une seule nanoparticule est impliquée. Lorsque plusieurs particules sont impliquées dans un réseau périodique, elles peuvent être amenées à se coupler entre elles. Cela intervient quand la résonance de plasmon de surface localisée de chaque entité coïncide avec la résonance propre du réseau. Ainsi,

tous les dipôles induits oscillent en phase grâce à l'hybridation des modes donnant lieu à une résonance, la résonance de réseau de surface (SLR), où la perte de cohérence de l'oscillation des électrons serait moindre. La facilité de perdre cette cohérence ou non se traduit par une largeur spectrale de la résonance plus ou moins prononcée. Le fait de passer d'un système unique à un comportement collectif permet donc d'améliorer la qualité de la résonance plasmonique et donc de la quantité d'énergie absorbée par le système.

Par ailleurs, la résolution spatiale de l'AO-HIS est limitée à une dizaine de micromètres ce qui n'est absolument pas compétitif en comparaison des disques durs actuels qui travaillent à l'échelle nanométrique. Dans ce sens, la plasmonique est requise puisqu'elle fournit également les outils pour manipuler la lumière à l'échelle nanométrique, surpassant la limite fixée par la diffraction de la lumière<sup>20</sup>. Plusieurs études ont déjà montré que l'on pouvait soit effectuer de l'AO-HIS dans des nanostructures magnétiques<sup>126,327-329</sup> soit utiliser des modes localisés, via des nanoantennes d'or, pour rendre l'AO-HIS possible à l'échelle nanométrique dans un film mince magnétique combiné à un coût énergétique réduit<sup>168</sup>. Nous explorons dans cette thèse la possibilité de coupler les deux approches via l'excitation de résonances de réseau de surface dans des arrangements périodiques de nanodisques magnétiques constitués de plusieurs motifs de [Co/Gd/Pt].

En réalité, la plasmonique a déjà été intégrée dans certains dispositifs à mémoire de données. Le matériau impliqué dans les disques durs est granulaire, constitué de grains de FePt<sup>320,321,336</sup>, matériau présentant une forte anisotropie. Cette propriété est importante pour éviter les fluctuations thermiques menant à des retournements d'aimantation non voulus. Cependant cette forte anisotropie rentre en conflit avec la volonté de retourner l'aimantation de grains plus petits puisque ces derniers requiert un champ magnétique bien plus élevé pour qu'ils puissent voir leur aimantation changer d'orientation. L'industrie de stockage de données doit ainsi faire face à un trilemme. Le développement de l'enregistrement magnétique assisté par la chaleur (HAMR) a permis d'y remédier et d'obtenir d'une densité atteignant 1 Tb/in<sup>23,4,316,317</sup>. L'idée est de chauffer localement le matériau magnétique avec un laser focalisé pour le rendre plus mou de manière à réduire le champ magnétique nécessaire pour observer un renversement d'aimantation. La résolution des technologies HAMR est cependant limitée par la taille du faisceau optique dont les dimensions sont au dessus de la limite de diffraction. Ainsi l'utilisation de transducteur de champ proche permet via l'excitation de résonance plasmonique localisée permet de chauffer localement le matériau granulaire magnétique<sup>5</sup>. L'intégration de la plasmonique dans les technologies HAMR permet d'utiliser des matériaux magnétique à forte anisotropie avec une taille de grain inférieure à 7 nm<sup>318-321</sup>. Cette configuration permet de réduire rapidement le champ

## RÉSUMÉ DE LA THÈSE

---

coercitif quand le matériau est irradié et une couche adjacente, jouant le rôle de dissipateur de chaleur, permet de refroidir rapidement le matériau de manière à restaurer rapidement les propriétés magnétiques quand le laser n'irradie pas la zone. Nous intervenons également sur cette composante des futures technologies HAMR pour permettre l'AO-HIS possible pour des durées d'impulsion laser plus longues.

Ainsi, avant de présenter nos résultats, nous présentons le cadre conventionnelle de la dynamique d'aimantation et détaillons les propriétés magnétiques des matériaux que nous utilisons. Après avoir décrit les premiers travaux pionniers sur la désaimantation ultrarapide, nous montrons que ces matériaux peuvent voir leur aimantation se renverser sous l'action d'une impulsion de lumière ultrarapide dont la polarisation est linéaire. Puisque le mécanisme sous-jacent est purement thermique, nous suggérons que nous pouvons l'améliorer en utilisant des nanostructures constituées toujours du même matériau. De plus, l'intégration de la plasmonique ouvre de nouvelles perspectives en termes de densité d'écriture puisque les films minces magnétiques ne permettent pas de stabiliser des domaines magnétiques à l'échelle nanométrique. Après avoir revu les différents travaux utilisant la plasmonique non seulement pour un meilleur confinement de la lumière conduisant à un retournement d'aimantation exigeant moins d'énergie mais aussi pour une forte augmentation des effets magnéto-optiques, nous expliquons en quoi les travaux de recherche de cette thèse s'inscrivent dans cette dynamique et y apportent plus de profondeur. Nous expliquons quels moyens ont été mis à notre disposition pour faire vivre ces travaux, à la fois d'un point de vue expérimental mais aussi théorique.

L'idée générale de cette thèse est de savoir comment exploiter le mécanisme thermique de l'AO-HIS, comment le contrôler et comment l'améliorer. Dans un premier temps nous avons nanofabriqué des réseaux périodiques de nanodisques de [Co/Gd/Pt] afin d'exciter des résonances de réseau de surface. Après avoir caractérisé les échantillons à *Aalto University* au sein du groupe de Sebastiaan van Dijken, nous avons montré que nous pouvions contrôler la réduction l'énergie seuil pour l'AO-HIS avec la longueur d'onde, observée comme étant la plus importante lors de l'excitation du mode plasmonique. Nous avons remarqué que bien que le retournement soit déterministe sur le film mince, les nanodisques sont soumis à un retournement stochastique. En particulier, ce renversement incomplet dépend d'une probabilité de retournement qui ne dépend a priori que de la taille des nanodisques. Nous avons identifié que cette probabilité augmente pour des disques plus petits, suggérant que le retournement pourrait être déterministe pour des nanodisques encore plus petits que ceux étudiés. Puisque l'enregistrement magnétique a également besoin d'une méthode de lecture de l'information qui soit fiable, nous montrons qu'à la résonance plasmonique, la réponse magnéto-optique est exacerbée dans les nanostructures en

comparaison au film mince, jusqu'à un facteur d'amélioration de 60.

Nous soulignons le fait que, comme nous souhaitons lire uniquement l'information avec de la lumière grâce à la magnéto-optique, il est important de distinguer clairement les niveaux intensités lumineuses réfléchies par les échantillons dans les configurations up et down. Nous parlons alors de contraste magnéto-optique. Cette quantité a été mesurée en fonction de la longueur d'onde pour toutes les géométries de réseaux périodiques étudiées. De part ces mesures nous avons été en capacité d'extraire les spectres magnéto-optiques. Puisque la lumière incidente arrivait sur le système avec un angle d'incidence non-nul avec une polarisation  $s$ , c'est-à-dire que la composante du champ électrique est orthogonale au plan d'incidence, nous avons mis en lumière l'existence de résonances de réseaux d'origine magnétique. En effet, en comparant avec un système métallique non magnétique dans les mêmes conditions expérimentales, nous montrons la présence d'une résonance supplémentaire. Ceci est due au fait que des nanodisques magnétiques, sous l'action d'une onde incidente polarisée linéairement, manifestent deux dipôles électriques induits qui sont orthogonaux entre eux. Le premier est aligné avec le champ magnétique, il est d'origine purement optique. Le deuxième lui est orthogonal et existe du fait du caractère magnétique de la nanostructure. C'est donc le couplage radiatif de tous ces dipôles magnéto-optiques qui permet l'existence d'une résonance de réseau de surface additionnelle.

Dans un dernier temps, nous avons cherché à proposer de nouvelles stratégies pour être capable d'observer de l'AO-HIS pour des durées d'impulsion laser plus longues dans l'idée de pouvoir l'appliquer plus facilement dans les futures mémoires de données à enregistrement magnétique. En effet, la limite fixée par la lecture avoisine les 15 picosecondes<sup>139,143</sup> mais nos résultats suggèrent que nous pourrions retourner l'aimantation de couches atomiques de GdFeCo avec des impulsions laser dont la durée limite serait de 25 ps. Dans notre étude nous avons conservé une composition atomique de Gd de 24%. En revanche, nous avons fait varier l'épaisseur de la couche de cuivre adjacente à la couche magnétique, de 5 à 900 nm. Nous montrons que la fluence seuil pour observer du retournement d'aimantation induit par la lumière ne dépend presque pas que l'épaisseur de cuivre. En revanche, pour un temps d'impulsion laser donné, la fluence seuil pour obtenir un état multidomaine stochastique en dépend fortement. Elle tend à augmenter avec une couche de plus en plus épaisse. Ainsi, la couche de cuivre joue le rôle de dissipateur de chaleur permettant un refroidissement plus ou moins important du système électronique impliquant un retournement ou non de l'aimantation du GdFeCo. Cette étude permet d'affiner notre compréhension de l'AO-HIS, notamment via la confirmation de nos résultats par la théorie, couplant un modèle à deux températures (les électrons et les phonons) avec un modèle de dynamique de spin. Nous montrons que pour obtenir de l'AO-HIS, le système électronique,

## RÉSUMÉ DE LA THÈSE

---

lors de son état transitoire, doit dépasser une certaine température critique avant de se refroidir en dessous de la température de désordre magnétique avant un certain temps limite. Ainsi, nous affirmons que ce qui limite l'AO-HIS pour des temps d'impulsion trop longs n'est pas une faible diffusion d'échange (transfert d'énergie et de moment angulaire entre les électrons et les spins) mais bien un refroidissement inefficace du système électronique. Nous proposons ainsi de repousser cette limite avec des dissipateurs de chaleur. Une manière de représenter les conditions limites de l'AO-HIS est de représenter graphiquement les fluences seuil de retournement et d'état multidomaine en fonction du temps d'impulsion laser<sup>116,141</sup>. Ainsi, l'utilisation de dissipateurs de chaleur permet d'ouvrir la fenêtre de fluences utilisables pour observer de l'AO-HIS, ayant pour conséquence directe une augmentation du temps d'impulsion laser limite. Une extrapolation de nos données estime un temps d'impulsion limite de 25 picosecondes qui est propre à nos échantillons mais qui peut sans aucun doute être étendu pour d'autres compositions atomiques de Gd.

Ainsi cette thèse s'est concentrée sur deux des trois aspects importants des nouvelles technologies HAMR : le matériau granulaire et le dissipateur de chaleur. Nous avons développé un matériau granulaire artificiel via des arrangements périodiques de nanodisques magnétiques de [Co/Gd/Pt]. Ces derniers permettent l'excitation de résonances plasmoniques collectives menant à une augmentation de l'absorption de l'énergie lumineuse par le système. Cette approche permet non seulement de réduire l'énergie seuil pour observer de l'AO-HIS, mais il permet également de l'obtenir à une échelle spatiale qui n'est pas envisageable des films minces continus. Par ailleurs, ces résonances plasmoniques permettent de booster la réponse magneto-optique, prometteur pour une bonne sensibilité de lecture. Une étude faite pour un angle d'incidence non nul a permis de mettre en lumière des résonances de réseau d'origine magnétique. Le deuxième aspect que nous avons considéré est l'impact d'un dissipateur thermique sur le retournement. Ce dernier a pour effet d'étendre l'AO-HIS à des temps d'impulsion laser plus grands et pour une plage d'énergie du laser plus large pour une durée d'impulsion donnée. Cet aspect est prometteur pour une applicabilité moins contraignante de l'AO-HIS pour les futures mémoires de données tout optique.